Distribution Agreement

In presenting this thesis or dissertation as a partial fulfillment of the requirements for an advanced degree from Emory University, I hereby grant to Emory University and its agents the non-exclusive license to archive, make accessible, and display my thesis or dissertation in whole or in part in all forms of media, now or hereafter known, including display on the world wide web. I understand that I may select some access restrictions as part of the online submission of this thesis or dissertation. I retain all ownership rights to the copyright of the thesis or dissertation. I also retain the right to use in future works (such as articles or books) all or part of this thesis or dissertation.

Signature:

_____ _____

Noel X. Li Date

Amplification of amyloid-beta strains and their connection to tau in Alzheimer's Disease

By

Noel X. Li
Doctor of Philosophy

Chemistry

David G. Lynn, Ph.D.
Advisor

Vincent Conticello, Ph.D.
Committee Member

Stefan Lutz, Ph.D.
Committee Member

Accepted:

Lisa A. Tedesco, Ph.D.
Dean of the James T. Laney School of Graduate Studies

Date

Amplification of amyloid-beta strains and their connection to tau in Alzheimer's Disease

By

Noel X. Li
B.Sc. Nanyang Technological University, 2010

Advisor: David G. Lynn, Ph.D.

An abstract of
A dissertation submitted to the Faculty of the
James T. Laney School of Graduate Studies of Emory University
in partial fulfillment of the requirements for the degree of
Doctor of Philosophy in Chemistry
2018

Abstract

Amplification of amyloid-beta strains and their connection to tau in Alzheimer's Disease

By Noel X. Li

The formation of amyloid-beta (Aβ) and tau aggregates are pathological hallmarks of Alzheimer's disease (AD), yet their etiological roles in the disease are unknown despite decades of research. Different strains, or polymorphic structures, of Aβ have been resolved and it is thought that their conformations have an influence on their downstream toxicities. To determine how Aβ fibrils in AD and ND (non-demented healthy control) brains are different, we amplified them by seeding into synthetic Aβ. Disaggregation of purified Aβ peptides with NH_4OH was essential for maximizing seeding efficiency. Brain homogenates were enriched for Aβ to reach the critical seed concentration, and we seeded them into Aβ40 and Aβ42 sequentially for two generations. The oligothiophene HS-68 spectrally distinguished quiescent, agitated and brain-seeded Aβ40, but not between AD- and ND-seeded Aβ40. Oligothiophene binding to seeded Aβ42 showed more differences, with pentamer formyl thiophene acetic acid (pFTAA) displaying different relative peak intensities at 425 nm in frontal lobe-seeded AD and ND brain. A 1% molar equivalent of assembled Aβ sufficiently lowered the critical assembly concentration of PHF6 (the nucleating core of tau) and catalyzed fibrillization. Both Aβ seeds and fibrils had similar cross-seeding rates, suggesting a combination of elongation and secondary nucleation mechanisms. PHF6 monomers cross-seeded by brain-seeded Aβ42 showed biphasic growth, which we attribute to cross-seeding in the initial ten hours and self-seeding taking over after a critical mass of PHF6 fibrils have formed. AD frontal lobe-seeded Aβ42 cross-seeded the formation of short PHF6 fibrils which self-seeded efficiently, while ND frontal lobe-seeded Aβ42 cross-seeded the formation of long, bundled PHF6 fibers which were ineffective seeds, analogous to observations in yeast prion strains. Our results suggest that structural differences in Aβ can be directly propagated to tau in AD, highlighting an attractive therapeutic opportunity at the Aβ-tau triggering point that needs to be explored, rather than current Aβ-focused approaches.

Amplification of amyloid-beta strains and their connection to tau in Alzheimer's Disease

By

Noel X. Li
B.Sc. Nanyang Technological University, 2010

Advisor: David G. Lynn, Ph.D.

A dissertation submitted to the Faculty of the
James T. Laney School of Graduate Studies of Emory University
in partial fulfillment of the requirements for the degree of
Doctor of Philosophy in Chemistry
2018

Acknowledgements

Wow. I'm finally seeing the light at the end of the tunnel. Research in grad school feels like a solitary journey on many days but in retrospect, I wouldn't have gotten here without the help of so many people.

I would like to express my deepest gratitude to my advisor Dr. David Lynn for his guidance and mentorship, and especially having the patience and confidence in me when I'm deep in the weeds of failed experiments. His insights, resilience and work ethic never fail to amaze me as I continue to look up to him.

I am thankful for my committee members, Dr. Stefan Lutz and Dr. Vincent Conticello, for imparting their knowledge, advice and constructive feedback during exams, classes and rotations over the years. I will remember their teachings for many years to come.

Our collaborators, Dr. Lary Walker and Dr. Yury Chernoff, have been a great pleasure to work with. I have learned a lot history and knowledge of amyloid diseases, rodent and non-human primate models, yeast prions, etc. from them. Hearing them talk about science was certainly helpful in finding the motivation to recover from failures. Their graduate students, Dr. Amarallys Cintron and Dr. Pavithra Chandramowlishwaran, have also been instrumental in expanding my research.

I am thankful for Dr. Anil Mehta's guidance and teachings on experiments, NMR, data analyses, troubleshooting instrument problems and getting me started on the synthesis and purification of Aβ40 and 42. I am fortunate to have worked with past and present members of our lab, Dr. Jay Goodwin, Dr. Dan Pierce, Dr. Jillian Smith, Dr. Dibyendu Das, Dr. Junjun Tan, Dr. Savannah Johnson, Dr. Chenrui Chen, Dr. Tolulope Omosun, Dr. Sha

(Lisa) Li, Dr. Li Zhang, Dr. Allisandra Rha, Dr. Rolando Rengifo, Dr. Chen Liang, Dr. Jackey Hsieh, Dr. Yushi Bai, Dr. Olga Taran, Ting (Fish) Pan, Anthony Sementilli, Siying Cen, Youngsun Kim, Christella Dhammaputri and Mandy Chan. They make the lab a nice place to work in, and I have learned a lot of experimental techniques, received feedback and assistance with administrative and lab stuff from them. I am also thankful to the students whom I've had the opportunity to mentor in the lab, Rebekah Brooks, Jenny Tran, Dhruv Khurana, Avi Tuachi and Anirudh Pidigu, for allowing me to hone my mentoring skills and assisting me in one way or another.

I am grateful to Hong Yi, Jeannette Taylor and Arthur McCanna of the Electron Microscopy Core for TEM training and support. Steve Krebs and Claire Scott in the stockroom were essential in ensuring that any problems with my orders were resolved, and I thank them for making this as stress-free as possible. I am also thankful to the staff at CEM, Chris James, Michael Sciole and Greg LeBlanc, for walking me through troubleshooting on our peptide synthesizer. Our downtimes would have been significantly longer if I didn't know what to look for on the instrument.

I am lucky to have enrolled in grad school with Samuel Jeong, who has given me suggestions and ideas, troubleshooted instruments and experiments with me, shared the latest news in science over lunch, and being my tech support every time I had computer issues.

I thank my family and parents for their support over the years and understanding that I've had to miss many events at home.

Finally, I am grateful to my wife Felicia, for her patience in letting me hold off life in general to pursue my graduate degree, ensuring I have food at home, and having enough confidence in me to relocate here.

Table of Contents

Chapter 1. Introduction

Chapter 4. Seeding of brain extracts into synthetic Aβ

Chapter 5. Amyloid-β and Tau Interactions

List of Figures

Chapter 1.

Chapter 2.

Chapter 3.

Chapter 4.

Chapter 5.

List of Tables

List of Abbreviations

ADRC	Alzheimer's Disease Research Center
AFM	Atomic force microscopy
Ag	Agitated
Aβ	Amyloid beta
CD	Circular dichroism
CJD	Creutzfeldt-Jakob disease
DCM	Dichloromethane
DMF	Dimethylformamide
ECM	Extracellular matrix
FTIR	Fourier transform infrared
HFIP	1,1,1,3,3,3-hexafluoroisopropanol
HPLC	High-performance liquid chromatography
LCO	Luminescent conjugated oligothiophene
MALDI-MS	Matrix-assisted laser desorption/ionization mass spectrometry
MWCO	Molecular weight cut-off
NFT	Neurofibrillary tangle
PAGE	Polyacrylamide gel electrophoresis
PBS	Phosphate-buffered saline
PES	Polyethersulfone
PET	Positron emission tomography
PiB	Pittsburgh Compound B
Q	Quiescent (when not used in the context of a peptide sequence)
SDS	Sodium dodecyl sulfate
SEM	Scanning electron microscopy
TEM	Transmission electron microscopy
ThT	Thioflavin T
UA	Uranyl acetate

Chapter 1. Introduction

Alzheimer's Disease (AD)

Alzheimer's disease (AD) is the most common form of dementia and is characterized by progressive memory loss, cognitive decline and eventual death. It is the 6th leading cause of death in the United States, with an estimated 5.7 million Americans living with AD in 2018. The costs for healthcare and long-term care were approximately $277 billion in 2018 and are projected to reach $1.1 trillion in 2050 as the population ages and the number of patients rise, placing an immense economic burden on society [1]. Among the top ten leading causes of death in the US, AD is the only cause that cannot be prevented, slowed or cured, largely due to our lack of understanding of the exact cause(s) of the disease. Consequently, AD drug candidates are one of the least successful in clinical trials, where between 2002 and 2012, the failure rate was 99.6% compared to 81% for cancer [2].

However, since AD was first reported by Alois Alzheimer in 1906 [3], many discoveries have been made about the clinicopathological features of the disease. The two neuropathological hallmarks of AD pathology are the cerebral deposition of extracellular senile plaques composed of aggregated amyloid-beta (Aβ) peptides and intracellular neurofibrillary tangles (NFTs) consisting of aggregated tau proteins. Amyloid plaque deposition is thought to precede NFT formation during the clinically silent phase, which could span two decades in sporadic or late-onset AD (LOAD) where symptoms manifest after the age of 65 years. Thereafter, AD-related neuropathology and brain atrophy set in, leading to the initial appearance of symptoms, especially memory impairment, in the mild cognitive impairment (MCI) stage [4]. Functional MRI (fMRI) studies show that early MCI patients have increased neuronal activity over healthy controls while performing memory

tasks, indicative of a compensatory mechanism being used to aid with task completion, perhaps via altered neuronal connections. However, the mechanism fails as brain atrophy continues, causing both late MCI and AD patients to show neuronal hypoactivation during tasks [5,6]. Further cognitive decline results in the progressive deterioration of performing daily tasks until the time of death (**Figure 1.1**).

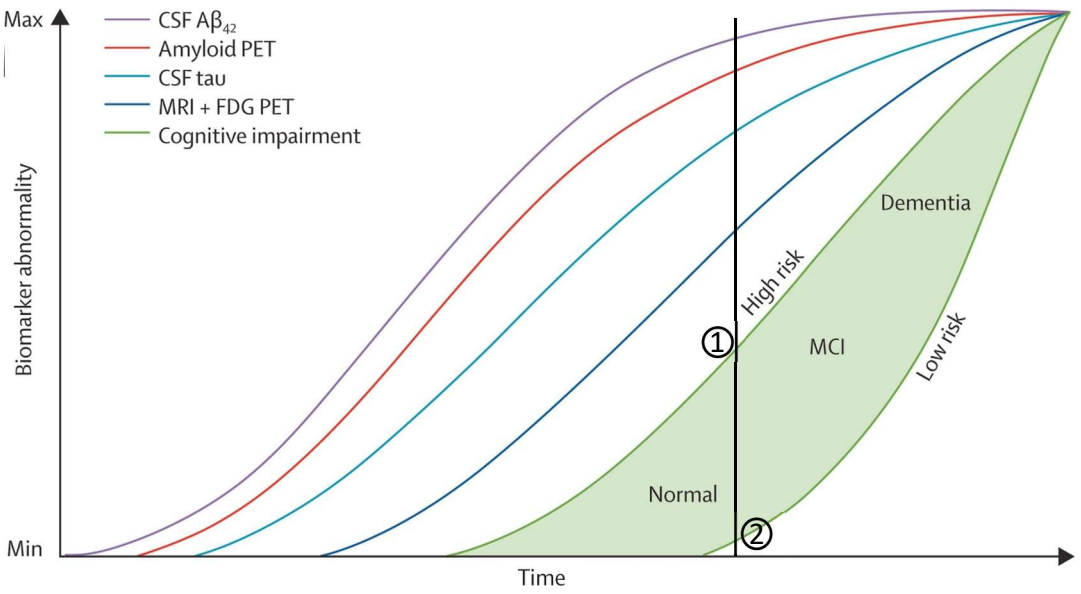

Figure 1.1. Model of biomarker changes in the progression of AD. The earliest detectable event is the presence of Aβ in the CSF, followed by the formation of amyloid plaques (PET imaging). Thereafter, tau accumulates in the CSF before neurodegeneration (FDG PET) and brain atrophy (MRI) set in. Since cognitive impairment is influenced by the genetics, lifestyle and cognitive reserve of each individual, it is depicted as a zone with varying levels of risk. For example, at a given time point (black vertical line) the CSF Aβ is likely to be the most abnormal biomarker and individuals with a high risk for AD will likely show clinical symptoms ①, while individuals with low risk for AD may be asymptomatic ②. FDG: fluorodeoxyglucose, MCI: mild cognitive impairment. Figure adapted from ref. [7].

Extensive research has explored stages from the earliest detectible abnormalities to the final stages of AD, and this chapter will highlight our current understanding of the

neuropathological events in the preclinical stage, the biomarkers developed for detecting plaques and tangles, and some of the strategies used for developing therapeutics.

Molecular pathology

1.1 Amyloid precursor protein (APP)

Aβ is produced from the APP, a type I membrane protein where the N-terminus is on the extracellular surface and the C-terminus is in the cytoplasm joined by a single transmembrane domain (**Figure 1.2A**). As the APP gene is located in chromosome 21, individuals with Down's syndrome have an increased risk for AD and cerebral amyloid angiopathy (CAA), develop symptoms earlier and show accelerated AD progression due to increased APP expression and Aβ production [8]. The three most common isoforms of APP are 695, 751 and 770aa long, with APP695 being the most abundant isoform [9].

While the normal physiological function of APP remains unclear, overexpression of the APP ortholog in *Drosophila* was found to rescue short-memory impairment, suggesting that APP may be involved in memory formation [10]. APP knockout mice show reduced grip strength, locomotor activity and impaired learning and memory deficits compared to age-matched wild type mice [11]. Other studies suggest a role in axonal pruning, neuronal death [12] and cell adhesion via integrin-like receptors [13].

1.2 Amyloid-beta (Aβ) production

Aβ is secreted when APP is first cleaved extracellularly by β-secretase (also known as BACE1, beta-site APP cleaving enzyme 1) at the N-terminus of the Aβ sequence, producing the membrane-bound C99 or C-terminal fragment (CTF). Thereafter, γ-secretase cleaves the C-terminal end of Aβ, releasing the APP intracellular domain (AICD) fragment into the

cytoplasm and the Aβ peptide into the brain interstitial fluid (ISF) (**Figure 1.2C**). Depending on where γ-secretase cleaves, the length of the Aβ peptide can range from 38 to 43 residues, although Aβ40 and Aβ42 are the dominant species. Aβ42 is predominant within senile plaques while Aβ40 is more abundant in the CSF [14,15], consistent with findings that Aβ42 aggregates faster than Aβ40 *in vitro* and that low Aβ42:Aβ40 ratios in blood plasma are significantly associated with the development of AD [16]. If APP is cleaved by α-secretase between residues 16 and 17 of Aβ instead of β-secretase, a non-amyloidogenic p3 (Aβ17-42) fragment is eventually released (**Figure 1.2B**).

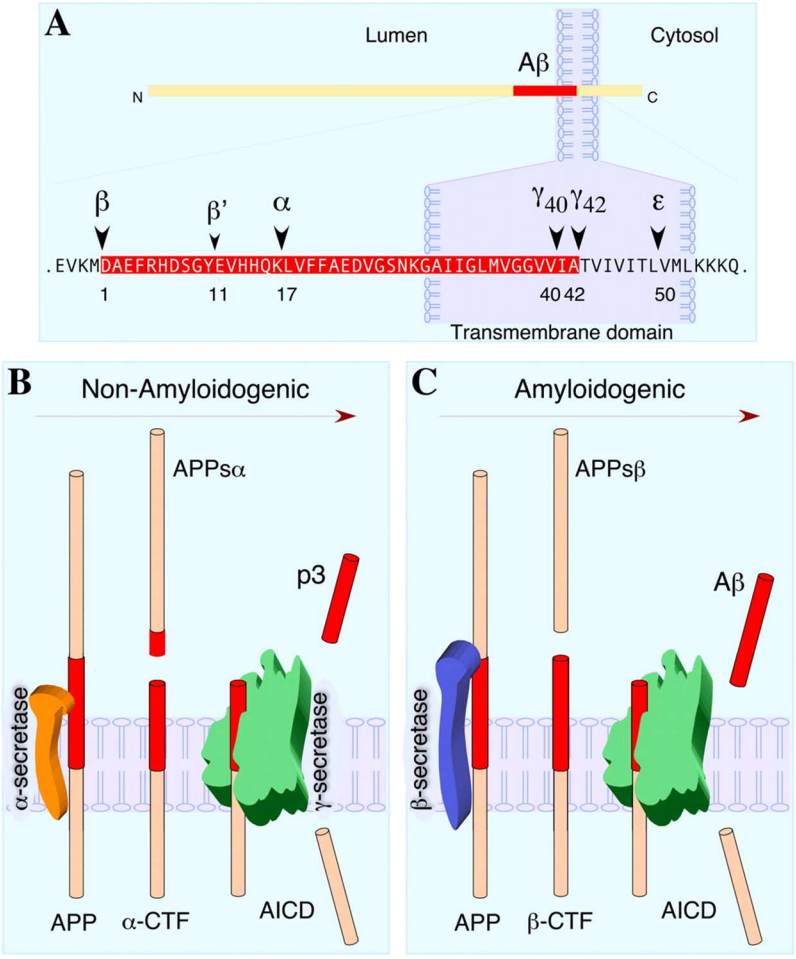

Figure 1.2. Proteolytic cleavage of APP (amyloid precursor protein). (A) The Aβ domain of APP is highlighted in red and the secretase cleavage sites are indicated. (B) Sequential cleavage by α- and γ-secretase eventually results in the release of the non-

amyloidogenic p3 peptide. (C) Initial cleavage by β-secretase instead of α-secretase leads to the release of the amyloidogenic Aβ peptide into the extracellular domain. Figure reproduced from ref. [17].

γ-Secretase consists of four subunits, presenilin 1 or 2 (PS1 and PS2), nicastrin, anterior pharynx defective 1 (APH-1), and presenilin enhancer 2 (PEN-2) [18]. Almost all mutations discovered in APP, PS1 and PS2 lead to an increased Aβ production and plaque formation, and are typically associated with familial or early onset AD (EOAD) where symptoms appear before the age of 65 years, representing about 5% of AD cases [19]. In contrast, most AD patients with no heritable mutations develop LOAD.

The kinetics of Aβ aggregation follows the nucleation-dependent polymerization model [20], which depends on peptide concentration and time. Below the critical assembly concentration, monomeric peptides do not nucleate and assemble into fibrils. Above this threshold, Aβ monomers nucleate and form oligomers in the lag phase, where they sample the conformational landscape to find thermodynamically stable states and transition from α-helical and random coil states to β-sheet-rich structures [21]. The cross-β structure is a defining feature of amyloid fibrils, where x-ray diffractions show orthogonal reflections at approximately 4.8 and 10 Å spacings, corresponding to the hydrogen bonding distance along the fibril axes and β-sheet lamination perpendicular to the fibril axes respectively.

The critical assembly concentration of Aβ40 *in vitro* is estimated to range from 10-40 μM at neutral pH and 5-fold lower for Aβ42 [22], but CSF concentrations of Aβ are in the low nanomolar range [23]. As such, there must be a local supersaturation mechanism which allows Aβ to nucleate and propagate. It is thought that Aβ is concentrated *in vivo* within cellular compartments such as lysosomes [24-26], or that the critical concentration is lowered when Aβ binds to a phospholipid [27] or protein [28] surface. The aggregated Aβ would then

be below its critical concentration upon release into the ECM, but the slow kinetics of fibril disassembly likely favors aggregation with plaques [22].

The lag phase can be bypassed by the introduction of pre-formed seeds, where they provide a template for the monomers to propagate. Seeding eliminates the lag time and the system immediately enters the elongation phase, just as in salt crystallization. This requires that the end of the seed and incoming monomer be in complementary conformations for the hydrogen bonds to be aligned, but the Aβ monomers are likely in random coil conformations. A widely-accepted model for fibril seeding and elongation is the dock-and-lock model, where the incoming peptide binds reversibly to the seed (docking), undergoes a conformational rearrangement to assume that of the seed, before it is irreversibly bound (locking) and then serves as a template for the next incoming peptide [29].

While there are conflicting studies and views on whether the oligomers [30-36] (also referred to as ADDLs; Aβ-derived diffusible ligands) or fibrils [37] are the neurotoxic species, it is generally agreed upon that Aβ monomers must at least oligomerize to have a detrimental effect [30,38]. It may be possible that the higher toxicity of oligomers results from their higher diffusibility into cellular compartments and synapses [39] while the fibrils are immobilized in the plaques, or simply by the law of mass action that there are more oligomers than fibrils for a given number of peptides. Other proposed mechanisms by which Aβ oligomers induce toxicity include (i) binding to lipid rafts and receptors to interfere with signal transduction [40-42], (ii) membrane disruption and leakage through pore formation [43] and (iii) disrupting intracellular processes such as calcium homeostasis and mitochondrial function [44-46]. However, the presence of a mixture of Aβ species ranging from monomers to fibrils in the brain makes it difficult to attribute the toxicity to one

species while ruling out the rest, and characterization of oligomers can be challenging due to their transient, heterogeneous and metastable nature.

The presence of Aβ in the media of neuronal cell cultures [47], CSF and plasma in healthy volunteers [48,49] suggest that APP metabolism and Aβ production are not solely pathological events but may, to some extent, be normal physiological processes. In AD, amyloid toxicity may result from the loss of protein function, mislocation or sequestration of proteins, but the favored hypothesis is a gain of toxic function [50,51].

1.3 Structural heterogeneity in amyloid fibrils

The concept of Aβ strains is borrowed from the prion field, where alternative conformations of the protein are manifested in the phenotypes. For example, there are hyper and drowsy PrP^{Sc} strains in hamster transmissible mink encephalopathy where the infected hamsters would display hyperactivity or lethargy respectively [52]. Other variabilities in prion phenotypes include the incubation time to onset of symptoms, deposition pattern in the brain, physicochemical features of the prion aggregates, and clinical symptoms [53]. Aβ fibril heterogeneity may be one factor that explains why the number, size or density of amyloid plaques are weakly correlated with the degree of cognitive impairment [54], or how patients may have asymptomatic AD (Aβ and tau neuropathology without clinical symptoms) or rapidly progressive AD [55,56].

Synthetic Aβ40 was reported to form polymorphs as observed by electron microscopy and solid-state NMR, when assembled under quiescent or agitated conditions, demonstrating that the structure was not exclusively dictated by the amino acid sequence [57]. Quiescent Aβ40 forms twisted fibrils with a trimeric protofilament cross-section (**Figure 1.3A**) while agitated Aβ40 forms straight, bundled fibers with a dimeric

protofilament cross-section (**Figure 1.3B**), which can also be propagated when those seeds are added to Aβ40 monomers under quiescent growth conditions [57]. Seeding of AD brain extract into Aβ40 fibrils yielded fibers with an altered trimeric structure. Compared to quiescent Aβ40, the AD-seeded Aβ40 had more pronounced kinks in the beta-fold and the first nine residues at the N-terminus are ordered, making them resolvable (**Figure 1.3C**). Polymorphs of Aβ42 assembled under various conditions have also been resolved (**Figure 1.3**), but identifying pathologically-relevant structural features and correlating them to their downstream functions or toxicities remain a major challenge for the field.

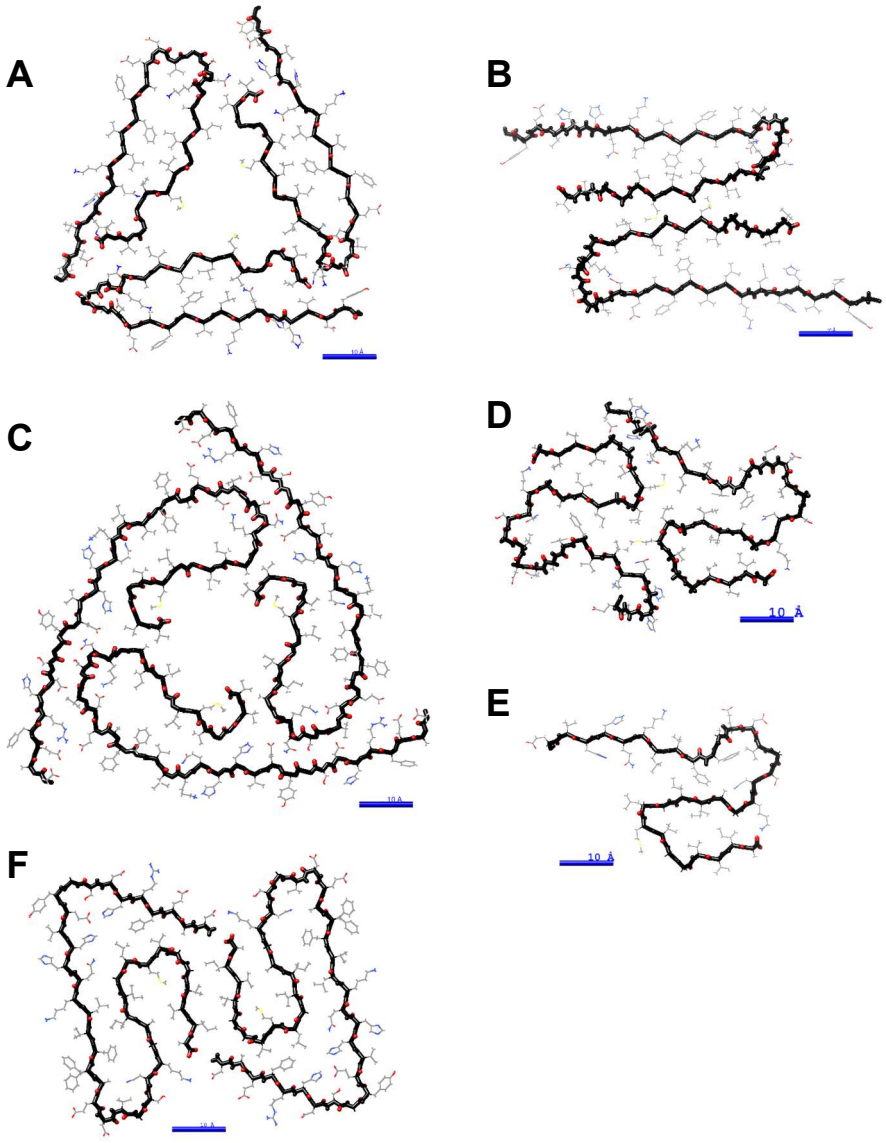

Figure 1.3. Cross-sectional folds of Aβ40 and Aβ42 fibrils. (A) Quiescent Aβ40, PDB: 2LMP, (B) agitated Aβ40, PDB: 2LMN, (C) AD brain-seeded Aβ40, PDB: 2M4J, (D) Aβ42, PDB: 5KK3, (E) Aβ42, 2MXU, (F) Aβ42, PDB: 5OQV. Images generated with UCSF Chimera [58]. Scale bar: 1 nm.

1.4 Tau hyperphosphorylation and aggregation

Under physiological conditions, the mainly axonal tau protein binds, stabilizes and promotes the assembly of microtubules. In the disease state, however, tau is

hyperphosphorylated (p-tau) and undergoes a conformational change that inhibits normal binding to microtubules and is also mislocalized into the somatodendritic compartment [59]. This results in axonal destabilization, impaired transport along axons and eventual neuronal dysfunction and death. Microtubule densities in neurons are also reduced but weakly correlated to PHF densities, meaning that the loss of tau function is insufficient to account for microtubule loss [60]. Depending on the sites of phosphorylation, p-tau may also have a higher propensity for aggregation into β-sheet-rich paired helical filaments (PHF) which are the primary component of NFTs [61].

Hyperphosphorylation, however, is not a reliable indicator of neurodegeneration. PHF-like tau hyperphosphorylation has been detected in arctic ground squirrels, Syrian hamsters and black bears during hibernation, but upon arousal to the normal state, the phosphorylation levels return to normal within hours [62]. Furthermore, fetal tau is also highly phosphorylated during development and has a low binding affinity to microtubules, allowing for a flexible cytoskeleton that increases neural plasticity for synapse formation [63]. Therefore, the pathological relevance of tau hyperphosphorylation is debatable since it can reversibly occur under certain physiologically normal conditions.

The human tau gene is located on chromosome 17 and undergoes alternative splicing to produce six isoforms of tau, each consisting of either zero, one or two N-terminal inserts (0N, 1N, 2N) and three or four microtubule binding repeats (3R, 4R). The N-terminal domain containing the inserts is also called the projection domain because they project away from the microtubules; the middle region of tau has a proline-rich domain; and the C-terminal half contains the repeat domains also known as the microtubule binding region (MTBR). The R2 and R3 repeat domains contain the nucleating cores of tau, PHF6 (^{306}VQIVY^{311}K) in R3 and PH6* (^{275}VQIIN^{280}K) in R2 (**Figure 1.4**).

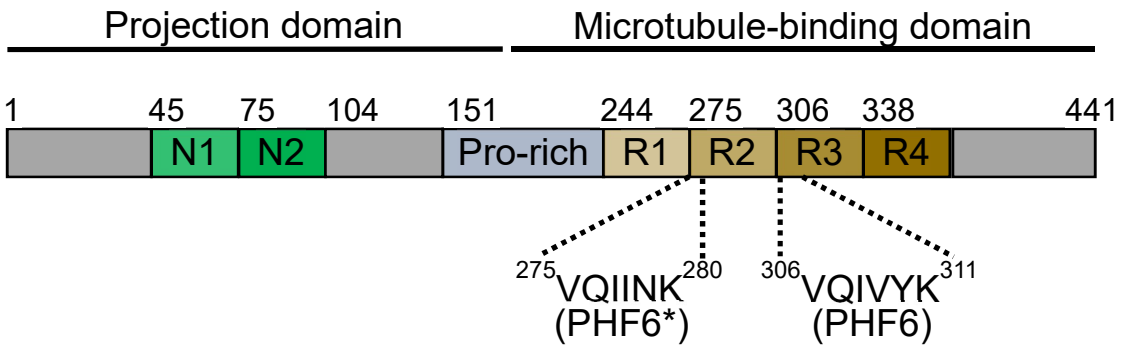

Figure 1.4. Overview of tau structure and domains. The longest isoform of human tau (2N4R) shown here is 441 residues long and has two N-terminal inserts and four repeat domains. Six isoforms of tau are expressed in adult neurons depending on alternative splicing of exons 2, 3 and 10 of the tau gene corresponding to N1, N2 and R2. The PHF6* and PHF6 nucleating cores are located at the beginning of the R2 and R3 domains.

Aβ aggregates derived from patients were found to trigger tau hyperphosphorylation, cytoskeletal disruption and cell death in neuronal cell cultures [36]. Furthermore, synthetic Aβ42 [64] and brain extracts from APP transgenic mice [65] injected into the brains of tau transgenic mice resulted in widespread NFT formation. While these experiments provide strong evidence that Aβ aggregates trigger tauopathy, cellular and animal models are inherently black boxes so the exact mechanistic link between Aβ and tau aggregation remains unknown. Elucidation of the mechanism, whether it is via direct cross-seeding, kinase overactivation/phosphatase inhibition, or decline of protein clearance mechanisms, can reveal another therapeutic opportunity by preventing tauopathy from being triggered.

Probes for detecting Aβ and tau

1.5 Pittsburgh compound B (PiB)

One of the most common PET radioligands used to image amyloid plaques in living patients is ^{11}C-PiB, a neutral, lipophilic derivative of thioflavin T (ThT) that has a different

binding site than Congo red (CR) or ThT [66]. Unlike other charged amyloid ligands, uncharged molecules such as PiB bind more effectively to amyloids in the brain because they can penetrate the blood-brain barrier.

Compared to healthy controls, PiB retention in AD patients were significantly higher in brain regions where extensive amyloid deposition is observed in postmortem tissues (frontal, parietal, temporal and occipital cortices and striatum) while no differences in PiB retention were observed in areas known to have insignificant amyloid deposition (subcortical white matter, pons, and cerebellum). Autopsies of patients who previously had PiB PET scans confirmed the distribution of Aβ deposits in the brains [67-69]. PiB retention in the cortices was also inversely correlated to cerebral glucose metabolism measured by ^{18}F-FDG binding, indicative of neuronal dysfunction [70]. Almost two-thirds of MCI patients show significant amyloid deposition based on PiB binding and they also have a higher likelihood for progressing to AD [71,72]. Additionally, only minor differences in PiB retention between AD and MCI patients have been observed [73] and longitudinal studies of AD patients showed no significant changes in PiB retention over two years [74,75], both of which are consistent with the model that amyloid deposition has plateaued in the prodromal stage before the appearance of any symptoms.

Radio-ligand binding assays of [^{3}H]PiB to brain homogenates and pure Aβ assemblies have demonstrated that high-affinity PiB binding ($K_d \leq 5$ nM) is unique to human AD brains and is negligible in other Aβ sources such as nonhuman primates, transgenic rodent models, synthetic or recombinant Aβ (**Figure 1.5A**) [76,77]. A study by Klunk et al. reported that even for transgenic PS1/APP mice depositing 30-fold more insoluble Aβ than human AD brain per unit mass of brain tissue, *in vitro* PiB binding was

~1000-fold lower than for AD brain homogenate. The PiB binding profiles of synthetic Aβ40 and Aβ42 were similar to PS1/APP brain with low B_{max} values, and mixing experiments between AD homogenates, mice homogenates and synthetic Aβ showed additive, not cooperative, PiB binding. As such, they concluded that the high-affinity PiB binding was to Aβ alone and that the formation of the binding sites was 1000-fold more efficient in AD brains than in other environments [76].

A recent report by Yamin and Teplow evaluated PiB binding to synthetic Aβ oligomers, protofibrils and fibrils [78]. Greater binding to the fibrils was observed as compared to the protofibrils and oligomers (**Figure 1.5B**), suggesting that the high affinity PiB binding sites are more likely to be located on mature β-sheet structures than prefibrillar assemblies. However, they found that Aβ42 assemblies retained more PiB than Aβ40 did, which was inconsistent with the report above by Klunk et al.

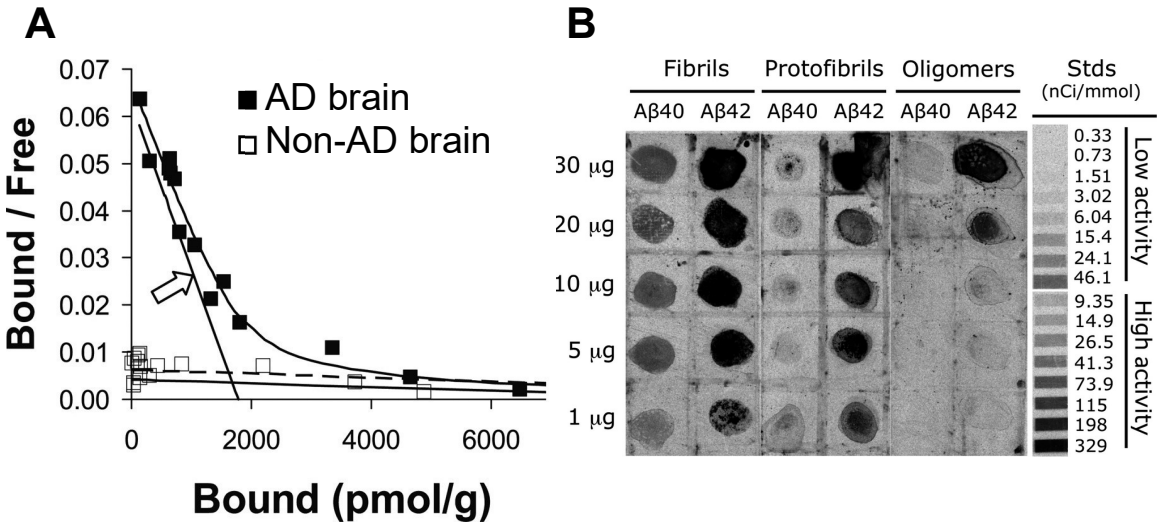

Figure 1.5. [^{3}H]PiB binds with higher affinity to AD brains over non-AD brains and to Aβ fibrils over protofibrils and oligomers. (A) Scatchard plot of [^{3}H]PiB binding to human AD brain homogenate showed significant high-affinity binding (white arrow, K_d = 2.8 nM and B_{max} = 1780 pmol/g) as well as low-affinity binding (K_d = 264 nM and B_{max} = 11,000 pmol/g). The healthy human brain only showed low-affinity binding (K_d = 242

nM and B_{max} = 15,000 pmol/g). Figure adapted from ref.[76] (B) Aβ40 and Aβ42 fibrils and oligomers, and Aβ40(E22G) and Aβ42(E22G) protofibrils were spotted on PVDF membranes, probed with [^{3}H]PiB, before the phosphorimage was acquired. Figure reproduced from ref.[78]

Since then, work on amyloid PET tracers have shifted towards the incorporation of ^{18}F isotopes because the longer half-life (109.8 min vs 20.4 min for ^{11}C) allows for more widespread availability at locations farther away from cyclotrons. Flutemetamol (3'-F-PiB, Vizamyl) was developed by replacing a proton on the aniline ring with ^{18}F, while elimination of the thiazole ring and addition of a PEG moiety gave rise to Florbetaben (Neuraceq) and Florbetapir (Amyvid) (**Appendix 1**). As with the parent PiB molecule, these compounds bind with high selectivity and affinity to fibrillar Aβ but not to NFTs [67].

1.6 Luminescent conjugated oligothiophenes (LCOs)

LCOs are a class of flexible molecules consisting of covalently-linked thiophene moieties. Binding to different amyloid polymorphs can give distinct fluorescence spectra, and this is attributed to the different conformations of the LCOs taken as they wrap around the different fibers [79-83]. Competition binding assays indicate that LCOs bind to the X-34/CR binding sites and not the PiB binding site, potentially revealing another diagnostic or therapeutic target in addition to PiB [84]. The anionic tetrameric LCO, HS-68, was shown to bind differently to amyloid plaques from young and old APPS1 with the emission spectra blue-shifting as the mice aged (**Figure 1.6**) [81]. This study provided compelling evidence that senile plaques are not just static amyloid sinks, but that they are dynamic, where perhaps the compositions or fibril conformations evolve with pathology.

While LCOs are useful probes for screening amyloids, most of the studies performed thus far involve binding to tissue sections, where other cofactors such as nucleic acids, metal

ions, tau, etc. are likely to be present in the amyloid plaques. Additional studies are needed to answer if the LCOs are also binding to Aβ-cofactor complexes, how they influence the LCO binding, and if they can structurally distinguish or resolve disease-relevant conformations.

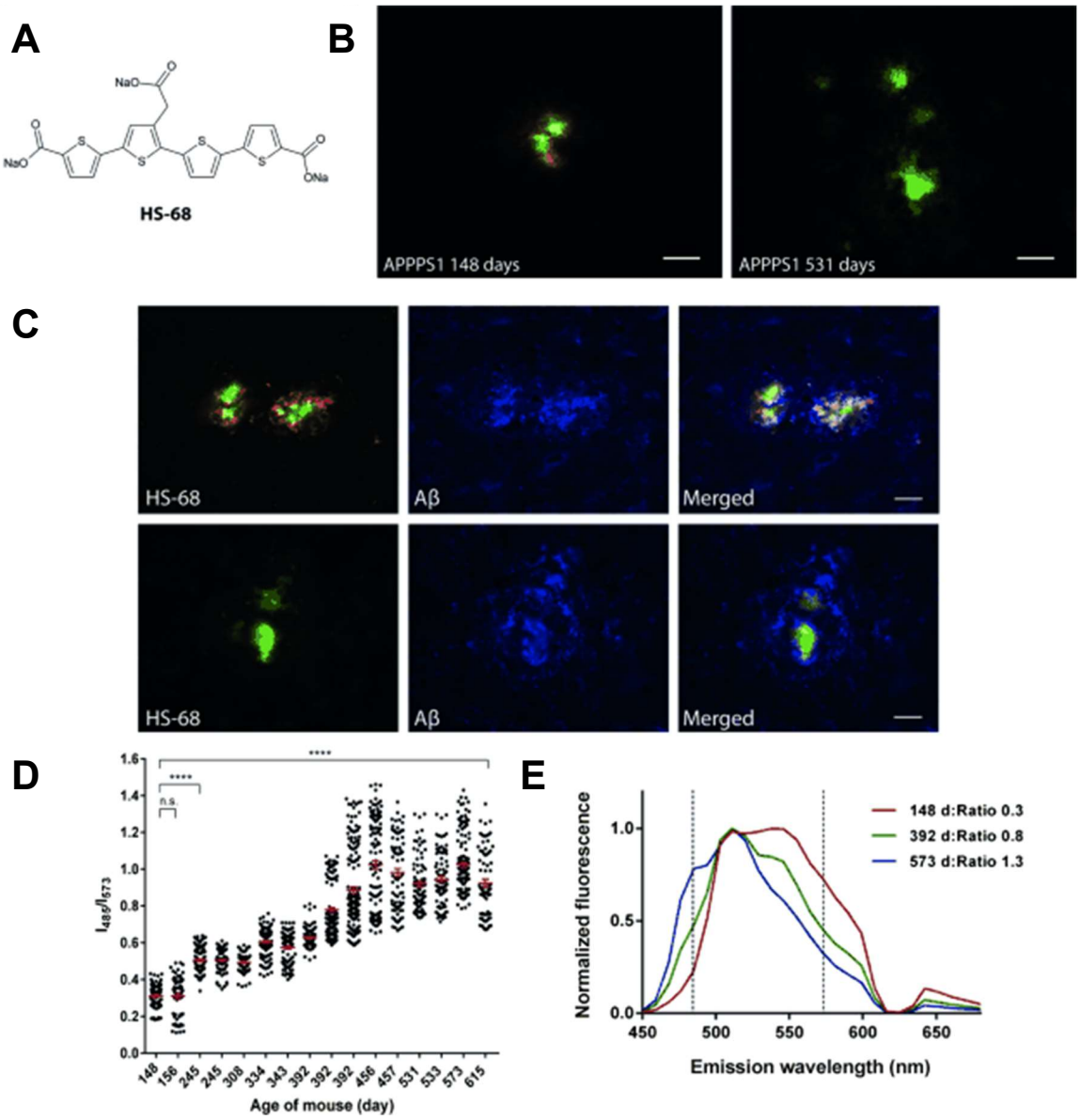

Figure 1.6. Fluorescence of HS-68 changes when bound to Aβ deposits from transgenic mice of different ages. (A) Structure of HS-68. (B) Fluorescence imaging of HS-68 bound to Aβ plaques in ethanol-fixed brain sections from APPPS1 mice sacrificed at 148 or 531 days, with HS-68 showing a blue-shifted emission for the older mouse. (C) Fluorescent co-labeling of the anti-Aβ antibody (6E10) and HS-68 in acetone-fixed brain sections from young (top) and old (bottom) APPPS1 mice. (D) Ratios of the emission intensities at 485 and 573 nm increase as the APPPS1 mice age, indicating a blueshift. (E)

Emission spectra of HS-68 bound to Aβ plaques in APPPS1 mice sacrificed at 148, 392, or 573 days. Scale bars: 20 μm. Figure adapted from ref. [81].

1.7 Tau-specific ligands

More recently, tau-specific PET tracers [85,86] are being developed to image tau deposits *in vivo* which are not only useful for studying AD patients but could potentially be used for other tauopathies such as frontotemporal dementia (FTD), progressive supranuclear palsy (PSP) and chronic traumatic encephalopathy (CTE). One of the most promising tau PET ligands, ^{18}F- T807 (also known as ^{18}F- AV-1451), binds with nanomolar affinity to PHF-tau which is >25-fold stronger than its binding to Aβ [86], and has a binding site that is distinct from PiB or THK-523 (another tau ligand) based on competition binding assays to AD brain homogenates [87]. T807 retention patterns in healthy, MCI and AD patients parallel the Braak staging of NFT distribution and accumulation, and the retention levels were associated with the cognitive state of the patients as measured by the mini mental state examination (MMSE), adding to its promise as a biomarker for tau in AD patients [88-90]. Although T807 does not bind to other amyloids such as α-synuclein and TDP-43, it binds with nanomolar affinities to monoamine oxidase A and B enzymes which may unfortunately limit its use *in vivo* [91,92].

An FDA-approved tau PET ligand will be useful for predicting MCI conversion to AD and the early diagnosis of AD, since PiB retention between MCI and AD cases are similar but the spatiotemporal pattern of tau burden has a higher correlation to synapse loss and clinical symptoms than amyloid deposition. However, significant challenges lie ahead because the ligand not only has to cross the BBB, but also penetrate cell membranes to bind selectively to intraneuronal PHFs and have a suitable clearance time.

Strategies for developing AD therapeutics

1.8 β- and γ-secretase inhibitors

One of the most common strategies involves targeting the proteases that cleave APP to reduce Aβ production and deposition, thereby inhibiting the amyloid cascade at the beginning. Unfortunately, many drug candidates have been unsuccessful in improving cognition, likely because amyloid deposition has plateaued in symptomatic patients. The small molecule γ-secretase inhibitor Semagacestat (Eli Lilly) was terminated in phase 3 trials due to worsened cognition in treatment and placebo groups and adverse effects such as skin cancer and infections [93]. Additionally, there are concerns that these inhibitors may also interfere with Notch signaling pathways, since gamma secretase also performs intramembranous cleavage of Notch receptors [94]. On a positive note, a number of γ-secretase inhibitors are being repurposed as cancer therapeutics [95].

1.9 Aggregation inhibitors and modulators

Another approach involves modulating the aggregation pathways. Inhibitors such as rifampicin [96], curcumin [97] and peptides [98] can decelerate Aβ aggregation by either capping the fibril ends or destabilizing the steric zipper interface, while modulators such as L2-b and DMPD (*N,N*-dimethyl-*p*-phenylenediamine) redirect Aβ monomers off-pathway and produce nontoxic amorphous oligomers [99,100]. LMTM (leuco-methylthioninium-bis(hydromethanesulfonate)) has been shown to inhibit tau aggregation *in vitro* and in transgenic mice supposedly by a combination of cysteine oxidation and demethylation into azure A and azure B which bind to aromatic residues, keeping tau in the monomeric form [101]. The molecule is currently in phase 3 trials, although an initial report has cited a negative result [102,103].

While these compounds can reduce toxicity in cell and animal models, they typically fail in clinical trials. Furthermore, they are likely to be ineffective even for patients with MCI, again due to the likelihood that plaque and tangle formation have essentially plateaued. Instead, these therapeutics would have to be taken prophylactically in the preclinical stage before neurodegeneration sets in.

1.10 Metal protein-attenuating compounds (MPACs)

Another strategy involves targeting cations such as Cu^{2+} and Zn^{2+} to chelate free and Aβ-bound metals, thus reducing metal-induced Aβ aggregation. Clioquinol, an antifungal and antiprotozoal, was found to reduce Aβ deposits by half in AD transgenic mice [104] and improve cognition in patients with severe AD, but the trial was terminated because a toxic side product could not be removed from the formulation [105]. Prana Biotechnology then developed PBT-2 (hydroxyquinoline) which is an ionophore that translocates Cu^{2+} and Zn^{2+} into the cells, thus decreasing their extracellular concentrations. However, since no significant difference in cognitive improvement and amyloid load by PiB retention were observed between the PBT2 and placebo groups, the drug has been on hold at phase 2 since 2014.

1.11 Immune system activation

As an individual's immune system and protein clearance mechanisms deteriorates with age, one therapeutic approach being explored is the upregulation of microglial phagocytosis to clear amyloid deposits [106]. The major disadvantage with this approach is the risk of over-activation, which causes microglia to release toxic levels of inflammatory cytokines and chemokines, resulting in further neuronal damage.

Another method of engaging the immune system is through active immunization by vaccination with Aβ. However, this should only be applied as a preventive strategy since inoculation of Aβ during AD will only increase the amyloid burden and there is also a chance that the immune response may non-specifically target APP in normal neurons. In APP transgenic mice, vaccination with Aβ42 resulted in a ~50% decrease in the number and size of Aβ dense-core plaques and improved cognitive function [107]. Immunization of patients with synthetic Aβ42 showed a decrease in amyloid plaques with an increased presence of microglia, but no changes in NFTs or neural loss [108]. Furthermore, cognitive function and memory were not restored in patients, in contrast to experiments with transgenic mice. The trial was ultimately terminated in phase 2A after six percent of patients showed signs of meningoencephalitis [109].

Humanized anti-Aβ antibodies form a large class of AD drug candidates, which bind to amyloid and facilitate clearance by microglial phagocytosis. When the m266 antibody was injected into PDAPP transgenic mice expressing higher Aβ42/Aβ40 ratios, learning and memory performance improved without a decrease in Aβ burden. However, m266-Aβ complexes were detected in the plasma and CSF, suggesting that clearance of soluble Aβ oligomers may be a viable treatment option [110]. Many other highly-anticipated antibodies such as Bapineuzumab (Janssen, Pfizer), Solanezumab (Eli Lilly) and Crenezumab (Genentech) have similarly dropped out of clinical trials due to lack of cognitive benefits despite reducing amyloid burden. These failures indicate that targeting amyloid reduction and clearance after the onset of symptoms is ineffective due to the co-existence of other ongoing pathological events.

1.12 Focused ultrasound (FUS)

A major obstacle in increasing the bioavailability of AD therapeutics is the ineffectiveness of crossing the blood-brain barrier (BBB), where the brain-to-plasma ratio for systematically-delivered antibodies is typically around 0.1% [111]. Using MRI-guided focused ultrasound (FUS) in combination with intravenously injected microbubbles (ultrasound contrast agent), FUS can aid drug delivery by generating localized cavities that mechanically stretch endothelial cell membranes and briefly open the BBB [112]. When FUS was selectively targeted to four foci in the right hemisphere of TgCRND8 mice while the anti-Aβ BAM-10 antibody was intravenously delivered, BAM-10 binding to plaques was only detected in the right side of the brain up to 4 days after treatment [113].

Conclusion

Current treatments for AD are limited to behavior-modifying drugs and symptomatic interventions such as acetylcholinesterase inhibitors and NMDA receptor agonists [2], which are minimally effective and do not reverse or halt disease progression. An effective treatment will likely have to be administered in the presymptomatic phase, which in turn requires both early detection and a more complete understanding of the disease etiology to find therapeutic targets.

In this dissertation, I report our efforts to seed Aβ from AD brain extracts into synthetic Aβ for characterization and cross-seeding between Aβ and the PHF6 peptide derived from tau. In chapter 2, we explore methods of disaggregating purified peptides for seeding experiments, a crucial step in suppressing self-nucleation and maximizing the amount of peptide amenable for templated growth. Chapter 3 looks at the fluorescent properties of PiB and the feasibility of developing a fluorescence PiB binding assay.

Thereafter, we established procedures for seeding brain extracts and synthetic controls into Aβ40 and 42 in chapter 4. Finally, in chapter 5, we cross-seeded PHF6 with Aβ to determine if a direct interaction between these two events is a possible mechanism in AD.

References

1. Alzheimer's Association: **2018 Alzheimer's Disease Facts and Figures**. *Alzheimer's & dementia* 2018, **14**:367-429.

2. Cummings JL, Morstorf T, Zhong K: **Alzheimer's disease drug-development pipeline: few candidates, frequent failures**. *Alzheimer's Research & Therapy* 2014, **6**:37.

3. Alzheimer A: **Uber eine eigenartige Erkrankung der Hirnrinde**. *Allgemeine Zeitschrife Psychiatrie* 1907, **64**:146-148.

4. Petersen RC, Smith GE, Waring SC, Ivnik RJ, Tangalos EG, Kokmen E: **Mild cognitive impairment: clinical characterization and outcome**. *Arch Neurol* 1999, **56**:303-308.

5. Celone KA, Calhoun VD, Dickerson BC, Atri A, Chua EF, Miller SL, DePeau K, Rentz DM, Selkoe DJ, Blacker D, et al.: **Alterations in Memory Networks in Mild Cognitive Impairment and Alzheimer's Disease: An Independent Component Analysis**. *The Journal of Neuroscience* 2006, **26**:10222-10231.

6. Dickerson BC, Salat DH, Greve DN, Chua EF, Rand-Giovannetti E, Rentz DM, Bertram L, Mullin K, Tanzi RE, Blacker D, et al.: **Increased hippocampal activation in mild cognitive impairment compared to normal aging and AD**. *Neurology* 2005, **65**:404-411.

7. Jack CR, Knopman DS, Jagust WJ, Petersen RC, Weiner MW, Aisen PS, Shaw LM, Vemuri P, Wiste HJ, Weigand SD, et al.: **Tracking pathophysiological processes in Alzheimer's disease: an updated hypothetical model of dynamic biomarkers**. *The Lancet Neurology* 2013, **12**:207-216.

8. Hartley D, Blumenthal T, Carrillo M, DiPaolo G, Esralew L, Gardiner K, Granholm A-C, Iqbal K, Krams M, Lemere C, et al.: **Down syndrome and Alzheimer's disease: Common pathways, common goals**. *Alzheimer's & Dementia* 2015, **11**:700-709.

9. Bayer TA, Cappai R, Masters CL, Beyreuther K, Multhaup G: **It all sticks together--the APP-related family of proteins and Alzheimer's disease**. *Mol Psychiatry* 1999, **4**:524-528.

10. Bourdet I, Preat T, Goguel V: **The Full-Length Form of the Drosophila Amyloid Precursor Protein Is Involved in Memory Formation**. *The Journal of Neuroscience* 2015, **35**:1043-1051.

11. Senechal Y, Kelly PH, Dev KK: **Amyloid precursor protein knockout mice show age-dependent deficits in passive avoidance learning**. *Behav Brain Res* 2008, **186**:126-132.

12. Nikolaev A, McLaughlin T, O'Leary DD, Tessier-Lavigne M: **APP binds DR6 to trigger axon pruning and neuron death via distinct caspases**. *Nature* 2009, **457**:981-989.

13. Ghiso J, Rostagno A, Gardella JE, Liem L, Gorevic PD, Frangione B: **A 109-amino-acid C-terminal fragment of Alzheimer's-disease amyloid precursor protein contains a sequence, -RHDS-, that promotes cell adhesion**. *Biochem J* 1992, **288 (Pt 3)**:1053-1059.

14. Gravina SA, Ho L, Eckman CB, Long KE, Otvos L, Younkin LH, Suzuki N, Younkin SG: **Amyloid β Protein (Aβ) in Alzheimeri's Disease Brain: BIOCHEMICAL AND IMMUNOCYTOCHEMICAL ANALYSIS WITH ANTIBODIES SPECIFIC FOR FORMS ENDING AT Aβ40 OR Aβ42(43)**. *Journal of Biological Chemistry* 1995, **270**:7013-7016.

15. Roher AE, Lowenson JD, Clarke S, Woods AS, Cotter RJ, Gowing E, Ball MJ: **beta-Amyloid-(1-42) is a major component of cerebrovascular amyloid deposits: implications for the pathology of Alzheimer disease**. *Proceedings of the National Academy of Sciences of the United States of America* 1993, **90**:10836-10840.

16. Koyama A, Okereke OI, Yang T, Blacker D, Selkoe DJ, Grodstein F: **Plasma amyloid-beta as a predictor of dementia and cognitive decline: a systematic review and meta-analysis**. *Arch Neurol* 2012, **69**:824-831.

17. Thinakaran G, Koo EH: **Amyloid precursor protein trafficking, processing, and function**. *J Biol Chem* 2008, **283**:29615-29619.

18. Zhang X, Li Y, Xu H, Zhang Y-w: **The γ-secretase complex: from structure to function**. *Frontiers in Cellular Neuroscience* 2014, **8**:427.

19. Zhu XC, Tan L, Wang HF, Jiang T, Cao L, Wang C, Wang J, Tan CC, Meng XF, Yu JT: **Rate of early onset Alzheimer's disease: a systematic review and meta-analysis**. *Ann Transl Med* 2015, **3**.

20. Jarrett JT, Lansbury PT, Jr.: **Seeding "one-dimensional crystallization" of amyloid: a pathogenic mechanism in Alzheimer's disease and scrapie?** *Cell* 1993, **73**:1055-1058.

21. Kumar S, Rezaei-Ghaleh N, Terwel D, Thal DR, Richard M, Hoch M, Mc Donald JM, Wüllner U, Glebov K, Heneka MT, et al.: **Extracellular phosphorylation of the amyloid β-peptide promotes formation of toxic aggregates during the pathogenesis of Alzheimer's disease**. *The EMBO Journal* 2011, **30**:2255-2265.

22. Harper JD, Lansbury PT, Jr.: **Models of amyloid seeding in Alzheimer's disease and scrapie: mechanistic truths and physiological consequences of the time-dependent solubility of amyloid proteins**. *Annu Rev Biochem* 1997, **66**:385-407.

23. Nitsch RM, Rebeck GW, Deng M, Richardson UI, Tennis M, Schenk DB, Vigo-Pelfrey C, Lieberburg I, Wurtman RJ, Hyman BT, et al.: **Cerebrospinal fluid levels of amyloid beta-protein in Alzheimer's disease: inverse correlation with severity of dementia and effect of apolipoprotein E genotype**. *Ann Neurol* 1995, **37**:512-518.

24. Glabe C: **Intracellular mechanisms of amyloid accumulation and pathogenesis in Alzheimer's disease**. *Journal of Molecular Neuroscience* 2001, **17**:137-145.

25. Gouras GK, Tsai J, Naslund J, Vincent B, Edgar M, Checler F, Greenfield JP, Haroutunian V, Buxbaum JD, Xu H, et al.: **Intraneuronal Aβ42 Accumulation in Human Brain**. *The American Journal of Pathology* 2000, **156**:15-20.

26. D'Andrea MR, Nagele RG, Wang HY, Peterson PA, Lee DH: **Evidence that neurones accumulating amyloid can undergo lysis to form amyloid plaques in Alzheimer's disease**. *Histopathology* 2001, **38**:120-134.

27. Terzi E, Hölzemann G, Seelig J: **Self-association of β-Amyloid Peptide (1–40) in Solution and Binding to Lipid Membranes**. *Journal of Molecular Biology* 1995, **252**:633-642.

28. Inestrosa NC, Alvarez A, Perez CA, Moreno RD, Vicente M, Linker C, Casanueva OI, Soto C, Garrido J: **Acetylcholinesterase accelerates assembly of amyloid-beta-peptides into Alzheimer's fibrils: possible role of the peripheral site of the enzyme**. *Neuron* 1996, **16**:881-891.

29. Esler WP, Stimson ER, Jennings JM, Vinters HV, Ghilardi JR, Lee JP, Mantyh PW, Maggio JE: **Alzheimer's Disease Amyloid Propagation by a Template-Dependent Dock-Lock Mechanism**. *Biochemistry* 2000, **39**:6288-6295.

30. Selkoe DJ: **Soluble Oligomers of the Amyloid β-Protein Impair Synaptic Plasticity and Behavior**. *Behavioural brain research* 2008, **192**:106-113.

31. Walsh DM, Selkoe DJ: **A beta oligomers - a decade of discovery**. *J Neurochem* 2007, **101**:1172-1184.

32. Klein WL, Krafft GA, Finch CE: **Targeting small Aβ oligomers: the solution to an Alzheimer's disease conundrum?** *Trends in Neurosciences* 2001, **24**:219-224.

33. Lacor PN, Buniel MC, Furlow PW, Sanz Clemente A, Velasco PT, Wood M, Viola KL, Klein WL: **Aβ Oligomer-Induced Aberrations in Synapse Composition, Shape, and Density Provide a Molecular Basis for Loss of Connectivity in Alzheimer's Disease**. *The Journal of Neuroscience* 2007, **27**:796-807.

34. Lesné S, Koh MT, Kotilinek L, Kayed R, Glabe CG, Yang A, Gallagher M, Ashe KH: **A specific amyloid-[beta] protein assembly in the brain impairs memory**. *Nature* 2006, **440**:352-357.

35. Shankar GM, Li S, Mehta TH, Garcia-Munoz A, Shepardson NE, Smith I, Brett FM, Farrell MA, Rowan MJ, Lemere CA, et al.: **Amyloid-[beta] protein dimers isolated directly from Alzheimer's brains impair synaptic plasticity and memory**. *Nat Med* 2008, **14**:837-842.

36. Jin M, Shepardson N, Yang T, Chen G, Walsh D, Selkoe DJ: **Soluble amyloid β-protein dimers isolated from Alzheimer cortex directly induce Tau hyperphosphorylation and neuritic degeneration**. *Proceedings of the National Academy of Sciences* 2011, **108**:5819-5824.

37. Lorenzo A, Yankner BA: **Beta-amyloid neurotoxicity requires fibril formation and is inhibited by congo red**. *Proc Natl Acad Sci U S A* 1994, **91**:12243-12247.

38. Pike CJ, Walencewicz AJ, Glabe CG, Cotman CW: **In vitro aging of ß-amyloid protein causes peptide aggregation and neurotoxicity**. *Brain Research* 1991, **563**:311-314.

39. Shankar GM, Walsh DM: **Alzheimer's disease: synaptic dysfunction and Abeta**. *Mol Neurodegener* 2009, **4**:48.

40. Talantova M, Sanz-Blasco S, Zhang X, Xia P, Akhtar MW, Okamoto S-i, Dziewczapolski G, Nakamura T, Cao G, Pratt AE, et al.: **Aβ induces astrocytic glutamate release, extrasynaptic NMDA receptor activation, and synaptic loss**. *Proceedings of the National Academy of Sciences* 2013, **110**:E2518-E2527.

41. Um JW, Nygaard HB, Heiss JK, Kostylev MA, Stagi M, Vortmeyer A, Wisniewski T, Gunther EC, Strittmatter SM: **Alzheimer amyloid-beta oligomer bound to postsynaptic prion protein activates Fyn to impair neurons**. *Nat Neurosci* 2012, **15**:1227-1235.

42. Kawarabayashi T, Shoji M, Younkin LH, Wen-Lang L, Dickson DW, Murakami T, Matsubara E, Abe K, Ashe KH, Younkin SG: **Dimeric Amyloid β Protein Rapidly Accumulates in Lipid Rafts followed by Apolipoprotein E and Phosphorylated Tau Accumulation in the Tg2576 Mouse Model of Alzheimer's Disease**. *The Journal of Neuroscience* 2004, **24**:3801-3809.

43. Sciacca M FM, Kotler S A, Brender J R, Chen J, Lee D, Ramamoorthy A: **Two-Step Mechanism of Membrane Disruption by Aβ through Membrane Fragmentation and Pore Formation**. *Biophys J* 2012, **103**:702-710.

44. Resende R, Ferreiro E, Pereira C, Resende de Oliveira C: **Neurotoxic effect of oligomeric and fibrillar species of amyloid-beta peptide 1-42: involvement of endoplasmic reticulum calcium release in oligomer-induced cell death**. *Neuroscience* 2008, **155**:725-737.

45. Cho DH, Nakamura T, Fang J, Cieplak P, Godzik A, Gu Z, Lipton SA: **S-nitrosylation of Drp1 mediates beta-amyloid-related mitochondrial fission and neuronal injury**. *Science* 2009, **324**:102-105.

46. Umeda T, Tomiyama T, Sakama N, Tanaka S, Lambert MP, Klein WL, Mori H: **Intraneuronal amyloid beta oligomers cause cell death via endoplasmic reticulum stress, endosomal/lysosomal leakage, and mitochondrial dysfunction in vivo**. *J Neurosci Res* 2011, **89**:1031-1042.

47. Haass C, Schlossmacher MG, Hung AY, Vigo-Pelfrey C, Mellon A, Ostaszewski BL, Lieberburg I, Koo EH, Schenk D, Teplow DB, et al.: **Amyloid [beta]-peptide is produced by cultured cells during normal metabolism**. *Nature* 1992, **359**:322-325.

48. Seubert P, Vigo-Pelfrey C, Esch F, Lee M, Dovey H, Davis D, Sinha S, Schiossmacher M, Whaley J, Swindlehurst C, et al.: **Isolation and quantification of soluble Alzheimer's [beta]-peptide from biological fluids**. *Nature* 1992, **359**:325-327.

49. Shoji M, Golde TE, Ghiso J, Cheung TT, Estus S, Shaffer LM, Cai XD, McKay DM, Tintner R, Frangione B, et al.: **Production of the Alzheimer amyloid beta protein by normal proteolytic processing**. *Science* 1992, **258**:126-129.

50. Eisenberg D, Jucker M: **The amyloid state of proteins in human diseases**. *Cell* 2012, **148**:1188-1203.

51. Olzscha H, Schermann SM, Woerner AC, Pinkert S, Hecht MH, Tartaglia GG, Vendruscolo M, Hayer-Hartl M, Hartl FU, Vabulas RM: **Amyloid-like Aggregates**

Sequester Numerous Metastable Proteins with Essential Cellular Functions. *Cell* 2011, **144**:67-78.

52. Bessen RA, Marsh RF: **Identification of two biologically distinct strains of transmissible mink encephalopathy in hamsters**. *J Gen Virol* 1992, **73 (Pt 2)**:329-334.

53. Head MW, Ironside JW: **Review: Creutzfeldt–Jakob disease: prion protein type, disease phenotype and agent strain**. *Neuropathology and Applied Neurobiology* 2012, **38**:296-310.

54. Terry RD, Masliah E, Salmon DP, Butters N, DeTeresa R, Hill R, Hansen LA, Katzman R: **Physical basis of cognitive alterations in Alzheimer's disease: synapse loss is the major correlate of cognitive impairment**. *Ann Neurol* 1991, **30**:572-580.

55. Driscoll I, Troncoso J: **Asymptomatic Alzheimer's disease: a prodrome or a state of resilience?** *Curr Alzheimer Res* 2011, **8**:330-335.

56. Cohen ML, Kim C, Haldiman T, ElHag M, Mehndiratta P, Pichet T, Lissemore F, Shea M, Cohen Y, Chen W, et al.: **Rapidly progressive Alzheimer's disease features distinct structures of amyloid-β**. *Brain* 2015, **138**:1009-1022.

57. Petkova AT, Leapman RD, Guo Z, Yau W-M, Mattson MP, Tycko R: **Self-Propagating, Molecular-Level Polymorphism in Alzheimer's ß-Amyloid Fibrils**. *Science* 2005, **307**:262-265.

58. Pettersen EF, Goddard TD, Huang CC, Couch GS, Greenblatt DM, Meng EC, Ferrin TE: **UCSF Chimera--a visualization system for exploratory research and analysis**. *J Comput Chem* 2004, **25**:1605-1612.

59. Zempel H, Mandelkow E: **Lost after translation: missorting of Tau protein and consequences for Alzheimer disease**. *Trends in Neurosciences* **37**:721-732.

60. Cash AD, Aliev G, Siedlak SL, Nunomura A, Fujioka H, Zhu X, Raina AK, Vinters HV, Tabaton M, Johnson AB, et al.: **Microtubule reduction in Alzheimer's disease and aging is independent of tau filament formation**. *Am J Pathol* 2003, **162**:1623-1627.

61. Liu F, Li B, Tung EJ, Grundke-Iqbal I, Iqbal K, Gong CX: **Site-specific effects of tau phosphorylation on its microtubule assembly activity and self-aggregation**. *Eur J Neurosci* 2007, **26**:3429-3436.

62. Stieler JT, Bullmann T, Kohl F, Toien O, Bruckner MK, Hartig W, Barnes BM, Arendt T: **The physiological link between metabolic rate depression and tau phosphorylation in mammalian hibernation**. *PLoS One* 2011, **6**:e14530.

63. Yoshida H, Ihara Y: **Tau in paired helical filaments is functionally distinct from fetal tau: assembly incompetence of paired helical filament-tau**. *J Neurochem* 1993, **61**:1183-1186.

64. Götz J, Chen F, van Dorpe J, Nitsch RM: **Formation of Neurofibrillary Tangles in P301L Tau Transgenic Mice Induced by Aβ42 Fibrils**. *Science* 2001, **293**:1491-1495.

65. Bolmont T, Clavaguera F, Meyer-Luehmann M, Herzig MC, Radde R, Staufenbiel M, Lewis J, Hutton M, Tolnay M, Jucker M: **Induction of tau pathology by intracerebral infusion of amyloid-beta -containing brain extract and by amyloid-beta deposition in APP x Tau transgenic mice**. *Am J Pathol* 2007, **171**:2012-2020.

66. Lockhart A, Ye L, Judd DB, Merritt AT, Lowe PN, Morgenstern JL, Hong G, Gee AD, Brown J: **Evidence for the Presence of Three Distinct Binding Sites for the Thioflavin T Class of Alzheimer's Disease PET Imaging Agents on β-Amyloid Peptide Fibrils**. *Journal of Biological Chemistry* 2005, **280**:7677-7684.

67. Mathis CA, Mason NS, Lopresti BJ, Klunk WE: **Development of positron emission tomography beta-amyloid plaque imaging agents**. *Semin Nucl Med* 2012, **42**:423-432.

68. Ikonomovic MD, Klunk WE, Abrahamson EE, Mathis CA, Price JC, Tsopelas ND, Lopresti BJ, Ziolko S, Bi W, Paljug WR, et al.: **Post-mortem correlates of in vivo PiB-PET amyloid imaging in a typical case of Alzheimer's disease**. *Brain* 2008, **131**:1630-1645.

69. Bacskai BJ, Frosch MP, Freeman SH, Raymond SB, Augustinack JC, Johnson KA, Irizarry MC, Klunk WE, Mathis CA, Dekosky ST, et al.: **Molecular imaging with Pittsburgh Compound B confirmed at autopsy: a case report**. *Arch Neurol* 2007, **64**:431-434.

70. Klunk WE, Engler H, Nordberg A, Wang Y, Blomqvist G, Holt DP, Bergstrom M, Savitcheva I, Huang GF, Estrada S, et al.: **Imaging brain amyloid in Alzheimer's disease with Pittsburgh Compound-B**. *Ann Neurol* 2004, **55**:306-319.

71. Johnson KA, Fox NC, Sperling RA, Klunk WE: **Brain Imaging in Alzheimer Disease**. *Cold Spring Harbor Perspectives in Medicine* 2012, **2**.

72. Forsberg A, Engler H, Almkvist O, Blomquist G, Hagman G, Wall A, Ringheim A, Langstrom B, Nordberg A: **PET imaging of amyloid deposition in patients with mild cognitive impairment**. *Neurobiol Aging* 2008, **29**:1456-1465.

73. Risacher SL, Saykin AJ: **Neuroimaging and other biomarkers for Alzheimer's disease: the changing landscape of early detection**. *Annu Rev Clin Psychol* 2013, **9**:621-648.

74. Klunk WE, Mathis CA, Price JC, Lopresti BJ, DeKosky ST: **Two-year follow-up of amyloid deposition in patients with Alzheimer's disease**. *Brain* 2006, **129**:2805-2807.

75. Engler H, Forsberg A, Almkvist O, Blomquist G, Larsson E, Savitcheva I, Wall A, Ringheim A, Långström B, Nordberg A: **Two-year follow-up of amyloid deposition in patients with Alzheimer's disease**. *Brain* 2006, **129**:2856-2866.

76. Klunk WE, Lopresti BJ, Ikonomovic MD, Lefterov IM, Koldamova RP, Abrahamson EE, Debnath ML, Holt DP, Huang GF, Shao L, et al.: **Binding of the positron emission tomography tracer Pittsburgh compound-B reflects the amount of amyloid-beta in Alzheimer's disease brain but not in transgenic mouse brain**. *J Neurosci* 2005, **25**:10598-10606.

77. Rosen RF, Walker LC, Levine H, 3rd: **PIB binding in aged primate brain: enrichment of high-affinity sites in humans with Alzheimer's disease**. *Neurobiol Aging* 2011, **32**:223-234.

78. Yamin G, Teplow DB: **Pittsburgh Compound-B (PiB) binds amyloid β-protein protofibrils**. *Journal of Neurochemistry* 2017, **140**:210-215.

79. Nilsson KPR, Åslund A, Berg I, Nyström S, Konradsson P, Herland A, Inganäs O, Stabo-Eeg F, Lindgren M, Westermark GT, et al.: **Imaging Distinct Conformational**

States of Amyloid-β Fibrils in Alzheimer's Disease Using Novel Luminescent Probes. *ACS Chemical Biology* 2007, **2**:553-560.

80. Åslund A, Sigurdson CJ, Klingstedt T, Grathwohl S, Bolmont T, Dickstein DL, Glimsdal E, Prokop S, Lindgren M, Konradsson P, et al.: **Novel Pentameric Thiophene Derivatives for in Vitro and in Vivo Optical Imaging of a Plethora of Protein Aggregates in Cerebral Amyloidoses**. *ACS Chemical Biology* 2009, **4**:673-684.

81. Klingstedt T, Shirani H, Mahler J, Wegenast-Braun BM, Nyström S, Goedert M, Jucker M, Nilsson KPR: **Distinct Spacing Between Anionic Groups: An Essential Chemical Determinant for Achieving Thiophene-Based Ligands to Distinguish β-Amyloid or Tau Polymorphic Aggregates**. *Chemistry – A European Journal* 2015, **21**:9072-9082.

82. Klingstedt T, Shirani H, Åslund KOA, Cairns NJ, Sigurdson CJ, Goedert M, Nilsson* KPR: **The Structural Basis for Optimal Performance of Oligothiophene-Based Fluorescent Amyloid Ligands: Conformational Flexibility is Essential for Spectral Assignment of a Diversity of Protein Aggregates**. *Chemistry (Weinheim an Der Bergstrasse, Germany)* 2013, **19**:10179-10192.

83. Wegenast-Braun BM, Skodras A, Bayraktar G, Mahler J, Fritschi SK, Klingstedt T, Mason JJ, Hammarström P, Nilsson KPR, Liebig C, et al.: **Spectral Discrimination of Cerebral Amyloid Lesions after Peripheral Application of Luminescent Conjugated Oligothiophenes**. *The American Journal of Pathology* 2012, **181**:1953-1960.

84. Bäck M, Appelqvist H, LeVine H, Nilsson KPR: **Anionic Oligothiophenes Compete for Binding of X-34 but not PIB to Recombinant Aβ Amyloid Fibrils and Alzheimer's Disease Brain-Derived Aβ**. *Chemistry – A European Journal* 2016, **22**:18335-18338.

85. Fodero-Tavoletti MT, Furumoto S, Taylor L, McLean CA, Mulligan RS, Birchall I, Harada R, Masters CL, Yanai K, Kudo Y, et al.: **Assessing THK523 selectivity for tau deposits in Alzheimer's disease and non–Alzheimer's disease tauopathies**. *Alzheimer's Research & Therapy* 2014, **6**:11.

86. Xia CF, Arteaga J, Chen G, Gangadharmath U, Gomez LF, Kasi D, Lam C, Liang Q, Liu C, Mocharla VP, et al.: **[(18)F]T807, a novel tau positron emission tomography imaging agent for Alzheimer's disease**. *Alzheimers Dement* 2013, **9**:666-676.

87. Cai L, Qu B, Hurtle BT, Dadiboyena S, Diaz-Arrastia R, Pike VW: **Candidate PET Radioligand Development for Neurofibrillary Tangles: Two Distinct Radioligand Binding Sites Identified in Postmortem Alzheimer's Disease Brain**. *ACS Chemical Neuroscience* 2016, **7**:897-911.

88. Chien DT, Bahri S, Szardenings AK, Walsh JC, Mu F, Su MY, Shankle WR, Elizarov A, Kolb HC: **Early clinical PET imaging results with the novel PHF-tau radioligand [F-18]-T807**. *J Alzheimers Dis* 2013, **34**:457-468.

89. Scholl M, Lockhart SN, Schonhaut DR, O'Neil JP, Janabi M, Ossenkoppele R, Baker SL, Vogel JW, Faria J, Schwimmer HD, et al.: **PET Imaging of Tau Deposition in the Aging Human Brain**. *Neuron* 2016, **89**:971-982.

90. Johnson KA, Schultz A, Betensky RA, Becker JA, Sepulcre J, Rentz D, Mormino E, Chhatwal J, Amariglio R, Papp K, et al.: **Tau positron emission tomographic imaging in aging and early Alzheimer disease**. *Ann Neurol* 2016, **79**:110-119.

91. Vermeiren C, Motte P, Viot D, Mairet-Coello G, Courade JP, Citron M, Mercier J, Hannestad J, Gillard M: **The tau positron-emission tomography tracer AV-1451 binds with similar affinities to tau fibrils and monoamine oxidases**. *Mov Disord* 2018, **33**:273-281.

92. Marquie M, Normandin MD, Vanderburg CR, Costantino IM, Bien EA, Rycyna LG, Klunk WE, Mathis CA, Ikonomovic MD, Debnath ML, et al.: **Validating novel tau positron emission tomography tracer [F-18]-AV-1451 (T807) on postmortem brain tissue**. *Ann Neurol* 2015, **78**:787-800.

93. Doody RS, Raman R, Farlow M, Iwatsubo T, Vellas B, Joffe S, Kieburtz K, He F, Sun X, Thomas RG, et al.: **A phase 3 trial of semagacestat for treatment of Alzheimer's disease**. *N Engl J Med* 2013, **369**:341-350.

94. Shih I-M, Wang T-L: **Notch Signaling, γ-Secretase Inhibitors, and Cancer Therapy**. *Cancer Research* 2007, **67**:1879-1882.

95. Ran Y, Hossain F, Pannuti A, Lessard CB, Ladd GZ, Jung JI, Minter LM, Osborne BA, Miele L, Golde TE: **γ-Secretase inhibitors in cancer clinical trials are pharmacologically and functionally distinct**. *EMBO Molecular Medicine* 2017, **9**:950-966.

96. Umeda T, Ono K, Sakai A, Yamashita M, Mizuguchi M, Klein WL, Yamada M, Mori H, Tomiyama T: **Rifampicin is a candidate preventive medicine against amyloid-β and tau oligomers**. *Brain* 2016, **139**:1568-1586.

97. Yang F, Lim GP, Begum AN, Ubeda OJ, Simmons MR, Ambegaokar SS, Chen PP, Kayed R, Glabe CG, Frautschy SA, et al.: **Curcumin Inhibits Formation of Amyloid β Oligomers and Fibrils, Binds Plaques, and Reduces Amyloid in Vivo**. *Journal of Biological Chemistry* 2005, **280**:5892-5901.

98. Tjernberg LO, Näslund J, Lindqvist F, Johansson J, Karlström AR, Thyberg J, Terenius L, Nordstedt C: **Arrest of -Amyloid Fibril Formation by a Pentapeptide Ligand**. *Journal of Biological Chemistry* 1996, **271**:8545-8548.

99. Derrick JS, Kerr RA, Nam Y, Oh SB, Lee HJ, Earnest KG, Suh N, Peck KL, Ozbil M, Korshavn KJ, et al.: **A Redox-Active, Compact Molecule for Cross-Linking Amyloidogenic Peptides into Nontoxic, Off-Pathway Aggregates: In Vitro and In Vivo Efficacy and Molecular Mechanisms**. *Journal of the American Chemical Society* 2015, **137**:14785-14797.

100. Beck MW, Oh SB, Kerr RA, Lee HJ, Kim SH, Kim S, Jang M, Ruotolo BT, Lee J-Y, Lim MH: **A rationally designed small molecule for identifying an in vivo link between metal-amyloid-[small beta] complexes and the pathogenesis of Alzheimer's disease**. *Chemical Science* 2015, **6**:1879-1886.

101. Akoury E, Pickhardt M, Gajda M, Biernat J, Mandelkow E, Zweckstetter M: **Mechanistic Basis of Phenothiazine-Driven Inhibition of Tau Aggregation**. *Angewandte Chemie International Edition* 2013, **52**:3511-3515.

102. Gauthier S, Feldman HH, Schneider LS, Wilcock G, Frisoni GB, Hardlund J, Kook K, Wischik DJ, Schelter BO, Storey JM, et al.: **Phase 3 Trial of the Tau Aggregation Inhibitor Leuco-Methylthioninium-Bis (Hydromethanesulfonate) (Lmtm) in Mild to Moderate Alzheimer's Disease**. *Alzheimer's & Dementia* 2016, **12**:P351-P352.

103. Gauthier S, Feldman HH, Schneider LS, Wilcock GK, Frisoni GB, Hardlund JH, Moebius HJ, Bentham P, Kook KA, Wischik DJ, et al.: **Efficacy and safety of tau-aggregation inhibitor therapy in patients with mild or moderate Alzheimer's disease: a randomised, controlled, double-blind, parallel-arm, phase 3 trial**. *The Lancet* **388**:2873-2884.

104. Cherny RA, Atwood CS, Xilinas ME, Gray DN, Jones WD, McLean CA, Barnham KJ, Volitakis I, Fraser FW, Kim Y, et al.: **Treatment with a copper-zinc chelator markedly and rapidly inhibits beta-amyloid accumulation in Alzheimer's disease transgenic mice**. *Neuron* 2001, **30**:665-676.

105. Ritchie CW, Bush AI, Mackinnon A, Macfarlane S, Mastwyk M, MacGregor L, Kiers L, Cherny R, Li QX, Tammer A, et al.: **Metal-protein attenuation with iodochlorhydroxyquin (clioquinol) targeting Abeta amyloid deposition and toxicity in Alzheimer disease: a pilot phase 2 clinical trial**. *Arch Neurol* 2003, **60**:1685-1691.

106. Yoon SS, Jo SA: **Mechanisms of Amyloid-β Peptide Clearance: Potential Therapeutic Targets for Alzheimer's Disease**. *Biomol Ther (Seoul)* 2012, **20**:245-255.

107. Janus C, Pearson J, McLaurin J, Mathews PM, Jiang Y, Schmidt SD, Chishti MA, Horne P, Heslin D, French J, et al.: **A beta peptide immunization reduces behavioural impairment and plaques in a model of Alzheimer's disease**. *Nature* 2000, **408**:979-982.

108. Nicoll JA, Wilkinson D, Holmes C, Steart P, Markham H, Weller RO: **Neuropathology of human Alzheimer disease after immunization with amyloid-beta peptide: a case report**. *Nat Med* 2003, **9**:448-452.

109. Orgogozo JM, Gilman S, Dartigues JF, Laurent B, Puel M, Kirby LC, Jouanny P, Dubois B, Eisner L, Flitman S, et al.: **Subacute meningoencephalitis in a subset of patients with AD after Abeta42 immunization**. *Neurology* 2003, **61**:46-54.

110. Dodart J-C, Bales KR, Gannon KS, Greene SJ, DeMattos RB, Mathis C, DeLong CA, Wu S, Wu X, Holtzman DM, et al.: **Immunization reverses memory deficits without reducing brain A[beta] burden in Alzheimer's disease model**. *Nat Neurosci* 2002, **5**:452-457.

111. Banks WA, Terrell B, Farr SA, Robinson SM, Nonaka N, Morley JE: **Passage of amyloid beta protein antibody across the blood-brain barrier in a mouse model of Alzheimer's disease**. *Peptides* 2002, **23**:2223-2226.

112. Vykhodtseva N, McDannold N, Hynynen K: **Progress and problems in the application of focused ultrasound for blood-brain barrier disruption**. *Ultrasonics* 2008, **48**:279-296.

113. Jordão JF, Ayala-Grosso CA, Markham K, Huang Y, Chopra R, McLaurin J, Hynynen K, Aubert I: **Antibodies Targeted to the Brain with Image-Guided Focused**

Ultrasound Reduces Amyloid-β Plaque Load in the TgCRND8 Mouse Model of Alzheimer's Disease. *PLOS ONE* 2010, **5**:e10549.

Chapter 2. Disaggregation of peptides into monomers

Introduction

During the purification and lyophilization processes, synthetic amyloid peptides may form aggregates which persist when the sample is reconstituted in the assembly buffer. Aggregates present in the solution are likely to sequester additional monomers, mature and propagate into fibrils in the spontaneous nucleation pathway, resulting in heterogeneous fibrils from the seeded and spontaneous nucleation pathway. For effective seeding of amyloid fibrils in vitro, it is of fundamental importance that the added Aβ peptides be disaggregated into their monomeric state, also referred to as erasing the conformational memory of the peptide, so as to maximize the templated growth on the ends of the seeds in the seeded pathway.

Peptides in our lab are traditionally treated by dissolution in 1,1,1,3,3,3-hexafluoroisopropanol (HFIP), which reportedly disaggregates beta-sheet structures by stabilizing the alpha-helical conformation and through strong hydrogen bonding, as shown by CD and NOESY [1-3]. However, Pachahara et al.[4] reported that when Aβ40, Aβ42 and Aβ43 was incubated in HFIP for 4 months before drying, annular structures were visible by AFM and SEM. FTIR spectroscopy showed a peak shift from 1659 cm^{-1} to 1627 cm^{-1} from 0 to 4 months, indicating a structural transition from α-helical to β-sheet conformation. ThT fluorescence microscopy showed an enhanced ThT fluorescence, supporting the argument that these rings are amyloid-like with β-sheet structures (**Figure 2.1**). Therefore, the use of HFIP to prepare aggregate-free solutions of Aβ40 may be ineffective, given that the peptides can eventually assemble.

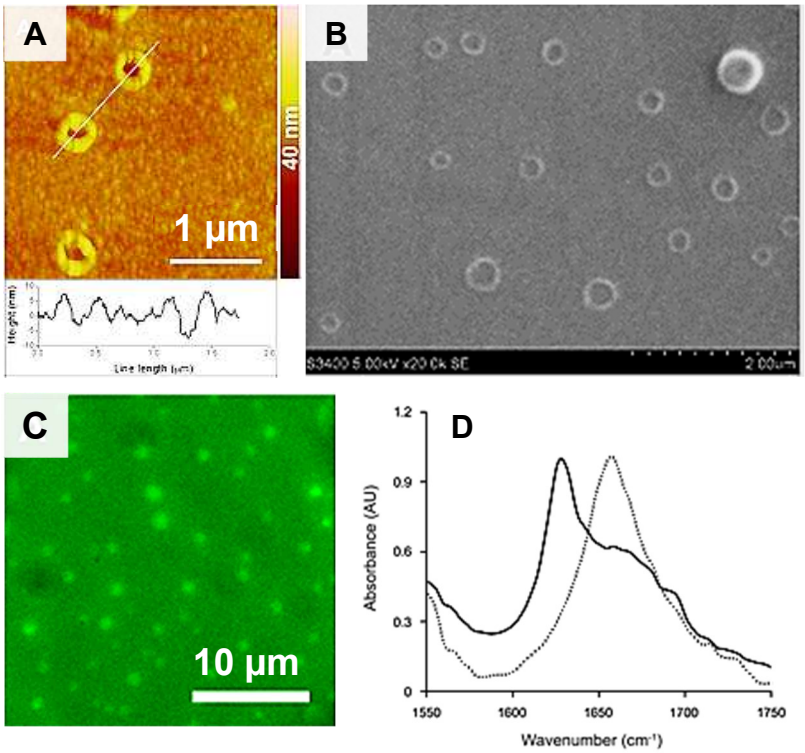

Figure 2.1. Aβ40 forms annular structures when incubated in HFIP for 4 months. Aβ40 rings visualized by (A) AFM, (B) SEM and (C) thioflavin T fluorescence microscopy. (D) FTIR spectra of freshly dissolved (---) Aβ40 shows a peak at 1659 cm^{-1} and 4-month old (—) Aβ40 shows a peak at 1627 cm^{-1}, suggesting a α-helical to β-conformation structural transition. Figure modified from Pachahara et al.[4]

Ryan et. al demonstrated that Aβ42 pre-treated with NH_4OH resulted in fewer aggregates as compared to Aβ42 treated with HFIP [5]. Briefly, the protocol involves dissolving the lyophilized Aβ peptide in 10% w/v NH_4OH at 0.5 mg/ml, a 10-min incubation at room temperature followed by a 5-min bath sonication, before lyophilization to remove the NH_4OH. The peptide was then dissolved in 60 mM NaOH before the monomeric solution was analyzed and allowed to self-assemble. Dynamic light scattering (DLS) and size exclusion chromatography (SEC) showed that the NH_4OH-treated Aβ42 solution contained smaller aggregates than the HFIP-treated Aβ42 solution (**Figure 2.2**), while having a longer lag phase during assembly as measured by TEM and thioflavin T

(ThT) fluorescence. In fact, HFIP treatment accelerated fibril formation as compared to untreated Aβ (**Figure 2.3**). The authors did not explain the mechanism by which NH_4OH disaggregates Aβ but hypothesized that altering the protonation state of the residues disrupts the electrostatic interactions within the aggregates.

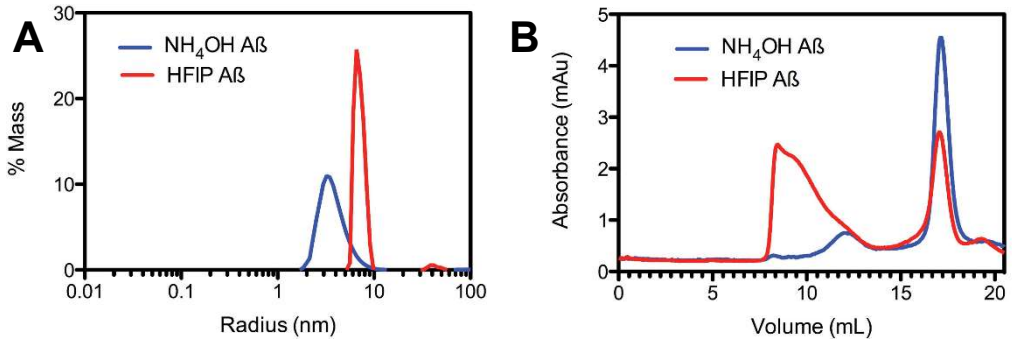

Figure 2.2. Aggregation states of Aβ42 pretreated with HFIP and NH_4OH. (A) Dynamic light scattering of 100 μM Aβ42 pretreated with NH_4OH (blue line) showed smaller hydrodynamic radii than when treated with HFIP (red line). (B) SEC chromatograms of 200 μM Aβ42 show fewer oligomers in the NH_4OH-treated Aβ. Figure adapted from ref. [5].

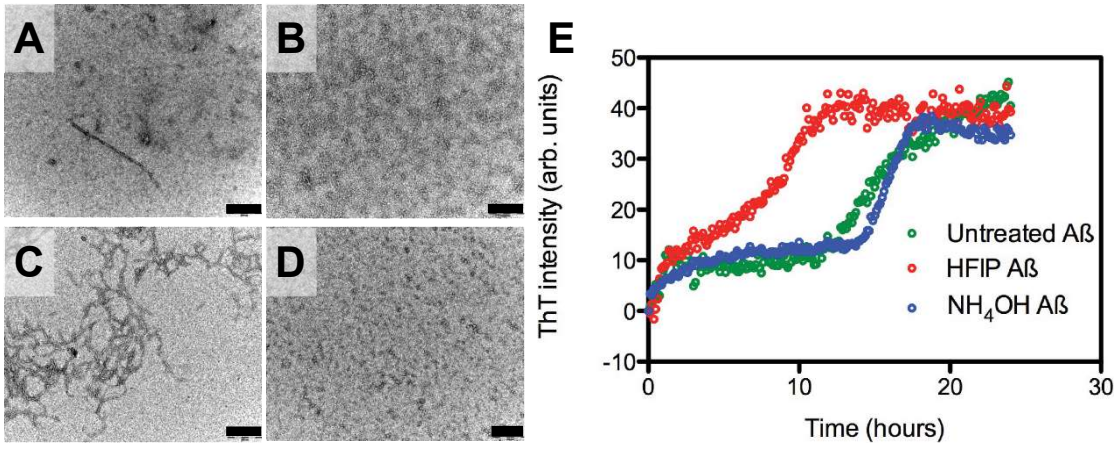

Figure 2.3. Aβ fibrillization is slower when pretreated with NH_4OH. HFIP-treated Aβ42 incubated after 20 min (A) and 6 hours (C). NH_4OH-treated Aβ42 incubated after 20 min (B) and 6 hours (D). (E) Compared to untreated Aβ42 (green, $t_{1/2}$ ~ 15 ± 2.6 h), HFIP treatment enhanced fibrillization (red, $t_{1/2}$ ~ 9 ± 1.9 h) while NH_4OH delayed fibrillization (blue, $t_{1/2}$ ~ 16.2 ± 1.3 h). Scale bars: 200 nm. Figure adapted from ref [5].

According to Teplow [6], it is the pH transition through the isoelectric point (pI) of Aβ that causes the aggregation. Peptide cleavage and purification occurs under acidic conditions which inevitably leaves behind acidic salts such as trifluoroacetate or formate in the lyophilized peptides. Reconstitution of the peptides into buffers at neutral pH leads to a pH change past the pI of Aβ (at 5.2), where the peptide is most insoluble and likely to aggregate. This explanation is experimentally supported by Wetzel and coworkers who showed that HFIP-treated Aβ40 assembled at pH 5.8 formed a turbid solution with amorphous aggregates visible by light and electron microscopy [7]. Instead, when the lyophilized peptides are dissolved in NH_4OH or NaOH and re-lyophilized, the treated peptide is in an alkaline environment and does not cross the pI when reconstituted in a buffer at neutral pH.

This chapter looks at the effects of three solvents we used in our attempts to disaggregate peptides before assembly or seeding experiments.

Results

2.1 Hexafluoroisopropanol (HFIP)

Lyophilized Aβ40 was dissolved in HFIP to a concentration of 1 mg/ml (231 μM) in a glass vial, taking care to avoid plastic lab consumables since HFIP dissolves many polymers. Following a 30-minute to 2-hour incubation in a bath sonicator, the solvent was evaporated under a steady stream of Ar or N_2 gas, forming a white film at the bottom of the vial. When the Aβ40 peptide film was reconstituted in sodium phosphate buffer and a sample was taken for TEM, numerous amorphous aggregates were observed on the grid (**Figure 2.4**) suggesting that when seeds are added to this solution of fresh monomers, those

seeds will compete with the aggregates for monomers. This likely explained why previous attempts at seeding agitated Aβ40 seeds under quiescent conditions were unsuccessful, yielding heterogeneous fibrils in the daughter generation.

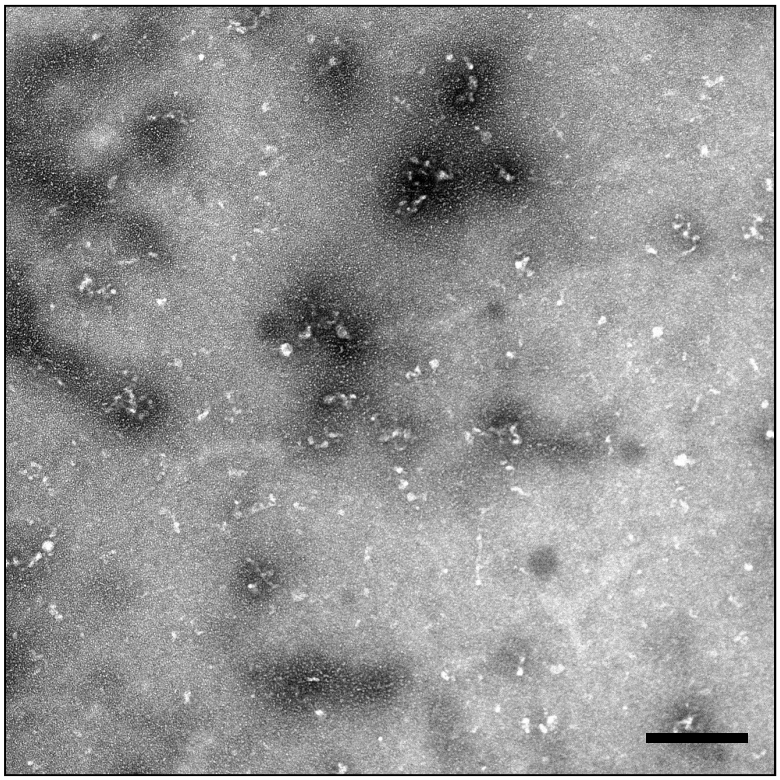

Figure 2.4. Aβ40 aggregates in monomeric solution at time zero. A film of HFIP-treated Aβ40 was reconstituted in 10 mM phosphate buffer and immediately spotted on a TEM grid. The aggregates observed indicate that the monomeric solution at time zero is not truly monomeric but contains a large number of oligomers. Scale bar: 200 nm.

To determine if those aggregates resulted from the concentration of Aβ when HFIP was evaporated or from an ineffective disaggregation during HFIP incubation, a sample of the Aβ40 dissolved in HFIP was taken for TEM. In both the 2-hour and 24-hour incubation samples (**Figure 2.5A and B**) numerous negatively-stained and positively-stained particles were observed on the grid. In the no-peptide control grid where pure HFIP excluding Aβ40 was spotted onto a grid, allowed to dry and stained with aq. UA, only positively-stained

particles were on the grid (**Figure 2.5C**). Negatively-stained particles were only observed, however, when the Aβ40 in HFIP was stained with UA that was dissolved in HFIP (**Figure 2.5D**). These controls indicated that Aβ40 formed negatively-stained particles in HFIP while the positively-stained particles are artefacts resulting from residual HFIP on the grid interacting with aq. UA.

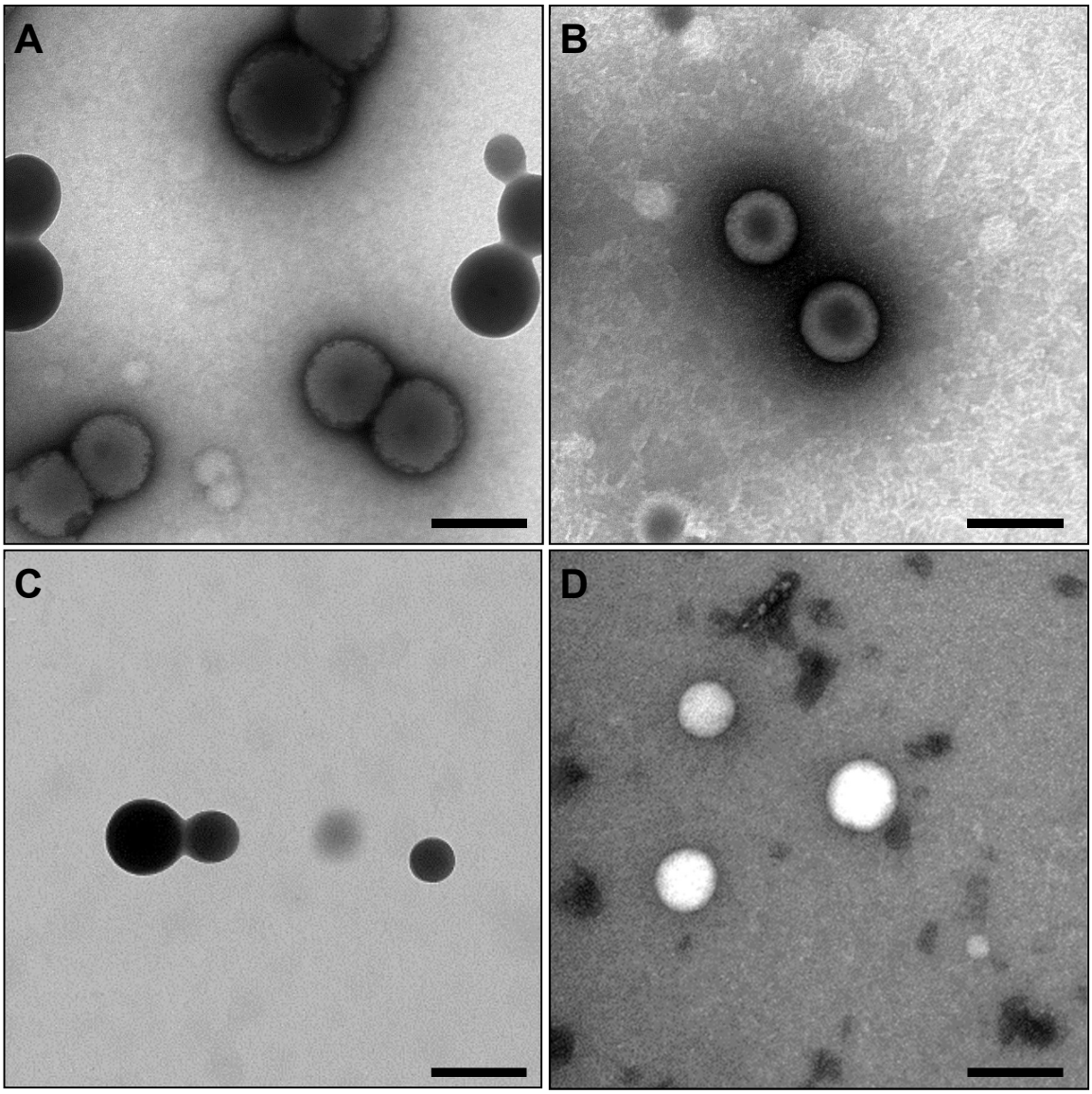

Figure 2.5. Aβ40 forms particles in HFIP. Aβ40 incubated in HFIP for (A) 2 hours and (B) 24 hours. (C) Empty grid spotted with HFIP then stained with aq. UA. (D) Aβ40 incubated with HFIP and stained with 2% w/v UA dissolved in HFIP. Scale bars: 200 nm.

Since a considerable number of Aβ particles appeared to be conjoined, it was not clear whether these particles are fusing or splitting. Do the particles grow or shrink in HFIP over time? To answer the question, samples were taken at various time points over 48 hours and particle widths were measured on the TEM images. For precise measurements, only negatively-stained particles with defined edges were measured while particles with faint or unclear edges were excluded. For an unbiased selection of particles that represented the entire grid, the first 500 observed particles with well-defined edges were measured along their longest diameters. Histograms of the particle widths showed that they were mostly normally distributed around 200 nm (n= 3,000, **Figure 2.6**), except for the 8-hour sample where the average increased to around 275 nm (**Figure 2.6D**, **Figure 2.7**).

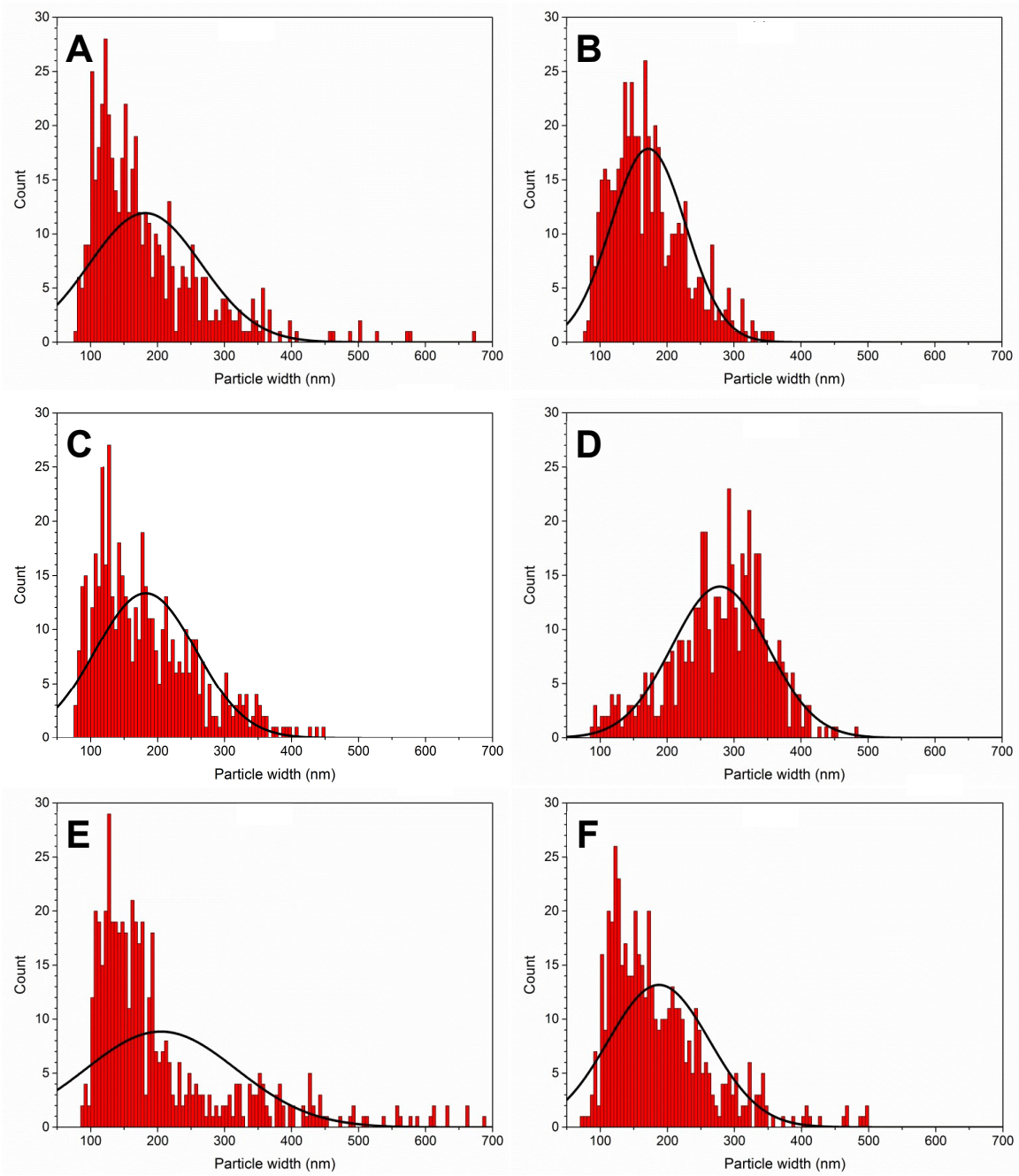

Figure 2.6. Size distributions of Aβ40 particles in HFIP. Particle widths were measured from samples taken at (A) 30 min, (B) 1 hour, (C) 2 hours, (D) 8 hours, (E) 24 hours and (F) 48 hours. Each histogram consists of 500 measurements sorted into 5 nm bin sizes and the black line is the normal distribution curve.

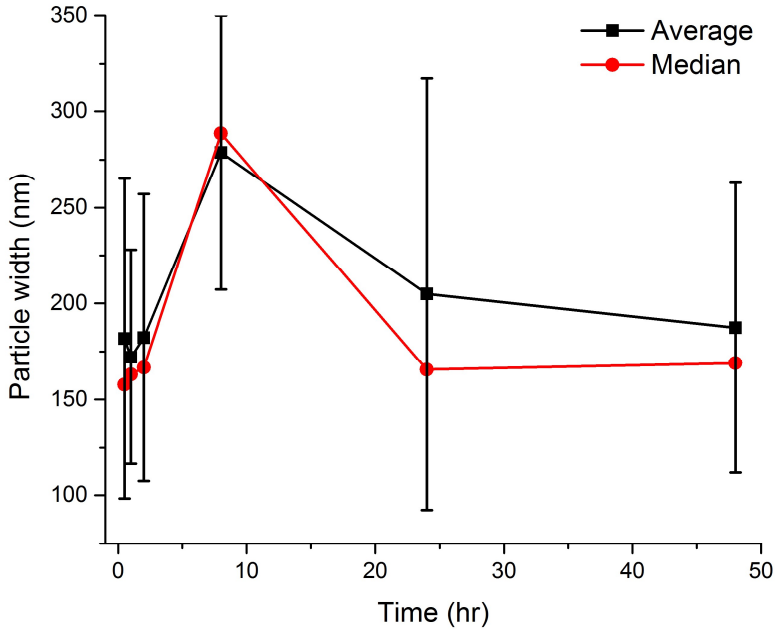

Figure 2.7. Aβ40 particle sizes in HFIP over 48 hours. The average particle widths (black squares with standard deviations) and medians (red circles) of 500 particles at each time point were generally stable over 48 hours, except for a slight increase at 8 hours, possibly due to a sampling error.

These particles are also resistant to disaggregation by SDS-PAGE, where a ~250 kDa band corresponding to a 58-mer is visible (**Figure 2.12**). The stability of these particles suggests that HFIP induces Aβ molecules to coalesce with some degree of order (spherical particles) and remain in close proximity to each other, thus forming aggregates quickly when the peptide film is reconstituted in buffer. Our recent experiments using excitation polarization resolved fluorescence on spherical particles of rhodamine110-tagged HHQLVFFA peptides have revealed a significantly higher fluorescence anisotropy as compared to the peptides in solution, supporting the argument that there is order in the particle [8]. Incubation beyond 48 hours is also unlikely to dissolve the Aβ40 particles, but instead allow them to eventually transition into annular assemblies at 4 months as reported by Pachahara et al.[4]

To examine if HFIP has a similar effect on shorter amyloidogenic peptides, we dissolved PHF6 (Ac-VQIVYK-NH_2) in HFIP and incubated it in a bath sonicator for 30 min. An aliquot analyzed by TEM showed a mixture of short fibrils and oligomers (**Figure 2.8A**), suggesting that PHF6 has a higher aggregation propensity than Aβ40. Instead of extending the incubation time in HFIP to see if disaggregation will eventually occur, we repeated the HFIP treatment twice more as was done by Ryan et al.[5] After the second treatment cycle, tiny particles < 20 nm in width and short fibrils were observed on the grid (**Figure 2.8B**), which were mostly absent after the third cycle (**Figure 2.8C**). Upon extended searching of that grid, however, we observed isolated clusters of larger particles and short fibrils (**Figure 2.8D**), indicating that while multiple treatment cycles can reduce the number of fibrils, HFIP does not completely disaggregate PHF6.

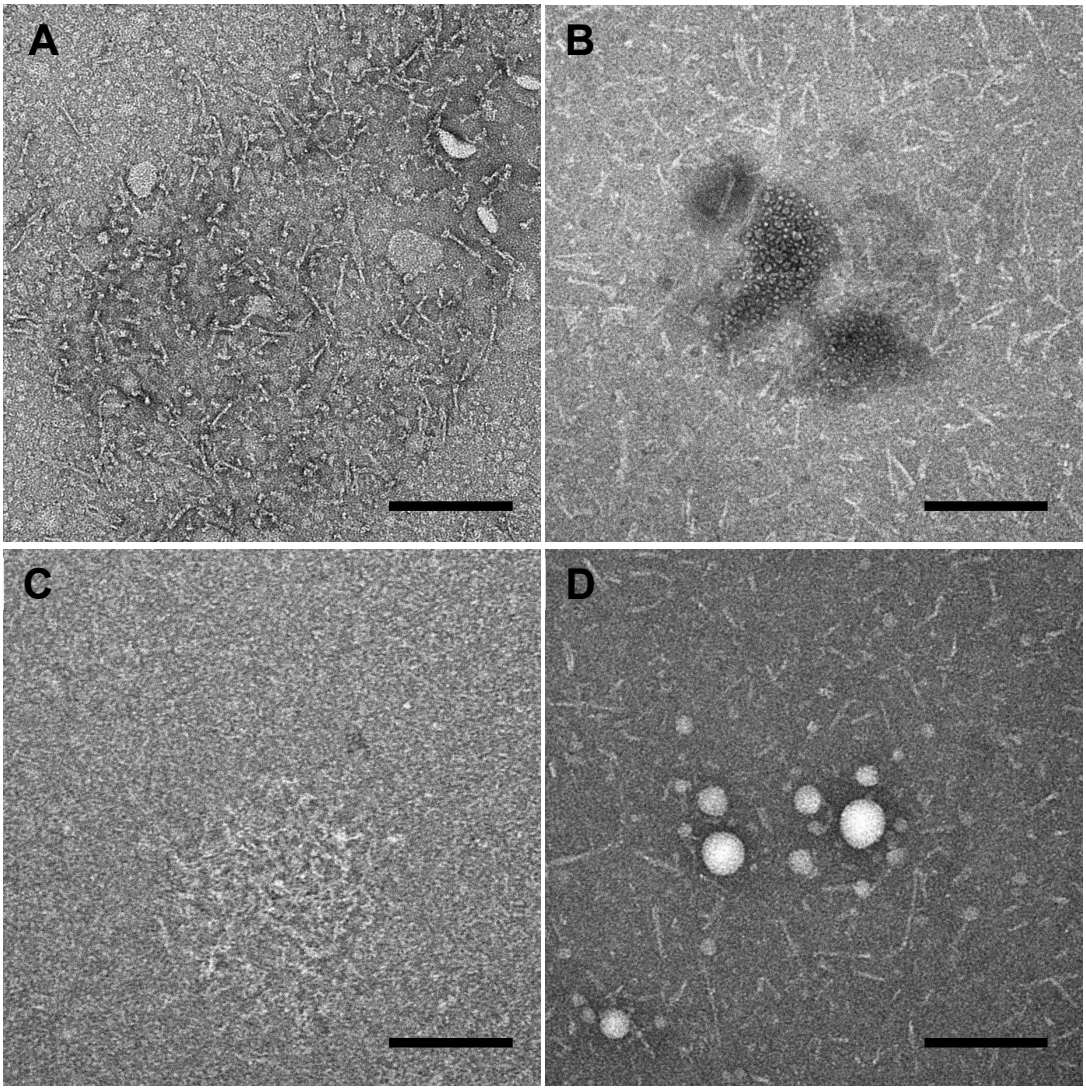

Figure 2.8. PHF6 eventually forms particles when dissolved in HFIP. PHF6 was dissolved to 200 μM in HFIP and bath-sonicated for 30 min, then an aliquot was spotted on a TEM grid and stained with UA. The rest of the HFIP in the sample was evaporated under a stream of N_2, forming a peptide film. This cycle was repeated twice. (A) PHF6 after the 1st cycle of sonication in HFIP. (B) 2nd cycle in HFIP. (C) 3rd cycle in HFIP; most areas of the TEM grid. (D) 3rd cycle in HFIP; very isolated areas of the grid. Scale bars: 200 nm.

2.2 Dimethyl sulfoxide (DMSO)

Dimethyl sulfoxide (DMSO) was used to disaggregate Aβ in Lu et al.[9] for seeding experiments. Briefly, Aβ40 was dissolved in DMSO to 6 mM (26 mg/ml) to form a clear

solution, before it was diluted to 100 μM by adding it to phosphate buffer containing sonicated brain extract. Therefore, it would be reasonable to assume that DMSO will be equally or more effective in disaggregating Aβ40 at a peptide concentration of 1 mg/ml.

When Aβ40 was incubated in DMSO for an hour, widespread amorphous aggregates were observed on the TEM grid (**Figure 2.9A**), which persisted even after a 24-hour incubation (**Figure 2.9B**). Although these aggregates are SDS-labile (**Figure 2.12**), the presence of aggregates on the TEM grids indicate that DMSO is ineffective at producing an aggregate-free solution.

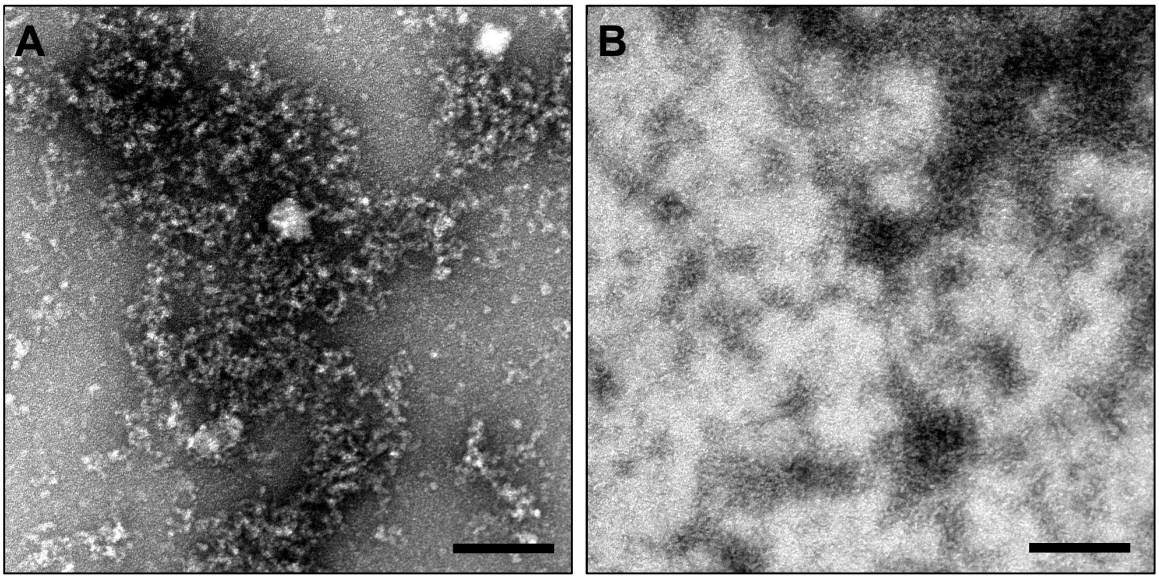

Figure 2.9. Aβ40 forms amorphous aggregates in DMSO. Aβ40 incubated in DMSO for (A) 1 hour and (B) 24 hours. Scale bar: 200 nm

When we dissolved PHF6 in DMSO, however, short fibers were observed by TEM after a 30-min incubation, which elongate after an additional 1.5-hour incubation, forming clusters of long fibers with a background that was largely free of fibril fragments (**Figure 2.10**). Taken together, these experiments suggest that DMSO is ineffective for

monomerizing amyloid peptides and is useful only for initially dissolving the peptide powders before dilution into the assembly buffer.

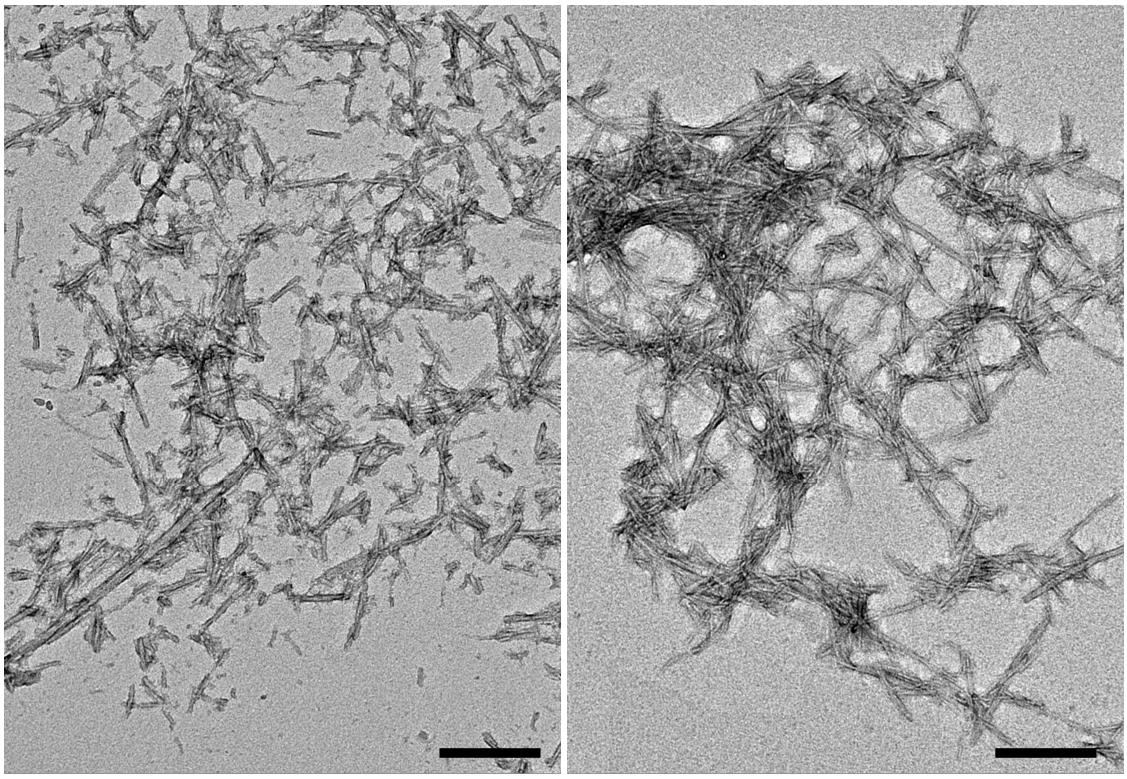

Figure 2.10. PHF6 forms fibers in DMSO. 5 mM (3.95 mg/ml) PHF6 incubated in DMSO and bath-sonicated for (A) 30 min and (B) 2 hrs. Scale bars: 200 nm.

2.3 Ammonium hydroxide

The observations that NH_4OH-treated Aβ produced smaller aggregates that had a longer lag time during fibril assembly as compared to HFIP-treated Aβ suggested that it is a more effective method of preparing monomeric Aβ for seeding amyloid structures[5]. Therefore, we dissolved Aβ40 in 10% w/v NH_4OH for 15 min before a sample was taken for TEM imaging. Although aggregates were still observed on the grid (**Figure 2.11**), they were much fewer than observed on the DMSO-treated Aβ40 grid. Furthermore, the NH_4OH-treated Aβ40 showed an intense band in the monomeric (~4 kDa) region on SDS-

PAGE, while most of the DMSO-treated Aβ40 were in the dimeric (~8 kDa) region of the gel (**Figure 2.12**). These results strongly suggested that the Aβ40 synthesized in our lab is more effectively disaggregated by NH_4OH than by HFIP.

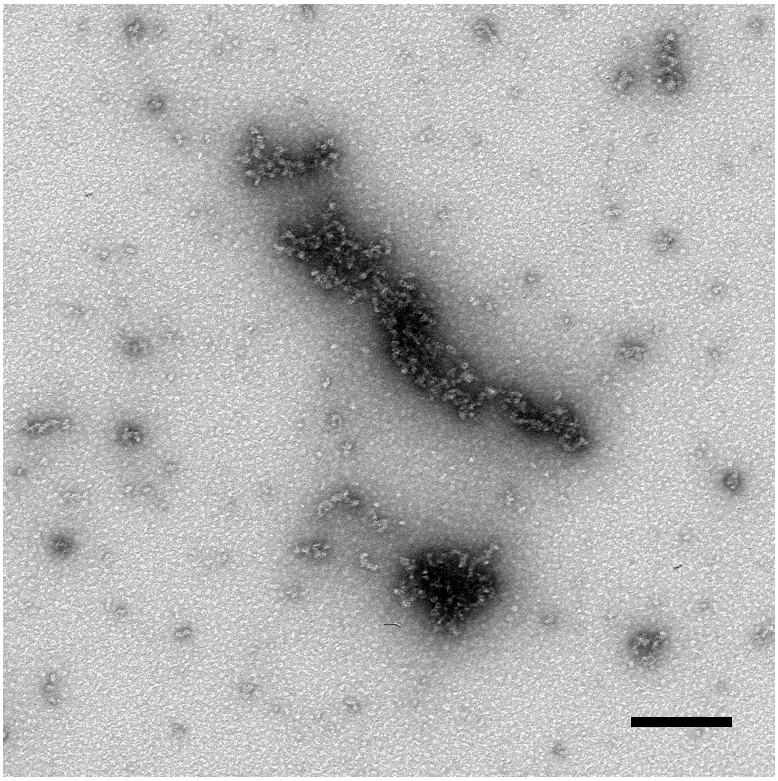

Figure 2.11. Aβ40 aggregates in 10% w/v NH_4OH. The region of the TEM grid where the largest deposit was observed is shown here. Scale bar: 200 nm

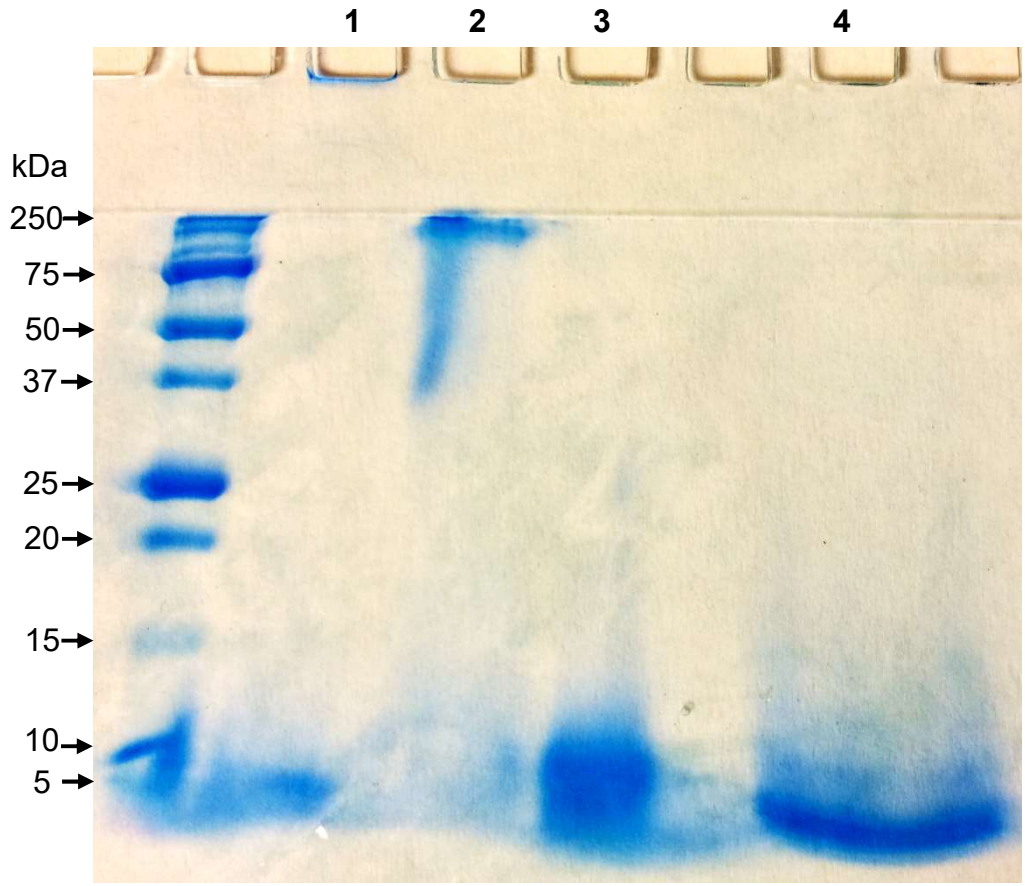

Figure 2.12. Aβ40 in disaggregating solvents. Lane 1: mature Aβ40 assembled in 10 mM sodium phosphate buffer, pH 7.4; lane 2: Aβ40 incubated in HFIP for 2 hours; lane 3: Aβ40 incubated in DMSO for 2 hours; lane 4: Aβ40 incubated in NH_4OH for 15 min. 12% SDS PAGE visualized with Coomassie Brilliant Blue. ~10 μg peptide per lane.

When the NH_4OH-treated lyophilized Aβ40 was reconstituted to 100 μM in assembly buffer (10 mM sodium phosphate, 0.02% sodium azide, pH 7.4) and incubated for 1 day at 37°C, no fibrils were visible by TEM. Even the samples that were seeded with synthetic Aβ40 or brain extract were largely devoid of fibrils. This was likely due to the difficulty in dissolving lyophilized peptide directly in the assembly buffer, leading to a monomeric solution having an effective concentration well below 100 μM and the critical assembly concentration.

The preparation protocol was thus modified to promote the solubility of the lyophilized peptide before it was used for self-assembly or seeding. Since Aβ is more soluble in high pH, the lyophilized peptide was dissolved in 1 mM NaOH (pH ~ 10.8, 90% of the volume to make a 100 μM solution) until the solution was visibly clear of white powder, before 10X sodium phosphate buffer with 0.2% NaN_3, pH 7.1 (the remaining 10% volume) was added, bringing the final concentration to 100 μM Aβ in 10 mM sodium phosphate with 0.02% NaN_3 at pH 7.4. Finally, large aggregates were removed by filtration through a pre-rinsed 0.22 μm filter before the sample was ready for use.

To determine if the NH_4OH treatment is indeed more effective than the HFIP treatment at producing fewer/smaller Aβ aggregates after reconstitution in assembly buffer, monomeric Aβ40 solutions from both methods were prepared and samples were filtered through a 0.22 μm syringe filter. The solutions were then analyzed with the BCA assay for peptide content. An 87% peptide recovery was obtained after filtration of the HFIP-treated peptide ($p = 0.00008 < 0.05$; Student's *t*-test) compared to a 97% peptide recovery for NH_4OH ($p = 0.08 > 0.05$), suggesting that there were significantly more aggregates larger than 0.22 μm in the HFIP-treated solution that were retained by the filter (**Figure 2.13**). The NH_4OH treatment for disaggregating Aβ peptides is therefore more desirable, since it results in more monomers and fewer aggregates.

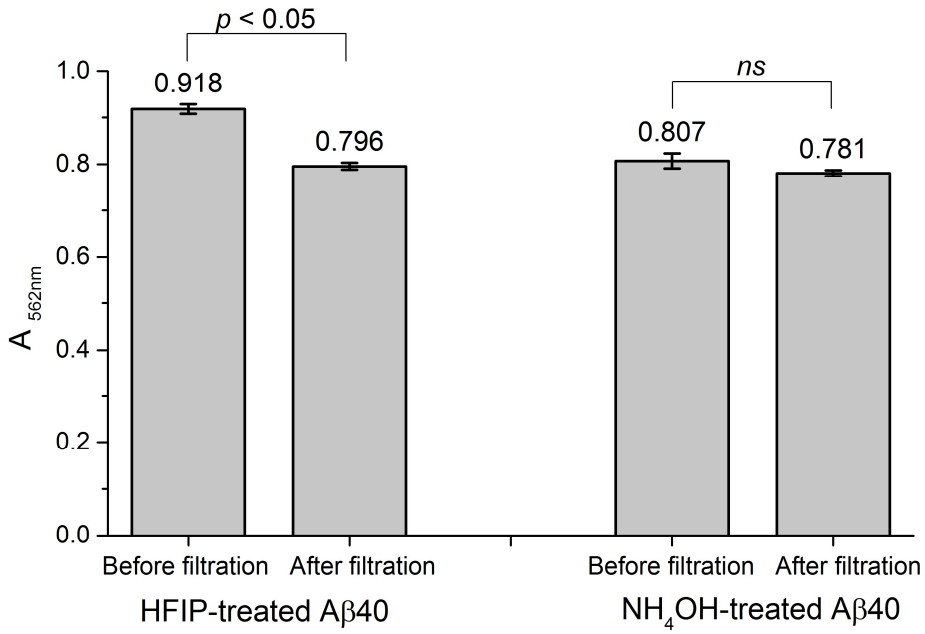

Figure 2.13. Treatment of Aβ40 with NH_4OH leads to higher recovery after filtration compared to treatment with HFIP. HFIP- and NH_4OH-treated Aβ40 were reconstituted to 100 μM in 10 mM phosphate buffer + 0.02% NaN_3, pH 7.4 and half of each sample was filtered through a 0.22 μm PES syringe filter. The filtered and unfiltered samples were then diluted to 10 μM before they were analyzed by the BCA assay. The peptide loss from filtration was significant (Student's *t*-test, $p < 0.05$) for HFIP-treated Aβ40 but not significant (*ns*) for NH_4OH-treated Aβ40.

When applied to the PHF6 peptide, however, numerous clusters of needle-like fibrils were found on the grid (**Figure 2.14**), indicating that a high pH environment is also favorable for the assembly of the peptide. This finding demonstrated that NH_4OH is not a universal solution to disaggregating amyloidogenic peptides and stresses the importance of checking the state of a peptide before it is used for seeding.

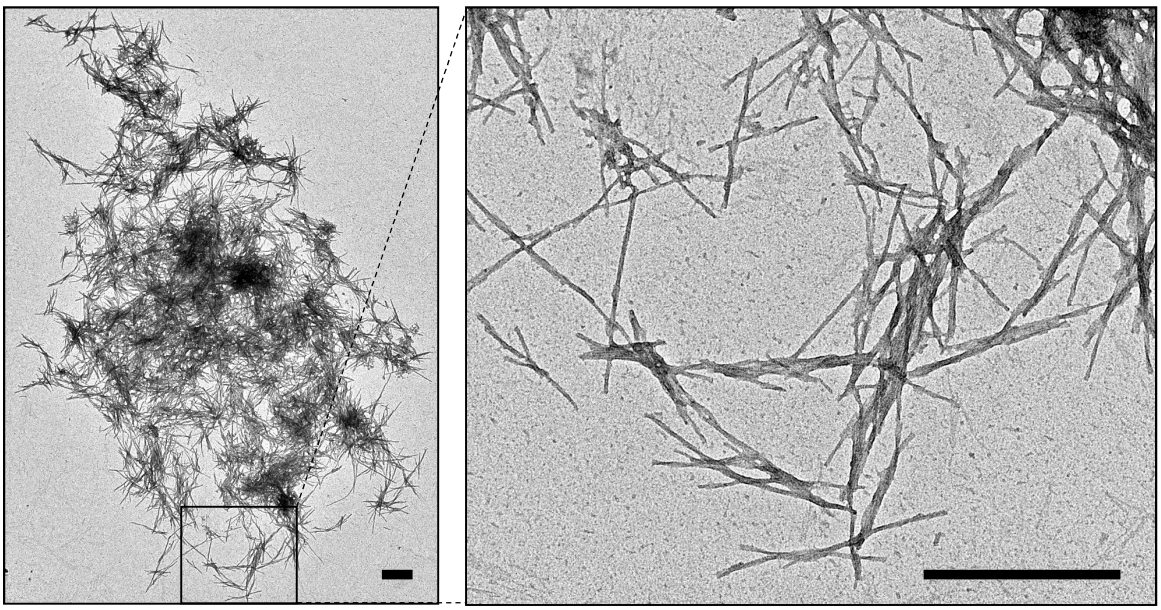

Figure 2.14. PHF6 forms clusters of needle-like fibrils in NH_4OH. PHF6 was dissolved in NH_4OH following the procedure used for Aβ40 and a sample was taken for TEM imaging. Scale bars: 500 nm

Conclusion

In selecting a solvent for peptide disaggregation, one should consider the method of solvent removal, especially if the solvent affects a downstream assay. HFIP can be evaporated since it is volatile, although our results suggest that HFIP is only useful for peptide dissolution and not disaggregation. NH_4OH can be neutralized by the assembly buffer, while DMSO can be diluted to a sufficiently low concentration or even dialyzed off, although the peptides may begin to assemble during that process.

Other possible solvents include formic acid, which has been shown to increase antibody detection in immunohistological staining of brain sections by increasing antigen exposure [10] and also solubilize polyglutamine (Q_{20}) peptides [11]. However, if the

formation of aggregates is caused by crossing the isoelectric point of the peptide, then using acids will not be ideal for Aβ assembly in neutral buffers.

It is likely that the formation of pre-existing aggregates not only depends on the aggregation propensity of the primary sequence of the peptide/protein but is also affected by many variables along the synthesis and purification process. Therefore, a range of solvents or denaturants may need to be tested when attempting to disaggregate peptides.

Materials and Methods

Peptide synthesis and purification

Peptides were synthesized on a CEM Liberty automated microwave peptide synthesizer. Fmoc-Val-PAL-PEG-PS resin (0.19 mmol/g, Applied Biosystems) or Fmoc-Val-TentaGel R PHB resin (0.20 mmol/g, Rapp Polymere GmbH, Tübingen, Germany) were used for Aβ40; Fmoc-Ala-PAL-PEG-PS resin or Fmoc-Ala-TentaGel R PHB resin were used for Aβ42. Resins were swollen in 50% DMF/ 50% DCM for at least 15 min before the first deprotection reaction. Deprotections were performed with 20% v/v piperidine + 0.1 M hydroxybenzotriazole (HOBt) in DMF at 75 °C for 3 min and couplings were performed with 1 M HOBt in DMF and 0.5 M N,N'-Diisopropylcarbodiimide (DIC, Aapptec, Louisville, KY) in DMF at 75 °C for 5.5 min. However, histidine was double coupled at 50 °C for 8 min and arginine was double coupled at 75 °C for 10 min.

For PHF6 and other short peptides synthesized, Fmoc-rink amide MBHA resin (Anaspec, CA) was used. Deprotections were performed in 20% v/v piperidine without HOBt and activations were done with 0.1 M 2-(1H-Benzotriazole-1-yl)-1,1,3,3-tetramethyluronium hexafluorophosphate (HBTU) and 0.2 M N,N–Diisopropylethylamine

(DIEA) in DMF. N-termini were acetylated by the addition of 20% v/v acetic anhydride in DMF.

The resins were then filtered, washed with DCM and dried overnight in a desiccator. Peptide cleavage was done using 10 mL of TFA/thioanisole/1,2-ethanedithiol/anisole (90:5:3:2% v/v/v/v) at room temperature for 3 hours. The mixture was then filtered drop-wise into cold (-20 °C) diethyl ether and the precipitated peptide was collected by centrifugation at 4,000 rpm, 4 °C for 10 min. The pellet was washed three times with cold diethyl ether by resuspension and centrifugation and then dried in a desiccator overnight.

The crude peptide was then dissolved in a minimal amount of 15% MeCN + 0.1% formic acid and purified by RP-HPLC using a semipreparative C18 column (Waters Corp., Milford, MA) with a 1%/min acetonitrile-water + 0.1% formic acid gradient. Aβ40 typically elutes between 26.8-28.0% MeCN as a broad peak on the chromatogram and fractions are analyzed by MALDI-MS with α-cyano-4-hydroxycinnamic acid (Sigma-Aldrich) as the matrix. Fractions containing peptides were pooled and acetonitrile was removed by rotary evaporation. The peptides were then lyophilized to dryness.

For some batches of Aβ40, the mass spectra of the of the solutions after rotary evaporation show a hump in the baseline between 2400 to 2900 m/z and the lyophilized peptides had to be re-purified on the HPLC for a second time to reduce the magnitude of the hump to <10% of the total intensity on the mass spectra. The double-purified peptides were then dried by rotary evaporation and lyophilization.

Quantification of peptide content in Aβ40 and Aβ42

Since the lyophilized peptides contain residual salts and water of hydration, preparing Aβ solutions by weighing out the required mass of dry powder will lead to inaccurate concentrations. Therefore, the peptide content of each batch was determined by dissolving a

small amount of Aβ peptide in water (~0.2 mg in 1 ml) and measuring the concentrations of serially diluted peptides with the BCA (bicinchoninic acid) assay (Thermo Fisher Scientific). The average peptide content was about 73.3 ± 6.8 % (n=6) for Aβ40 and 76.0 ± 10.6% (n=6) for Aβ42. By correcting for peptide content each time the lyophilized powders are weighed out, batch-to-batch variations in concentrations can be minimized.

Transmission electron microscopy

Peptide solutions in HFIP were deposited on TEM grids (200 mesh formvar/carbon-coated copper grids, Electron Microscopy Sciences) and air-dried on the grids for at least 5 min. Peptides in all other solvents or buffers were incubated for 1.5 -2 min on the grids. The excess solution was then wicked away with filter paper, before the grid was stained with 2% w/v uranyl acetate in water for 1.5 min. Grids were imaged on a Hitachi H7500 or HT7700 with a tungsten filament at an accelerating voltage of 80 kV and the pixel input ranges of the image files were adjusted in GIMP 2 (GNU Image Manipulation Program) for clarity.

References

1. D'Ursi AM, Armenante MR, Guerrini R, Salvadori S, Sorrentino G, Picone D: **Solution Structure of Amyloid β-Peptide (25−35) in Different Media**. *Journal of Medicinal Chemistry* 2004, **47**:4231-4238.
2. Crescenzi O, Tomaselli S, Guerrini R, Salvadori S, D'Ursi AM, Temussi PA, Picone D: **Solution structure of the Alzheimer amyloid beta-peptide (1-42) in an apolar microenvironment. Similarity with a virus fusion domain**. *Eur J Biochem* 2002, **269**:5642-5648.
3. Tomaselli S, Esposito V, Vangone P, van Nuland NA, Bonvin AM, Guerrini R, Tancredi T, Temussi PA, Picone D: **The alpha-to-beta conformational transition of Alzheimer's Abeta-(1-42) peptide in aqueous media is reversible: a step by step conformational analysis suggests the location of beta conformation seeding**. *Chembiochem* 2006, **7**:257-267.
4. Pachahara SK, Chaudhary N, Subbalakshmi C, Nagaraj R: **Hexafluoroisopropanol induces self-assembly of β-amyloid peptides into highly ordered nanostructures**. *Journal of Peptide Science* 2012, **18**:233-241.

5. Ryan TM, Caine J, Mertens HD, Kirby N, Nigro J, Breheney K, Waddington LJ, Streltsov VA, Curtain C, Masters CL, et al.: **Ammonium hydroxide treatment of Abeta produces an aggregate free solution suitable for biophysical and cell culture characterization**. *PeerJ* 2013, **1**:e73.

6. Teplow DB: **Preparation of amyloid beta-protein for structural and functional studies**. *Methods Enzymol* 2006, **413**:20-33.

7. Wood SJ, Maleeff B, Hart T, Wetzel R: **Physical, Morphological and Functional Differences between pH 5.8 and 7.4 Aggregates of the Alzheimer's Amyloid Peptide A β**. *Journal of Molecular Biology* 1996, **256**:870-877.

8. Rengifo RF, Brockman JM, Sementilli A, Liang C, Li NX, Mehta AK, Salaita K, Lynn DG.: **Amyloid Dynamics and the Oligomer Cascade Hypothesis**. *manuscript in preparation*.

9. Lu J-X, Qiang W, Yau W-M, Schwieters Charles D, Meredith Stephen C, Tycko R: **Molecular Structure of β-Amyloid Fibrils in Alzheimer's Disease Brain Tissue**. *Cell* 2013, **154**:1257-1268.

10. Cummings BJ, Mason AJL, Kim RC, Sheu PCY, Anderson AJ: **Optimization of techniques for the maximal detection and quantification of Alzheimer's-related neuropathology with digital imaging**. *Neurobiology of Aging* 2002, **23**:161-170.

11. Iuchi S, Hoffner G, Verbeke P, Djian P, Green H: **Oligomeric and polymeric aggregates formed by proteins containing expanded polyglutamine**. *Proceedings of the National Academy of Sciences* 2003, **100**:2409-2414.

Chapter 3. Pittsburgh Compound B fluorescence binding assay

Introduction

Pittsburgh Compound B (PiB) binding to amyloid has traditionally been evaluated by PET imaging *in vivo* (both live patients and animals) [1,2], radio-ligand binding assays to brain homogenates [2-6] and autoradiography of tissue sections [7]. Saturation binding analyses of [^{3}H]PiB binding to brain homogenates, synthetic, and recombinant amyloid fibrils are typically done with a ligand concentration between 0.1 to 300 nM [6,8]. The presence of high-affinity binding sites ($K_d \leq 5$ nM) and a low-affinity binding sites ($K_d \sim 50$-300 nM) have been detected with this assay, with the former being 1000-fold more abundant in AD brains compared to other Aβ sources.

Radiochemical assays however, are expensive and cumbersome since they require regulatory approval and the use of dedicated equipment, apparatus, and lab space. Therefore, a non-radioactive assay that can distinguish between the high- and low-affinity PiB binding sites will be desirable. While PiB has been utilized to image amyloid deposits in tissue sections with multiphoton fluorescence microscopy [9], little else is known about the spectroscopic properties of PiB.

This chapter aims to understand the fluorescent properties of PiB, how it binds to Aβ, and to explore the feasibility of an *in vitro* PiB fluorescence assay to evaluate Aβ fibrils.

Results

3.1 Factors influencing the fluorescence of PiB

Thioflavin T (ThT), the fluorescent dye that PiB was derived from, is commonly used to monitor amyloid fibrillization because it is weakly fluorescent (quantum yield, $q \approx 0.0001$) in the presence of monomers and oligomers but becomes highly fluorescent ($q \approx 0.43$) in the presence of β-sheet-rich fibrils [10]. One of the proposed reasons for ThT's increased fluorescence upon binding to amyloid fibrils is that the immobilization of the molecule restricts its flexibility, especially rotation around the C-C bond between the benzothiazole and aminobenzyl groups of ThT. Therefore, when bound ThT is in the excited state where nonradiative transitions such as vibrational relaxation and formation of the twisted intramolecular charge transfer (TICT) state are less favored, a higher proportion of molecules in the excited state is driven to relax to the ground state through fluorescence [11,12].

To reduce the flexibility of PiB in solution, the temperature can be reduced, or the solvent viscosity can be increased. Since temperature control was not available on the spectrofluorometers, PiB fluorescence was measured in phosphate buffers with increasing amounts of glycerol. As the glycerol content increased from 0 to 80% v/v, a 3-fold increase in the fluorescence intensity was observed with no blue- or red-shift in the λ_{max} (**Figure 3.1**). This finding suggests that one of the mechanisms for the increase in PiB fluorescence upon binding to amyloids is due to the steric hindrance encountered in the microenvironments when immobilized in the binding sites.

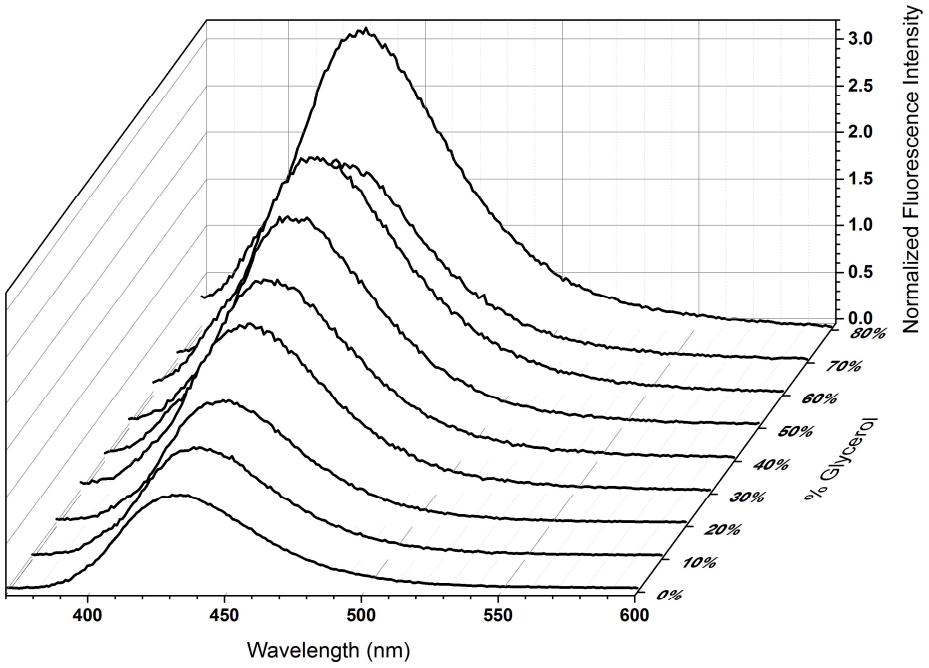

Figure 3.1. PiB fluorescence intensity increases with glycerol content. PiB was dissolved to 10 nM in mixtures of glycerol and 10 mM sodium phosphate buffer, pH 7.4 and the emission spectra (ex = 348 nm) were recorded.

Tryptophan (Trp) residues in proteins can be used as intrinsic fluorescent probes to study protein structures and dynamics. One factor that influences Trp fluorescence is the polarity of its microenvironment. When buried in the hydrophobic interior of a protein, Trp typically has a λ_{max} < 330 nm but when the protein unfolds and Trp is exposed to the polar solvent, the λ_{max} can red-shift to > 330 nm [13]. ANS (1-anilinonaphthalene-8-sulfonate) is a fluorophore commonly used as an extrinsic fluorescent probe for protein characterization. In a polar aqueous environment, ANS is weakly fluorescent, but when dissolved in a non-polar solvent or bound to a hydrophobic pocket in a protein, has a higher fluorescence together with a blue-shift in the λ_{max} [11,14].

To probe the effects of solvent polarity on PiB fluorescence, we dissolved PiB in a series of solutions containing increasing amounts of MeOH in the assembly buffer and the fluorescence was measured. As the percentage of MeOH in the buffer increased from 0 to 100%, a linear decrease in the λ_{max} of the emission peaks was observed from 432.5 nm to 418 nm (**Figure 3.2A**). The emission intensities increased by up to 15-fold (**Figure 3.2B**), although it was more prone to error and thus the relationship is unclear. Additionally, when PiB was dissolved in a variety of organic solvents, the λ_{max} of the emission spectra decreased as the dielectric constant of the solvent decreased (**Figure 3.3**). These results show that PiB fluorescence increases and blue-shifts in a hydrophobic environment, suggesting that these spectral signatures observed when Aβ is added to PiB are indicative of PiB binding sites on the fibrils that are more hydrophobic than the bulk solution.

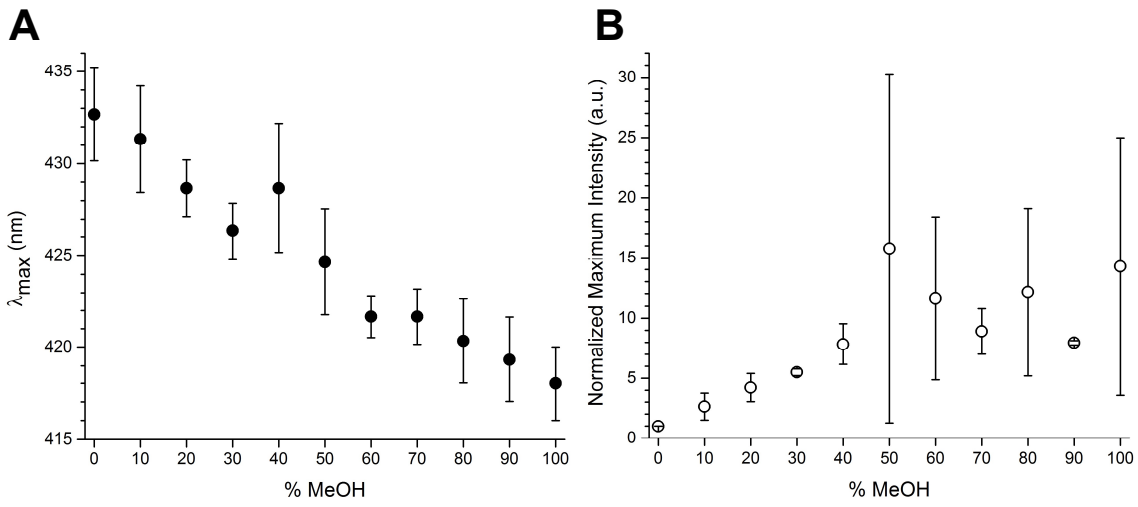

Figure 3.2. PiB fluorescence emission blue-shifts and increases with the percentage of MeOH in buffer. PiB was dissolved to 10 nM in various mixtures of phosphate buffer and MeOH and the emission spectra (ex = 348 nm) were recorded. The λ_{max} (A) and maximum intensity normalized to the intensity in phosphate buffer alone (B) of each peak was then plotted against the % of MeOH in the solution.

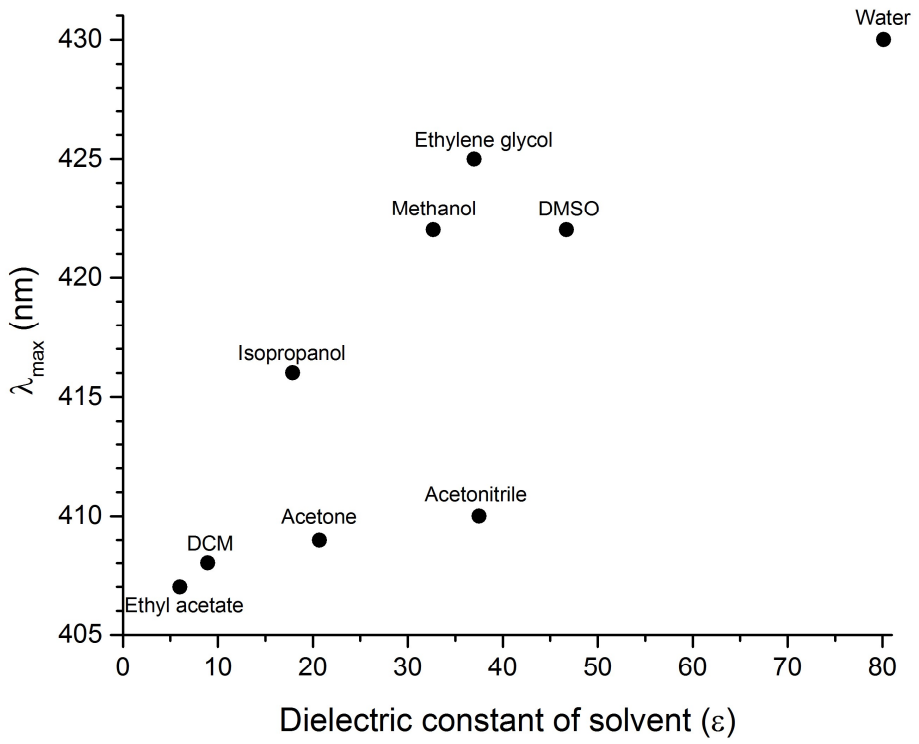

Figure 3.3. PiB fluorescence emission blue-shifts in hydrophobic solvents. PiB was dissolved in various solvents to 10 nM and the emission spectra (ex = 348 nm) were recorded. The λ_{max} of each peak was then plotted against the dielectric constant of the solvent that PiB was dissolved in. It is noteworthy that emission spectra were not obtained for 10 nM PiB in hexane (ε_r = 1.88) and chloroform (ε_r = 4.81), because emulsions were formed.

To look at how PiB fluorescence changes in the presence of Aβ, we performed a reverse titration experiment with a fixed amount of PiB and increasing amounts of Aβ40 fibrils. At low concentrations of Aβ, we expect only a small population of PiB to be bound to Aβ, while at high Aβ concentrations, we assume that all the PiB is in the bound state with a negligible unbound population in solution. **Figure 3.4** shows that as the peptide concentration increased from 0.5 μM to 25 μM, the fluorescence of 10 nM PiB intensifies and blueshifts, which we interpret as a signature for binding to β-sheets. However, the fluorescence intensity peaks at 20 μM Aβ40 and decreases at 25 μM Aβ40 likely due to

quenching by the inner filter effect, indicating that for maximal fluorescence signal, the upper limit for peptide concentration should not be exceeded.

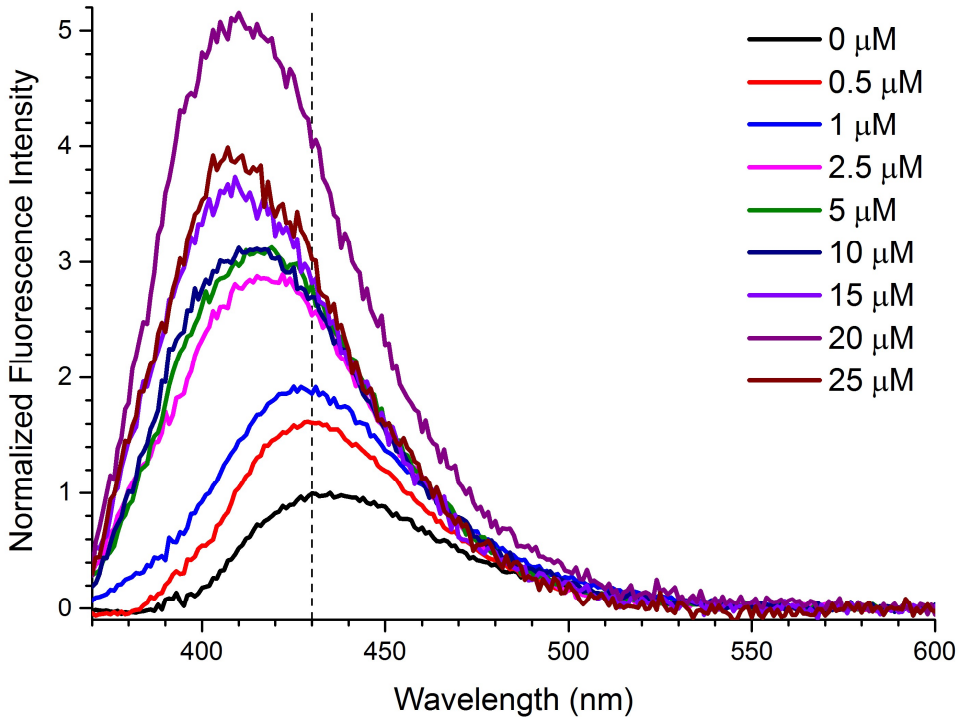

Figure 3.4. PiB fluorescence emission blue-shifts and intensifies as Aβ concentration increases. The fluorescence of 10 nM PiB was measured in the presence of 0 to 25 μM synthetic Aβ40 (ex = 348 nm).

To determine the approximate incubation time needed for PiB binding to Aβ in vitro, PiB was added to a solution of Aβ40 in the fluorescence cuvette and the emission spectra were recorded continuously over 2 hours (**Figure 3.5A**). **Figure 3.5B** showed a rapid decrease in the λ_{max} where most of the blue-shift has occurred within the first 10 minutes. In fact, this assay does not report on the initial binding and blue-shifting during the lag time (~15 s to mix PiB with Aβ, place the cuvette in the cuvette holder, close the lid on the fluorometer and begin scan) of the experiment, since unbound PiB has a λ_{max} of 430 nm but the first emission spectrum only began from a λ_{max} of 408 nm. Thus, for the purposes of

measuring PiB fluorescence binding to Aβ fibrils *in vitro*, it is safe to conclude that an incubation of at least 10 minutes before spectral acquisition is sufficient for reaching equilibrium binding. The fluorescence intensity of PiB binding to Aβ was also observed to exponentially decrease to 20% of the initial intensity over 2 hours (**Figure 3.5C**) with a $t_{1/2}$ ≈50 min. Since the fluorescence was measured in a cuvette with excitation and emission beams in the horizontal plane instead of in a vertical plane as in microplate readers, the most plausible reason for the decrease in fluorescence would be due to bound PiB settling to the bottom of the cuvette over time and absorbing less of the excitation light, leading to decreased emission. To test this, the experiment was repeated but the sample in the cuvette was mixed by pipetting after 1 hour of monitoring (**Figure 3.6A**), to resuspend the fibrils. As predicted, the fluorescence increased after mixing and decayed exponentially in the second hour, although the fluorescence was <90% of the initial intensity, possibly due to sample adsorption on the pipette tip.

The absorbance of Aβ40 at 225 nm in both the presence and absence of PiB was also monitored over 2 hours (**Figure 3.6B**) and was observed to decrease over time, although it did not follow an exponential decay as in **Figure 3.6A**. This is due to the presence of Aβ oligomers and monomers in solution that did not settle to the bottom of the cuvette. The fluorescence assay, however, was largely reporting on bound PiB, suggesting that there is a higher binding affinity to fibrils than to oligomers and monomers.

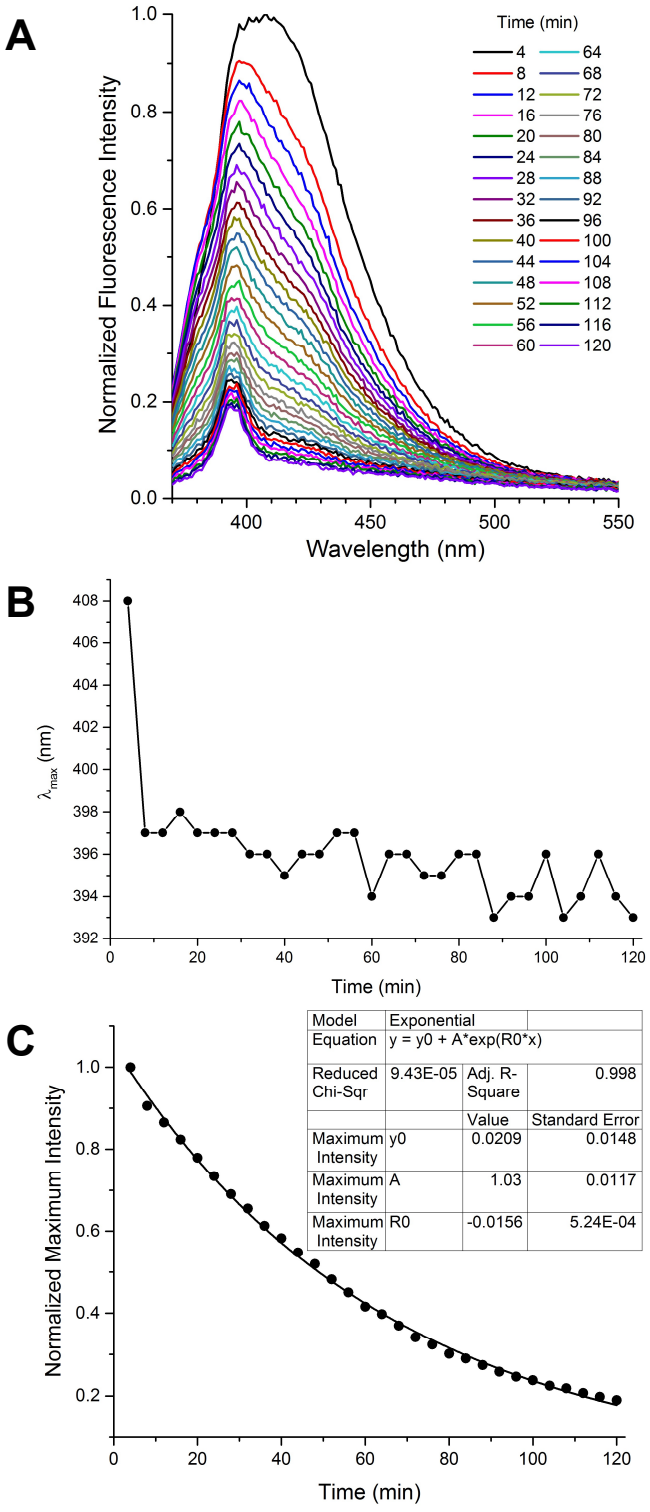

Figure 3.5. PiB fluorescence emission blue-shifts quickly upon binding to Aβ and diminishes over time. (A) PiB was added to synthetic Aβ40 and the fluorescence was acquired over 2 hours in 4-minute intervals (10 nM PiB with 20 μM Aβ40, ex = 348 nm). The λ_{max} (B) and maximum intensity fitted with an exponential decay function (C) of each spectrum of each peak was then plotted against time.

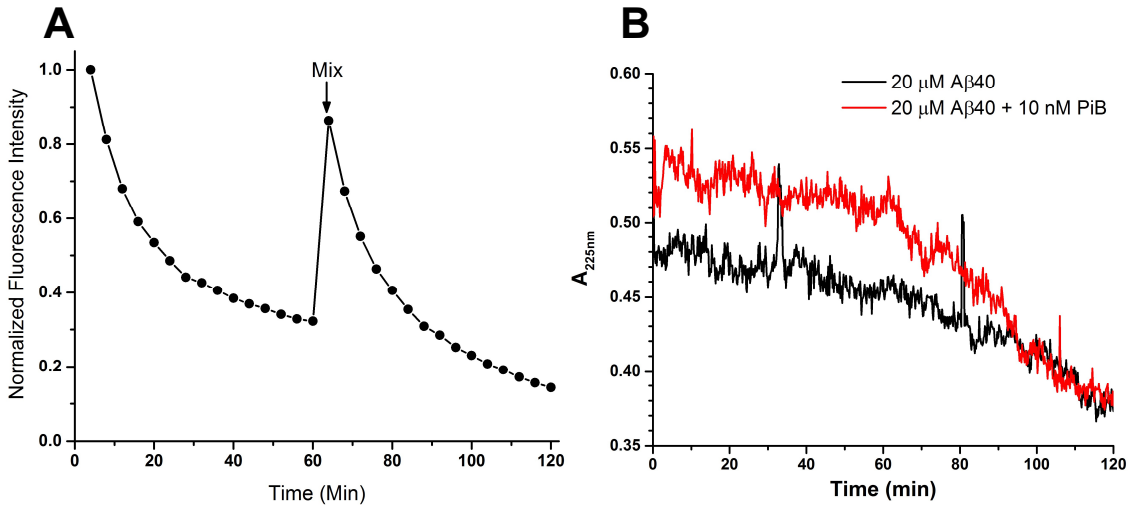

Figure 3.6. PiB fluorescence decreases over time when bound to amyloid due to settling in the cuvette. (A) The fluorescence (ex = 348 nm) of 10 nM PiB with 20 μM synthetic Aβ40 was acquired over 2 hours in 4-minute intervals and the maximum intensity was plotted. After 1 hour, the sample in the cuvette was briefly mixed by pipetting before resuming spectral acquisition. (B) The absorbance of Aβ40 (black line) and Aβ40 with PiB (red line) at 225 nm was monitored over two hours. The spikes in the traces are due to software glitches when the computer was moved out of screensaver mode. 10 nM PiB has no absorbance at 225 nm.

We then acquired PiB fluorescence in the presence of freshly dissolved Aβ40 monomers and unlike binding to Aβ fibrils, we only observed an increase in emission intensity with no change in the λ_{max} (**Figure 3.7A**). Similarly, PiB binding to an equivalent mass of the BSA protein showed higher fluorescence with no blue-shift (**Figure 3.7B**). Since both the Aβ monomers and BSA have low β-sheet content, the results here indicate that the blue-shift observed in the presence of Aβ fibrils is due to binding to β-sheets while non-specific binding only increases fluorescence.

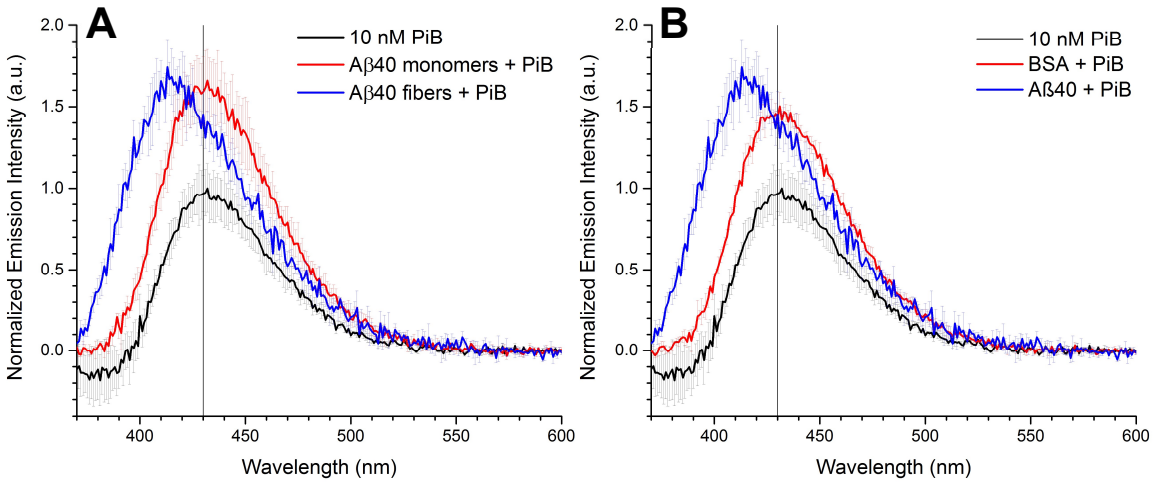

Figure 3.7. PiB fluorescence intensifies but does not blue-shift in the presence of Aβ monomers and BSA. Fluorescence emission spectra of 10 nM PiB alone in phosphate buffer and in the presence of 20 μM assembled Aβ40 fibrils, 20 μM Aβ40 monomers (A) or 1.3 μM BSA (0.87 mg/ml, equivalent to 20 μM Aβ40) (B).

To determine if PiB binds preferably to the sides or ends of Aβ fibrils, we compared PiB fluorescence binding to synthetic Aβ fibrils and seeds. The hypothesis is that if PiB has a higher binding affinity to the ends of the fibrils over the sides of the fibrils, then creating more fibril ends should result in a higher and more blue-shifted fluorescence spectrum due to a higher population of bound PiB. The Aβ concentration was reduced from 20 to 1 μM to reduce the number of binding sites at the sides of the fibrils, which would increase the proportion of unbound PiB available for binding to the ends of the fibrils. We observed no increase or greater blue-shift in the emission spectrum upon binding to Aβ seeds compared to the fibrils but instead, a small decrease in intensity (**Figure 3.8A**). A t-Test for the normalized intensities of the fibrils (1.97 ± 0.36) and seeds (1.79 ± 0.47) indicated that the difference is insignificant ($p = 0.59$), so this could be due to the disassembly of some peptide into monomers during sonication. CD experiments support this explanation, where the

magnitude of the negative ellipticity decreased after sonication (**Figure 3.8B**). Overall, these results suggest that PiB does not bind to the ends of the Aβ fibrils.

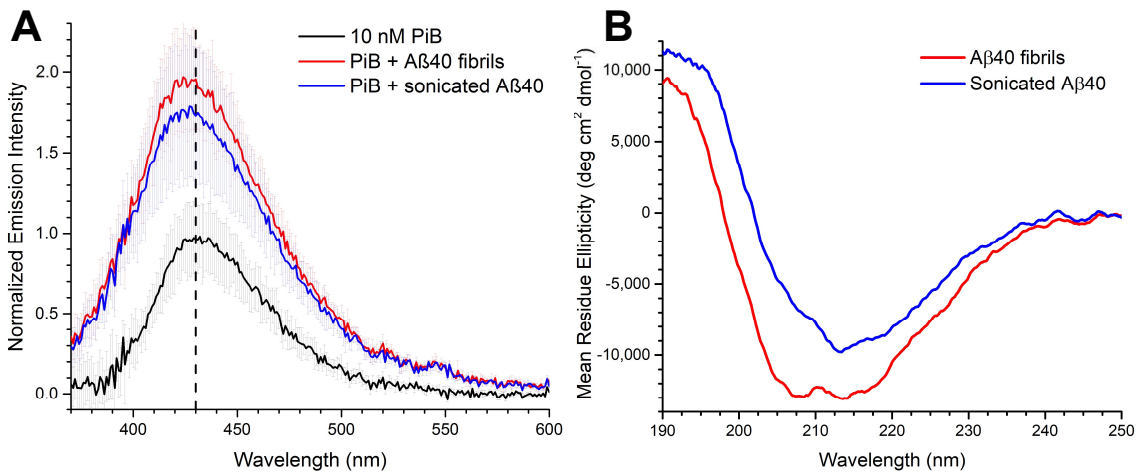

Figure 3.8. PiB fluorescence is similar in the presence of Aβ40 fibrils or seeds. (A) 1 μM synthetic Aβ40 fibrils were probe-sonicated for 30 secs to produce fragmented seeds. The fluorescence of 10 nM PiB was then measured in the presence of the fibrils or seeds. (B) CD spectra of 100 μM Aβ40 fibrils before and after sonication.

Having obtained a better understanding of how PiB fluoresces under various conditions, we then set out to determine if a fluorescent assay can be developed for PiB binding to Aβ.

3.2 Separation of bound and unbound PiB with spin filters

In radio-ligand binding assays, the bound ligands are separated from the unbound ligands by filtering the solution. The ligand-receptor complexes are trapped on the filters, which are placed in scintillation fluid for detection. However, this method is unsuitable for fluorescence because a filter in the cuvette would absorb light, so the protocol needs to be modified. To separate the bound PiB from free PiB, a centrifugal spin filter typically used for concentrating proteins can be used to retain the Aβ fibrils including the bound PiB, while the unbound PiB should be filtered through the membrane. Since the protein recovery of

the retentate will be less than 100% due to protein adsorption on the membrane and filter housing, the assessment of PiB binding to Aβ may be more accurate by inferring from the fluorescence of unbound PiB in the filtrate.

To test if the 10 kDa MWCO filter is effective at retaining Aβ40 (MW = 4.3 kDa) fibrils, Aβ40 was centrifuged through the device and samples of the retentate and filtrate were taken for TEM. **Figure 3.9** shows that a dense network of fibrils was concentrated in the retentate while the filtrate was free of fibrils and oligomers. Therefore, if synthetic Aβ has few high-affinity PiB binding sites, we should be able to detect unbound PiB in the filtrate.

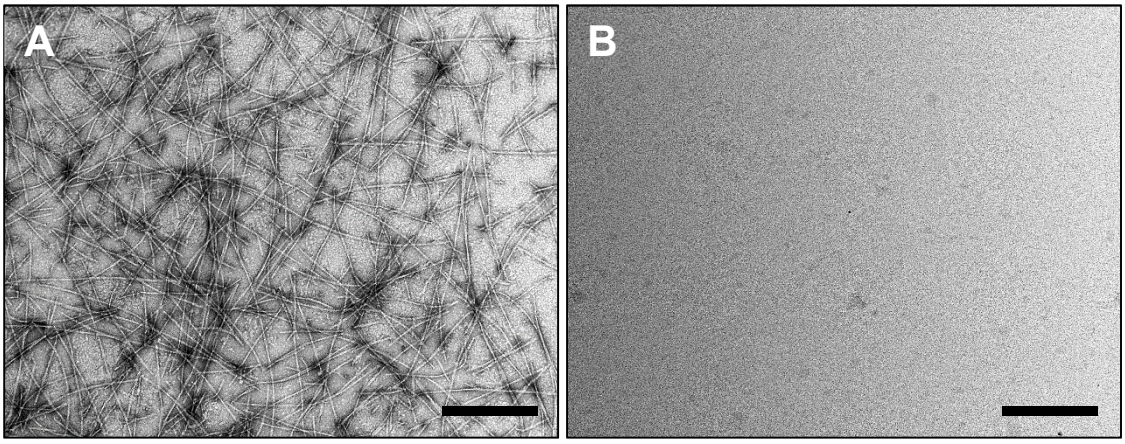

Figure 3.9. Centrifugal filter devices are effective at retaining Aβ40 fibrils. Synthetic Aβ40 (100 μM, 200 μl) was added to a 10 kDa MWCO Amicon ultra-0.5 ml centrifugal filter and centrifuged at 15k rpm for 5 min. Numerous fibrils were present in the retentate (A) as observed by TEM, while the filtrate (B) was visibly free of any fibrils or oligomers. Scale bars: 500 nm

PiB was then incubated with Aβ40 before the mixture was centrifuged in a spin filter, washed and resuspended in phosphate buffer (**Figure 3.10A**). The fluorescence spectrum of the retentate 2 (R2) is characteristic of the autofluorescence of Aβ fibrils. Additionally, the Aβ-only sample showed some fluorescence in both filtrates 1 and 2, where some monomers

and low-molecular weight oligomers have filtered through. Surprisingly, no fluorescence was detected in the filtrates or retentate for the PiB-only control, suggesting that PiB was retained in the membrane.

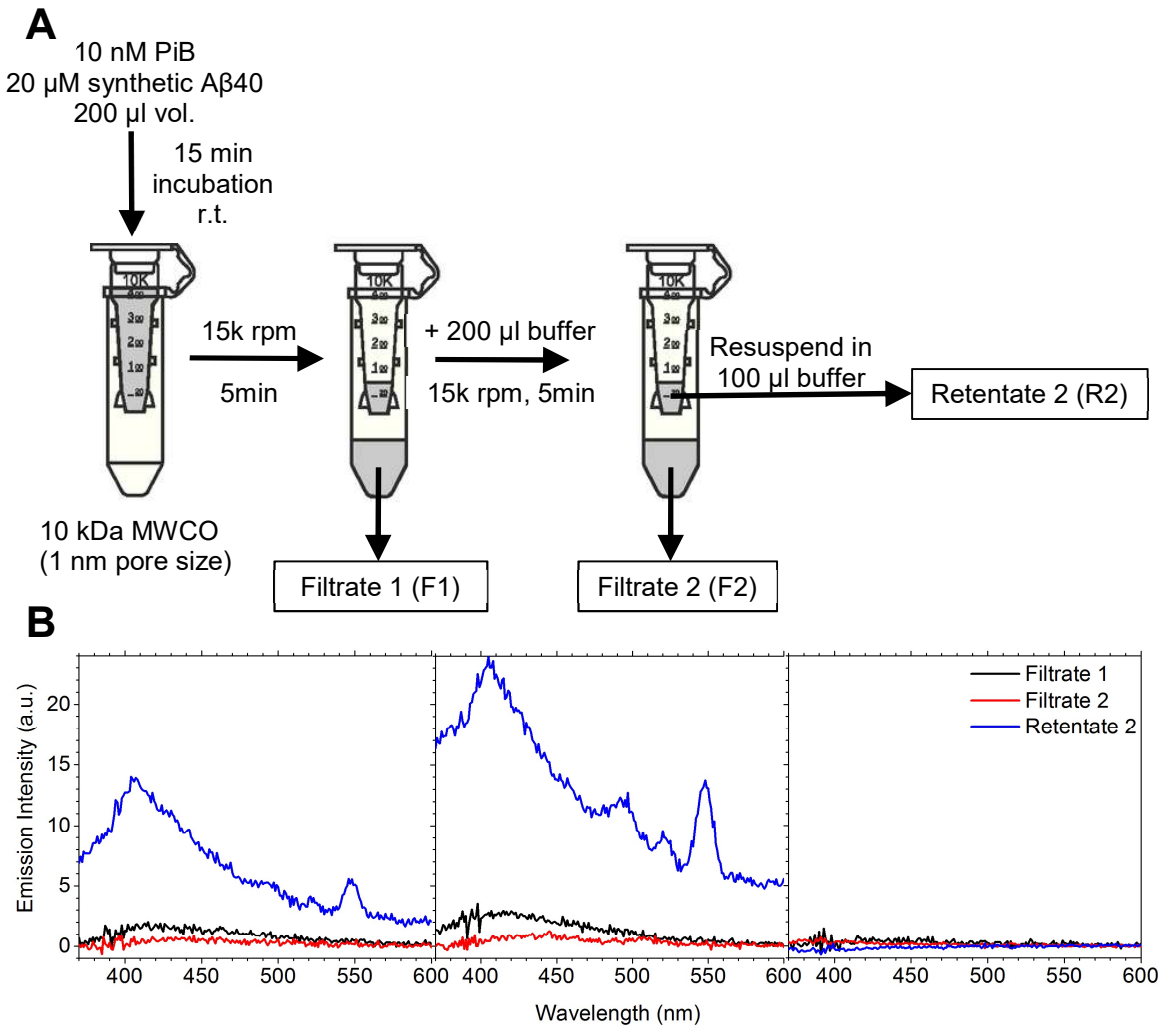

Figure 3.10. Separation of Aβ-bound PiB with spin filters. (A) Protocol used to separate bound and unbound PiB with spin filter. (B) Fluorescence spectra of filtrates and retentates. Emission spectra of 10 nM PiB + 20 µM Aβ40 (left), 20 µM Aβ40 control (middle) and 10 nM PiB control (right).

If PiB loss during filtration is due to using a concentration that is too low, would higher PiB concentrations overcome this problem? To answer this, we increased the concentration of PiB up to 100 nM (**Figure 3.11A**) and filtered them through the spin filters. While some weak fluorescence was observed in the filtrates, the intensity from the 20 nM PiB was higher than that of the 50, 75 and 100 nM samples (**Figure 3.11B**), suggesting that the noise was larger than the signal and PiB is effectively trapped in the membrane.

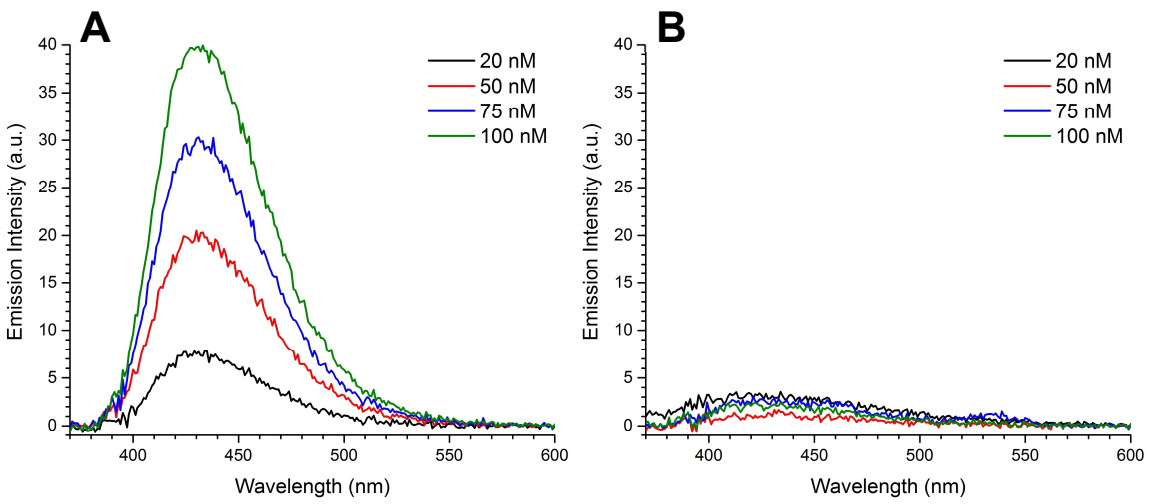

Figure 3.11. PiB fluorescence is diminished after centrifugation in spin filters. (A) Fluorescence spectra of 20 to 100 nM solutions of PiB in phosphate buffer. (B) The PiB solutions were centrifuged through the spin filters and the fluorescence of the filtrates were measured.

At this point, the concentration of PiB was increased by a few orders of magnitude up to 100 μM to evaluate the binding affinity onto the membrane. At high concentrations, PiB fluorescence does not need to be measured in a spectrofluorometer because it is visibly fluorescent under a handheld UV light (**Figure 3.12A**). The PiB solutions were then filtered through pre-rinsed centrifugal filters, after which the filters were washed by centrifugation of buffer alone. When the filters were cracked open and visualized under UV light, all

membranes were visibly fluorescent indicating that PiB was still bound after washing (**Figure 3.12B**). We then looked at binding of PiB to filter paper, since both the membrane and paper are cellulose-based materials. When spotted onto filter paper, PiB quickly binds to the filter paper while the buffer spreads out on the paper, so most of the fluorescence was localized to the center of each spot (**Figure 3.12C**). The strip of paper was then immersed for 15 min in a 50-ml centrifuge tube containing water, before it was removed and visualized (**Figure 3.12D**). Given that a large volume of water was used to wash the filter paper, we expected that the fluorescence intensity of the spots will decrease as the adsorbed PiB diffuses into the water, but instead, the intensities before and after washing are similar. These experiments show conclusively that PiB strongly binds to the filter membranes and detecting unbound PiB in the filtrates will be near-impossible. The filters could be passivated by BSA to reduce PiB adsorption, but this may lead to clogging of the pores and unnecessarily complicates the goal of a simple fluorescence assay for determining bound and unbound PiB fractions.

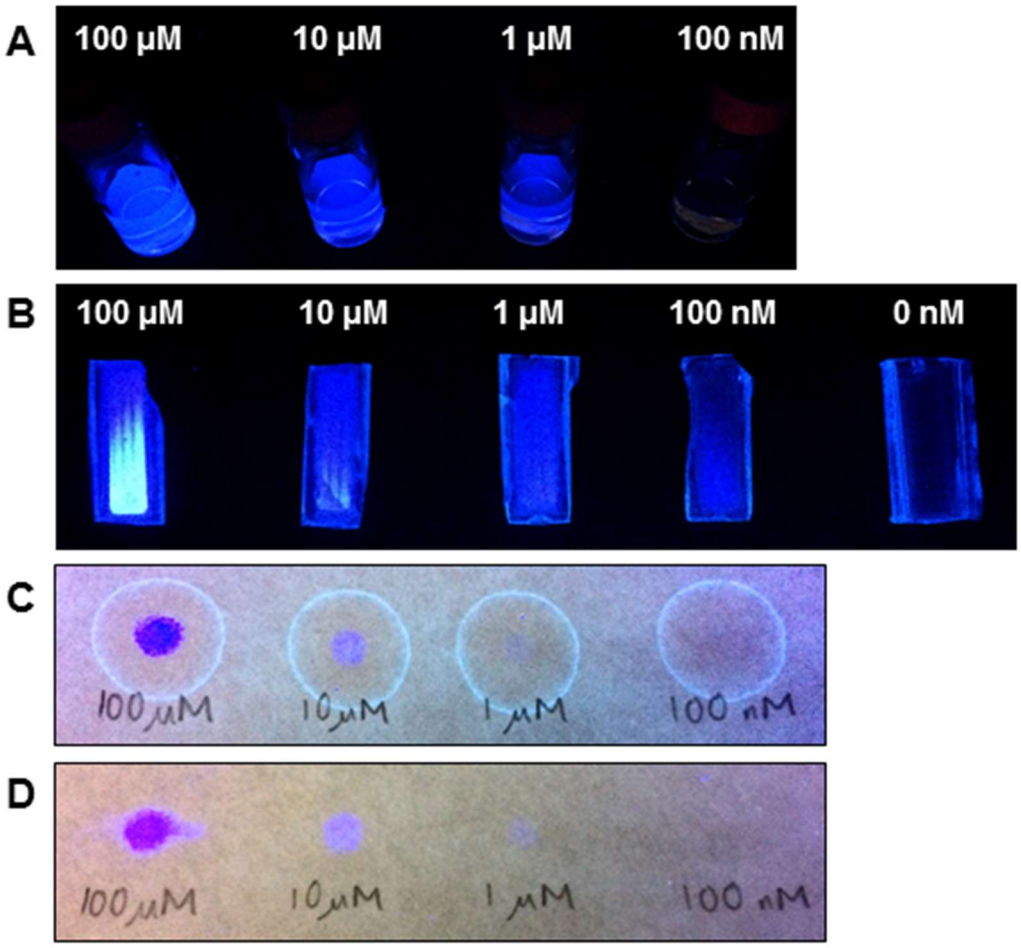

Figure 3.12. PiB is visibly fluorescent and binds to cellulose/paper. (A) PiB was dissolved at 100 µM, 10 µM, 1 µM, and 100 nM in 10 mM phosphate buffer pH 7.4 and visualized under uv light (365 nm). (B) 500 µl PiB at 100 µM, 10 µM, 1 µM, 100 nM and buffer (0 nM) was filtered through a 10 kDa MWCO centrifugal filter (15k rpm, 5 min) and washed by adding 500 µl buffer and centrifuging the filters. The filter units were then removed from the centrifuge tubes and broken with a hammer. One of the two membranes (regenerated cellulose) was then visualized under uv light. (C) 10 µl of PiB at 100 µM, 10 µM, 1 µM, and 100 nM was spotted onto a filter paper dropwise and allowed to dry before it was imaged under uv light. The filter paper was then washed by immersion in a centrifuge tube containing 50 ml of distilled water for 15 min, before it was dried and imaged again (D). The white rings on the filter paper are the edges of the waterfront when PiB was spotted on.

3.3 Separation of bound and unbound PiB by centrifugation

We then turned to simple centrifugation to separate bound and unbound PiB, where bound PiB should be in the pellet with the Aβ fibrils while unbound PiB should be in the

supernatant with the unassembled Aβ. To test how effectively Aβ fibrils can be pelleted and removed from the supernatant, synthetic Aβ40 was centrifuged and the fibril content in the pellet and supernatant were quantified with ThT fluorescence. Since a solid pellet was not visible after centrifugation, the top and bottom halves of the solution were regarded as the supernatant and pellets respectively (**Figure 3.13A**). Before centrifugation, ThT binding to the 20 μM Aβ40 solution was 2.5-fold over ThT alone, and after centrifugation, ThT fluorescence of the supernatant decreased to 1.2-fold while the resuspended pellet had a 3.5-fold intensity (**Figure 3.13B**). The relative amounts of fibrils in the TEM images corroborate with the ThT fluorescence results, with the pellet having the highest density of fibrils (**Figure 3.13E**) while the supernatant having sparser fibrils (**Figure 3.13D**) than before centrifugation (**Figure 3.13C**).

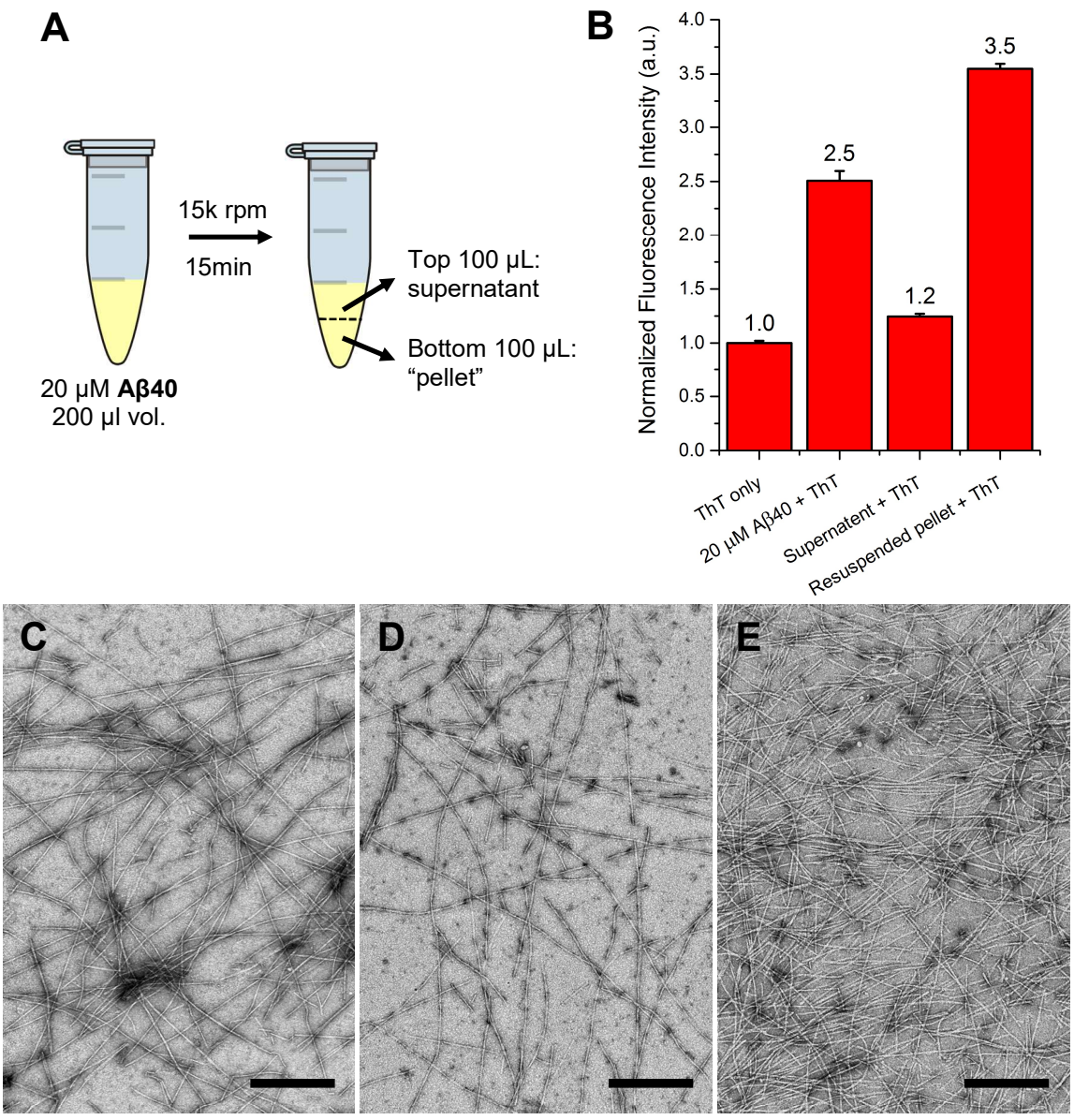

Figure 3.13. Aβ40 fibrils can be enriched by centrifugation. (A) Schematic of protocol used to concentrate Aβ fibrils. (B) ThT fluorescence of 20 µM Aβ40, supernatant and resuspended pellet normalized to the fluorescence of ThT alone. TEMs of samples (C) before centrifugation, (D) supernatant and (E) resuspended pellet. Scale bars: 500 nm.

PiB was then incubated with Aβ40 before centrifugation and the fluorescence spectra of the supernatants and pellets were acquired. As predicted, the raw fluorescence was more intense in the pellet than in the supernatant (**Figure 3.14**, left), but surprisingly, the

fluorescence of the Aβ-only samples was only slightly higher in the pellet as compared to the supernatant, suggesting that the autofluorescence from the Aβ in the supernatant is not negligible (**Figure 3.14**, middle). Another unanticipated observation was that PiB fluorescence can be enhanced in the pellet (**Figure 3.14**, right), suggesting that invisible precipitates or micelles were forming when PiB is not bound to Aβ. Since we are unable to quantify how much of the increased fluorescence in the pellet of a PiB-Aβ sample is due to sedimentation of free PiB or pelleting of bound PiB, the centrifugation approach was abandoned.

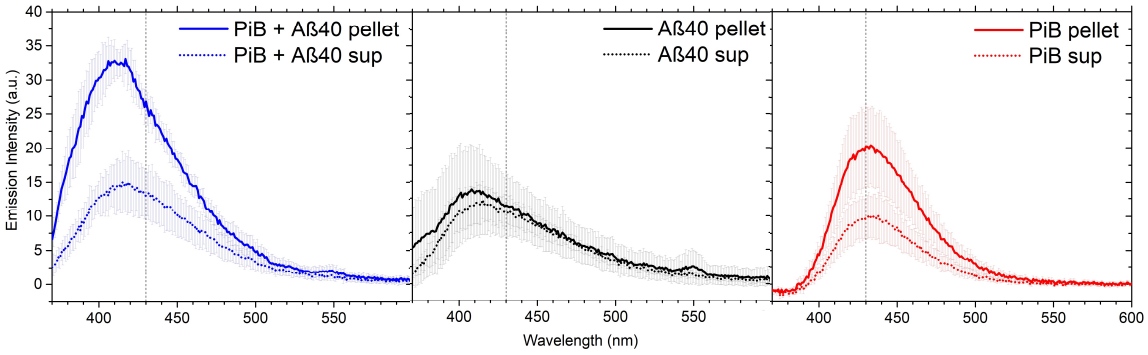

Figure 3.14. PiB fluorescence can be enhanced by centrifugation. 10 nM PiB + 20 μM Aβ40 (left), 20 μM Aβ40 control (middle) and 10 nM PiB control (right) incubated for 15 min before centrifugation at 15k rpm for 15 min, and the fluorescence of the pellets (solid lines) and supernatants (dash lines) were measured.

3.4 Separation of bound and unbound PiB with fiberglass filters

We then returned to the filtration approach, but this time using the same Whatman GF/B glass fiber filters that are used in the ^{3}H-PiB radio-ligand binding assays [5,15-17], rationalizing that they should not retain PiB since unbound PiB can be washed off before they are immersed in scintillation fluid. The 100 nM PiB solutions that were filtered showed a decreased fluorescence intensity as compared to the unfiltered solutions, and this was also

observed when the PiB concentration was increased ten-fold to 1 μM (**Figure 3.15**). Although the glass fiber filters retained substantially less PiB than the cellulose-based filters, it is likely that some extra washes will be required to elute the remaining PiB from the filter, further diluting the fluorophore concentration of the filtrate. If this method were to be applied at a 10 nM PiB concentration when evaluating binding to Aβ fibrils, the PiB fluorescence in the filtrates will likely be too weak for a reliable comparison. As such, we conclude that this approach is also not feasible.

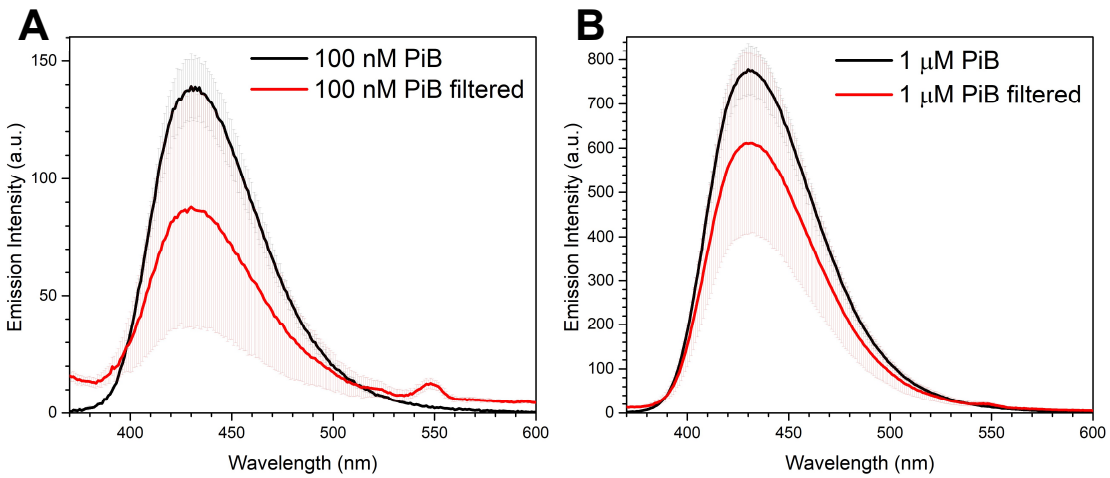

Figure 3.15. PiB fluorescence decreases after filtration through glass fiber filters. GF/B filters were cut to size and placed in 12 ml syringes. 1 ml of 100 nM PiB (A) or 1 μM PiB (B) was then pipetted into each of the syringes, then filtered through. The fluorescence spectra of the filtrates were then compared with unfiltered samples.

Conclusion

Our efforts to develop a quick and easy fluorescence assay for quantifying bound and unbound PiB using filtration or centrifugation were unsuccessful due to retention by the filters and the unexpected property that PiB can be concentrated by centrifugation. Therefore, quantitative *in vitro* PiB binding is still best evaluated by a radio-ligand binding assay. However, we can still ascertain if PiB binds or does not bind to an amyloid sample by

acquiring the total PiB fluorescence spectrum and comparing the λ_{max} relative to that of PiB alone. We discovered that a blue-shift in the PiB fluorescence spectrum indicates either binding to β-sheet-rich fibrils and/or the molecule is in a hydrophobic environment, which also suggests that PiB binds to the exposed or accessible hydrophobic residues in Aβ. Other factors that affect PiB fluorescence are summarized in **Table 3.1**.

Table 3.1. Factors influencing the fluorescence of PiB

Increased fluorescence intensity	**Blue-shift in emission**
Larger mass of amyloid fibrils	Larger mass of amyloid fibrils
Hydrophobic environment	Hydrophobic environment
Higher solution viscosity	
Non-specific binding to monomers/aggregates, BSA	

Materials and Methods

Pittsburgh compound B (PiB) fluorescence

PiB (ABX GmbH, Radeberg, Germany) was dissolved to 10 mM in DMSO and stored in aliquots at -20 °C and working solutions were serially diluted from the stock solutions into phosphate buffer. PiB fluorescence was measured in a quartz cuvette (Hellma Analytics 105.251-QS, 3x3 mm light path, 100 µl volume) with either a Horiba Jobin-Yvon Fluoromax 3 or an Agilent Cary Eclipse spectrofluorometer. On the Fluoromax, emission spectra were acquired in 1 nm data intervals at 1 nm/s, 1 s averaging time with excitation and emission slit widths of 5 nm, while on the Cary Eclipse, spectral acquisition was done at 1 nm data intervals at 2 nm/s, 0.5 s averaging time and a PMT voltage of 800 V with

excitation and emission slit widths of 5 and 10 nm respectively. The raman scattering peak at 396 nm for each spectrum was removed by subtracting the emission spectrum of phosphate buffer[18]. Unless otherwise stated, the fluorescence spectra of PiB in the presence of Aβ was corrected by subtracting the auto-fluorescence of the Aβ-alone spectra from the PiB + Aβ spectra. Normalized spectra were obtained by setting the baselines between 550-600 nm to zero, before dividing by the maximum intensity of the 10 nM PiB baseline-corrected spectrum.

Thioflavin T (ThT) fluorescence

Thioflavin T (AnaSpec, ultrapure grade, Cat. No. AS-88306) was dissolved to 10 mM in 10 mM phosphate buffer, pH 7.4 and frozen at -20 ºC in aliquots until ready for use. End point assays were performed using black 96 well plates with clear flat bottoms (Corning, Cat. No. 3631) in a Biotek Synergy HT plate reader controlled by KC4 software. Each well had a 100 μl total volume containing 10 μM Aβ and 10 μM ThT in 50 mM glycine buffer pH 8.5. The plate was briefly shaken for 3 seconds with the intensity set at 3 before fluorescence was measured at the bottom of the wells with 440/20 and 485/20 nm excitation and emission filters respectively and sensitivity at 50. Fluorescence values were divided by the average values of the standard wells containing 100 μl of 10 μM ThT only.

Absorbance spectroscopy

Aβ and PiB absorbance were measured in a 1 cm path length quartz cuvette with a Jasco V-530 spectrophotometer at 225 nm every 10 sec. Absorbance values were corrected by using phosphate buffer as the background.

Circular Dichroism

Aβ40 aliquots were placed in a 0.10 mm path length quartz cuvette and CD spectra were recorded at room temperature from 190-250 nm wavelengths in a Jasco J-810 spectropolarimeter. Samples were scanned at a 100 nm/min rate with 0.2 nm resolution and 2 nm bandwidth for 3 accumulations. Sample spectra were corrected by subtracting the buffer control spectrum and then converted to mean residue ellipticity with the formula $[\theta] = [\theta]_{obs}/(10 \times n \times C \times l)$, where $[\theta]_{obs}$ is observed ellipticity (in mdeg), n is the number of peptide bonds, C is concentration (M) and l is path length (cm). Each spectrum is an average of triplicate aliquots.

References

1. Morris JC, Roe CM, Grant EA, Head D, Storandt M, Goate AM, Fagan AM, Holtzman DM, Mintun MA: **Pittsburgh compound B imaging and prediction of progression from cognitive normality to symptomatic Alzheimer disease**. *Arch Neurol* 2009, **66**:1469-1475.
2. Price JC, Klunk WE, Lopresti BJ, Lu X, Hoge JA, Ziolko SK, Holt DP, Meltzer CC, DeKosky ST, Mathis CA: **Kinetic modeling of amyloid binding in humans using PET imaging and Pittsburgh Compound-B**. *J Cereb Blood Flow Metab* 2005, **25**:1528-1547.
3. Fodero-Tavoletti MT, Smith DP, McLean CA, Adlard PA, Barnham KJ, Foster LE, Leone L, Perez K, Cortés M, Culvenor JG, et al.: **In Vitro Characterization of Pittsburgh Compound-B Binding to Lewy Bodies**. *The Journal of Neuroscience* 2007, **27**:10365-10371.
4. Rosen RF, Ciliax BJ, Wingo TS, Gearing M, Dooyema J, Lah JJ, Ghiso JA, LeVine H, 3rd, Walker LC: **Deficient high-affinity binding of Pittsburgh compound B in a case of Alzheimer's disease**. *Acta Neuropathol* 2010, **119**:221-233.
5. Matveev SV, Spielmann HP, Metts BM, Chen J, Onono F, Zhu H, Scheff SW, Walker LC, LeVine H, 3rd: **A distinct subfraction of Abeta is responsible for the high-affinity Pittsburgh compound B-binding site in Alzheimer's disease brain**. *J Neurochem* 2014, **131**:356-368.
6. Ni R, Gillberg PG, Bergfors A, Marutle A, Nordberg A: **Amyloid tracers detect multiple binding sites in Alzheimer's disease brain tissue**. *Brain* 2013, **136**:2217-2227.

7. Hong YT, Veenith T, Dewar D, et al.: **Amyloid imaging with carbon 11–labeled pittsburgh compound b for traumatic brain injury**. *JAMA Neurology* 2014, **71**:23-31.

8. Yamin G, Teplow DB: **Pittsburgh Compound-B (PiB) binds amyloid β-protein protofibrils**. *Journal of Neurochemistry* 2017, **140**:210-215.

9. Bacskai BJ, Hickey GA, Skoch J, Kajdasz ST, Wang Y, Huang GF, Mathis CA, Klunk WE, Hyman BT: **Four-dimensional multiphoton imaging of brain entry, amyloid binding, and clearance of an amyloid-beta ligand in transgenic mice**. *Proc Natl Acad Sci U S A* 2003, **100**:12462-12467.

10. Sulatskaya AI, Maskevich AA, Kuznetsova IM, Uversky VN, Turoverov KK: **Fluorescence Quantum Yield of Thioflavin T in Rigid Isotropic Solution and Incorporated into the Amyloid Fibrils**. *PLoS ONE* 2010, **5**:e15385.

11. Hawe A, Sutter M, Jiskoot W: **Extrinsic Fluorescent Dyes as Tools for Protein Characterization**. *Pharmaceutical Research* 2008, **25**:1487-1499.

12. Stsiapura VI, Maskevich AA, Kuzmitsky VA, Turoverov KK, Kuznetsova IM: **Computational Study of Thioflavin T Torsional Relaxation in the Excited State**. *The Journal of Physical Chemistry A* 2007, **111**:4829-4835.

13. Vivian JT, Callis PR: **Mechanisms of tryptophan fluorescence shifts in proteins**. *Biophys J* 2001, **80**:2093-2109.

14. Stryer L: **The interaction of a naphthalene dye with apomyoglobin and apohemoglobin**. *Journal of Molecular Biology* 1965, **13**:482-495.

15. Ikonomovic MD, Klunk WE, Abrahamson EE, Mathis CA, Price JC, Tsopelas ND, Lopresti BJ, Ziolko S, Bi W, Paljug WR, et al.: **Post-mortem correlates of in vivo PiB-PET amyloid imaging in a typical case of Alzheimer's disease**. *Brain* 2008, **131**:1630-1645.

16. Klunk WE, Lopresti BJ, Ikonomovic MD, Lefterov IM, Koldamova RP, Abrahamson EE, Debnath ML, Holt DP, Huang GF, Shao L, et al.: **Binding of the positron emission tomography tracer Pittsburgh compound-B reflects the amount of amyloid-beta in Alzheimer's disease brain but not in transgenic mouse brain**. *J Neurosci* 2005, **25**:10598-10606.

17. Fosso MY, McCarty K, Head E, Garneau-Tsodikova S, LeVine H: **Differential Effects of Structural Modifications on the Competition of Chalcones for the PIB Amyloid Imaging Ligand-Binding Site in Alzheimer's Disease Brain and Synthetic Aβ Fibrils**. *ACS Chemical Neuroscience* 2016, **7**:171-176.

18. Lakowicz JR: *Principles of Fluorescence Spectroscopy* edn 3rd: Springer; 2006.

Chapter 4: Seeding of brain extracts into synthetic Aβ

Introduction

One of the major efforts in understanding the disease etiology is directed at solving amyloid structures on the premise that the toxicities of the aggregates are related to their structure. Based on the strain hypothesis (chapter 1, section 1.3), it is thought that Aβ fibrils in AD brains have common structural features while Aβ in non-AD brains have another distinct set of structures, leading to different downstream effects or toxicities. High-resolution techniques such as solid-state NMR and cryo-EM have been used to obtain structural models of the paracrystalline fibrils [1-11], but most of these were pure synthetic fibrils assembled *in vitro* because of the difficulty in obtaining fibrils of sufficient purity, homogeneity and mass directly from brain tissue.

Amyloid structures can be cyclically amplified for structural characterization through protein misfolding cyclic amplification (PMCA), which is analogous to DNA amplification by PCR [12]. The difference however, is that PMCA (also referred to as templated protein corruption or seeding) amplifies structural information instead of genetic information. This concept has recently been used for the early diagnosis of Creutzfeldt-Jakob disease (CJD) by amplifying patient CSF into recombinant PrP for detection [13,14]. Tycko and co-workers have also seeded synthetic Aβ from enriched AD brain extracts and showed that the molecular structures of the resulting fibrils are different from that of Aβ assembled *in vitro* [15,16]. This raises additional questions about the nature of the seeded fibrils. Do they also bind to PiB with high affinity as observed for Aβ from AD brains but not for Aβ from all other sources? Do they retain the bioactivities of the parent seeds?

To gain insight into these questions, we first established protocols for seeding various forms of Aβ before evaluating the differences in the seeded fibrils by TEM and binding to ligands.

Results

4.1 Propagation of agitated Aβ fibrils under quiescent conditions

To be confident that the fibrils obtained after seeding the brain extracts into synthetic Aβ result from the propagation of seeds and not from the self-nucleation of the synthetic Aβ monomers, a positive control for the seeding protocol had to be established. We used synthetic agitated (Ag) Aβ40 as a positive control since Ag fibrils have a different morphology from fibrils assembled under quiescent conditions (Q), thus the fidelity of the seeding protocol can be assessed by TEM.

To determine the proportion of seeds needed to seed the growth of Aβ40, we incubated the monomers in the presence of 1 to 50% w/w Ag seeds and monitored fibril assembly with ThT fluorescence (**Figure 4.1**). The results show that a 5% seed concentration is sufficient to accelerate fibril assembly to maximal ThT fluorescence in a day. Within this timeframe, the ThT fluorescence for the unseeded Aβ remains constant, indicating that it is still in the lag phase with negligible fibril formation. However, TEMs of the 5%-seeded fibrils showed a heterogeneous mixture of Ag and Q fibril morphologies, so we used a 10% seed concentration (where the Ag morphology was much more prevalent in the seeded fibrils) in the following experiments.

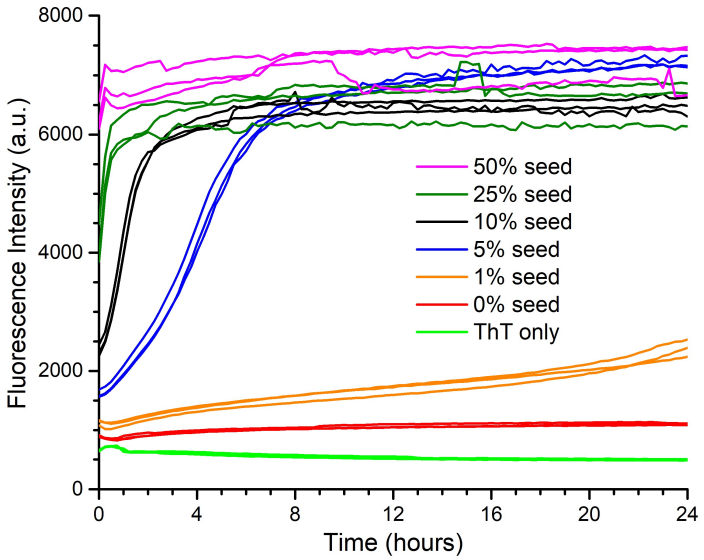

Figure 4.1. Kinetics of seeding agitated (Ag) fibrils under quiescent conditions. 100 μM Aβ40 was incubated with increasing amounts of 100 μM Ag Aβ40 seeds under quiescent conditions at 37°C in the presence of ThT. The seed amount is reported as a percentage of the total volume in each replicate.

Another aliquot of Ag fibrils (**Figure 4.2A**) was probe-sonicated to yield Ag seeds (**Figure 4.2B**), which are shorter but still untwisted and bundled, therefore retaining the morphology of the Ag fibers. Freshly prepared Aβ40 monomers were then added to the seeds to create the daughter or 1st generation consisting of 10% seeds. After incubation at 37 °C for 1 day in the absence of ThT, an aliquot of the daughter generation fibrils was used to seed another batch of Aβ40 monomers to give the granddaughter or 2nd generation, which was also incubated for 1 day at 37 °C. TEMs of these seeded assemblies show that they also have the untwisted, bundled Ag fibril morphology (**Figure 4.2C** and **D**), although some quiescent fibril morphology was observed in the granddaughter generation. This experiment showed that Ag fibrils can be propagated under quiescent conditions for up to two generations using this protocol, and we can expect it to be transferrable to the brain extracts.

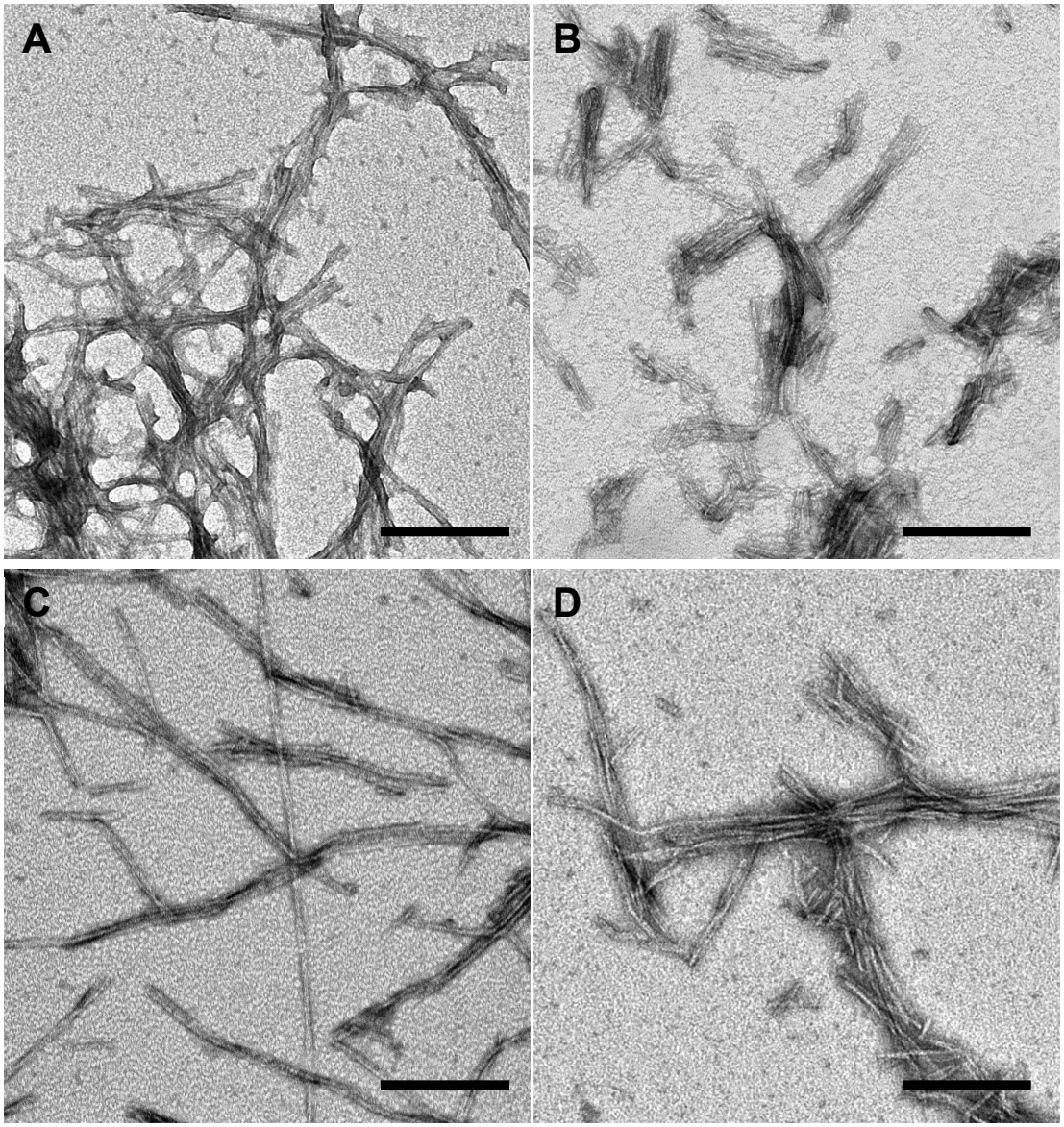

Figure 4.2. Seeding of agitated synthetic Aβ40 under quiescent conditions. (A) Parent Ag fibrils, (B) seeds derived from Ag fibrils, (C) daughter Ag fibrils after one round of seeding and (D) granddaughter Ag fibrils. Scale bars: 200 nm

4.2 Seeding of LSS (low-speed supernatant) brain extracts into synthetic Aβ

Brain extracts used for seeding (**Table 4.1** and **Table 4.2**) were prepared from frozen brain tissue obtained from the Emory ADRC through Dr. Lary Walker. Unlike other brain homogenate purification protocols that involve the use of detergents and proteinases

[16-18], the brain homogenates processed here were essentially supernatants of low speed centrifugation (LSS, low-speed supernatants) and underwent no chemical treatment (see methods section), thus allowing us to use seeds that are much closer to their biological conformations instead of selecting for nuclease- and proteinase-resistant strains. Additionally, since the LSS human brain extracts were sufficiently potent to induce *in vivo* seeding in APP-transgenic rats [19] and LSS APP-transgenic mice brain extracts could induce Aβ amyloidosis in other APP-transgenic mice [20], we assumed that they can retain their seeding efficacy *in vitro*.

Table 4.1. Patient profiles of brain extracts used for seeding

Brain extract	Emory ADRC case number	Pathology	Age (years)	Race/Sex	Brain region	ApoE genotype	PMI (hr)
AD 1	OS02-159	AD	61	Male	Occipital	3/4	5.5
AD 2	OS03-300	AD	75	White female	Occipital	4/4	12
AD 3	OS02-163	AD	70	White male	Occipital	3/4	11
ND 1	OS02-35	Normal brain	75	White female	Occipital	3/3	6
ND 2	E11-33	Microinfarction	43	Black female	Occipital	3/3	15

ApoE: Apolipoprotein E.
PMI: post mortem interval.

Table 4.2. Profiles of monkey brain extracts used for seeding

Brain extract	Emory ADRC case number	Species	Age (years)	Sex	Brain region	PMI (hr)
M1	Yale	*Macaca mulatta*	35	Female	-	0
M2	90T	*Saimiri sciureus*	-	-	-	-

To characterize the contents of the brain extracts, BCA assays of the diluted brain extracts were performed to measure the protein concentrations. AD2, M1 and M2 were found to have much higher protein contents than AD1, AD3 and ND (**Figure 4.3A**), and therefore were diluted to 2.33 mg/ml (the average for AD1, AD3 and ND) in the following seeding experiments (diluted seeds are denoted with a *). By using seeds with approximately equal protein contents, we aim to compare seeding efficiencies between different strains. SDS-PAGE of the brain extracts showed no striking difference between the AD and non-AD brains (**Figure 4.3B**).

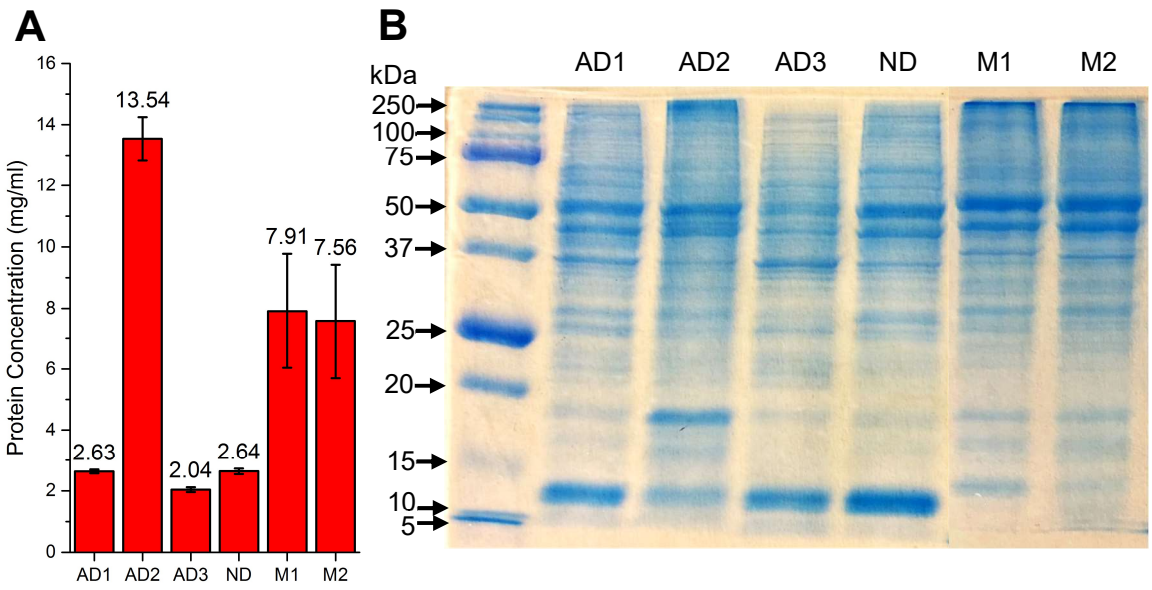

Figure 4.3. Brain extracts have different protein compositions. (A) Protein concentration in 10% w/v brain extract supernatant measured by the BCA assay. (B) Brain extracts analyzed by SDS PAGE and visualized by staining with Coomassie Blue. 10 μg protein per lane.

We then made seeds from the LSS brain extracts through sonication and seeded them into synthetic Aβ40 for two generations. While the parent fibrils appeared polymorphic between and within the samples, the daughter and granddaughter Aβ40 fibrils had less

heterogeneity. Unlike the pure synthetic Aβ40 controls, the brain-seeded fibrils generally had oligomers bound to the sides of the fibrils, giving them a rough appearance (**Figure 4.4**) that was also reported by Lu et al. [16]. We also observed a similar trend for the two non-human primate brain extracts (**Figure 4.5**).

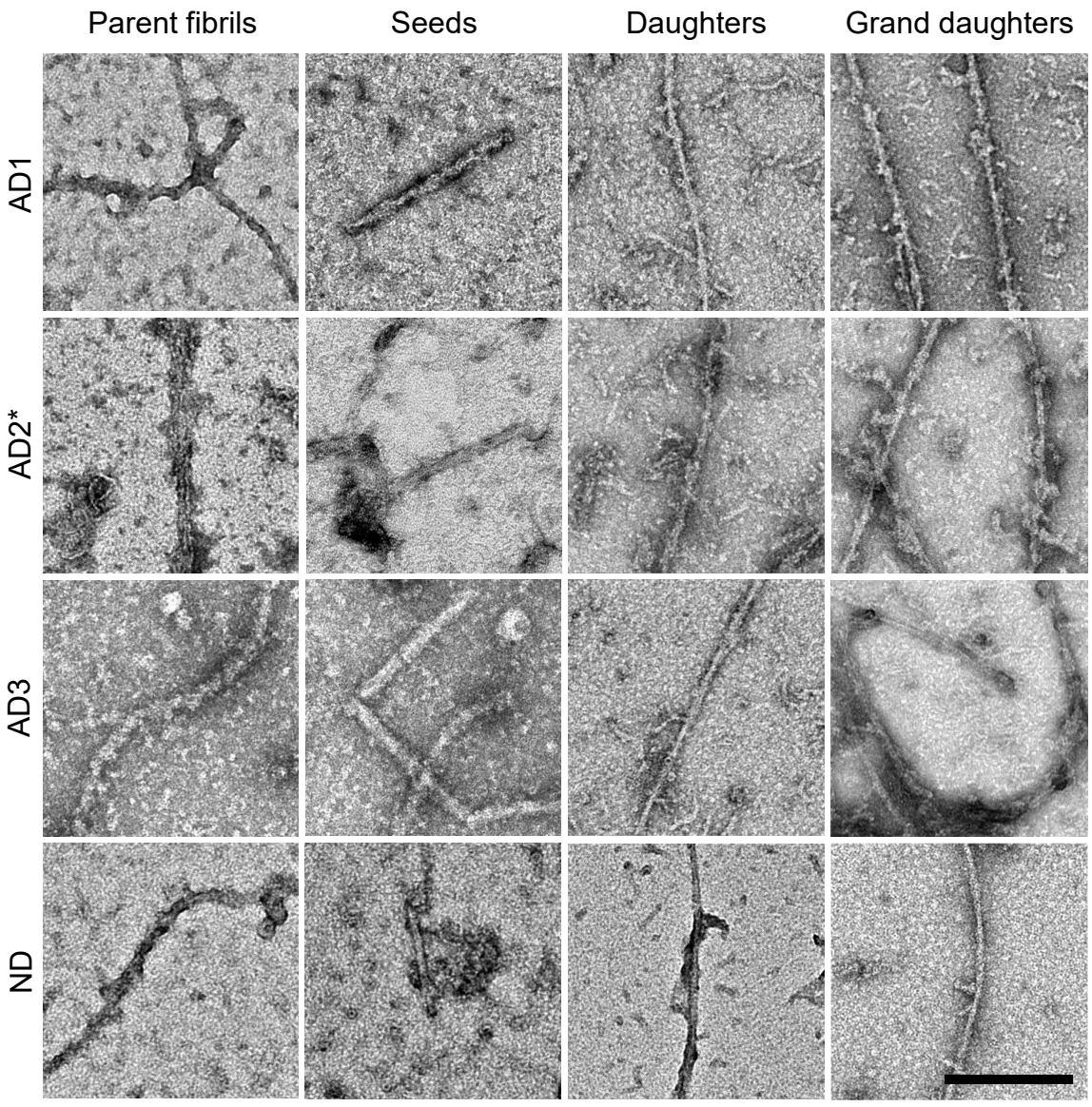

Figure 4.4. Morphologies of fibrils found in human brains and after seeding into synthetic Aβ40. All images to scale. Scale bar: 200 nm

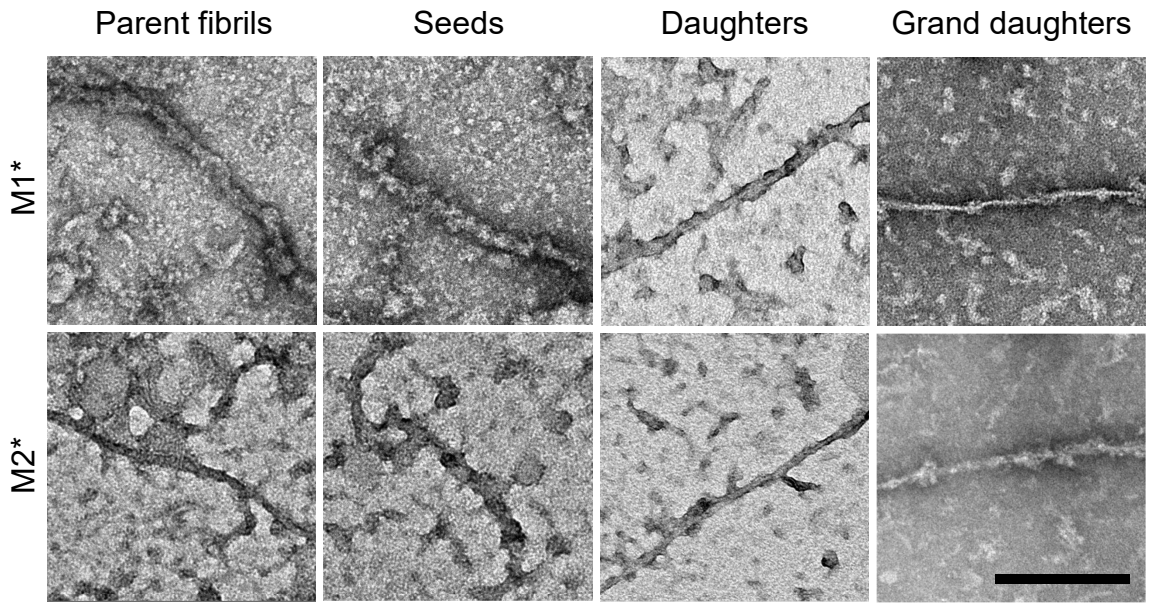

Figure 4.5. Morphologies of fibrils found in monkey brains and after seeding into synthetic Aβ40. M1: rhesus macaque, M2: squirrel monkey. All images to scale. Scale bar: 200 nm

4.3 Stability of seeded Aβ fibrils to freeze-thawing

To evaluate the binding of ^{3}H-PiB and ^{3}H-X34 binding to the brain extract-seeded Aβ40 fibrils, we froze the samples and shipped them to Dr. Harry LeVine at the University of Kentucky. However, to assess the stability of the fibrils to freeze-thawing, we first characterized the AD2*-seeded granddaughter Aβ40 fibrils (representative of all brain extract-seeded fibrils) and the Q Aβ40 granddaughter fibrils (assumed to be the most stable Aβ40 fibrils *in vitro*). The fibrils were then stored at -80 °C for one week, before they were thawed to room temperature and the same series of experiments were performed.

TEM imaging of the Q Aβ40 granddaughter fibrils showed that freeze-thawing caused the fibers to fragment into assemblies that look similar to seeds that are made by sonication of fibers (**Figure 4.6B**). A similar effect was observed for the AD2*

granddaughter fibers (**Figure 4.6D**), although the extents of fragmentation are difficult to quantify with TEM. The most plausible reason for the fragmentation is the formation of ice crystals when the Aβ samples were frozen by simply placing them in the -80 ^{o}C freezer. CD spectra of the fibrils showed marginal increases in intensities and red-shifting of the spectra after freeze-thawing (**Figure 4.6F**), suggesting that the degree of assembly remained the same.

It is noteworthy that the CD spectra for the AD2* granddaughter fibers in **Figure 4.6E** and **F** appear to be a combination of beta sheet and random coil structures as they show minima in the 217 and 196 nm regions respectively. This suggests that the seeding efficiency of the brain extracts into synthetic Aβ is lower than that of self-seeded synthetic Aβ, where a higher population of the peptide exists in the monomeric and oligomeric state rather than in the fibrillary state. ThT binding to the fibrils supports this hypothesis, where there was no observable increase in ThT fluorescence in the presence of the AD2* granddaughter fibrils before freezing (**Figure 4.7A**). Freeze-thawing had the effect of increasing ThT fluorescence for both samples (**Figure 4.7B**), where a 0 to 3-fold and 11 to 13-fold increase was recorded for the AD2* and Q Aβ40 granddaughter fibrils respectively. Since the primary effect of freeze thawing was fibril fragmentation which produces more fibrillary ends, the increased ThT fluorescence suggests that ThT is also binding to the ends of the fibers.

Congo red (CR) binding to the fibrils showed little difference before and after freezing (**Figure 4.7C** and **D**) with Q Aβ40 granddaughter showing a larger increase in absorbance and red shift than AD2* granddaughter, in agreement with ThT binding. The difference spectra (**Figure 4.7E** and **F**, obtained by taking [CR+Aβ] – [CR alone]) shows the

change in CR absorbance upon binding to Aβ and interestingly, the increase at 534 nm is greater than at 513 nm for Q Aβ40 granddaughter while for AD2* granddaughter, CR shows an equal increase at both wavelengths. This suggests that there are two binding modes which are present in different ratios in these samples. The minor differences in absorbance magnitudes are most likely from experimental error and instrument variation, since there is variation in the CR-alone spectrum taken before and after freezing.

More importantly, PiB binding fluorescence spectra before and after freezing showed no distinguishable difference for AD2* granddaughter and only a slight increase in fluorescence for Q granddaughter after freeze-thawing (**Figure 4.7G** and **H**). Comparing these findings to ThT fluorescence, it appears that there are PiB binding sites at the ends of the fibrils which are abundant in the Q granddaughter but insufficient in the AD2* granddaughter to elicit a change in fluorescence.

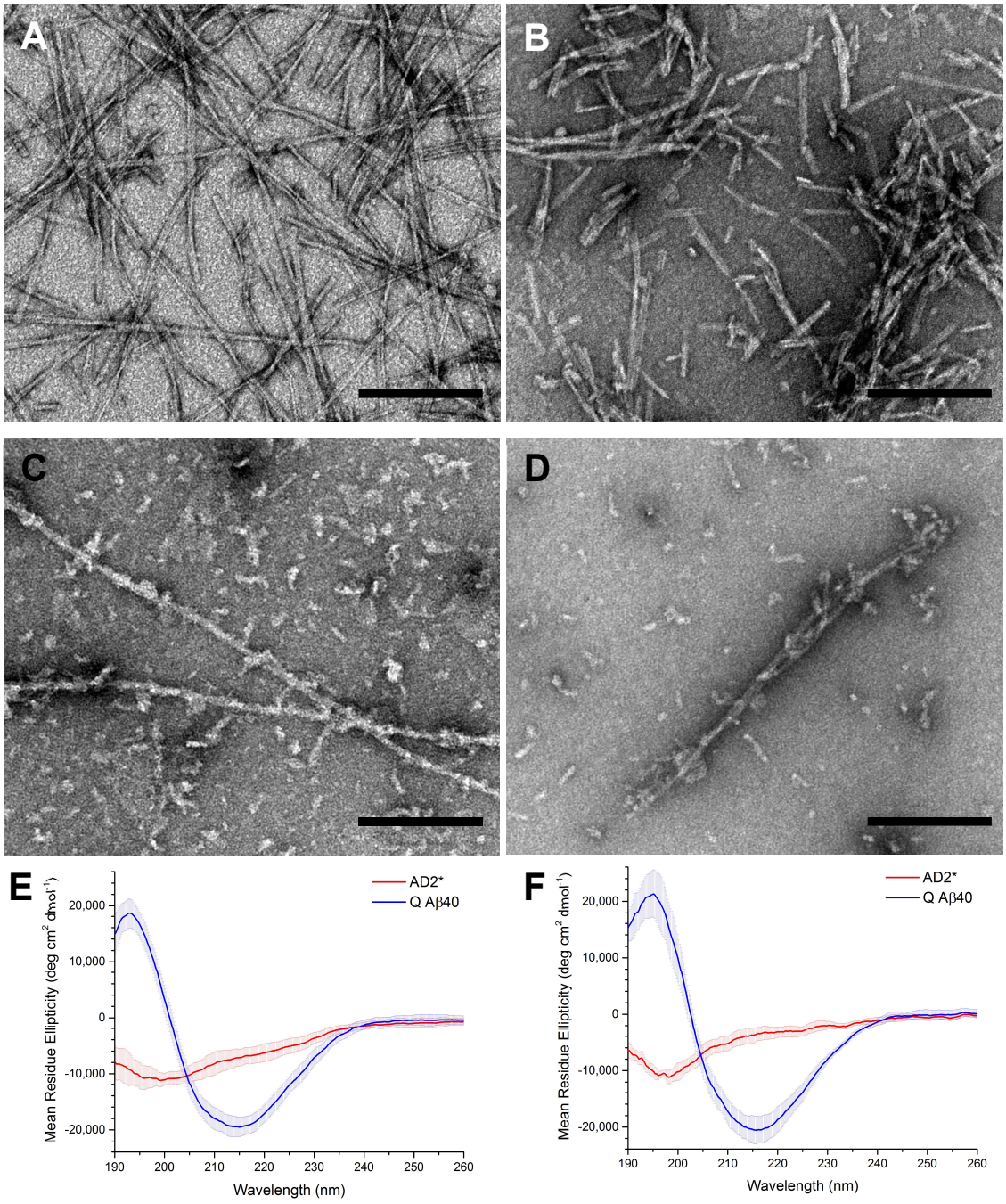

Figure 4.6. Freeze-thawing causes Aβ fibrils to fragment. Q Aβ40 granddaughter forms long fibrils before freezing (A) but freezing for one week at -80 ºC followed by thawing results in fragmented fibrils (B). A similar effect was observed for AD2* granddaughter fibrils before (C) and after freeze-thawing (D). CD spectra of the fibrils showed minimal differences before (E) and after freeze-thawing (F). Scale bars: 200 nm

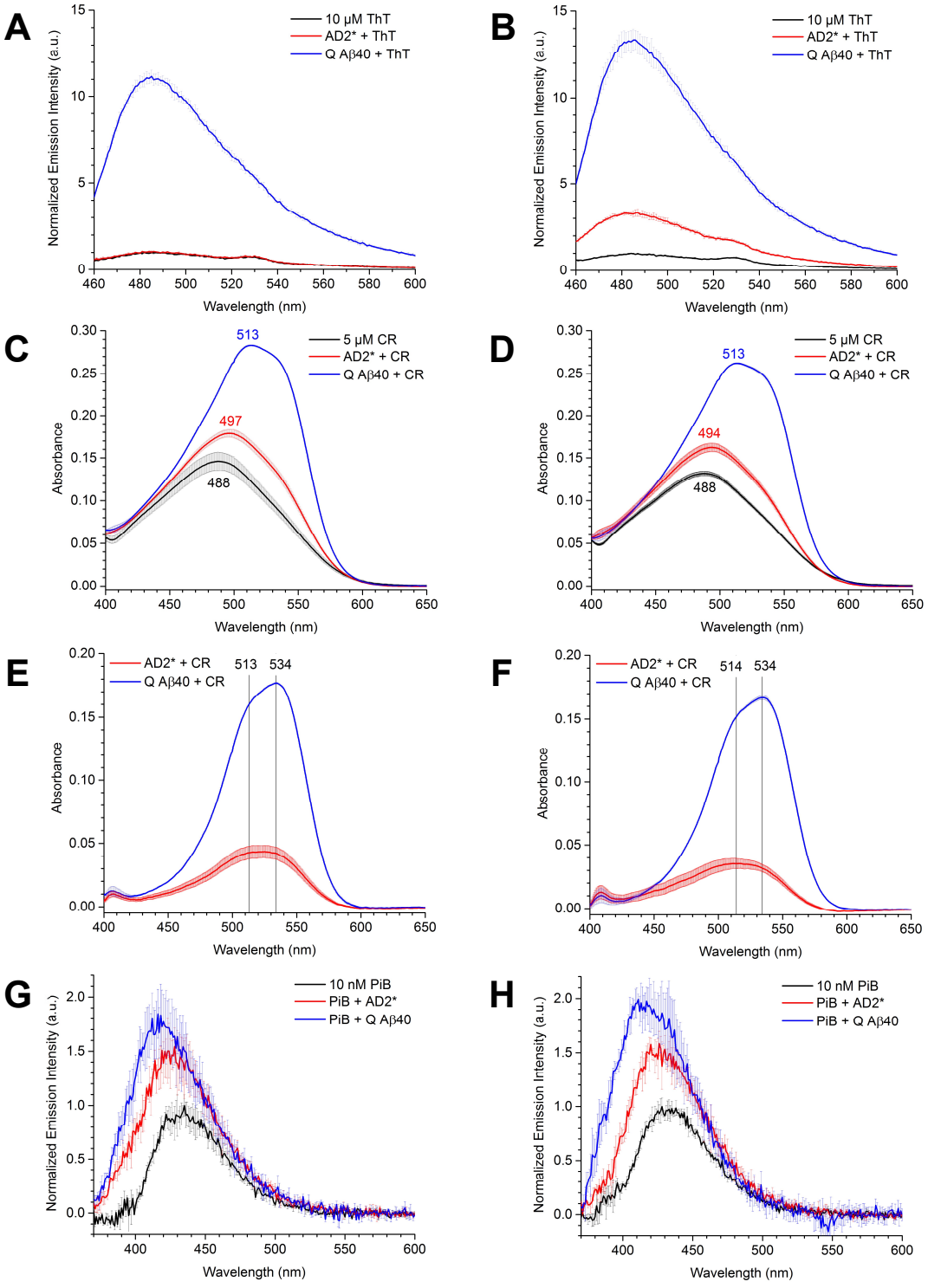

Figure 4.7. Binding profiles of ThT, CR and PiB to Q Aβ40 and AD2* granddaughter before (left) and after (right) freeze-thawing. Q Aβ40 and AD2* granddaughter fibrils ThT binding fluorescence spectra before (A) and after (B) freeze thawing. CR absorbance spectra (C and D) and CR difference spectra (E and F) before (C and E) and after (D and F) freeze thawing. PiB binding fluorescence spectra before (G) and after (H) freeze-thawing.

If fibril fragmentation is to be avoided during freezing, then the formation of crystalline ice should be minimized during the process. To rapidly freeze the peptide solution and favor vitreous ice formation over crystalline ice, we maximized the surface area to volume ratio of the peptide solution that contacts the liquid N_2 by dropwise addition of the peptide into liquid N_2. Upon thawing, the fibrils were observed to be both bundled and fragmented (**Figure 4.8B**), suggesting that crystalline ice still formed during freezing. A more drastic way to prevent crystalline ice formation would be to modify the protocols used in cryo EM where thin (<1 μm) aqueous layers are frozen in liquid ethane, but that would be too extreme for our purposes. Since PiB fluorescence was minimally affected by the effects of freeze-thawing, the fragmentation issue was not pursued further, and the samples were simply flash frozen by dropping the microfuge tubes in liquid N_2.

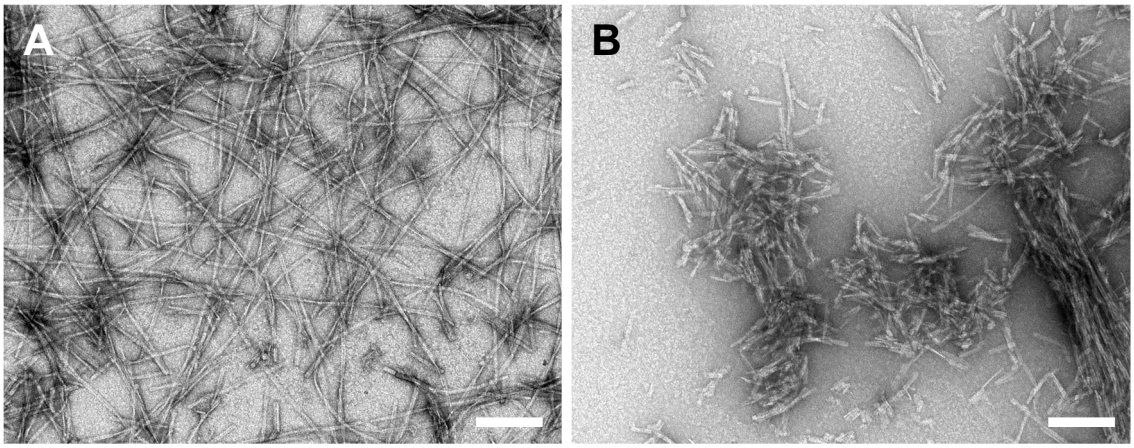

Figure 4.8. Dropwise flash freezing of Q Aβ40 fibrils produced fragmented and bundled fibers. (A) The fibrils (100 μM) were pipetted dropwise (~20 μL) into a 1.5 mL centrifuge tube containing liquid N2. (B) The frozen pellets were stored at -80 °C for one day before they were thawed and adsorbed on a TEM grid. Scale bars: 200 nm.

4.4 [^{3}H]-PiB, [^{3}H]-X-34 and pFTAA binding to brain-seeded fibrils

Having established that the PiB binding to the seeded fibrils remains relatively unchanged after freeze-thawing, the samples were flash-frozen and shipped to Dr. Harry LeVine at the University of Kentucky for ^{3}H-PiB and ^{3}H-X-34 [21] binding analyses. The results showed that almost all samples had lower specific binding to ^{3}H-PiB than the fibrillar Aβ40 control (F40), except for the Ag-seeded granddaughter (sample #7, **Figure 4.9A**). However, both the Ag and Q-seeded granddaughter (sample #7 and 8) had higher specific binding to ^{3}H-X-34 compared to the F40 control (**Figure 4.9B**). ThT fluorescence indicated that only the Ag granddaughter had fibrillized to a detectable extent, although not as much as the F40 control, while the other samples had higher populations of monomers and oligomers over fibers. Taken together, the results showed that PiB binds to fibers with the Ag morphology more strongly than it does to fibers with the Q morphology, and that Q-seeded aggregates (but not fibers) have an unusually high binding to X-34 but not to PiB or ThT. Additionally, given that the LSS brain extracts can seed Aβ aggregation in transgenic rats but not *in vitro*, our findings suggest that exogenous Aβ seeds can be retained and concentrated in the brain, allowing seeding to take place.

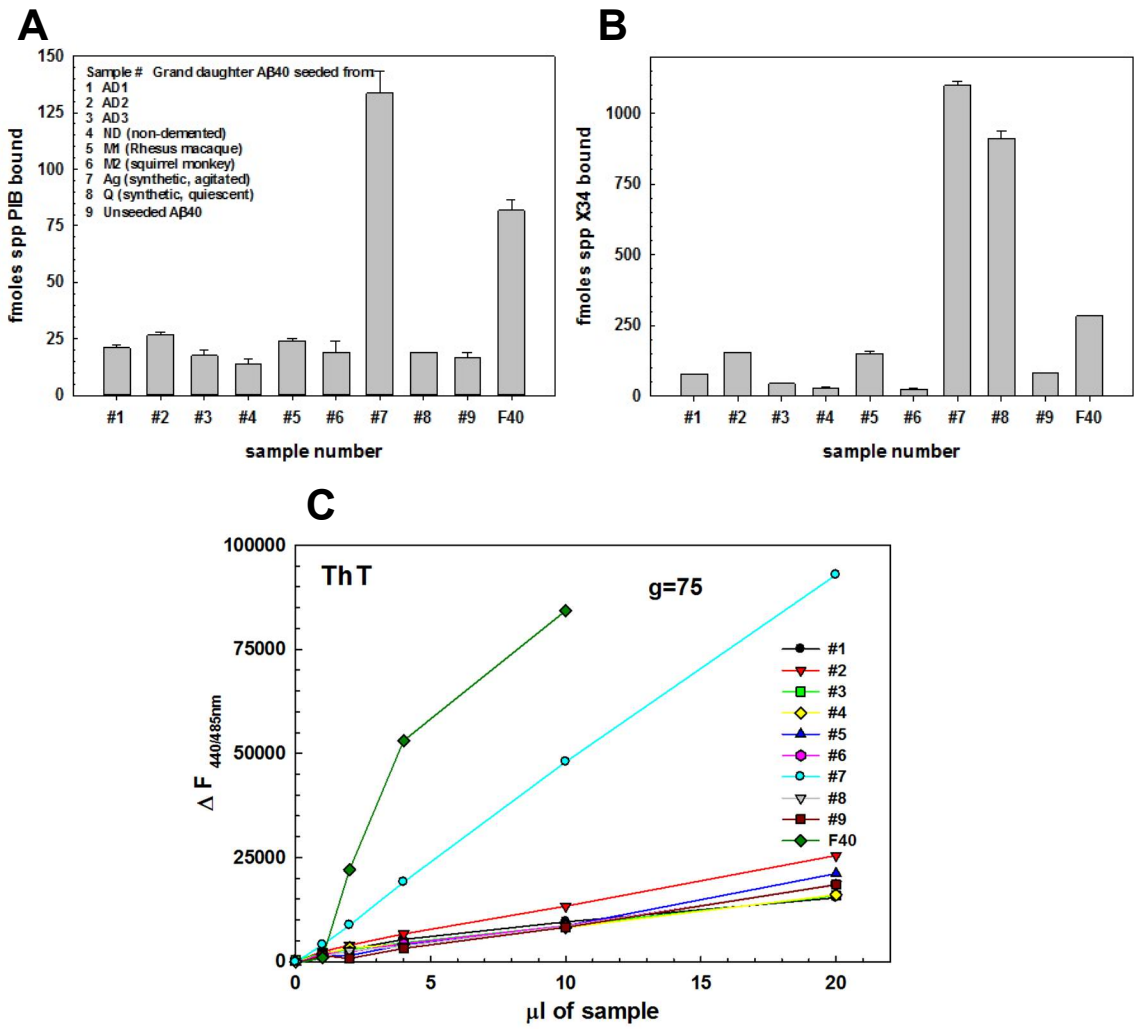

Figure 4.9. Brain extract-seeded Aβ40 had low ^{3}H PiB, ^{3}H-X34 and ThT binding. Granddaughter Aβ40 seeded from low speed supernatant brain extracts, synthetic quiescent Aβ40 generally had low specific binding to (A) ^{3}H-PiB, (B) ^{3}H-X34 and (C) ThT, except for agitated Aβ40.

Since the data above indicated that the oligomeric Aβ population was dominant in the brain-seeded samples, we sought to determine if there are differences in the aggregates using LCO as a reporter. pFTAA (pentamer formyl thiophene acetic acid) was shown to bind to pre-fibrillar Aβ40 aggregates and yield a different emission spectrum than when bound to Aβ fibrils [22]. **Figure 4.10** shows that the spectral profiles of brain-seeded Aβ were similar to that of pFTAA alone where $I_{510nm} < I_{540nm}$, suggesting that most of the

pFTAA were unbound. However, the Q-seeded oligomers had a higher fluorescence intensity with $I_{510nm} = I_{540nm}$ indicating a different oligomeric conformation, and the relative intensities for the two peaks were reversed for the Ag-seeded fibrils, with $I_{506nm} < I_{540nm}$.

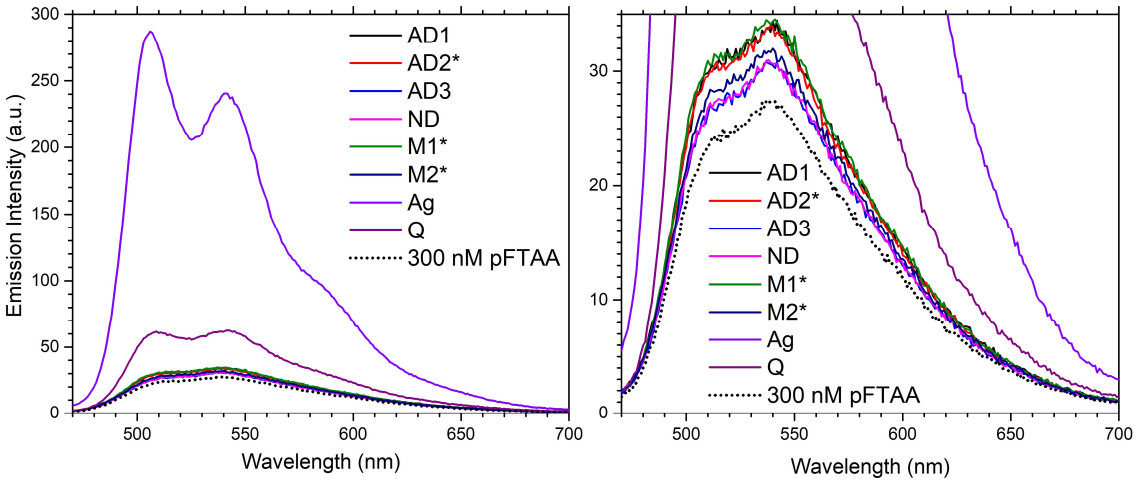

Figure 4.10. Brain extract-seeded Aβ40 had similar pFTAA binding. Fluorescence emission spectra of 300 nM pFTAA binding to 10 μM granddaughter Aβ40 seeded from low speed supernatant brain extracts. The low-intensity spectra are magnified on the right. Ex = 456 nm.

4.5 Enrichment of brain extracts for more specific amyloid seeding

Based on the previous section, we rationalized that seeding from the near-native low speed supernatant brain extracts was hindered by non-specific binding to other non-amyloid components in the brain extracts. This may explain why papers reporting on the seeding of brain extracts into synthetic Aβ all involve treatment of the brain homogenates with detergents, proteases, nucleases, EDTA, etc. [15,16,23]. We therefore enriched the amyloid content in the LSS brain extracts following a protocol by Wenborn et. al [24] used for purifying prion assemblies from rodent and human brains, since it did not require access to an ultracentrifuge. Additionally, the Aβ seeds should retain their seeding potency since the

reagents used in this protocol do not appear to be extremely harsh, and Aβ seeds have been reported to be resistant to formaldehyde, boiling or drying [25-27].

In an initial evaluation of this protocol, we enriched the AD1 and AD2 extracts where the fourth pellets (P4) would be used as seeds. TEM images of the P4 samples reveal a much cleaner background as compared to the LSS extracts, with fibrils appearing to be 'wet', clumped and have less distinct edges than observed for synthetic Aβ (**Figure 4.11A** and **C**). Other structures observed on the grids include collagen fibrils (**Figure 4.11D**), clusters of globular aggregates (**Figure 4.11B**), lipid/membrane-like sheets (**Figure 4.11A** and **C**) and banded, typically ovoid structures with 3nm bandwidths (**Figure 4.11A**, **C**, **D**).

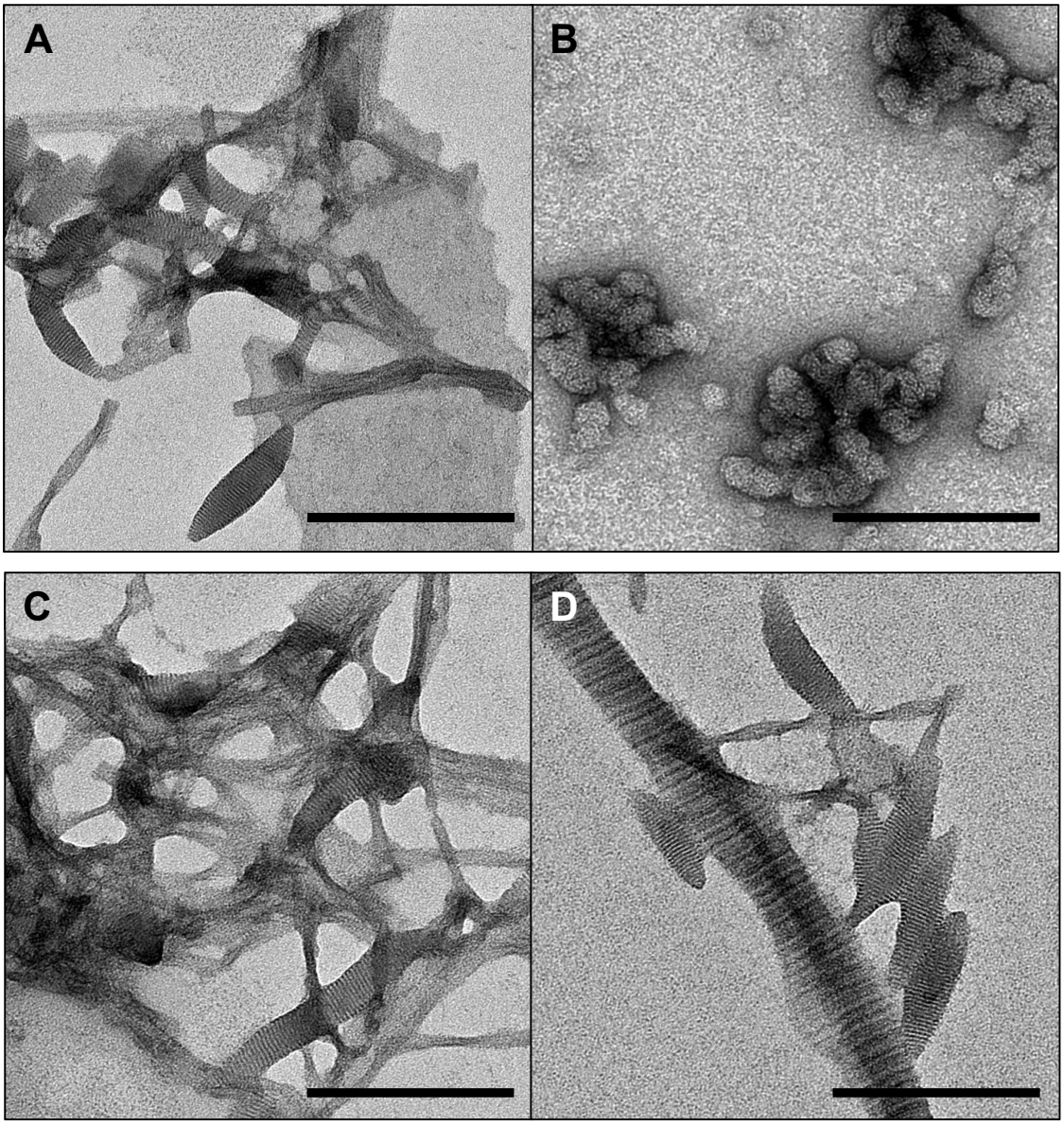

Figure 4.11. Structures observed in pellet 4 of enriched AD1 and AD2 LSS brain extracts. Representative images of structures seen in P4 of enriched AD1 (A and B) and AD2 (C and D) brain extracts. Scale bars: 200 nm

We then looked at the purity of the P4 aliquots on a denaturing gel to confirm that the enrichment protocol had removed most of the proteins in the starting samples, since TEMs do not reveal the presence of soluble proteins. **Figure 4.12A** showed no visible bands in the lanes where P4 were loaded, indicating that that virtually all gel-penetrable proteins

were removed in the P4 fractions. However, no bands <5 kDa corresponding to Aβ40/42 were detected in the P4 lanes, suggesting that Aβ either did not enter the gel or were discarded during the enrichment process. SDS-PAGE of the discarded fractions (**Figure 4.12B**) showed bands ~5 kDa which may contain Aβ, and they were mostly present in the pellet 1, surface layer and supernatant 2 fractions. The other SDS-soluble proteins in the brain extracts were not detectable in the gel likely because the supernatants are more dilute than the pellets and/or they were digested into small fragments.

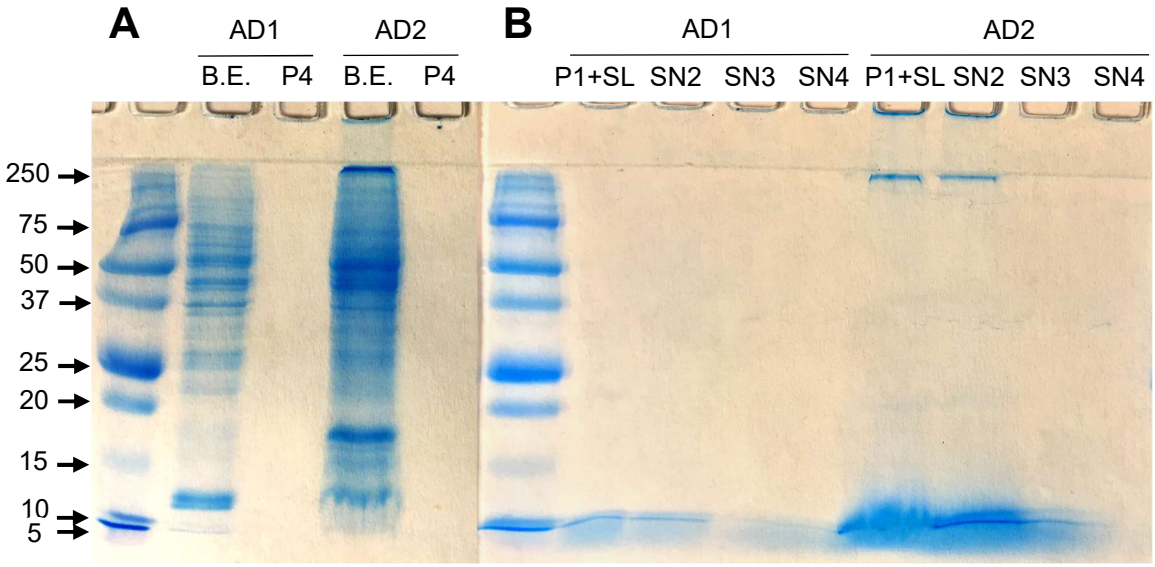

Figure 4.12. Brain extract enrichment protocol removes SDS-soluble proteins. (A) SDS-PAGE of the LSS samples before (B.E.) and after (P4) amyloid enrichment. (B) SDS-PAGE of the proteins that were removed during the process. 12% SDS-PAGE. B.E.: brain extract, P: pellet, SN: supernatant, SL: surface layer.

Finally, we looked at the resistance of Aβ fibrils to denaturation by SDS and β-mercaptoethanol by boiling synthetic Aβ40 fibrils in laemmli sample buffer, just as how the brain extracts and 4th pellets would have been treated before gel electrophoresis. Before boiling, plenty of fibrils were observed when an aliquot was spotted on a TEM grid (**Figure 4.13A**) and fibrils were still present when the sample was boiled for 10 min (**Figure 4.13B**)

as in our protocol for SDS PAGE. Extension of the boiling time to 20 and 30 min (**Figure 4.13C** and **D**) also failed to eliminate the presence of Aβ fibrils on the EM grids. These results explain why Aβ fibrils were seen in the TEMs of AD1 and AD2 P4s (**Figure 4.11**) but were undetectable by SDS PAGE (**Figure 4.12**).

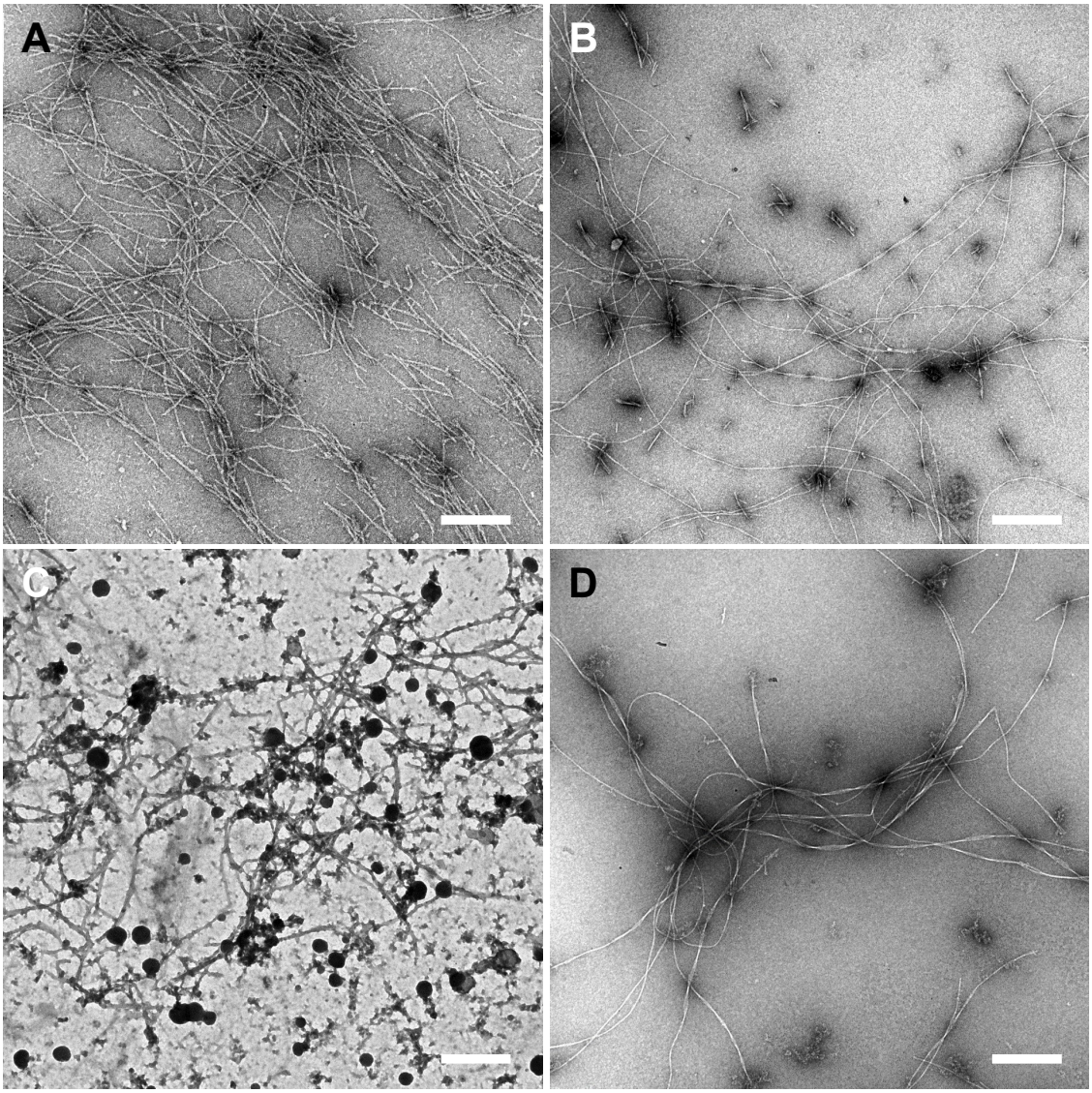

Figure 4.13. Synthetic Aβ40 resists boiling in a denaturing buffer. 4x Laemmli sample buffer was added to 100 μM Aβ40 to 1X final concentration and boiled for (A) 0 min, (B) 10 min, (C) 20 min and (D) 30min before spotting on an EM grid and stained with UA. Scale bars: 500 nm

4.6 Granddaughter Aβ40 fibrils seeded from enriched LSS brain extracts

We then seeded the enriched P4 fractions into synthetic Aβ40 using the same protocol and assessed the seeding efficiency by native PAGE. **Figure 4.14** shows that seeding with the enriched P4 fractions (lanes 3 and 4) resulted in approximately the same amount of unassembled peptide as seeding with the unenriched LSS fractions (lanes 1 and 2) and unseeded control (lane 7), demonstrating that enrichment of the LSS brain extracts was insufficient to increase the potency of the seeds.

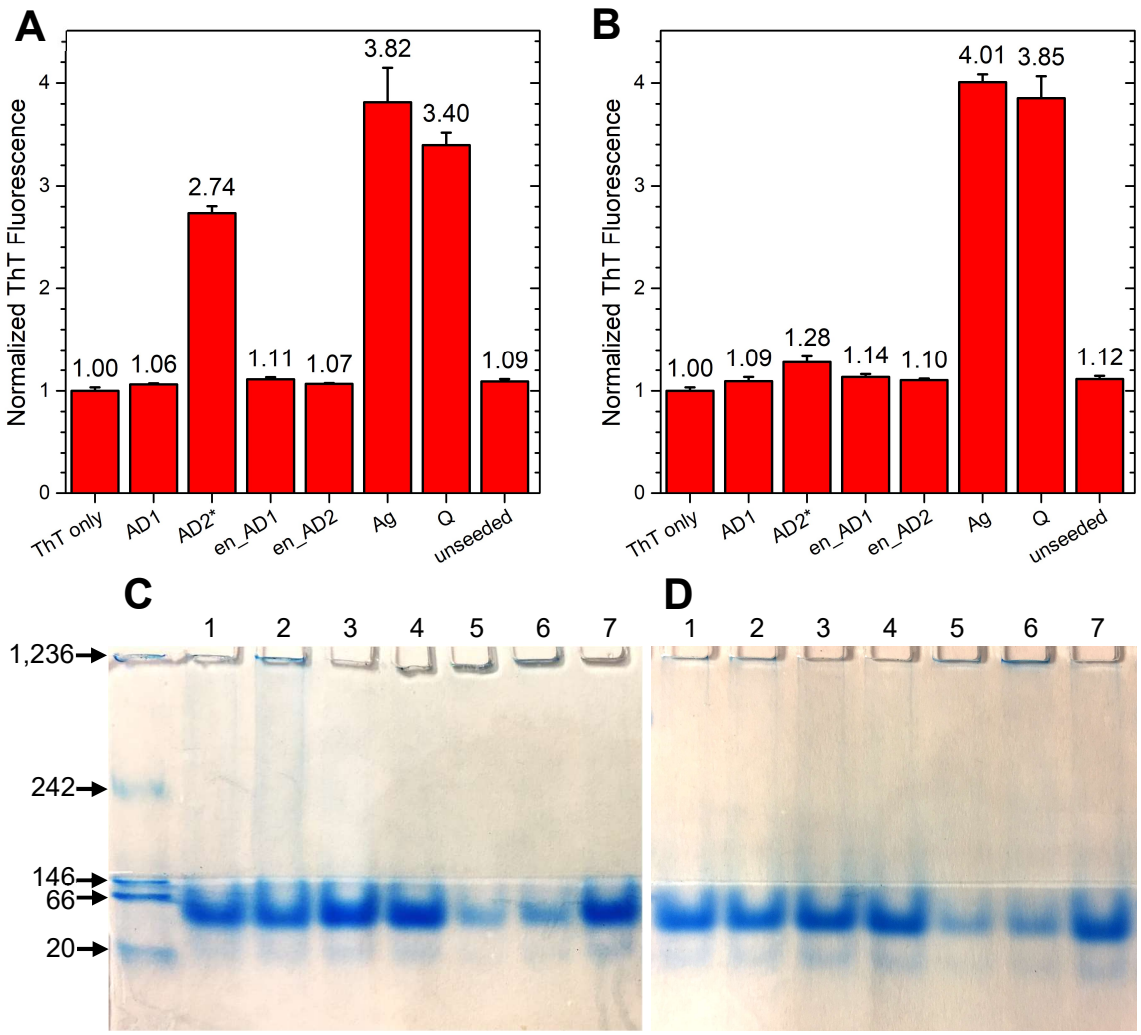

Figure 4.14. LSS brain extract enrichment did not improve seeding efficiency. ThT binding to (A) daughter and (B) granddaughter fibrils. (C) Daughter and (D) granddaughter

Aβ40 fibrils seeded from (lane 1) AD1, (2) AD2*, (3) enriched AD1, (4) enriched AD2, (5) Ag, (6) Q, (7) unseeded. 5-12% Native PAGE.

4.7 Seeding of enriched LSS extracts into Aβ42

Rationalizing that Aβ42 could be more abundant than Aβ40 in the LSS extracts as in the case for senile plaques, and that Aβ42 fibrils could be ineffective seeds for Aβ40 monomers due to their different cross-sectional folds in the fibril, we then attempted to seed the enriched LSS extracts into Aβ42. As Aβ42 aggregates faster than Aβ40, we decreased the Aβ42 peptide concentration two-fold to 50 μM and increased the seed concentration two-fold to 20% v/v. **Figure 4.15** shows that fibrils were present in all seeded and unseeded Aβ42 samples, and while the LSS AD2- and Q-Aβ42-seeded fibrils appear more positively stained as opposed to the enriched LSS AD2-seeded and unseeded fibrils appearing more negatively stained, few differences in fibril morphologies were observed. Native PAGE of the samples, however, showed no unassembled Aβ42 peptide (**Figure 4.16A**, lane 4) and therefore, we cannot be confident that the fibrils in the seeded samples have propagated from the seeds instead of spontaneously aggregating.

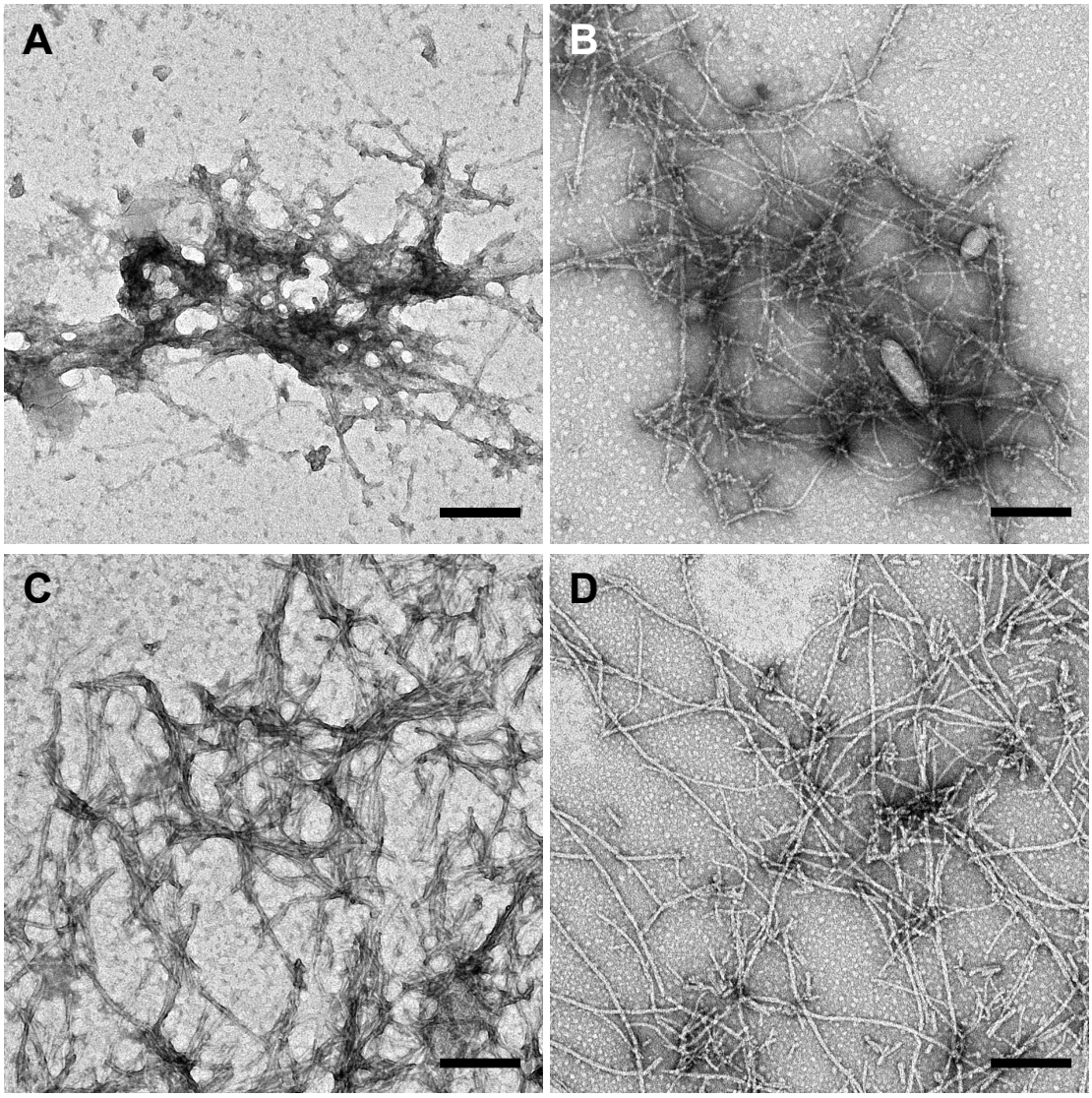

Figure 4.15. Morphologies of daughter generation Aβ42 fibrils. 50 μM Aβ42 was seeded with 20% v/v (A) AD2 LSS, (B) enriched AD2 LSS, (C) Q Aβ42 or (D) without seeds, and incubated for 1 day at 37 °C. Scale bars: 200 nm

Since Aβ42 assembly at 50 μM plateaued after 24 hours, we surveyed the assembly over the first 8 hours by analyzing samples to determine a suitable seeding incubation time where most of the Aβ42 is still unassembled. Native PAGE and ThT fluorescence showed that fibrillization had not plateaued yet and there is still unassembled peptide after 8 hours (**Figure 4.16B and C**). Since the midpoint of the ThT fluorescence between 0 and 8 hours

occurred approximately 2 hours into assembly, we chose a 2-hour seeding interval in the following experiments to be certain that the unseeded Aβ42 assembly will not be near completion.

When the enriched AD2 LSS was seeded into Aβ42, the resulting daughter fibrils showed higher ThT fluorescence over the unseeded Aβ42 (1.42 vs. 1.31, **Figure 4.16D**), but lower ThT fluorescence than the unseeded Aβ42 when propagated to the next generation. The self-seeded quiescent Aβ42 also showed lower ThT fluorescence than the unseeded controls in both generations, indicating that no seeding had taken place. To suppress the self-assembly of unseeded Aβ42, we lowered the incubation temperature from 37 °C to r.t., which decreased ThT binding to the unseeded controls, but inadvertently slowed down the growth of the seeded samples too (**Figure 4.16E**). We then increased the amyloid content in the AD2 seed fractions by directly enriching the 10% w/v brain homogenate instead of enriching the LSS fraction (i.e. including the low-speed pellet in the enrichment protocol) and seeded into synthetic Aβ42 at 37 °C with 2-hour seeding intervals. ThT fluorescence showed marginal improvements in seeding efficiency for the brain homogenate-enriched AD2 over the LSS AD2 in both the daughter and granddaughter generations, but virtually no difference compared to unseeded Aβ42 (**Figure 4.16F**).

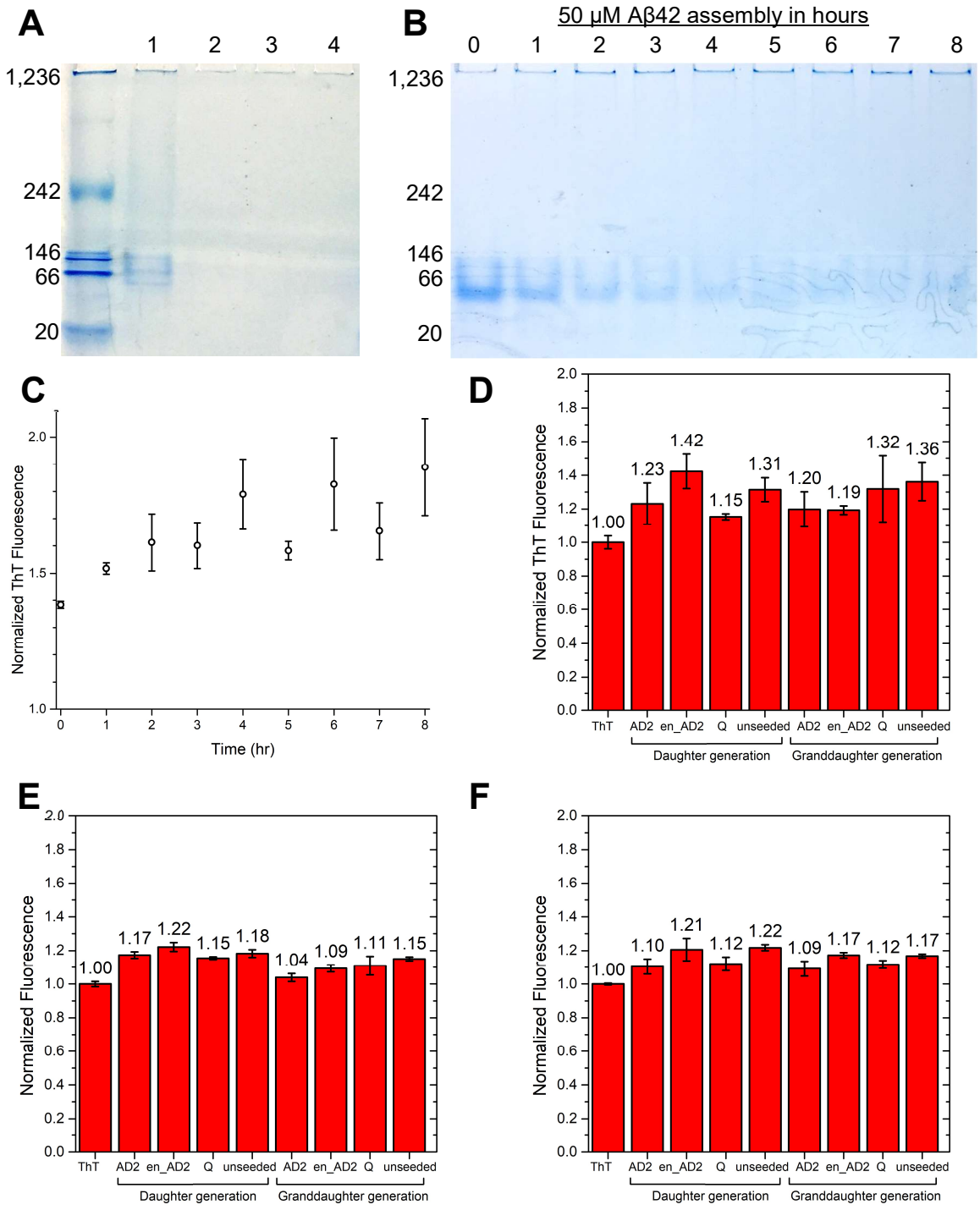

Figure 4.16. Assembly and seeding of 50 μM Aβ42. (A) Daughter generation 50 μM Aβ42 fibrils seeded from (lane 1) LSS AD2, (2) enriched LSS AD2 and (3) Q Aβ42, at 37°C for 24 hr, 20% v/v seed. Unseeded Aβ42 is in lane 4. (B, C) Native PAGE and ThT fluorescence of unseeded 50 μM Aβ42 assembly at 37 °C. (D, E) Seeding of AD2 LSS, LSS-enriched and Q Aβ42 fractions into 50 μM Aβ42 at (D) 37 °C and (E) r.t. for 2 hrs. (F) Seeding of AD2

LSS, brain homogenate-enriched AD2 and Q Aβ42 fractions into 50 μM Aβ42 at 37 °C for 2 hrs.

4.8 Enrichment of brain homogenates and seeding into Aβ40

Having already enriched AD2 brain homogenate from the previous section, we reattempted seeding into Aβ40. This time, we observed higher ThT binding to the enriched AD2-seeded Aβ40 over the unseeded Aβ40 controls in both daughter and granddaughter generations, indicating successful seeding of the Aβ40 monomers into fibrils. Native PAGE of the samples showed less unassembled peptide in the gel as compared to the unseeded control, supporting the ThT fluorescence data (**Figure 4.17**). By including the brain homogenate that was pelleted during the low speed centrifugation into the amyloid enrichment protocol, the resulting seed fraction was sufficiently potent to seed Aβ40, indicating that a critical concentration of seeds must be attained for seeding to occur.

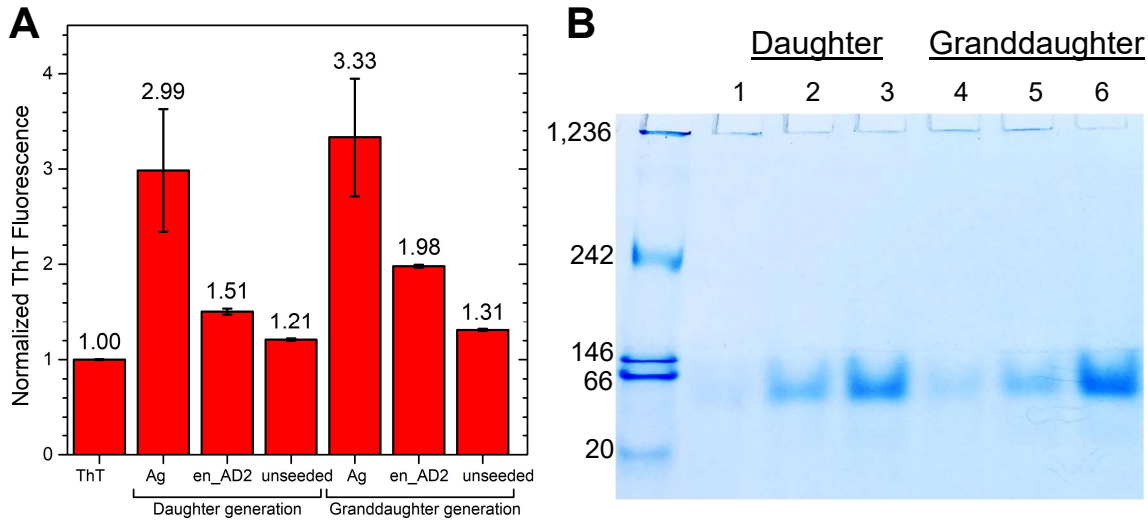

Figure 4.17. Brain homogenate enrichment improved seeding efficiency. (A) ThT binding to daughter and granddaughter Aβ40 fibrils seeded from Ag and enriched AD2 seeds. (B) Native PAGE of daughter and granddaughter Aβ40 fibrils seeded from (lanes 1 and 4) Ag seeds, (2 and 5) enriched AD2, and (3 and 6) unseeded controls. 20% v/v seeding, 1 day seeding intervals at 37°C.

To further increase the seeding efficiency, we increased the mass of brain tissue processed in each seed fraction from 20 mg to 90±3 mg and froze the P4 pellets without resuspending in 20 µl D-PBS to avoid diluting the seeds. We then seeded them into Aβ40 for two generations, where ThT fluorescence indicated reasonably good seeding of occipital (O) and frontal (F) AD2 brain regions in the daughter generation (**Figure 4.18**). However, when the daughter fibrils were propagated to the granddaughter generation, AD2 (O) and (F) had only marginally higher ThT binding than the unseeded control, even though the Ag and Q controls had higher ThT binding compared to the daughter fibrils. This suggests that the brain-seeded Aβ40 fibrils require different or a more specific set of seeding conditions than the synthetic controls.

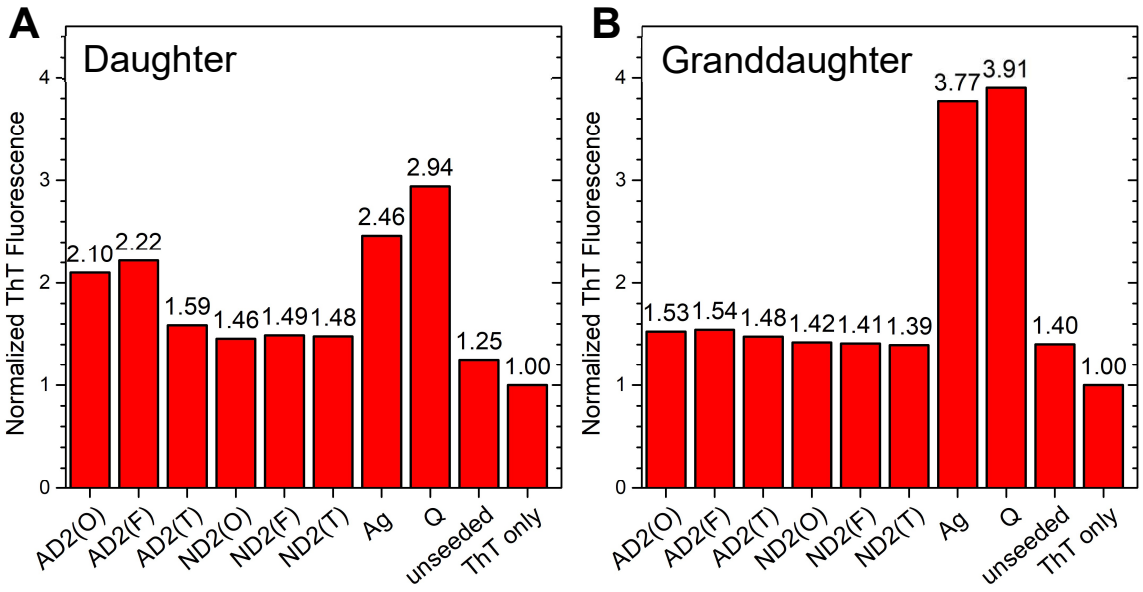

Figure 4.18. Enriched brain extracts propagated well into Aβ40 at a small scale but not at a larger scale. P4 fractions enriched from the occipital (O), frontal (F) and temporal (T) lobes of AD2 and ND2 patients were seeded into 100 µl Aβ40 to give the daughter generation (A). The daughter fibrils were then seeded into 500 µl Aβ40 to give the granddaughter generation (B).

The first difference between the two generations of seeding that came to mind were in the Aβ40 monomer preparation. Since the seeding of the daughter fibrils into the granddaughter fibrils involves a five-fold volume increase from 100 to 500 µl that necessitates filtering a larger volume of Aβ monomers, we use larger 28 mm diameter syringe filters by Corning (cat. # 431229) instead of 13 mm filters by Whatman (cat. #6780-1302). Although both filters have a 0.2 µm pore size and are made of PES, we thought that differences in manufacturing and filter housing dead volumes could affect filtration efficiency. To test if monomers prepared with the 28 mm filter were inefficient in seeding the AD daughter fibrils, we seeded enriched AD2 (F) and Ag Aβ40 to the daughter generation as usual, but seeded 20 µl of the daughter fibrils into 80 µl Aβ40 monomers filtered by either the 13 mm or 28 mm filters. ThT fluorescence showed that AD2(F) and Ag seeded into the daughter generation as expected, and surprisingly, also seeded well in the next generation regardless of the filter used in preparing the monomers (**Figure 4.19A**). This indicated that differences in monomer preparation was not the reason for failure to seed the AD daughter fibrils.

The next difference we looked at was in the sonication times of the daughter fibrils. Although there are more daughter fibrils than parent fibrils when we compare the two generations of seeding, the sonication time for making seeds was kept constant at 30 sec because it worked for the synthetic controls at all stages of seeding. To test if extended sonication times were essential for successful seeding of daughter fibrils at larger scales, we increased the sonication time of 100 µl of AD2(F) Aβ40 daughter fibrils by five-fold before adding 400 µl Aβ40 monomers. The resulting granddaughter fibrils finally showed high ThT binding indicating good seeding efficiency (**Figure 4.19B**). Our assumption that the seeding protocol established for Ag Aβ40 is transferable to brain extracts is therefore flawed,

perhaps because the brain-seeded fibrils are mechanically stronger and more resistant to sonication than the synthetic fibrils. One plausible explanation is that the N-termini of the brain-seeded Aβ40 fibrils are also highly-ordered as was reported by Lu et al.[16], in contrast to the pure synthetic fibrils where the first eight residues are disordered and unresolvable by solid state NMR. With the entire peptide backbone stabilized by hydrogen bonding in the fibrils, we can surmise that the brain-seeded fibrils require more energy for fragmentation. Furthermore, since sonication essentially creates more fibrillar ends for templated growth while keeping the total surface area of the fibrillar sides approximately constant, the data strongly suggests that the main mechanism of growth is by fibril elongation rather than secondary nucleation on the sides of the fibrils, and that a threshold number of ends must be reached to initiate seeding.

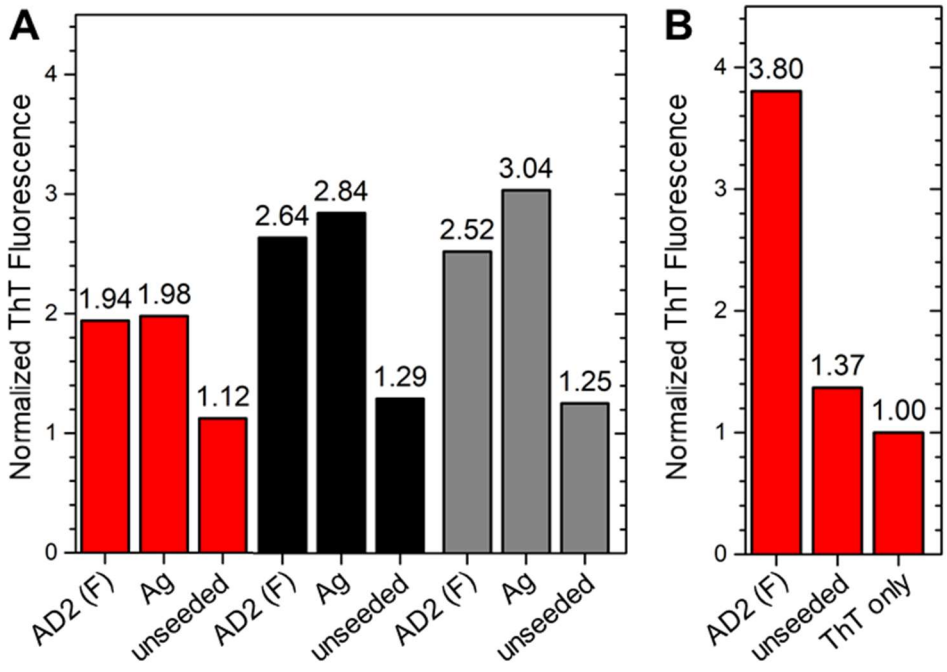

Figure 4.19. Seed preparation, not monomer preparation, was the determining factor in successful seeding of AD daughter fibrils to granddaughter fibrils at larger scales. (A) 20 μl of AD2(F) and Ag Aβ40 daughter fibrils (red) were seeded into the granddaughter generation using 80 μl of fresh Aβ40 solutions that were filtered with a 0.2 μm-pore size 13

mm diameter Whatman syringe filter (black) or 0.2 μm-pore size 28 mm diameter Corning filter (gray). (B) 100 μl AD2(F) Aβ40 daughter fibrils were sonicated for 5 cycles (30 sec on, 1 min off) on ice before 400 μl Aβ40 monomers were added, incubated for 1 day and the granddaughter fibrils quantified by ThT fluorescence.

With the confidence that we can seed brain extracts into Aβ40 to the granddaughter generation, we re-attempted seeding the enriched AD2 and ND2 brain extracts. ThT fluorescence indicated that there were more fibrils in all seeded samples than the unseeded controls in both generations (**Figure 4.20**). However, we did not expect the ND2 extracts to seed Aβ40, given that the patient was homozygous for ApoE 3 indicating a normal risk of developing AD. If she had lived long enough to develop late-onset AD at the age of 65, and if senile plaque formation begins about two decades before the appearance of symptoms, then there should be minimal Aβ deposits at the time of death (43 years old). TEMs of the ND2(T) enriched P4 fraction before seeding into Aβ40 showed widespread oligomeric structures but no fibrils (**Figure 4.21B**), implying that these oligomers have the capacity to seed Aβ40 monomers. We have yet to identify the composition of these oligomers, and although the results appear counterintuitive, they agree with reports that small and soluble Aβ seeds from APP transgenic mice and AD brains are sufficiently potent to seed Aβ deposition in young transgenic mice [28,29] and tau oligomers isolated from progressive supranuclear palsy (PSP) brains can seed recombinant tau aggregation *in vitro* [30].

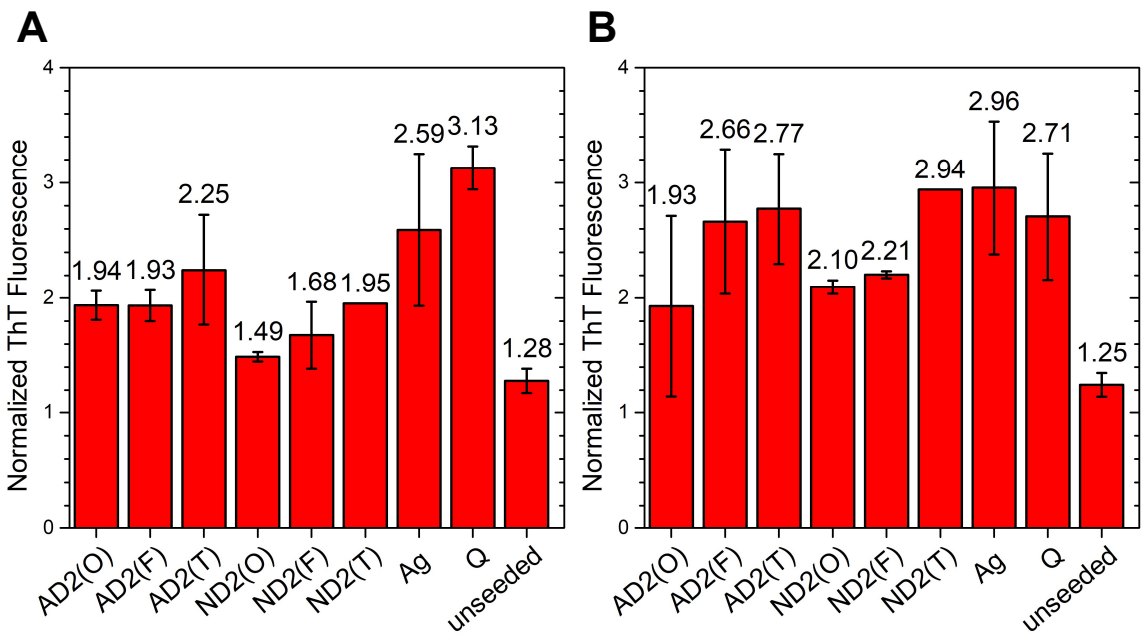

Figure 4.20. Aβ40 seeded from enriched brain homogenates have more fibrils than unseeded Aβ40 under optimized conditions. (A) Daughter and (B) granddaughter generation Aβ40 propagated from P4 fractions or synthetic Aβ40 fibrils have higher ThT binding as compared to the unseeded controls. The ND2(T) sample was only seeded once due to the lack of brain tissue.

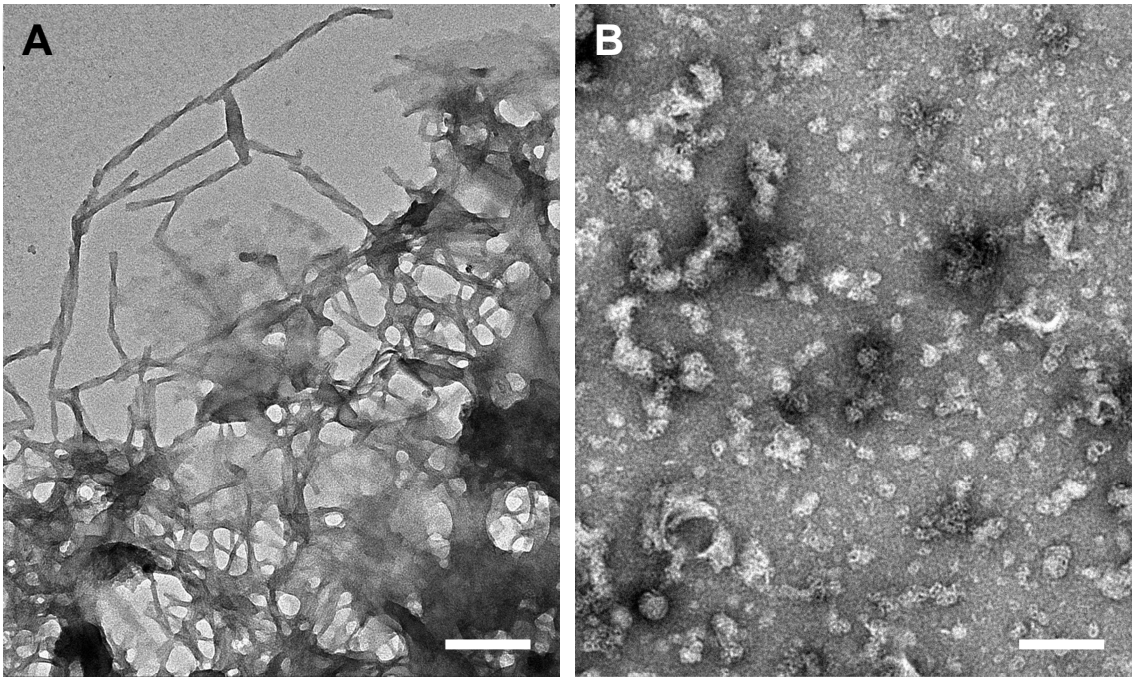

Figure 4.21. TEMs of (A) AD2(O) and (B) ND2(T) P4 fractions enriched from brain homogenates. Scale bars: 200 nm.

TEMs of the brain-seeded Aβ40 granddaughter samples showed more extensive fibrils on the grids relative to previous attempts at seeding, supporting the ThT binding data. However, the brain-seeded fibrils displayed polymorphic fibril morphologies even within the same TEM grid. **Figure 4.22** shows representative images of the AD2(O) Aβ40 granddaughter sample, where the fibrils can be negatively-stained (left panels) or positively-stained (right panels). Additionally, we observed amorphous deposits associated with the fibrils (bottom panels) which stain similarly to the membrane-like sheets in **Figure 4.11A**, and we therefore speculate that these are coacervates containing amyloids and lipids.

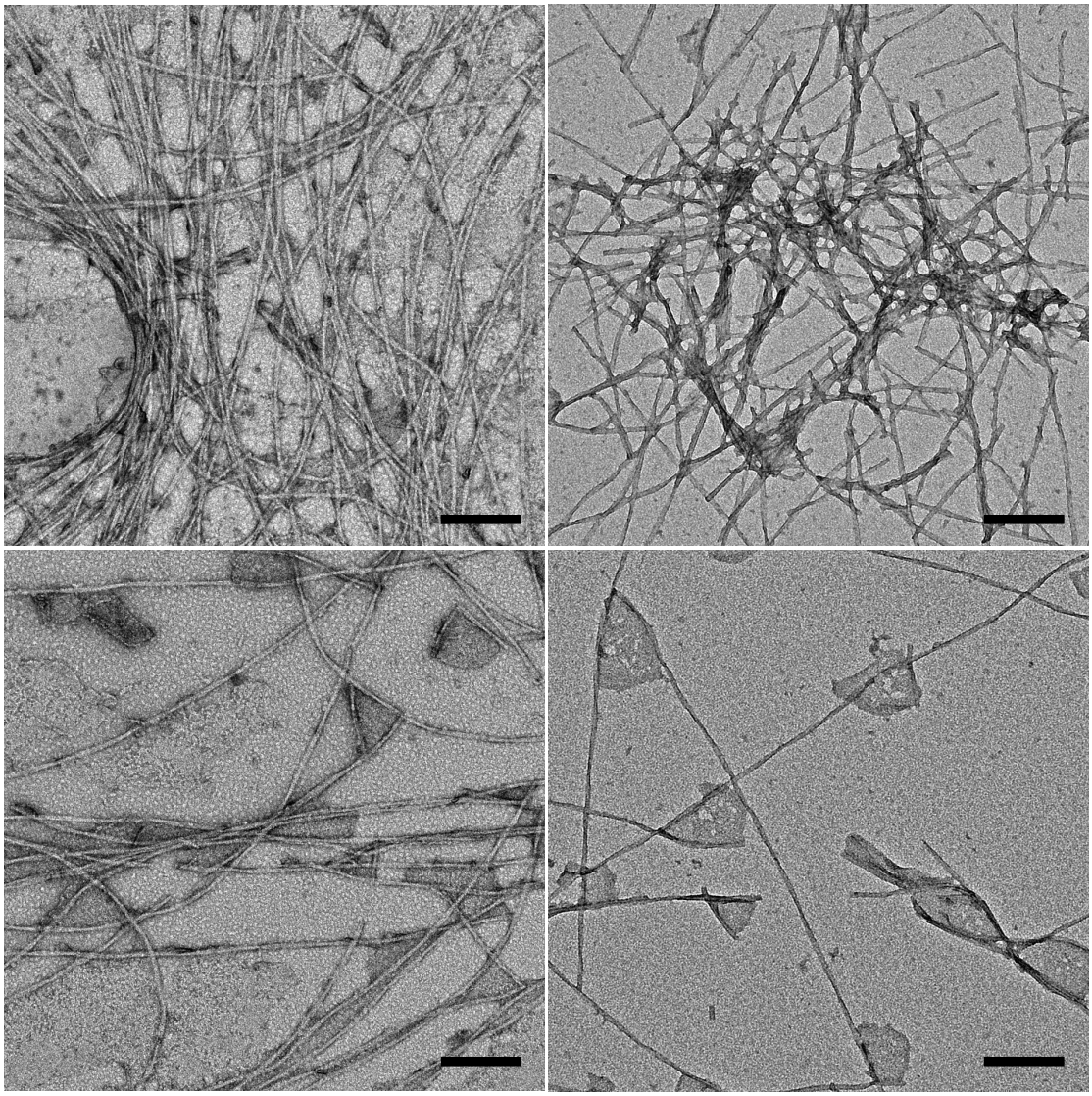

Figure 4.22. Representative TEMs of AD2(O) Aβ40 granddaughter fibrils on different areas of the same grid. Scale bars: 200 nm.

When we looked at the coacervates of the brain-seeded Aβ40 samples, we saw distinct differences in their deposition patterns. While the ND2(T)- and all the AD2-seeded granddaughter fibrils tend to have the coacervates associated at the ends of fibrils or at junctions where fibrils meet, the coacervates in the ND2(O) and (F)-seeded samples were deposited in circular patterns bordered by annular fibrils that may be partially or completely filled (**Figure 4.23**).

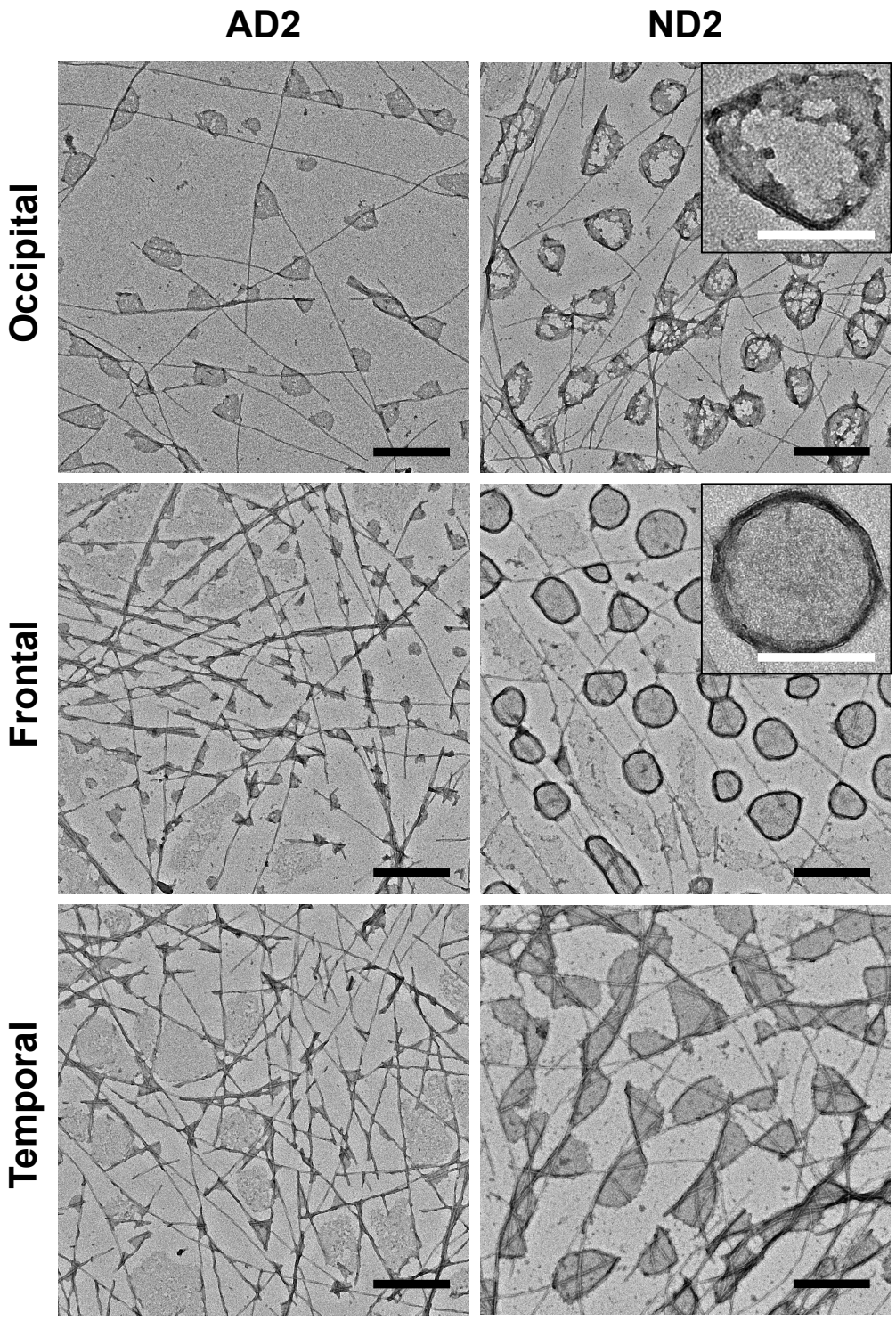

Figure 4.23. Diversity of coacervates associated with brain-seeded Aβ40 granddaughter fibrils. Scale bars: 500 nm (black) or 200 nm (white).

To further probe for differences in the seeded fibrils, we looked at the fluorescence binding spectra of three LCO dyes. As we were interested in looking for differences between AD- and ND-seeded fibrils, all the AD2-seeded spectra in the next three figures are plotted in red while the ND2-seeded spectra are plotted in blue, for simplicity.

The excitation and emission spectra for HS-68 show distinct spectral profiles for the pure synthetic and brain-seeded fibrils (**Figure 4.24**). Even within the synthetic controls, unseeded Aβ40, Ag and Q Aβ40 granddaughters have different spectral profiles, indicating that HS-68 can distinguish between fibrils with a trimeric (Q) or dimeric (Ag) protofilament structure while there is little to no binding with protofibrils and oligomers (unseeded). However, no differences were observed when we compare the AD2-seeded spectra with the ND2-seeded spectra, suggesting that there are no differences between these fibrils or that HS-68 is unable to report the fine structural differences.

Binding with pFTAA showed only a different spectral profile for Ag Aβ40 granddaughter while all the other seeded samples had similar profiles (**Figure 4.25**). The hFTAA (heptamer formyl thiophene acetic acid) fluorescence spectra showed no differences between all the seeded samples (**Figure 4.26**).

These results show an interesting trend based on the length of the LCO molecule. The shortest LCO here, HS-68, was able to distinguish between the Ag, Q and brain-seeded fibrils, whereas the longest LCO, hFTAA, was not able to differentiate between any of the seeded fibrils. Given that the polyanionic LCOs are likely to bind to the exposed positively charged residues of Aβ, this trend might be a result of hFTAA restricted to binding parallel to the fibril axes across multiple β strands, while the shorter HS-68 binds with more degrees of freedom in other conformations and/or is able to access smaller grooves/pockets in the

fibrils. Also, the lack of differences in the AD2 and ND2 spectra does not necessarily indicate that the fibrils are similar. LCOs have been reported to compete for the X-34/congo red binding site but not PiB's and therefore we are probing different regions of the fibrils [31].

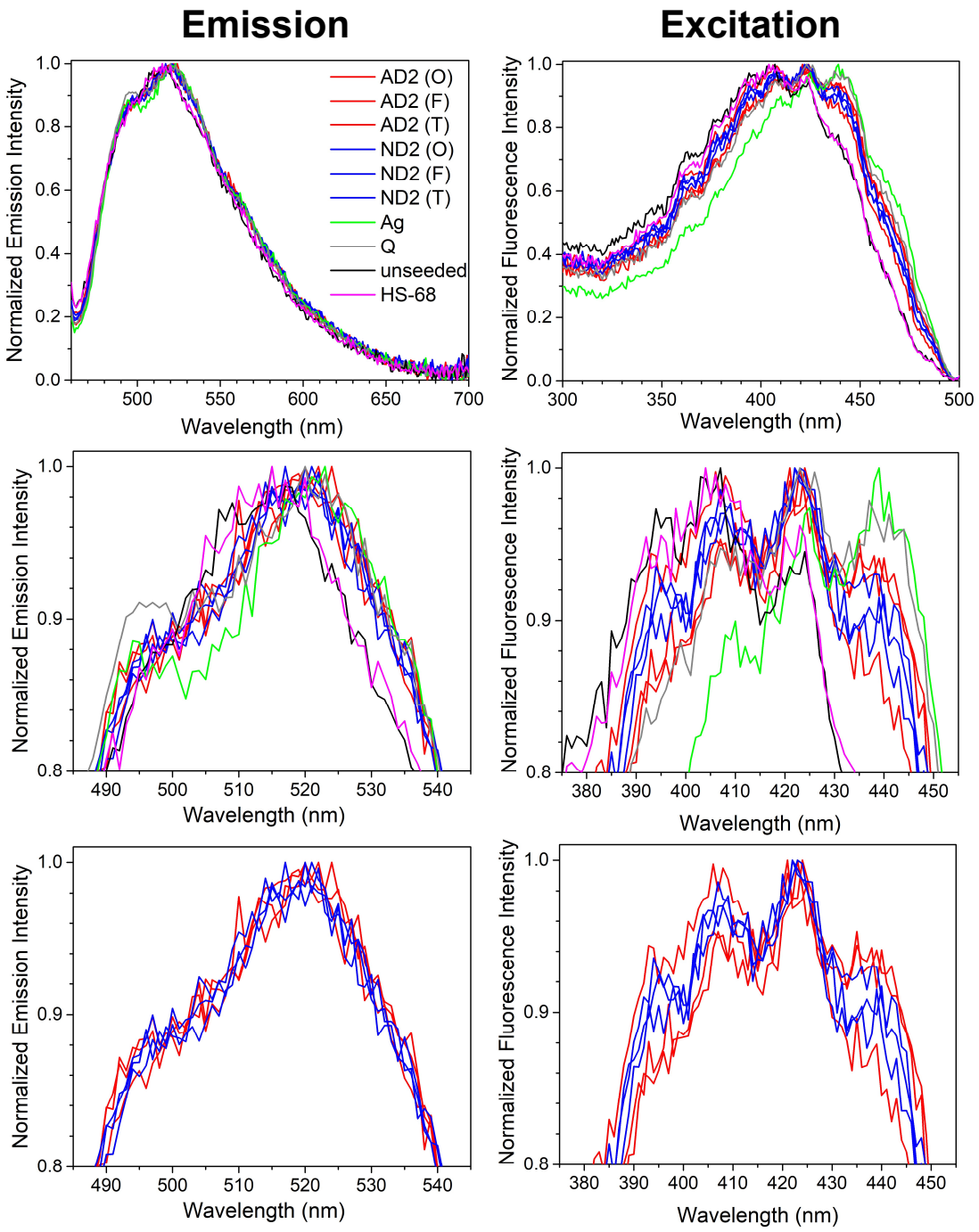

Figure 4.24. Fluorescence spectra of HS-68 binding to brain-seeded Aβ40 fibrils. The emission (left; ex=440 nm) and excitation (right; em=521 nm) spectra of 1 μM HS-68 were acquired in the presence of 10 μM granddaughter Aβ40 seeded from brain homogenate-enriched fractions. The spectral peaks are magnified in the middle row and the only the magnified AD2- and ND2-seeded peaks are shown in the bottom row. Each spectrum is an average of three replicates.

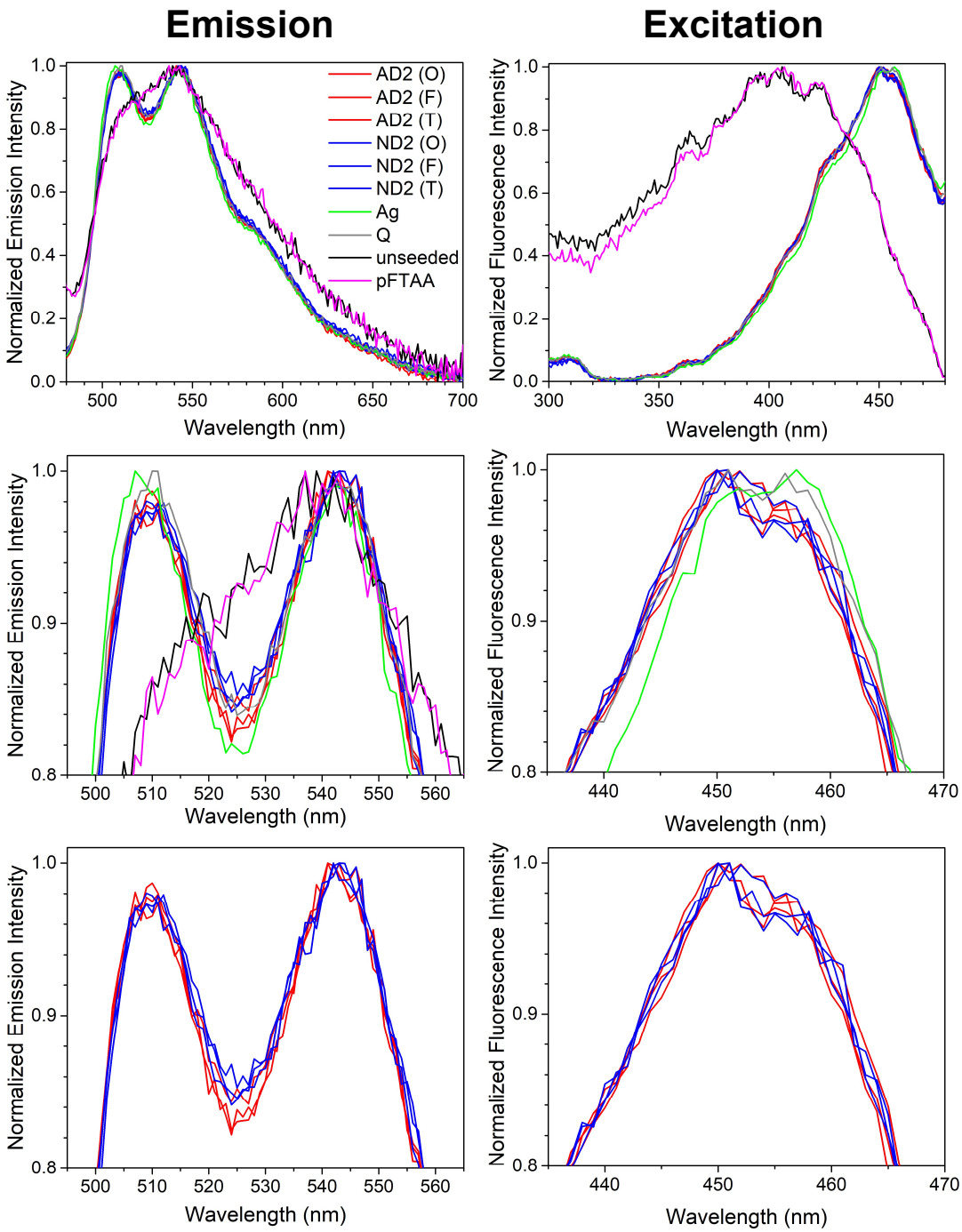

Figure 4.25. Fluorescence spectra of pFTAA binding to brain-seeded Aβ40 fibrils. The emission (left; ex=456 nm) and excitation (right; em=506 nm) spectra of 300 nM pFTAA were acquired in the presence of 10 μM granddaughter Aβ40 seeded from brain homogenate-enriched fractions. The spectral peaks are magnified in the middle row and only the magnified AD2- and ND2-seeded peaks are shown in the bottom row. Each spectrum is an average of three replicates.

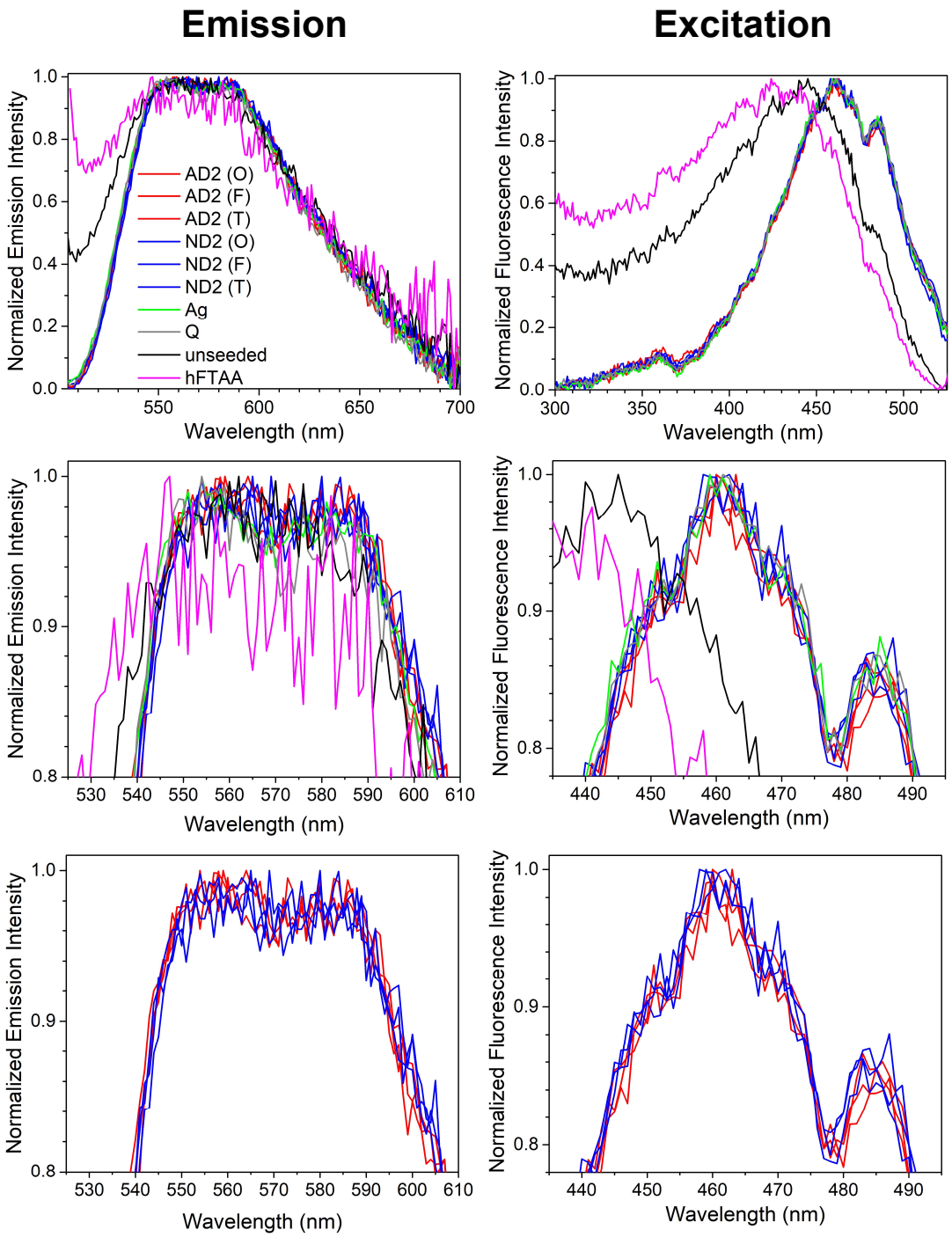

Figure 4.26. Fluorescence spectra of hFTAA binding to brain-seeded Aβ40 fibrils. The emission (left; ex=485 nm) and excitation (right; em=547 nm) spectra of 1 μM hFTAA were acquired in the presence of 10 μM granddaughter Aβ40 seeded from brain homogenate-enriched fractions. The spectral peaks are magnified in the middle row and only the magnified AD2- and ND2-seeded peaks are shown in the bottom row. Each spectrum is an average of three replicates, and the unseeded and hFTAA-only spectra are particularly noisy due to low raw intensities.

4.9 Seeding of enriched brain homogenates into Aβ42

Since LCO binding to the AD2- and ND2-seeded Aβ40 granddaughters revealed no differences, we seeded the enriched brain homogenates into Aβ42 to see if structural differences would be more prominent in Aβ42. To reduce fibrillization through primary nucleation, we decreased the peptide concentration five-fold to 20 μM and shortened each generation to five hours (see Methods and **Figure 4.38**). ThT binding to the samples showed that the brain-seeded granddaughter fibrils generally had lower ThT fluorescence than the daughter fibrils (**Figure 4.27**), suggesting that the seeding efficiency into Aβ42 was lower than into Aβ40 and ThT is binding non-specifically to other components in the brain extracts. Given that Tycko and co-workers reported a higher Aβ40/Aβ42 ratio in 16 out of 20 AD tissue samples [32] and most of the fibrils in the P4 seeds appear to be of the twisted morphology similar to quiescent Aβ40 fibrils (**Figure 4.21A**), the lower seeding efficiency we encountered may partly be due to the lower concentration of Aβ42 seeds.

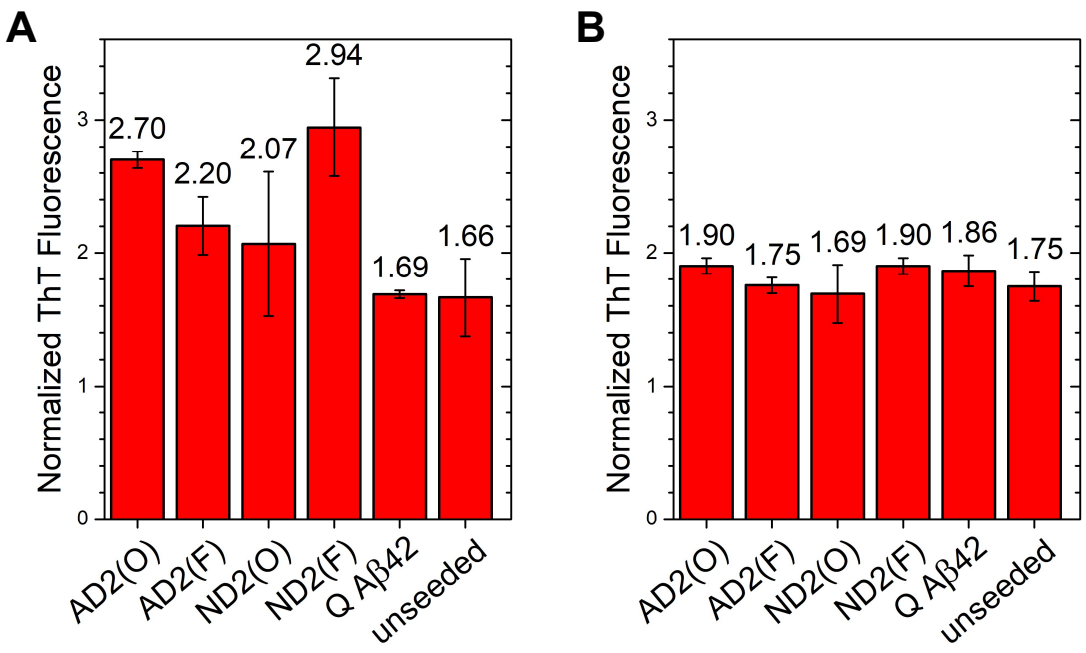

Figure 4.27. Enriched brain homogenates did not seed into Aβ42 as efficiently as into Aβ40. ThT fluorescence binding to (A) daughter and (B) granddaughter generations of Aβ42 seeded from P4 fractions or synthetic quiescent Aβ42 fibrils.

TEMs of the samples showed polymorphic fibrils even within each grid, as was the case for Aβ40. However, the most noticeable difference between samples were not in the fibril-associated coacervates, but in the fibrils with oligomers bound to their sides. In the AD2-seeded Aβ42, they appear as better-resolved, negatively-stained oligomers and protofibrils while in the ND2-seeded Aβ42, they appear to be more amorphous, positively-stained aggregates (**Figure 4.28**).

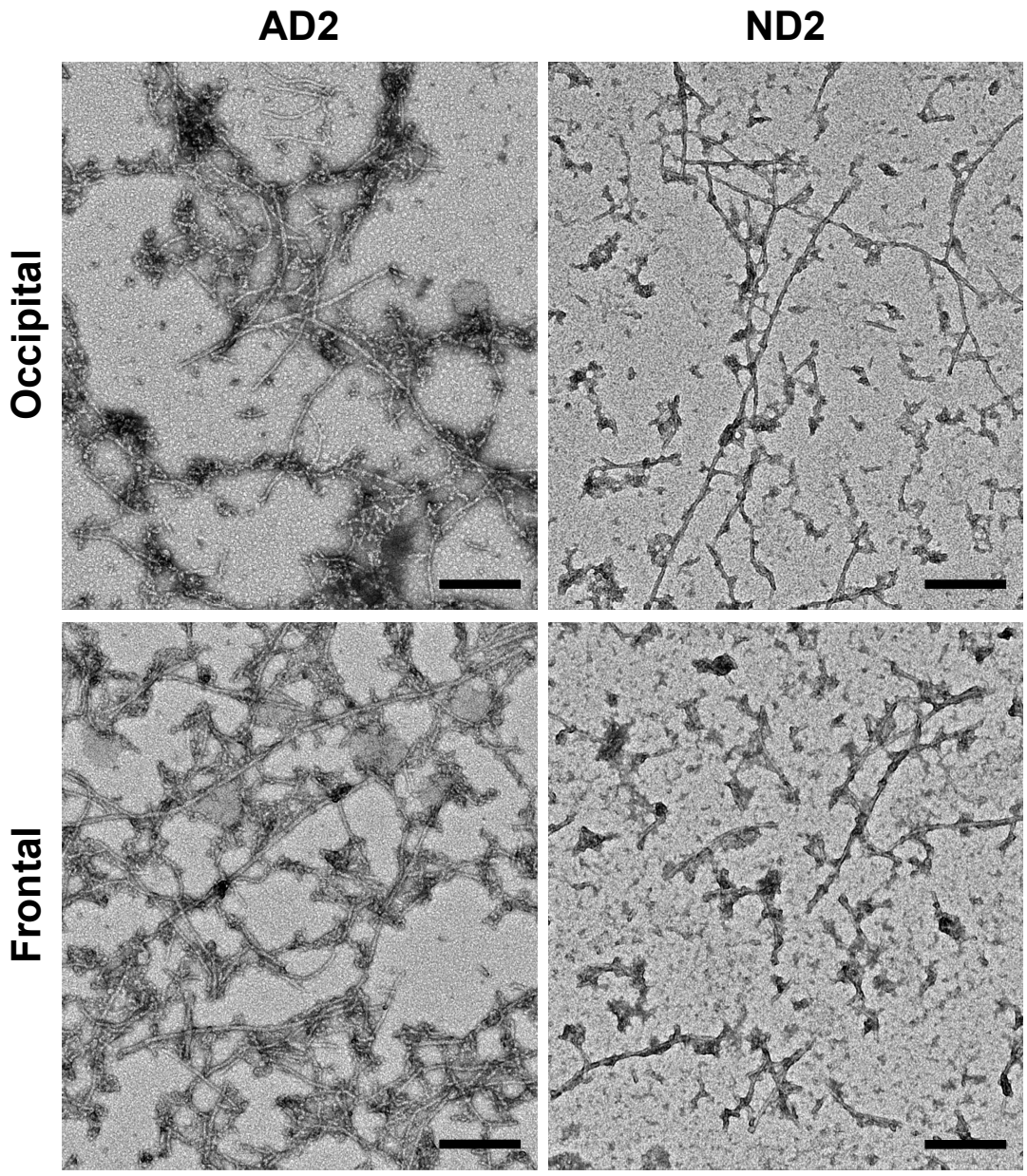

Figure 4.28. Oligomer-bound fibrils in brain-seeded Aβ42 granddaughter samples are morphologically distinct. Scale bars: 200 nm (black).

We then looked at the binding of LCOs to the Aβ42 fibrils. For HS-68, only the self-seeded Aβ42 fibrils showed different spectral profiles from the other samples containing Aβ42 (**Figure 4.29**). Likewise, pFTAA reported a different spectral profile for the Q Aβ42 granddaughter but also showed varied profiles for the AD2 and ND2 excitation spectra

(**Figure 4.30**). Interestingly, the AD2(O) and ND2(O) samples had similar excitation spectra, while AD2(F) and ND2(F) had distinct peaks at around 425 and 455 nm, suggesting that a population of the LCOs are binding in unique conformations to unique structures. However, the AD2(F) excitation spectrum is closer to that of the unseeded Aβ42, implying that the oligomeric seeds in the P4 fractions of ND2(F) have seeded a unique polymorph of Aβ42 fibrils that are distinguishable by pFTAA but not by TEM.

hFTAA binding reported another set of spectral differences. Between the brain-seeded Aβ42, the largest difference was between the AD2(O) and AD2(F) excitation spectra at 485 nm. This suggests that at the two extreme ends of the AD2 patient's brain, the Aβ42 in senile plaques had different conformations that propagated into synthetic Aβ42. Given that the plaques develop in the frontal and occipital lobes at approximately the same time during the disease process [33], having different strains of Aβ within the same brain is likely a result of concurrent but separate Aβ42 nucleation events *in vivo*.

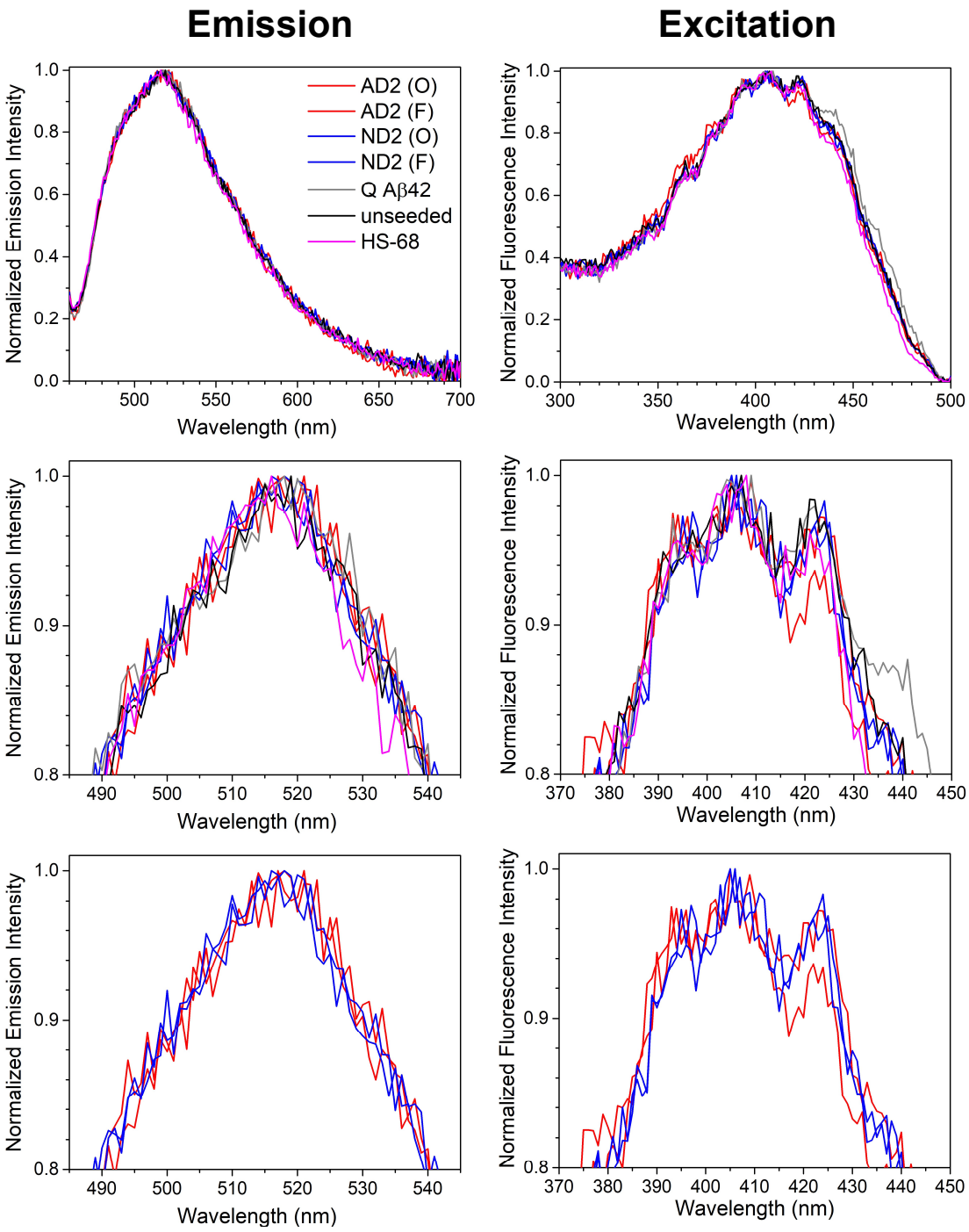

Figure 4.29. Fluorescence spectra of HS-68 binding to brain-seeded Aβ42 fibrils. The emission (left; ex=440 nm) and excitation (right; em=521 nm) spectra of 1 μM HS-68 were acquired in the presence of 8 μM granddaughter Aβ42 seeded from brain homogenate-enriched fractions. The spectral peaks are magnified in the middle row and the only the magnified AD2- and ND2-seeded peaks are shown in the bottom row. Each spectrum is an average of two replicates.

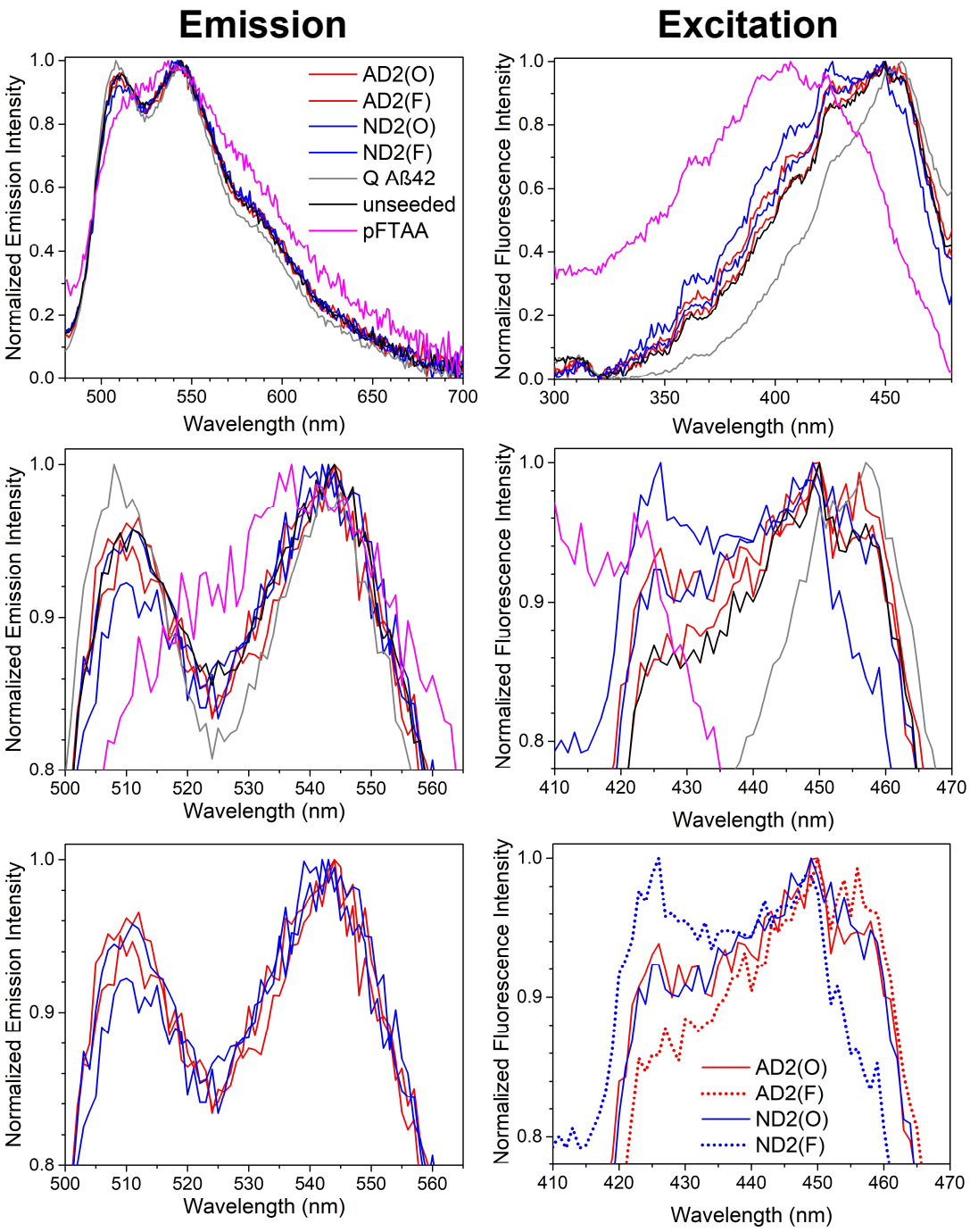

Figure 4.30. Fluorescence spectra of pFTAA binding to brain-seeded Aβ42 fibrils. The emission (left; ex=456 nm) and excitation (right; em=506 nm) spectra of 300 nM pFTAA were acquired in the presence of 8 μM granddaughter Aβ42 seeded from brain homogenate-enriched fractions. The spectral peaks are magnified in the middle row and only the magnified AD2- and ND2-seeded peaks are shown in the bottom row. Each spectrum is an average of two replicates.

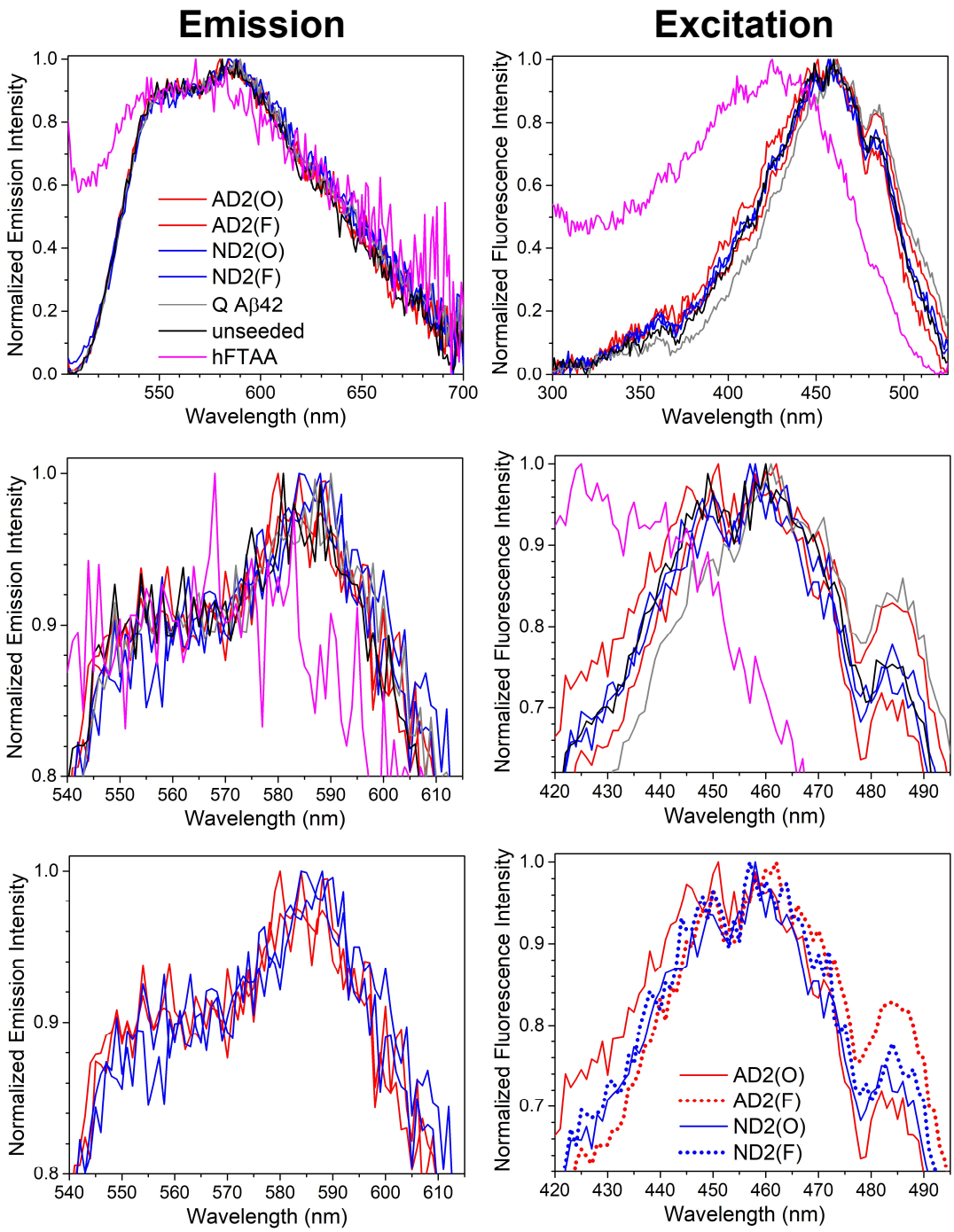

Figure 4.31. Fluorescence spectra of hFTAA binding to brain-seeded Aβ42 fibrils. The emission (left; ex=485 nm) and excitation (right; em=547 nm) spectra of 1 μM hFTAA were acquired in the presence of 8 μM granddaughter Aβ42 seeded from brain homogenate-enriched fractions. The spectral peaks are magnified in the middle row and the only the magnified AD2- and ND2-seeded peaks are shown in the bottom row. Each spectrum is an average of two replicates and the hFTAA-only spectrum is particularly noisy due to low raw intensities.

4.10 Immunogold labeling of a high-affinity PiB-binding fraction

Having received a PBC (PiB-binding Complex) fraction from Harry LeVine which was prepared through two centrifugation steps of AD brain homogenate (Materials and Methods, [34]), we sought to identify the amyloid fibrils that have the high-affinity PiB binding site using immunogold labeling with an anti-Aβ primary antibody. The structures on the TEM grid appeared to be mostly membrane/lipid-like fragments and collagen fibrils, while no discernable amyloid fibrils were found after extensive searching (**Figure 4.32A**). Since the 4G8 primary antibody recognizes both Aβ(17-24) and APP(688-695), it is unclear if the gold nanoparticles are labeling Aβ, APP or both, although APP was not detected by SDS-PAGE and western blot [34], suggesting that 4G8 is binding to Aβ only. When the primary antibody was excluded from the protocol, no gold nanoparticles were observed on the grid (**Figure 4.32B**), confirming specific binding to Aβ/APP in **Figure 4.32A**.

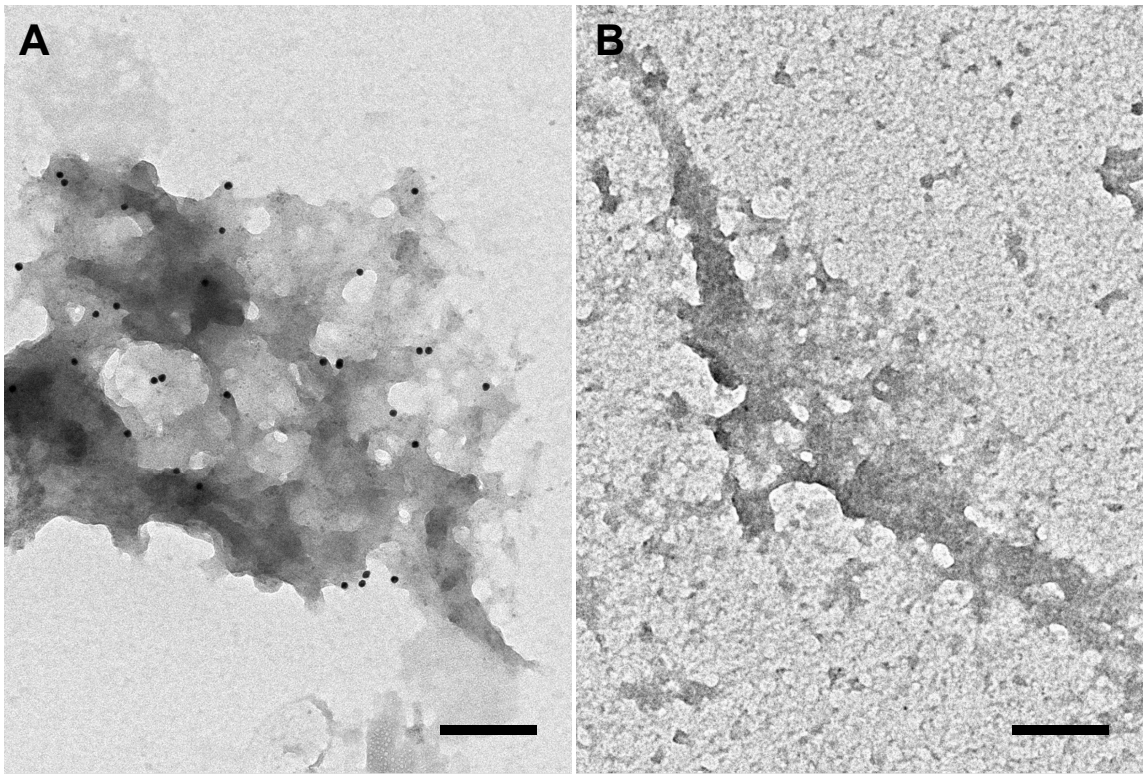

Figure 4.32. Immunogold labeling of PBC showed specific binding to membrane-like structures. (A) An aliquot of the high-affinity PiB-binding complex (PBC) was adsorbed on a TEM grid and labeled with 4G8 antibody and 10 nm gold nanoparticles. (B) Another aliquot of the same PBC was labeled following the same protocol, except without the primary 4G8 antibody. Scale bars: 200 nm.

4.11 Co-assembly of Aβ with nucleic acids and metal ions

Since amyloid plaques are composed of other non-Aβ components such as nucleic acids, cations and lipids [35], we wanted to test how these co-factors influenced Aβ assembly. Recent experiments in our lab with an amyloidogenic peptide, Ac-KLVIIAG-NH_2, showed that co-assembly with A_{10} DNA or RNA changed the morphology of the peptide from fibers to multi-lamellar nanotubes, with the anionic phosphodiester backbone stabilizing the lysine residues of the peptide [36].

Rationalizing that the DNA could accelerate the assembly of Aβ by acting as a template that stabilizes the positively-charged side chains, we co-assembled 100 μM Aβ40 and Aβ42 with up to 1 molar equivalent of A_{10} single-stranded DNA and monitored the assembly over two weeks with ThT fluorescence. **Figure 4.33A** shows that Aβ40 assembled with higher concentrations of DNA have slightly more ThT fluorescence even at time zero, suggesting that there is some non-specific binding of the positively-charged ThT to DNA. However, the kinetic profiles of the Aβ40 samples are very similar over the two-week period and little differences were observed in the fibril morphologies by TEM, except with 0.1 equivalents of DNA where the fibrils appeared more positively stained (**Figure 4.34**). For Aβ42, most of the fibril growth happened within the first day and plateaued after that, with no discernable trend in how DNA affected ThT fluorescence (**Figure 4.33B**). Since Aβ42 assembled rapidly at 100 μM, we decreased the peptide concentration five-fold to 20 μM and repeated the co-assembly. Although there was more noise in the ThT measurements, it appears that DNA had little effect on fibril growth (**Figure 4.33C**) or morphologies over two weeks (**Figure 4.34**). We then looked at the Aβ42-DNA co-assembly over a 16-hour period during which most of the fibril elongation should take place, but the kinetic profiles of the samples were essentially the same (**Figure 4.33D**).

Based on our results, it appears that the nucleic acids could be non-specifically co-aggregating with the plaques instead of accelerating amyloid accumulation or modulating fibril toxicity through structural changes. As such, we did not further characterize the Aβ-DNA coassemblies with LCO or PiB binding.

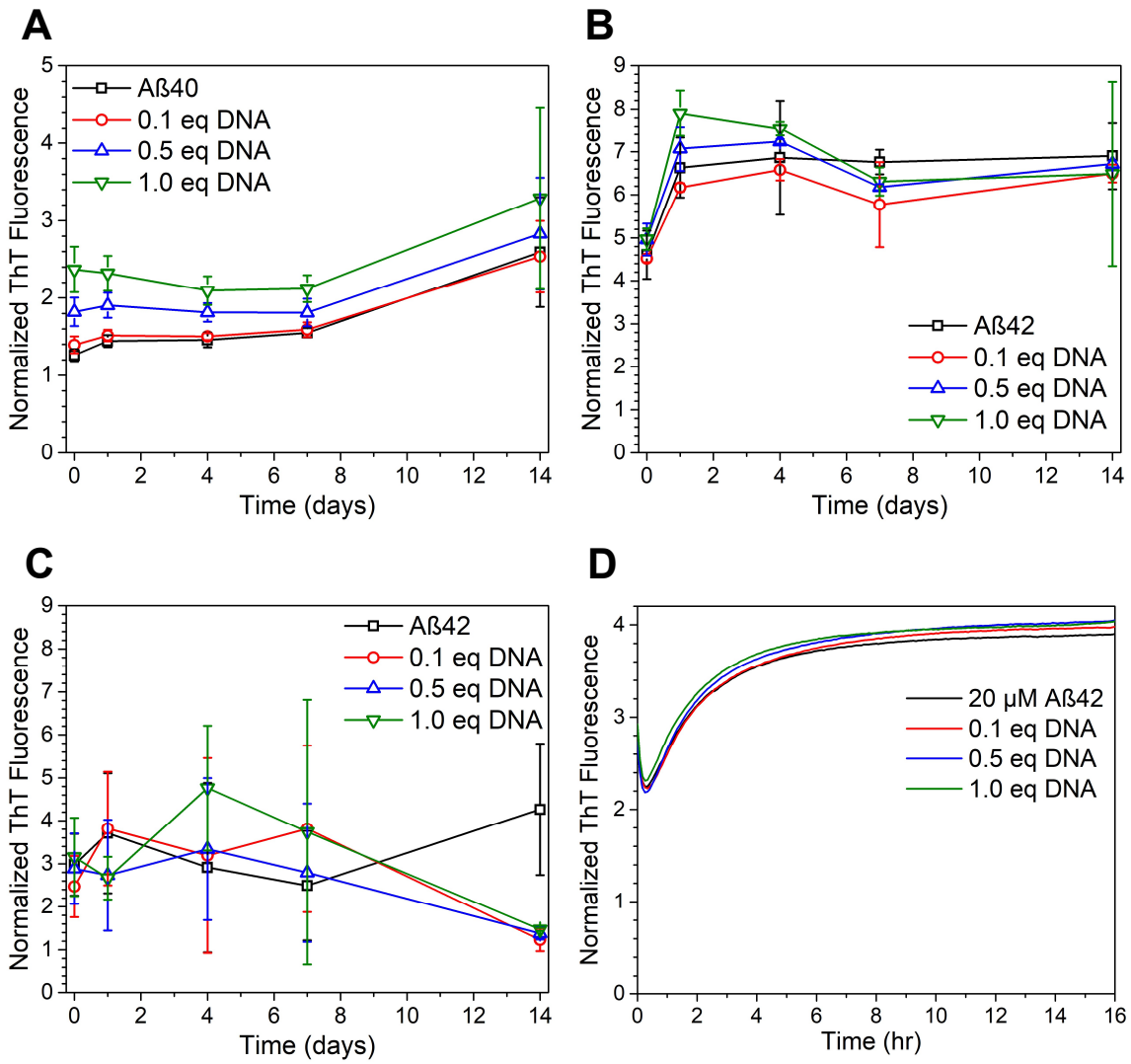

Figure 4.33. A_{10} DNA does not affect Aβ assembly kinetics. (A) 100 μM Aβ40, (B) 100 μM Aβ42 and (C) 20 μM Aβ42 were assembled over 2 weeks in the presence of up to 1 molar equivalent of single-strand A_{10} DNA. ThT fluorescence assay was then performed and the emission values were normalized to ThT-only solutions set to 1. (D) 20 μM Aβ42 was assembled in the presence of up to 1 molar equivalent of A_{10} DNA and ThT, and the average of triplicate samples are plotted.

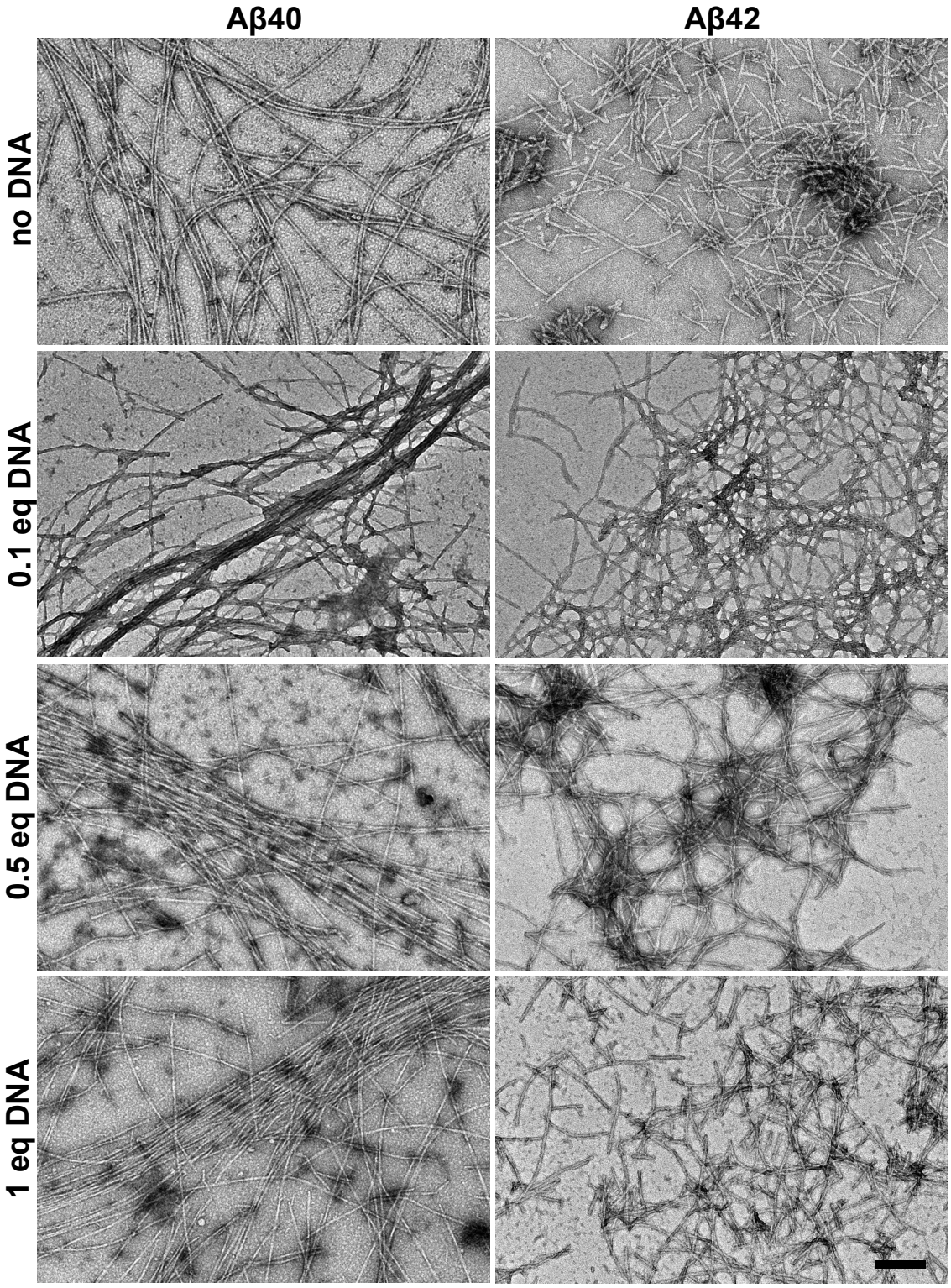

Figure 4.34. A_{10} DNA does not affect Aβ fibril morphologies. 100 μM Aβ40 (left) and 20 μM Aβ42 (right) 2-week assemblies at 37 °C without DNA and with 0.1 to 1 molar equivalents of A_{10} DNA. All images to scale. Scale bar: 200 nm

Although the effect of metals on Aβ assembly has been widely studied, conflicting results indicate that the macromolecular structures are highly dependent on the assembly conditions and that the effects are not well-understood. Studies of Aβ40 co-assembled with Cu^{2+} indicate that the cation does not alter the aggregation pathway and forms globally-ordered arrays of Aβ40-Cu^{2+} fibrils [37,38], but other studies reported that Cu^{2+} inhibits Aβ42 fibrillization [39-44]. This appears counterintuitive given that Aβ42 has a higher aggregation propensity than Aβ40 and the hydrogen bonding between Aβ42 peptides would be more likely to overcome the His-Cu^{2+} coordination than for Aβ40.

To determine what effect metals would have on Aβ fibrillization, we co-assembled Aβ40 and 42 with $CuCl_2$. Our experiments show that Cu^{2+} inhibits both Aβ40 and 42 fibrillization, forming large amorphous aggregates (**Figure 4.35**) that are likely the result of Cu^{2+} coordinating to His6, His13 and His14 of Aβ in a conformation that disfavors the rest of the peptide from forming ordered β-sheets. This concurs with the reports that Cu^{2+} inhibits Aβ42 fibril formation but disagrees with studies demonstrating ordered Cu^{2+} binding on Aβ40 fibrils, reinforcing our prediction that the influence of metal ions on Aβ assembly are context-dependent. While the Aβ-Cu^{2+} amorphous aggregates appear positively-stained by TEM as was the case for the high-affinity PiB binding complex (**Figure 4.32**), it remains to be tested if they bind to PiB with high-affinity.

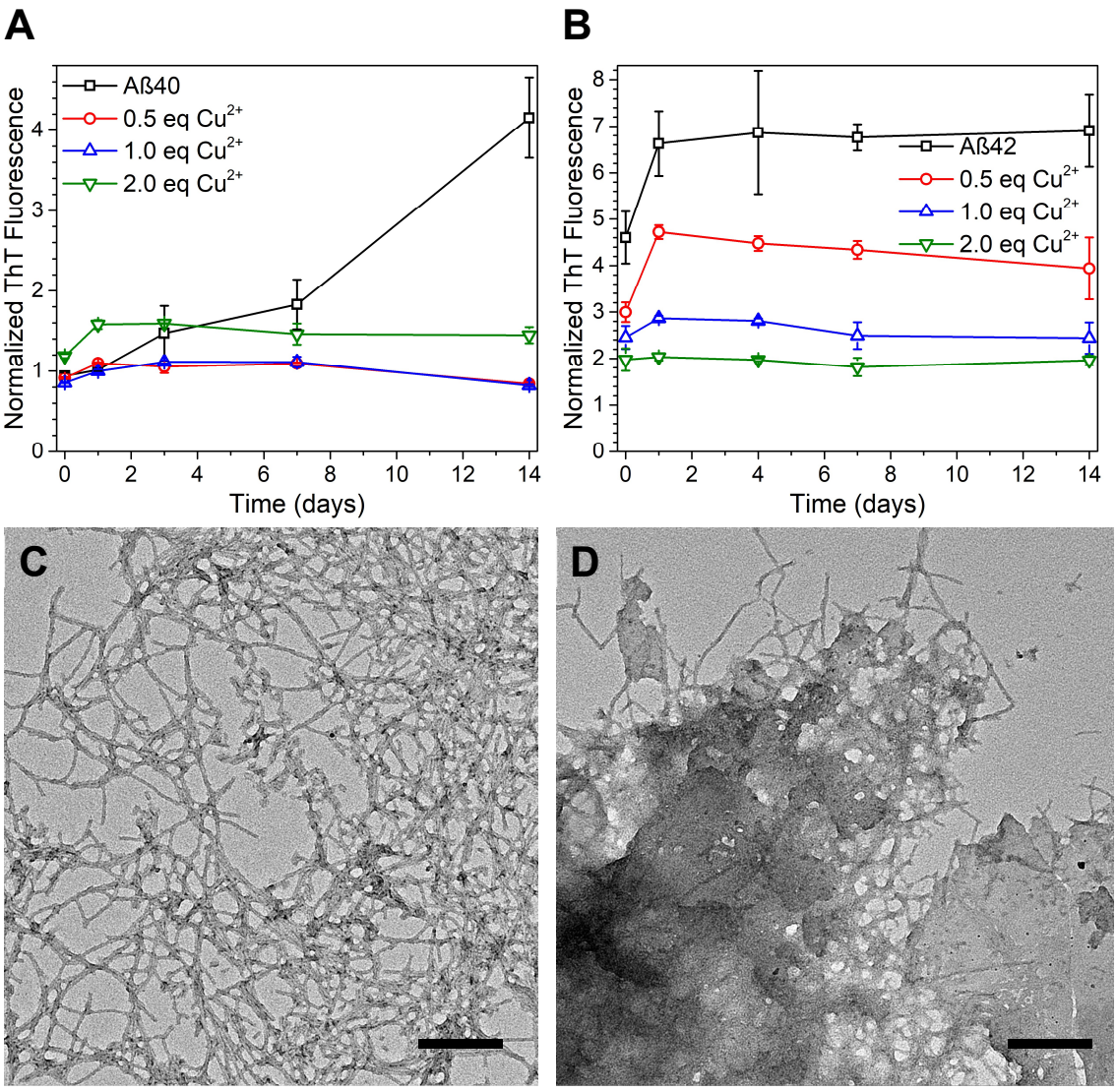

Figure 4.35. Cu^{2+} inhibits Aβ fibril assembly. (A) Aβ40 and (B) Aβ42 were assembled at 100 μM over 2 weeks in the presence of up to 2 molar equivalents of Cu^{2+} (200 μM $CuCl_2$). ThT fluorescence assay was then performed and the emission values were normalized to ThT-only solutions set to 1. TEMs of Aβ42 without added Cu^{2+} show widespread fibrils at 4 days (C), but large amorphous aggregates were present with 2 molar equivalents of Cu^{2+}(D). Scale bars: 200 nm.

Conclusion

In this chapter, we have established a method for amplifying amyloid structures from brain extracts into synthetic Aβ. Our finding that unenriched brain homogenates (LSS

fractions) are inefficient seeds for *in vitro* amplification indicate that a critical seed concentration must be reached for seeding to occur. For the LSS fractions to be sufficiently potent to seed Aβ deposition in AD rodent models[19], there must be an *in vivo* mechanism that concentrates the exogenous amyloid. We also discovered that brain-seeded Aβ40 propagate differently from synthetic Aβ40, requiring extended sonication to fragment the fibrils past the threshold to initiate seeding. The increased mechanical strength of the brain-seeded Aβ fibrils likely arise from the peptides packing in a fully-ordered β-sheet conformation that confers additional hydrogen bonding at the N-termini of the peptides, which are absent in the synthetic Aβ fibrils that have disordered N-termini. LCO binding to the seeded Aβ40 fibers showed that the short (16.4Å) HS-68 ligand was able to distinguish between agitated, quiescent and brain-seeded Aβ40 structures while the longer (27.7Å) hFTAA ligand was unable to report any differences between those structures. It is possible that hFTAA is restricted to binding parallel to the fibers along the positively-charged residues while HS-68, having one less negative charge and being shorter, can bind in multiple conformations and access smaller binding pockets. While the LCOs could not distinguish between AD- and ND-seeded Aβ40, they showed spectral differences when bound to the brain-seeded Aβ42 fibrils and even Aβ42 seeded from different lobes of the same brain. This is suggestive of multiple Aβ42 nucleation events in the brain leading to different amyloid structures. Ongoing transfection assays are being conducted to see if the brain-seeded Aβ40 and Aβ42 can seed Aβ-Sup35 chimeric amyloids in yeast cells and if there are differences in seeding efficiencies and phenotypes. If so, it would demonstrate the prion-like property of Aβ in maintaining structural information while crossing multiple species barriers (human → synthetic → yeast).

From a bottom-up approach, it appears that Aβ fibrils have higher PiB-binding affinity than the protofibrils and oligomers [45]. However, the top-down approach of identifying the PiB-binding complex by processing AD brain tissue suggests that an amorphous and lipid-associated aggregate of Aβ should be the target of interest (**Figure 4.32A**, [34]). Future experiments will need to test and rule out the presence of high-affinity PiB binding in the AD-seeded Aβ, since the LCO and PiB binding sites on Aβ are distinct [31]. Thereafter, synthetic Aβ could be co-assembled with one or more of the other components (ApoE, tau, ubiquitin and collagen) that were found in the PBC to determine if a heteromeric Aβ complex binds to PiB with high affinity.

Materials and Methods

Assembly of agitated Aβ40 fibrils

It has been reported that the average length of Aβ fibrils decreases as the speed of shaking increases [46]. Therefore, the shaking speed needs to be low to produce fibrils of sufficient length but high enough to produce the shear force required for assembly of the agitated conformation. The air-water interface is also known to influence amyloid fibril assembly by providing a hydrophobic surface for nucleation [47], so it (surface area, oscillation rate, etc.) has to be kept consistent for reproducible Ag fibrillization. After multiple attempts at assembling Ag fibrils, we determined that the most reproducible protocol is to add 1 ml of the Aβ40 monomeric solution to a 1.5 ml microfuge tube and lay it horizontally on a shaker at 100 rpm and room temperature.

Preparation of low-speed supernatant (LSS) brain extracts

LSS brain extracts were prepared by the Walker lab at the Yerkes National Primate Research Center. Briefly, one part frozen brain tissue (~ 300 mg) was added to nine parts of

cold PBS buffer and homogenized in a dounce homogenizer (20-40 strokes). The homogenate was then briefly probe-sonicated for ten quick pulses, then clarified by centrifugation at 5,000 g, 4 °C for 10 min. The resulting 'low speed supernatant' was aliquoted into microcentrifuge tubes and stored at -80 °C until ready for seeding.

Seeding of LSS brain extracts into synthetic Aβ40

100 µl of each brain extract or 100 µM synthetic Ag and Q Aβ was probe-sonicated at 30% amplitude for 30 sec (Cole-Palmer CPX 750). These conditions were sufficient for producing seeds with lengths in the 200 nm range (**Figure 4.36**) while longer sonication times caused the sample to get unnecessarily hot. 900 µl of 100 µM NH_4OH-treated Aβ40 monomers in 10 mM phosphate buffer was added to the sonicated extract and this daughter generation assembly was incubated at 37 °C for 1 day. For the grand-daughter generation, this procedure was repeated using 100 µl of the daughter fibrils as seeds.

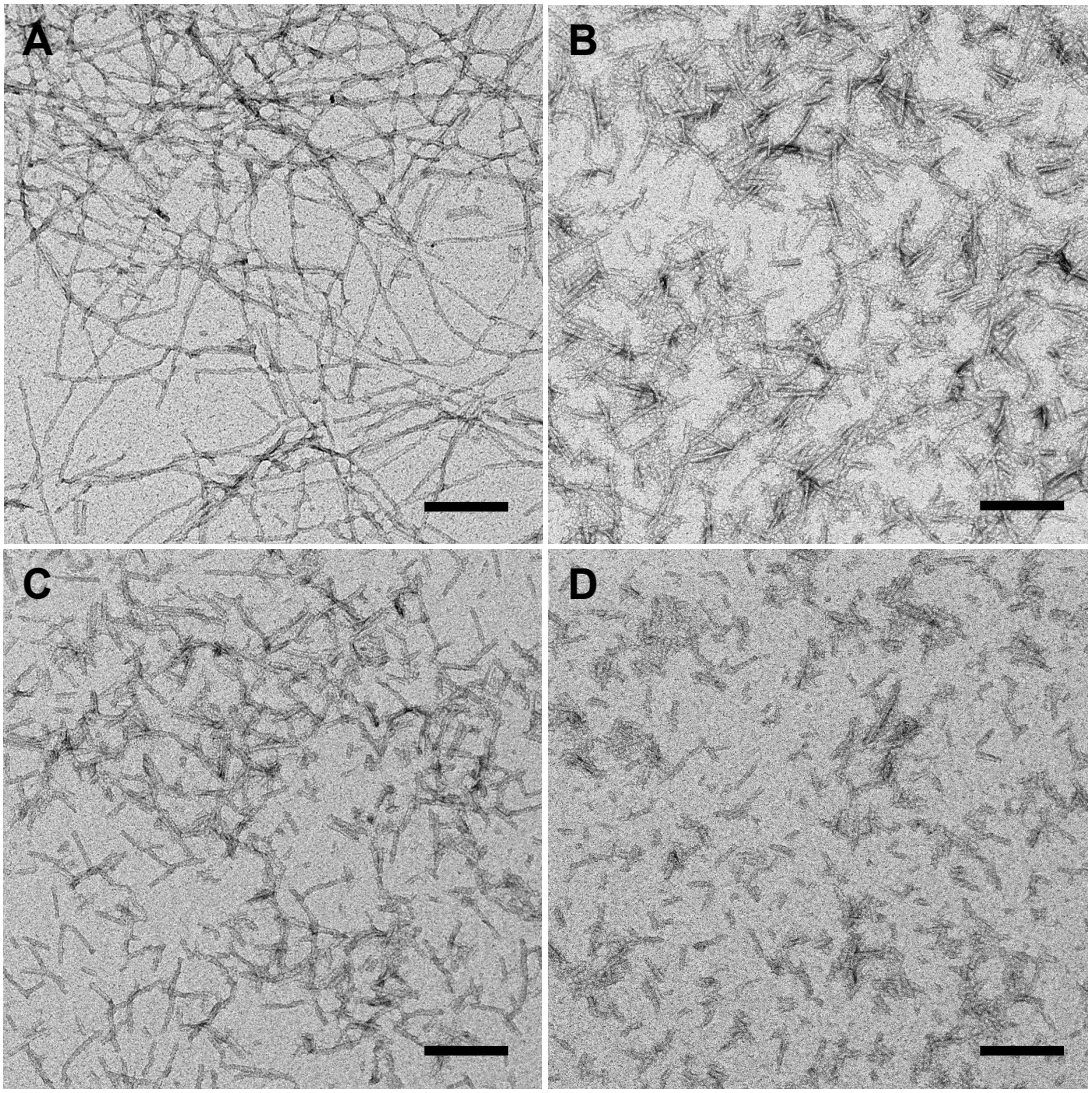

Figure 4.36. Probe sonication of synthetic Q Aβ40. (A) Before sonication, continuous probe sonication for (B) 30 sec, (C) 1 min and (D) 10 min. Scale bars: 200 nm.

Brain extract amyloid enrichment

This protocol is adapted from Wenborn et.al. [24]. Incubations were performed at 400 rpm in a 37 °C shaking incubator and centrifugations at 37 °C. 200 µl aliquots of 10% (w/v) brain homogenate low speed supernatant were dispensed into 1.5 ml microfuge tubes. For each aliquot, 2 µl of 10 mg/ml pronase E (Sigma-Aldrich) in water was added and incubated for 30 min. 4.1 µl of 0.5 M EDTA in water pH 8.0, 206 µl of 4% (w/v) sarkosyl in Dulbecco's phosphate buffered saline (D-PBS) lacking Ca^{2+} and Mg^{2+} (Life Technologies)

and 0.83 µl of 25 U/µl benzonase nuclease (EMD Millipore) were then added. After incubating for 10 min, 33.5 µl of 4% (w/v) NaPTA (sodium phosphotungstate hydrate, Sigma-Aldrich) in water pH 7.4 was added and incubated for 30 min. 705.3 µl of 60% (w/v) iodixanol (Optiprep™, Cosmo Bio USA) and 57. 2 µl of 4% NaPTA were added and thoroughly mixed. The sample was then centrifuged at 16,100 g for 90 min, where it yielded a barely visible pellet (P1), supernatant (SN1) and a yellowish, flocculated surface layer (SL). 1 ml of SN1 was carefully isolated from each tube and filtered through a pair of centrifugal filter units (0.45 µm pore size Durapore membrane, EMD Millipore Cat. No. UFC30HV00) at 12,000 g for 1 min. Each filter was pre-washed thrice with HPLC water by centrifugation and was used for filtering up to 1 ml of SN1. The filtered SN1 aliquots were transferred to new 1.5 ml microfuge tubes and well-mixed with an equal volume of 2% (w/v) sarkosyl in D-PBS containing 0.3% (w/v) NaPTA pH 7.4. Following a 10 min incubation at 37 °C, the samples were centrifuged for 90 min at 16,100 g. For LSS extract enrichments, the bottom 10-20 µL in each tube was assumed to be the pellet P2 since it was not clearly visible. For brain homogenate enrichments, P2 was sufficiently visible to avoid contact with a pipet tip. The supernatant SN2 was carefully removed and discarded, after which P2 was resuspended in 10 µl of wash buffer (17.5% (w/v) iodixanol and 0.1% (w/v) sarkosyl in D-PBS). 180 µl of wash buffer and 16.2 µl of 4% NaPTA was then added and the solution centrifuged at 16,100 g for 30 min to generate supernatant SN3 and an in visible pellet P3. SN3 was carefully removed and discarded after which P3 was resuspended in 200 µl of wash buffer followed by the addition of 16.2 µl of 4% NaPTA. Samples were centrifuged at 16,100 g for 30 min and SN4 was carefully removed and discarded. The P4 pellets of each sample were then resuspended in 20 µl of D-PBS containing 0.1% (w/v) sarkosyl, pooled and then stored in 20 µl aliquots at −80 °C.

For scaled-up enrichments of brain homogenates where each P4 fraction was processed from 90±3 mg brain tissue, the resuspended P2 pellets were dispensed into aliquots of equal volume (~90 μl) based on the mass of starting tissue, e.g. 270 mg of frozen brain will give three tubes of resuspended P2. The volumes of wash buffer and 4% NaPTA added to the P2 and P3 samples were scaled up four-fold. The final P4 pellets were frozen without resuspending in 20 μl D-PBS + 0.1% sarkosyl.

Seeding of P4 brain extracts into synthetic Aβ

In the optimized seeding protocols (**Figure 4.20** onwards) thawed P4 pellets were resuspended in 100 μl Aβ40, probe-sonicated at 30% amplitude for 30 sec and incubated at 37 °C for 1 day to yield the daughter fibrils. For the grand-daughter generation, the daughter fibrils can either be (i) sonicated for 5 cycles (30 sec on, 1 min off) while immersed in ice to reduce overheating, before the addition of 400 μl Aβ40 monomers, or (ii) they can be split into aliquots of 20 μl fibrils + 80 μl fresh Aβ40 monomers and probe-sonicated for 30 sec, before another 1-day incubation. Ag and Q fibrils were seeded at 10% v/v as described above. TEMs show that the Ag and Q Aβ40 granddaughter fibrils are morphologically different, while the unseeded Aβ40 is mostly oligomers and protofibrils (**Figure 4.37**).

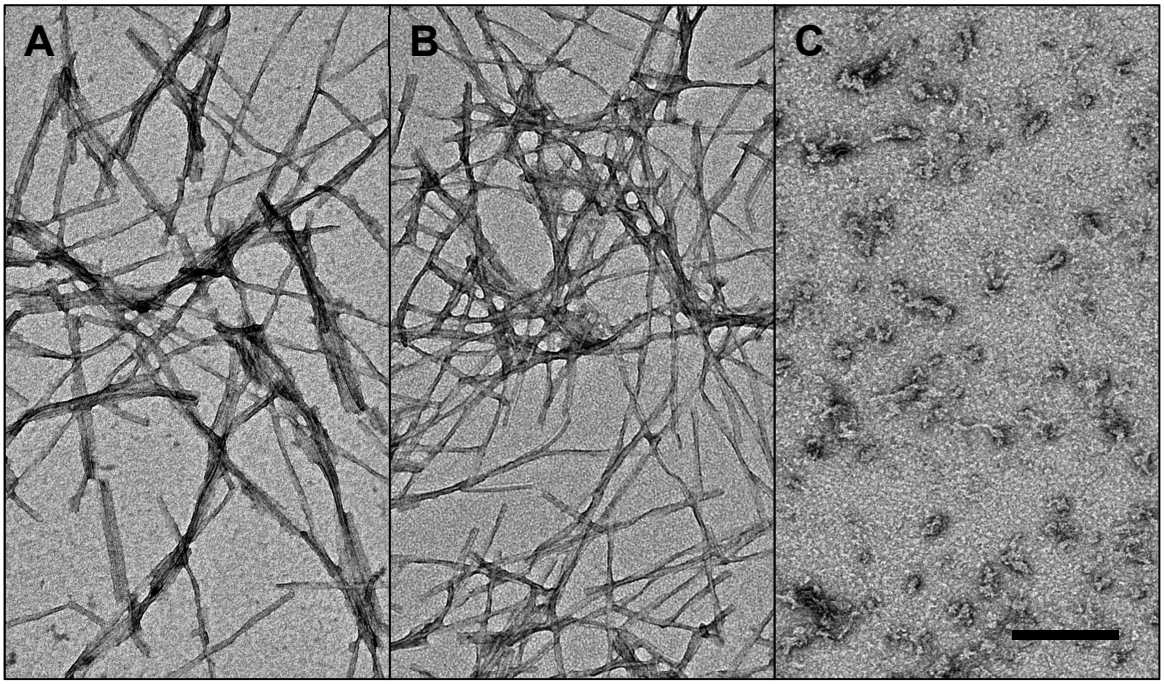

Figure 4.37. TEMs of synthetic granddaughter Aβ40 controls. (A) Ag Aβ40, (B) Q Aβ40 and (C) unseeded Aβ40. All images to scale. Scale bar: 200 nm.

For seeding into Aβ42, we had to decrease the peptide concentration to 20 μM to reduce fibrillization in the unseeded pathway. Even after 16 hours of incubation at 37 °C, the growth of unseeded Aβ42 was starting to plateau and abundant fibrils were observed by TEM (**Figure 4.38**). We therefore settled on a 5-hour seeding interval per generation after some failed attempts at longer intervals and because the seeded Aβ42 begins to plateau at that time. Even though fibrils were present in the unseeded sample (**Figure 4.39B**), we observed relatively less fibrils compared to the seeded samples and lower raw fluorescence intensities in the LCO binding assays.

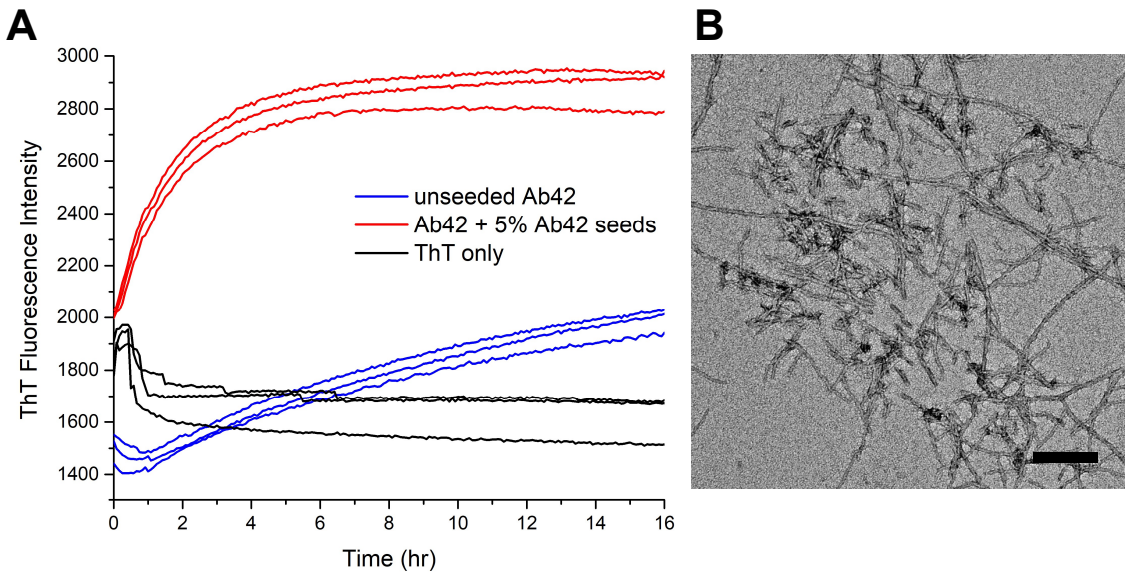

Figure 4.38. Aβ42 assembles quickly at 20 μM. (A) Fibrillization of unseeded and 5% seeded 20 μM Aβ42 monitored by ThT fluorescence. (B) TEM of unseeded 20 μM Aβ42 after 16 hr at 37 °C. Scale bar: 200 nm.

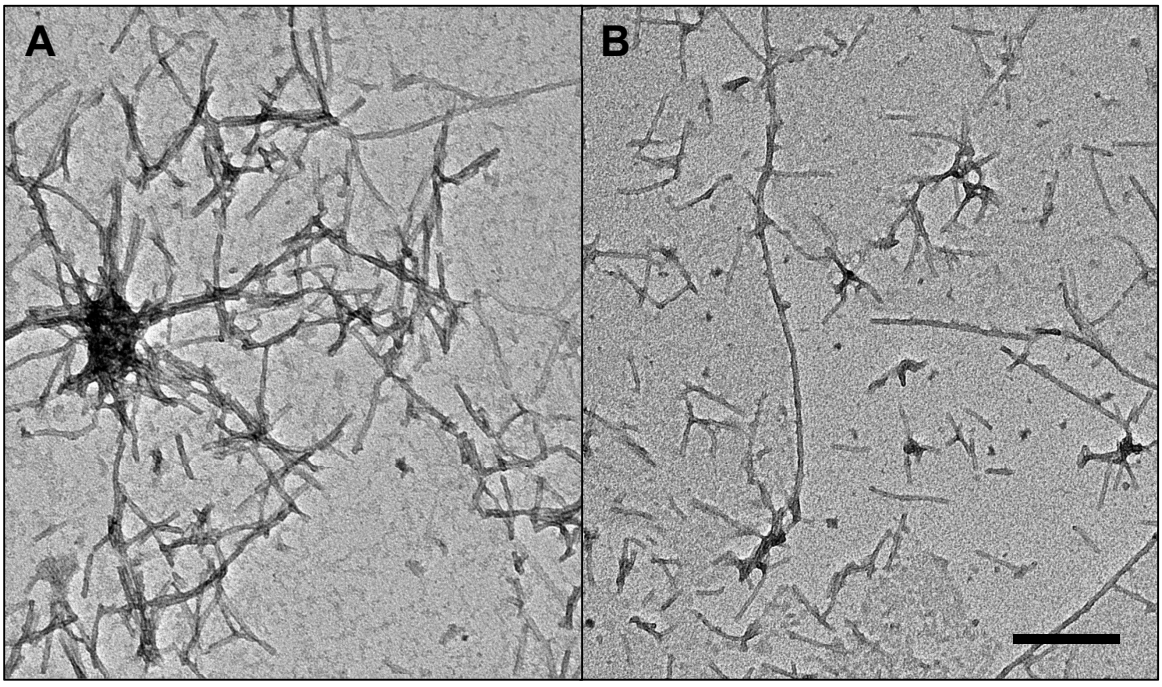

Figure 4.39. TEMs of synthetic granddaughter Aβ42 controls. (A) Q Aβ42 and (B) unseeded Aβ42. Both images to scale. Scale bar: 200 nm.

Thioflavin T (ThT) fluorescence

Thioflavin T (AnaSpec, ultrapure grade, Cat. No. AS-88306) was dissolved to 10 mM in 10 mM phosphate buffer, pH 7.4 and frozen at -20 °C in aliquots until ready for use. Kinetic assays were performed using black 96 well plates with clear flat bottoms (Corning, Cat. No. 3631) in a Biotek Synergy HT plate reader controlled by KC4 software. 200 μL of 100 μM Aβ peptide (or 10 mM phosphate buffer for ThT-only controls) was added to each well followed by 10 μL of 100 μM ThT to give a final concentration of 4.76 μM ThT. The plates were sealed with a plastic film and incubated in the plate reader at 37 °C quiescently, except before each reading where the plate was shaken for 3 seconds with the intensity set at 3. Fluorescence was measured at the bottom of the wells with 440/20 and 485/20 nm excitation and emission filters respectively and sensitivity at 50. Endpoint assays were performed as described in chapter 3.

Fluorescence spectra were acquired in a quartz micro cuvette (Hellma Analytics 105.251-QS, 3x3 mm light path, 100 μl volume) with an Agilent Cary Eclipse spectrofluorometer. Each sample containing 2 μM Aβ and 10 μM ThT in 10 mM phosphate buffer was excited at 450 nm and emission scans were collected at 1 nm data intervals at 2 nm/s, 0.5 s averaging time and a PMT voltage of 800 V with excitation and emission slit widths at 5 nm.

LCO (Luminescent Conjugated Oligothiophene) fluorescence

Stock solutions of HS-68, pFTAA and hFTAA were obtained from Dr. Peter Nilsson (Linköping University) through Dr. Lary Walker. LCOs were mixed with Aβ in 10 mM sodium phosphate buffer pH 7.4 in 96-well plates (Corning, Cat. No. 3631) and spectra were acquired with a Biotek Cytation 5 plate reader. Samples were scanned at the bottom

with a 1 nm step size and the gain at 100. Excitation and emission wavelengths are stated in the figure captions, and 9 nm bandwidths were used for both monochromators.

Preparation of the PiB-binding Complex (PBC)

Performed by the LeVine lab at the University of Kentucky, frozen brain powder was added to 20 mM sodium phosphate, pH 7.4, 150 mM NaCl, 2% SDS in a 1:6 w/v ratio. The sample was probe-sonicated 3 times at 25% power and each sonication cycle comprised 10 pulses of half-second sonication and half-second rest, with 3 min on ice between sonication cycles. Centrifugation at 15,000 g for 20 min yielded a supernatant, fluffy white pellet and black hard pellet. The supernatant and fluffy pellet were further centrifuged at 100,000 g, 4°C for 1hr and the resulting pellet was collected as the PiB Binding Complex [34].

Immunogold labeling

The PBC fraction obtained from Harry LeVine was labeled with gold nanoparticles following a published protocol [48]. Briefly, a drop of the PBC was adsorbed on a TEM grid before it was rinsed with PBS containing 50 mM glycine and 1% BSA. The grid was then incubated with a solution of 4G8 antibody before with was rinsed thrice over three separate drops of PBS + 1% BSA. The secondary antibody-conjugated 10 nm gold nanoparticle solution was incubated on the grid for an hour before it was rinsed three times with PBS + 1% BSA, another three times with water and then stained with uranyl acetate.

References

1. Sachse C, Fandrich M, Grigorieff N: **Paired beta-sheet structure of an Abeta(1-40) amyloid fibril revealed by electron microscopy**. *Proc Natl Acad Sci U S A* 2008, **105**:7462-7466.

2. Schmidt M, Sachse C, Richter W, Xu C, Fändrich M, Grigorieff N: **Comparison of Alzheimer Aβ(1–40) and Aβ(1–42) amyloid fibrils reveals similar protofilament structures**. *Proceedings of the National Academy of Sciences* 2009, **106**:19813-19818.

3. Zhang R, Hu X, Khant H, Ludtke SJ, Chiu W, Schmid MF, Frieden C, Lee JM: **Interprotofilament interactions between Alzheimer's Abeta1-42 peptides in amyloid fibrils revealed by cryoEM**. *Proc Natl Acad Sci U S A* 2009, **106**:4653-4658.

4. Sachse C, Xu C, Wieligmann K, Diekmann S, Grigorieff N, Fändrich M: **Quaternary Structure of a Mature Amyloid Fibril from Alzheimer's Aβ(1-40) Peptide**. *Journal of Molecular Biology* 2006, **362**:347-354.

5. Qiang W, Yau W-M, Luo Y, Mattson MP, Tycko R: **Antiparallel β-sheet architecture in Iowa-mutant β-amyloid fibrils**. *Proceedings of the National Academy of Sciences* 2012, **109**:4443-4448.

6. Xiao Y, Ma B, McElheny D, Parthasarathy S, Long F, Hoshi M, Nussinov R, Ishii Y: **Aβ(1-42) fibril structure illuminates self-recognition and replication of amyloid in Alzheimer's disease**. *Nat Struct Mol Biol* 2015, **22**:499-505.

7. Petkova AT, Ishii Y, Balbach JJ, Antzutkin ON, Leapman RD, Delaglio F, Tycko R: **A structural model for Alzheimer's β-amyloid fibrils based on experimental constraints from solid state NMR**. *Proceedings of the National Academy of Sciences* 2002, **99**:16742-16747.

8. Petkova AT, Leapman RD, Guo Z, Yau W-M, Mattson MP, Tycko R: **Self-Propagating, Molecular-Level Polymorphism in Alzheimer's ß-Amyloid Fibrils**. *Science* 2005, **307**:262-265.

9. Paravastu AK, Leapman RD, Yau W-M, Tycko R: **Molecular structural basis for polymorphism in Alzheimer's β-amyloid fibrils**. *Proceedings of the National Academy of Sciences* 2008, **105**:18349-18354.

10. Gremer L, Schölzel D, Schenk C, Reinartz E, Labahn J, Ravelli RBG, Tusche M, Lopez-Iglesias C, Hoyer W, Heise H, et al.: **Fibril structure of amyloid-β(1-42) by cryoelectron microscopy**. *Science* 2017, **358**:116-119.

11. Meinhardt J, Sachse C, Hortschansky P, Grigorieff N, Fändrich M: **Aβ(1-40) Fibril Polymorphism Implies Diverse Interaction Patterns in Amyloid Fibrils**. *Journal of Molecular Biology* 2009, **386**:869-877.

12. Saborio GP, Permanne B, Soto C: **Sensitive detection of pathological prion protein by cyclic amplification of protein misfolding**. *Nature* 2001, **411**:810-813.

13. Atarashi R, Satoh K, Sano K, Fuse T, Yamaguchi N, Ishibashi D, Matsubara T, Nakagaki T, Yamanaka H, Shirabe S, et al.: **Ultrasensitive human prion detection in cerebrospinal fluid by real-time quaking-induced conversion**. *Nat Med* 2011, **17**:175-178.

14. Bongianni M, Orrù C, Groveman BR, et al.: **Diagnosis of human prion disease using real-time quaking-induced conversion testing of olfactory mucosa and cerebrospinal fluid samples**. *JAMA Neurology* 2016, **74**:155-162.

15. Paravastu AK, Qahwash I, Leapman RD, Meredith SC, Tycko R: **Seeded growth of β-amyloid fibrils from Alzheimer's brain-derived fibrils produces a distinct fibril structure**. *Proceedings of the National Academy of Sciences* 2009, **106**:7443-7448.

16. Lu J-X, Qiang W, Yau W-M, Schwieters Charles D, Meredith Stephen C, Tycko R: **Molecular Structure of β-Amyloid Fibrils in Alzheimer's Disease Brain Tissue**. *Cell* 2013, **154**:1257-1268.

17. Watts JC, Condello C, Stohr J, Oehler A, Lee J, DeArmond SJ, Lannfelt L, Ingelsson M, Giles K, Prusiner SB: **Serial propagation of distinct strains of Abeta prions from Alzheimer's disease patients**. *Proc Natl Acad Sci U S A* 2014, **111**:10323-10328.

18. Stöhr J, Watts JC, Mensinger ZL, Oehler A, Grillo SK, DeArmond SJ, Prusiner SB, Giles K: **Purified and synthetic Alzheimer's amyloid beta (Aβ) prions**. *Proceedings of the National Academy of Sciences* 2012, **109**:11025-11030.

19. Rosen RF, Fritz JJ, Dooyema J, Cintron AF, Hamaguchi T, Lah JJ, LeVine H, 3rd, Jucker M, Walker LC: **Exogenous seeding of cerebral beta-amyloid deposition in βAPP-transgenic rats**. *J Neurochem* 2012, **120**:660-666.

20. Eisele YS, Obermüller U, Heilbronner G, Baumann F, Kaeser SA, Wolburg H, Walker LC, Staufenbiel M, Heikenwalder M, Jucker M: **Peripherally Applied Aβ-Containing Inoculates Induce Cerebral β-Amyloidosis**. *Science* 2010, **330**:980-982.

21. Scot D. Styren, Hamilton RL, Styren GC, Klunk WE: **X-34, A Fluorescent Derivative of Congo Red: A Novel Histochemical Stain for Alzheimer's Disease Pathology**. *Journal of Histochemistry & Cytochemistry* 2000, **48**:1223-1232.

22. Åslund A, Sigurdson CJ, Klingstedt T, Grathwohl S, Bolmont T, Dickstein DL, Glimsdal E, Prokop S, Lindgren M, Konradsson P, et al.: **Novel Pentameric Thiophene Derivatives for in Vitro and in Vivo Optical Imaging of a Plethora of Protein Aggregates in Cerebral Amyloidoses**. *ACS Chemical Biology* 2009, **4**:673-684.

23. Scherpelz KP, Lu JX, Tycko R, Meredith SC: **Preparation of Amyloid Fibrils Seeded from Brain and Meninges**. *Methods Mol Biol* 2016, **1345**:299-312.

24. Wenborn A, Terry C, Gros N, Joiner S, D'Castro L, Panico S, Sells J, Cronier S, Linehan JM, Brandner S, et al.: **A novel and rapid method for obtaining high titre intact prion strains from mammalian brain**. *Scientific Reports* 2015, **5**:10062.

25. Fritschi SK, Cintron A, Ye L, Mahler J, Buhler A, Baumann F, Neumann M, Nilsson KP, Hammarstrom P, Walker LC, et al.: **Abeta seeds resist inactivation by formaldehyde**. *Acta Neuropathol* 2014, **128**:477-484.

26. Eisele YS, Bolmont T, Heikenwalder M, Langer F, Jacobson LH, Yan Z-X, Roth K, Aguzzi A, Staufenbiel M, Walker LC, et al.: **Induction of cerebral β-amyloidosis: Intracerebral versus systemic Aβ inoculation**. *Proceedings of the National Academy of Sciences* 2009, **106**:12926-12931.

27. Meyer-Luehmann M, Coomaraswamy J, Bolmont T, Kaeser S, Schaefer C, Kilger E, Neuenschwander A, Abramowski D, Frey P, Jaton AL, et al.: **Exogenous induction of cerebral beta-amyloidogenesis is governed by agent and host**. *Science* 2006, **313**:1781-1784.

28. Langer F, Eisele YS, Fritschi SK, Staufenbiel M, Walker LC, Jucker M: **Soluble Aβ Seeds Are Potent Inducers of Cerebral β-Amyloid Deposition**. *The Journal of Neuroscience* 2011, **31**:14488-14495.

29. Fritschi SK, Langer F, Kaeser SA, Maia LF, Portelius E, Pinotsi D, Kaminski CF, Winkler DT, Maetzler W, Keyvani K, et al.: **Highly potent soluble amyloid-β seeds in human Alzheimer brain but not cerebrospinal fluid**. *Brain* 2014, **137**:2909-2915.

30. Gerson JE, Sengupta U, Lasagna-Reeves CA, Guerrero-Muñoz MJ, Troncoso J, Kayed R: **Characterization of tau oligomeric seeds in progressive supranuclear palsy**. *Acta Neuropathologica Communications* 2014, **2**:73.

31. Bäck M, Appelqvist H, LeVine H, Nilsson KPR: **Anionic Oligothiophenes Compete for Binding of X-34 but not PIB to Recombinant Aβ Amyloid Fibrils and Alzheimer's Disease Brain-Derived Aβ**. *Chemistry – A European Journal* 2016, **22**:18335-18338.

32. Qiang W, Yau WM, Lu JX, Collinge J, Tycko R: **Structural variation in amyloid-beta fibrils from Alzheimer's disease clinical subtypes**. *Nature* 2017, **541**:217-221.

33. Thal DR, Rüb U, Orantes M, Braak H: **Phases of Aβ-deposition in the human brain and its relevance for the development of AD**. *Neurology* 2002, **58**:1791-1800.

34. Matveev SV, Spielmann HP, Metts BM, Chen J, Onono F, Zhu H, Scheff SW, Walker LC, LeVine H, 3rd: **A distinct subfraction of Abeta is responsible for the high-affinity Pittsburgh compound B-binding site in Alzheimer's disease brain**. *J Neurochem* 2014, **131**:356-368.

35. Stewart KL, Radford SE: **Amyloid plaques beyond Abeta: a survey of the diverse modulators of amyloid aggregation**. *Biophys Rev* 2017, **9**:405-419.

36. Rha AK, Das D, Mehta AK, Taran O, Ke Y, Lynn DG: **Amyloid/RNA Co-assembly and the Transition to Informational Biopolymer Mutualism**. *In preparation* 2018.

37. Gunderson WA, Hernández-Guzmán J, Karr JW, Sun L, Szalai VA, Warncke K: **Local Structure and Global Patterning of Cu^{2+} Binding in Fibrillar Amyloid-β [Aβ(1–40)] Protein**. *Journal of the American Chemical Society* 2012, **134**:18330-18337.

38. Karr JW, Kaupp LJ, Szalai VA: **Amyloid-β Binds Cu^{2+} in a Mononuclear Metal Ion Binding Site**. *Journal of the American Chemical Society* 2004, **126**:13534-13538.

39. Bin Y, Li X, He Y, Chen S, Xiang J: **Amyloid-β peptide (1–42) aggregation induced by copper ions under acidic conditions**. *Acta Biochimica et Biophysica Sinica* 2013, **45**:570-577.

40. Mold M, Ouro-Gnao L, Wieckowski BM, Exley C: **Copper prevents amyloid-β(1–42) from forming amyloid fibrils under near-physiological conditions in vitro**. *Scientific Reports* 2013, **3**:1256.

41. Smith DP, Ciccotosto GD, Tew DJ, Fodero-Tavoletti MT, Johanssen T, Masters CL, Barnham KJ, Cappai R: **Concentration Dependent Cu^{2+} Induced Aggregation and Dityrosine Formation of the Alzheimer's Disease Amyloid-β Peptide**. *Biochemistry* 2007, **46**:2881-2891.

42. Tõugu V, Karafin A, Zovo K, Chung RS, Howells C, West AK, Palumaa P: **Zn(II)- and Cu(II)-induced non-fibrillar aggregates of amyloid-β (1–42) peptide are transformed to amyloid fibrils, both spontaneously and under the influence of metal chelators**. *Journal of Neurochemistry* 2009, **110**:1784-1795.

43. Matlack KES, Tardiff DF, Narayan P, Hamamichi S, Caldwell KA, Caldwell GA, Lindquist S: **Clioquinol promotes the degradation of metal-dependent amyloid-β (Aβ) oligomers to restore endocytosis and ameliorate Aβ toxicity**. *Proceedings of the National Academy of Sciences* 2014, 10.1073/pnas.1402228111.

44. House E, Mold M, Collingwood J, Baldwin A, Goodwin S, Exley C: **Copper abolishes the beta-sheet secondary structure of preformed amyloid fibrils of amyloid-beta(42)**. *Journal of Alzheimer's disease : JAD* 2009, **18**:811-817.

45. Yamin G, Teplow DB: **Pittsburgh Compound-B (PiB) binds amyloid β-protein protofibrils**. *Journal of Neurochemistry* 2017, **140**:210-215.

46. Cohen SIA, Linse S, Luheshi LM, Hellstrand E, White DA, Rajah L, Otzen DE, Vendruscolo M, Dobson CM, Knowles TPJ: **Proliferation of amyloid-β42 aggregates occurs through a secondary nucleation mechanism**. *Proceedings of the National Academy of Sciences* 2013, **110**:9758-9763.

47. Trigg Ben J, Lee Chiu F, Vaux David J, Jean L: **The air–water interface determines the outcome of seeding during amyloidogenesis**. *Biochemical Journal* 2013, **456**:67-80.

48. Maunsbach AB: **Immunolabeling and Staining of Ultrathin Sections in Biological Electron Microscopy.** In *Cell Biology: A Laboratory Handbook*, edn 2. Edited by; 1998:268-276. vol 3.]

Chapter 5. Amyloid β and Tau Interactions

Introduction

Since tauopathy follows amyloidosis in AD progression, understanding the mechanistic link between these events will provide valuable insight into AD pathology. Although Aβ plaques are generally extracellular and NFTs are mostly intracellular, tau has been detected in the ISF (interstitial fluid) and CSF of both wild type and tau transgenic mice [1] and CSF tau is one of the biomarker used for AD. The extracellular release of tau is thought to occur by a combination of mechanisms such as synaptic transfer, exocytosis and membrane leakiness [2-4], which could be the same mechanisms underlying the spread of tau aggregates throughout the brain via synaptically connected neural networks. Conversely, neuronal cell culture studies have shown that exogenous Aβ can be endocytosed and accumulated intracellularly [5], suggesting that Aβ from amyloid plaques could be internalized by neurons. It is therefore, very likely that Aβ and tau exists in both the intracellular and extracellular compartments *in vivo*.

In tauopathies such as frontotemporal dementia with parkinsonism, there are widespread NFTs of aggregated tau without amyloid plaques [6,7], suggesting that severe tauopathy is still insufficient to induce Aβ plaque formation. Furthermore, in mouse neuronal cell cultures expressing mouse or human tau, the addition of fibrillar Aβ40 resulted in neural degeneration while tau-depleted neurons showed no signs of degeneration in the presence of fibrillar Aβ40 [8]. Therefore, a unidirectional relationship of Aβ inducing tau deposition, rather than the reverse, is likely to be the case in AD.

Some possible mechanisms of Aβ-induced tangle formation include dysregulation of kinases and phosphatases, calcium homeostasis, inflammatory responses and oxidative stress. However, an indirect three-component system increases the number of variables to test and control for, therefore we opted to test the direct interactions between Aβ and tau peptides. Our goal here was to understand how different Aβ assemblies affected the aggregation of tau (cross-seeding), and we began with the Aβ and tau nucleating core sequences as model peptides to reduce complexity. Although tau has two nucleating cores, we focused on the PHF6 sequence because (1) it is present in all isoforms of tau whereas PHF6* is only present in 4R tau and (2) it has been shown to be essential for fibrillization, while deletion of the PHF6* sequence alone does not suppress fibril formation [9].

Results

5.1 Cross seeding of PHF6 by Aβ(16-22) E22Q and E22L variants

The Iowa mutation, APP D694N (Aβ D23N), is associated with early onset AD and cerebral amyloid angiopathy (CAA), with senile plaques containing a higher Aβ40/Aβ42 ratio than in wt AD [10]. *In vitro* studies of synthetic Aβ40 D23N showed that it aggregates faster than Aβ40 and approximately two-thirds of the fibrils have peptides oriented in the anti-parallel conformation [11]. We therefore wanted to determine if the peptide orientation of Aβ affects the aggregation and/or structure of tau fibrils. Using Aβ(16-22) E22Q fibers in which the peptides are in a parallel orientation and Aβ(16-22) E22L nanotubes which have an anti-parallel peptide orientation as model seeds, monomeric PHF6 peptides were added to the sonicated seeds and incubated. Additionally, one control sample containing PHF6 seeds was used as the benchmark for maximum seeding efficiency, while another sample containing no seeds was used as the negative control for no seeding effect.

After 1 day of cross-seeding, fibrils were observed in TEMs of all samples. However, the E22L-seeded and unseeded PHF6 had a large proportion of particles (**Figure 5.1B** and **D**) while the E22Q- and PHF6-seeded PHF6 assemblies had very few particles (**Figure 5.1A** and **C**). Since particle formation normally precedes fibril formation, these observations suggest that E22Q favors PHF6 fibrillization through elongation, while there are no interactions between E22L seeds and PHF6 or that E22L promotes secondary nucleation of PHF6. After 2 weeks, two types of fibrils were observed by TEM: straight fibrils that were aligned with each other and twisted fibrils that were randomly aligned (**Figure 5.2**). Interestingly, only randomly aligned fibrils were found on the E22L-seeded PHF6 grid (**Figure 5.2B**), suggesting that there is some interaction between E22L and PHF6 which favors the formation of one conformation of fibrils over another. However, it was difficult to further evaluate structural differences since there are no PHF6-specific ligands or antibodies currently available.

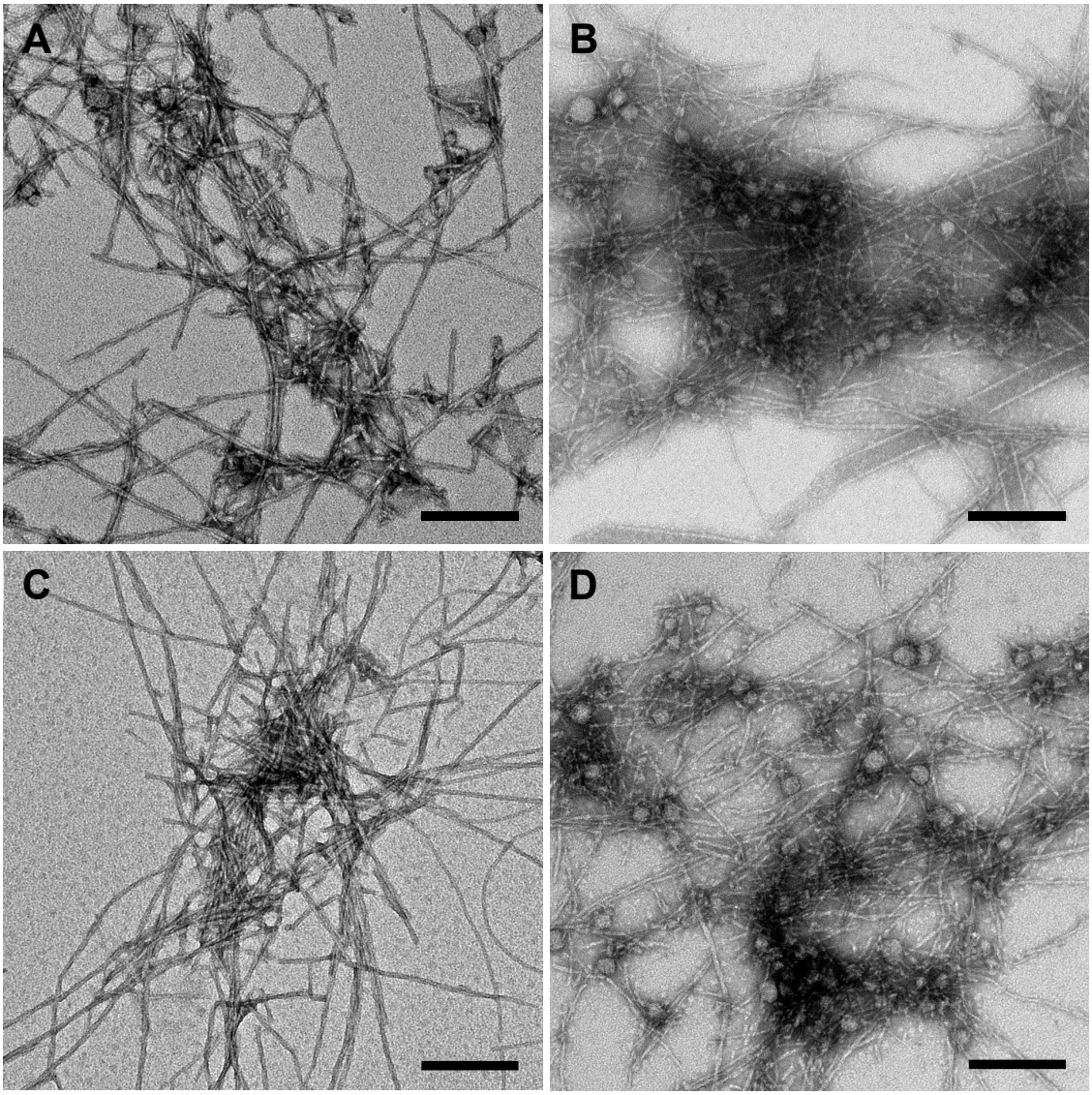

Figure 5.1. One-day morphologies of PHF6 assemblies are influenced by the seed used. PHF6 seeded by (A) E22Q, (B) E22L, (C) PHF6 and (D) unseeded PHF6 after 1 day, assembled at 1 mM in 20% MeCN, pH 2 with 10% seed. Scale bars: 200 nm.

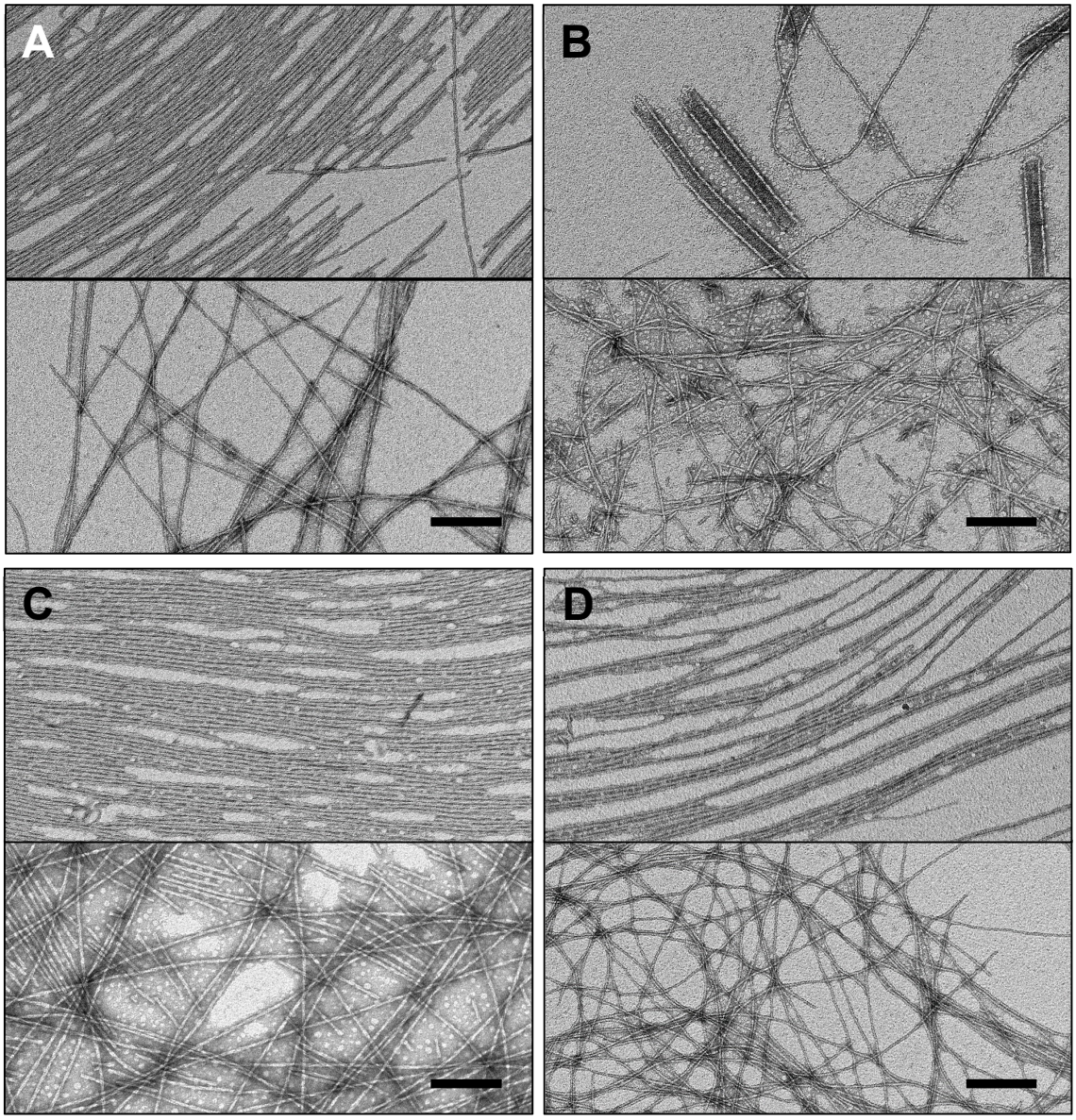

Figure 5.2. E22L does not seed heterogeneous PHF6 fibril formation. PHF6 seeded by (A) E22Q, (B) E22L, (C) PHF6 and (D) unseeded PHF6 after 2 weeks, assembled at 1 mM in 20% MeCN, pH 2 with 10% seed. Two images of each TEM grid are shown here, representing the two types of fibrils that can be found on different regions of a grid. All images are at the same magnification; scale bars: 200 nm.

To gain more structural insight into the peptide orientation of the PHF6 fibrils, we synthesized PHF6 where an isotope enriched $^{13}C{=}O$ is present before the second Val, Ac-VQI[1-^{13}C]VYK-NH_2 (hereafter referred to as ^{13}C-PHF6), for isotope-edited IR (IE-IR) experiments. However, attempts to reproduce the results above were unsuccessful, with all

assemblies showing large deposits of fibrils and very few particles within a day. This indicated that there was rapid assembly and the peptide concentration should be decreased below the current 1 mM to observe any seeding effect. PHF6 was then assembled at 0.2, 0.5 and 0.7 mM to get an idea of the assembly rates at those concentrations, where there was still rapid assembly at 0.7 mM and incomplete assembly after two weeks at 0.2 mM. The 0.5 mM sample appeared to have an intermediate assembly rate and this concentration was chosen for seeding of ^{13}C-PHF6.

The one-day ^{13}C-PHF6 seeded assemblies resembled the observations for PHF6 seeding in that numerous particles were observed for E22L-seeded and unseeded ^{13}C-PHF6, while few particles were observed in E22Q- and PHF6-seeded ^{13}C-PHF6 (**Figure 5.3**). This trend is observed for up to two weeks post seeding. After four weeks, fibrils were observed in all samples, with the PHF6-seeded sample displaying the most fibrils while the unseeded sample had the lowest number of fibrils. The E22L-seeded ^{13}C-PHF6 had a large population of particles and it is unclear why there is incomplete fibrillization, but this suggests that E22Q cross-seeds PHF6 more efficiently than E22L (**Figure 5.4**).

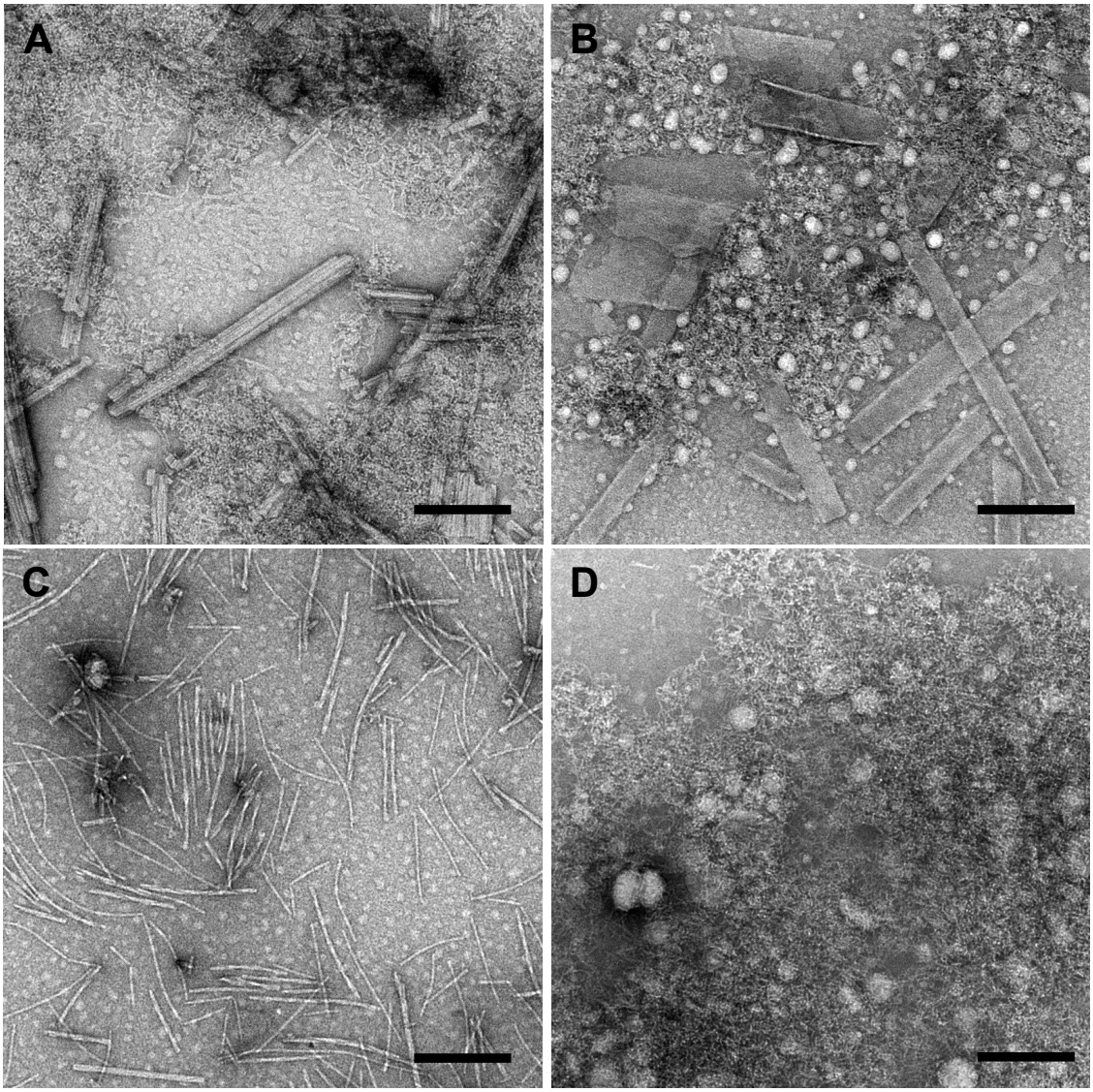

Figure 5.3. One-day morphologies of ^{13}C-PHF6 assemblies are similar to unenriched PHF6 assemblies. PHF6 seeded by (A) E22Q, (B) E22L, (C) PHF6 and (D) unseeded PHF6 after 1 day, assembled at 0.5 mM in 20% MeCN, pH 2 with 20% seed. Scale bars: 200 nm.

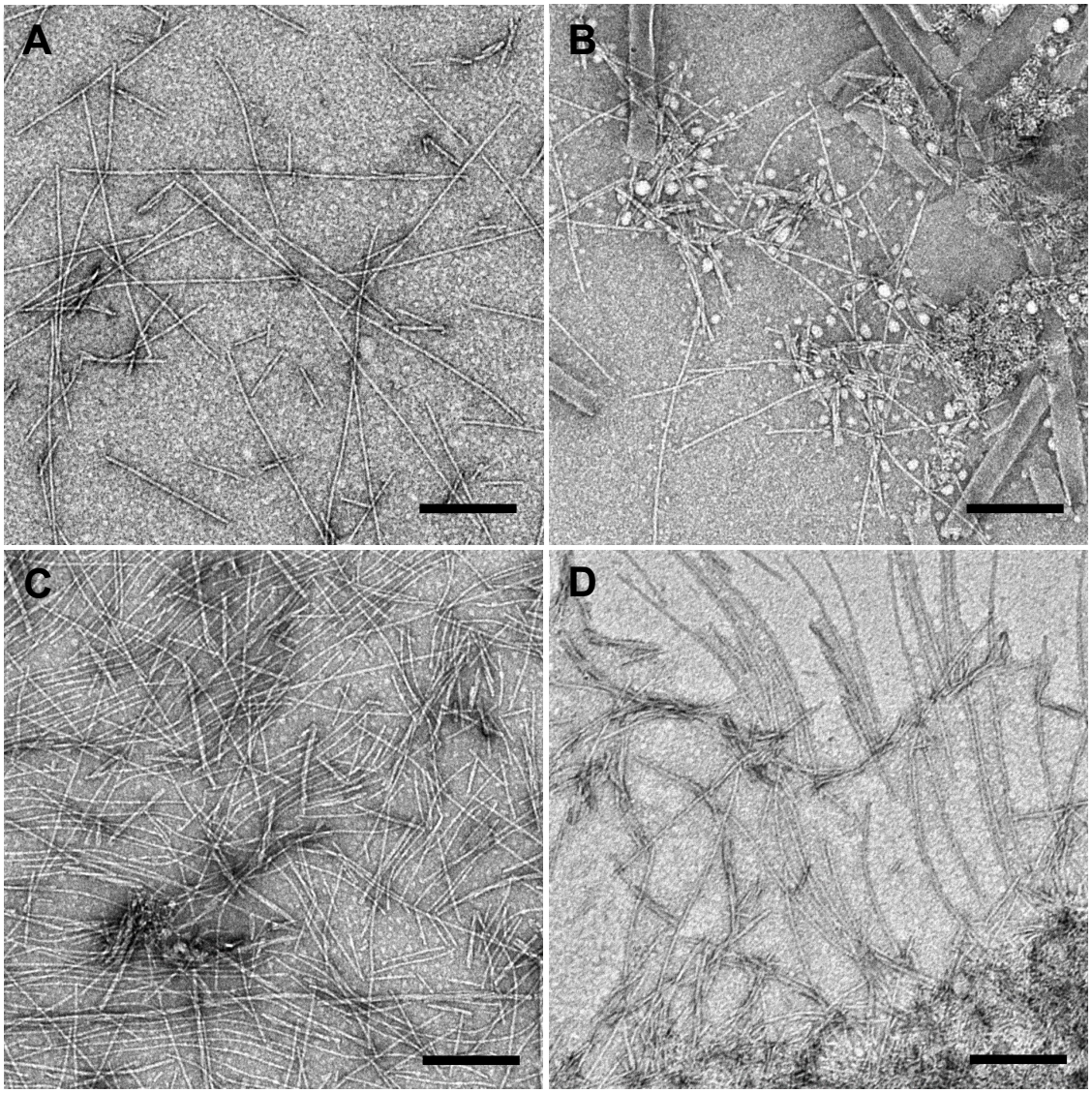

Figure 5.4. 4-week ^{13}C-PHF6 assemblies are mostly fibrillary except when seeded by E22L. PHF6 seeded by (A) E22Q, (B) E22L, (C) PHF6 and (D) unseeded PHF6 after four weeks, assembled at 0.5 mM in 20% MeCN, pH 2 with 20% seed. Scale bars: 200 nm.

The IE-IR spectra of these assemblies showed minimal changes for each sample over the 4-week period (**Figure 5.5**). We noticed that the ^{12}C/^{12}C amide I stretch was centered at 1626 cm^{-1} for the E22L-seeded sample whereas it was at 1630 cm^{-1} for the other samples, possibly due to the peptides in the particles having a different hydrogen bonding

network between the backbones and thus secondary structure, compared to the fibrils and nanotubes. Peptides with an anti-parallel arrangement typically show a peak at 1695 cm^{-1}, but this is unidentifiable here due to noisy spectra and the broad transitions centered around 1680 cm^{-1} that can be assigned to unassembled peptides. The ^{13}C vibrations are centered at 1593 ± 1 cm^{-1}, although the peak height was noticeably lower for the E22L-seeded peptide. Again, this band could be due to a population of peptides existing in a different conformation or environment.

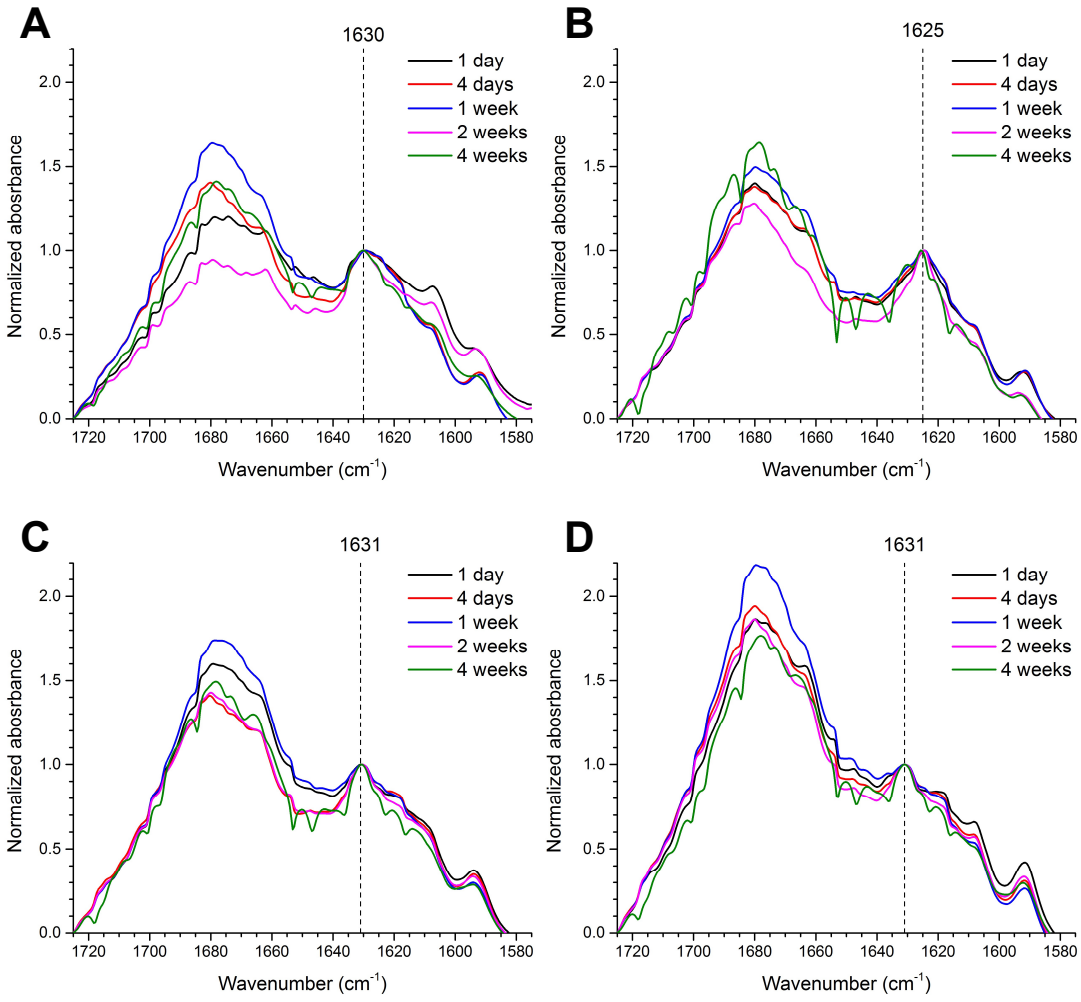

Figure 5.5. IE-IR spectra of ^{13}C-PHF6 seeded assemblies showed minimal changes over 4 weeks. Samples of the ^{13}C-PHF6 assemblies seeded by E22Q (A), E22L (B), PHF6

(C) and unseeded ^{13}C-PHF6 (D) were analyzed by IR and normalized to the ^{12}C amide I peak.

We also observed that the E22Q and E22L seeds remained short and did not disassemble nor elongate over the four weeks. To determine what effect the PHF6 monomers had on the Aβ seeds, 100 μM of E22Q fibers and E22L tubes were sonicated and left to incubate in the absence of PHF6 (**Figure 5.6A** and **C**). After four weeks, long fibers and tubes were observed in the E22Q and E22L samples respectively (**Figure 5.6B** and **D**), indicating that they can elongate in the absence of the PHF6 peptide. This also strongly suggests that in the cross-seeded PHF6 samples, the PHF6 peptides bind to the ends of the E22Q fiber and E22L nanotube seeds, capping their extension. However, no PHF6 fibrils were seen extending from the ends of E22Q or E22L, suggesting that the binding was not stable enough or in a favorable conformation for PHF6 monomers to nucleate or propagate from those seeds.

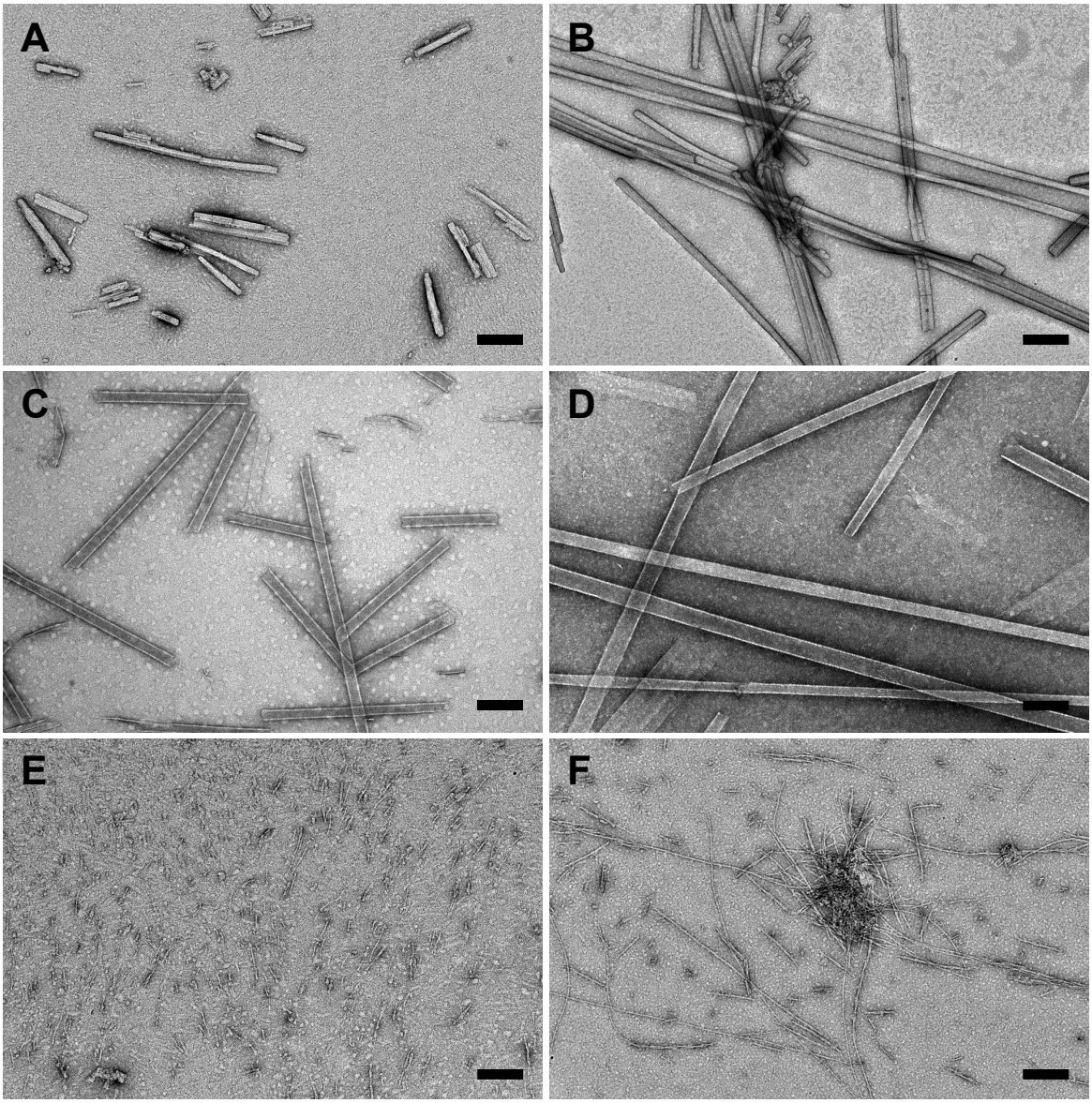

Figure 5.6. E22Q, E22L and PHF6 seeds can elongate in the absence of PHF6 monomers. 100 μM E22Q (A), E22L (C) and PHF6 (E) seeds were obtained by sonicating the mature assemblies. The seeds were then incubated for 4 weeks and imaged (B, D and F). Scale bars: 200 nm

Congo red (CR) absorbance binding assay

While ThT fluorescence is commonly used to quantify amyloid formation, we discovered that PHF6 fibrils assembled in 40% MeCN at pH 2 do not increase the fluorescence of ThT, possibly due to electrostatic repulsions between the exposed lysine of PHF6 and the positively-charged ThT molecules. Therefore, we turned to CR absorbance as a method for quantifying amyloid formation where a red-shift and increase in absorbance is observed upon binding to amyloid. Although it is possible to distinguish differences in CR spectra, it is difficult to quantify the relative differences between spectra, necessitating a standard curve to quantify binding. CR was therefore incubated with varying amounts of PHF6 (initially assembled at 1 mM) for at least 15 min before spectral measurement in a 1 cm pathlength quartz cuvette. Each 100 µl CR-PHF6 mixture contained 5 µM CR and 0-300 µM PHF6 in PBS, pH 7.4. To correct for the increase in absorbance due to light scattering by the peptide fibrils, absorbance spectra of the PHF6 peptides without CR were measured at the corresponding peptide concentrations, and subtracted from the CR-PHF6 spectra to obtain corrected spectra (**Figure 5.7**) in order to more accurately reflect the spectral changes of CR binding to amyloid.

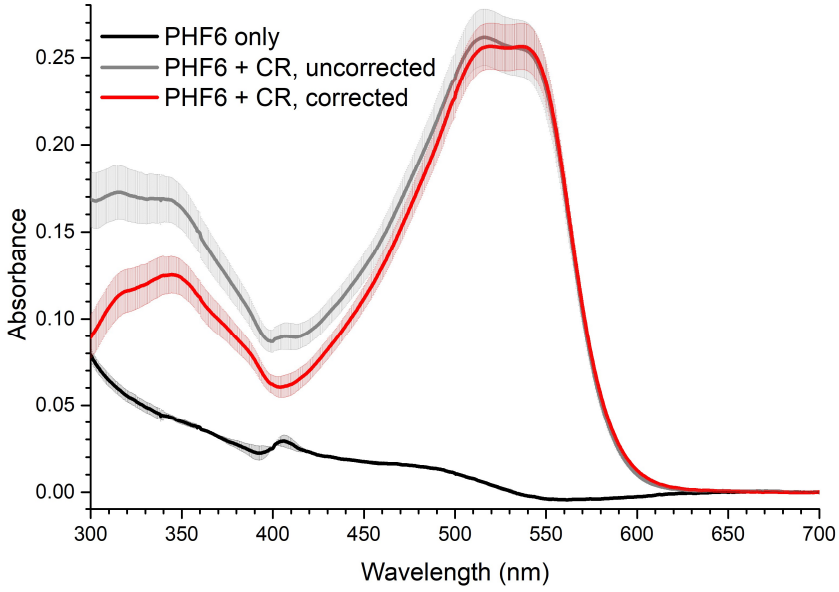

Figure 5.7. Spectral correction for binding of 5 μM CR to 300 μM PHF6. Each curve is the average of three replicates bordered by the standard deviation.

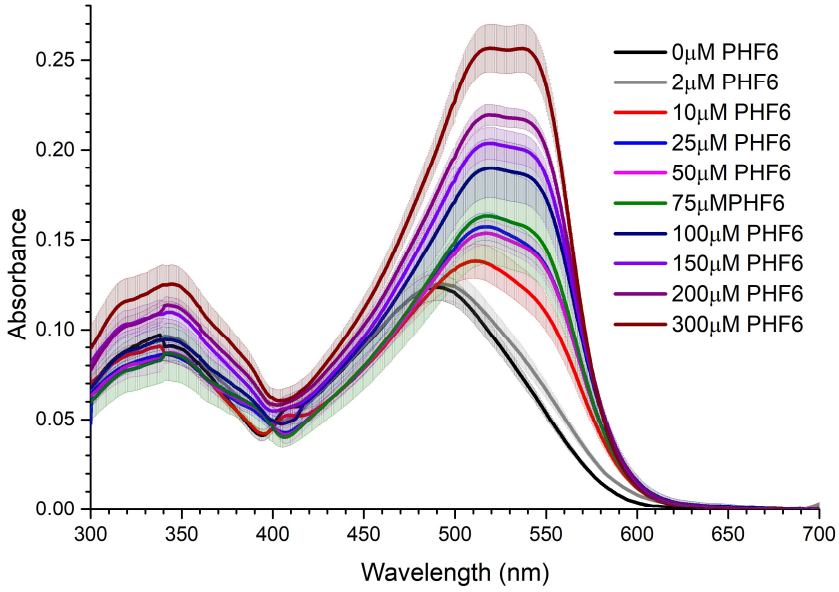

Figure 5.8. Corrected spectra of 5 μM CR bound to 0-300 μM PHF6 in PBS.

As the peptide concentration was increased from 0 to 300 μM, there was a red-shift and increase in absorbance of CR as expected. The isosbestic point, where both bound and unbound CR have the same absorbance, appears at 400 nm. However, the isosbestic point

appears to deviate from normality at PHF6 concentrations above 100 μM, where the absorbance at 400 nm increases. The spectral change can also be visualized by the difference spectra, which is the difference between the CR+PHF6 and CR alone spectra (**Figure 5.9**). With 300 μM PHF6, the point of maximal spectral difference occurs at 544 nm, which is an important parameter in estimating the amount of bound CR.

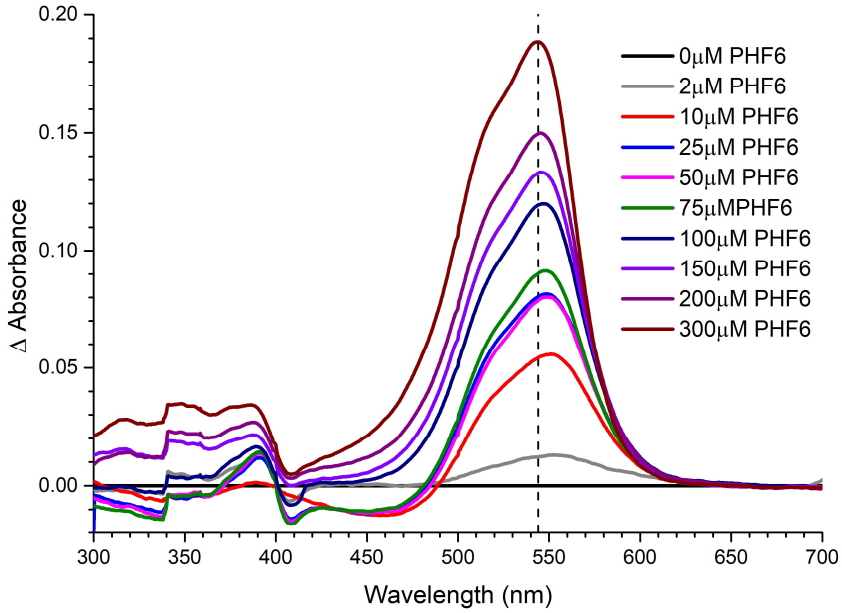

Figure 5.9. Difference spectra of 5 μM CR bound to 0-300 μM PHF6 in PBS.

Assuming that there is 0% CR binding with 0 μM PHF6 and 100% binding with 300 μM PHF6, the molar extinction coefficients (ε) of bound and unbound CR at the isosbestic and point of maximal difference can be derived using Beer's law:

Wavelength (nm)	$\varepsilon_{\text{bound CR}}$	$\varepsilon_{\text{unbound CR}}$
544	50 296	12 597
400	12 411	8 987

Plugging in these values into equation [7] of Klunk et. al., an equation for estimating the concentration of CR bound to Aβ (CR-Aβ) can be derived:

$$[\mathrm{CR}-\mathrm{A}\beta] = \frac{\frac{^{544}\mathrm{A}}{12597} - \frac{^{400}\mathrm{A}}{10699}}{\frac{50296}{12597} - 1}$$

$$= \frac{^{\mathbf{544}}\mathbf{A}}{\mathbf{37703}} - \frac{^{\mathbf{400}}\mathbf{A}}{\mathbf{32022}}$$

Plugging in the absorbance values at 400 and 544 nm of the corrected spectra into the equation above yields a binding curve that estimates the bound CR concentration with increasing concentrations of PHF6 fibrils (**Figure 5.10**). However, the binding seems to be increasing at the higher concentrations instead of reaching a plateau, suggesting that the binding sites in the fibrils are being altered as the sample becomes more concentrated. One possible explanation could be the bundling of fibers where the charges of the lysine residues are mediated by the phosphates in PBS buffer, and the degree of bundling increases with peptide concentration.

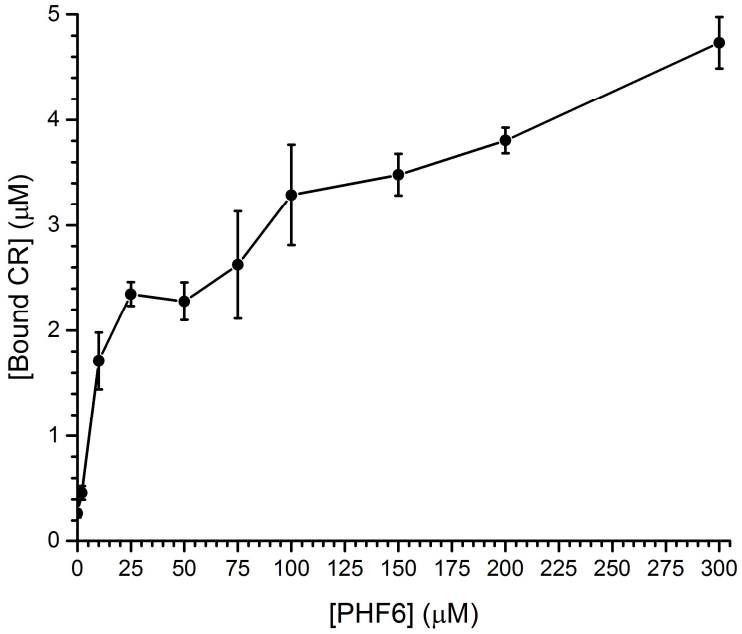

Figure 5.10. Binding isotherm of 5 μM CR with increasing concentrations of PHF6.

TEM images of the PHF6 fibrils diluted in water showed minimal bundling (**Figure 5.11A**), but when diluted into PBS, had noticeable bundling (**Figure 5.11B**) that did not change when CR was present (**Figure 5.11C**). In fact, when PHF6 was assembled in phosphate buffer instead of 20% MeCN, the fibrils showed even greater bundling (**Figure 5.11D**). If a multivalent anion causes PHF6 to bundle, then a buffer without phosphate (e.g. PBS) or sulfate (e.g. MES, MOPS, HEPES, etc.) groups should eliminate the bundling. When PHF6 fibrils were diluted into or assembled in 50 mM tris-HCl pH 7.4 buffer, no bundling of the fibers was seen and interestingly, the twisted and straight filament polymorphs became more obvious (**Figure 5.12**), both of which have been observed for the full-length tau protein fibrils isolated from an AD patient [12].

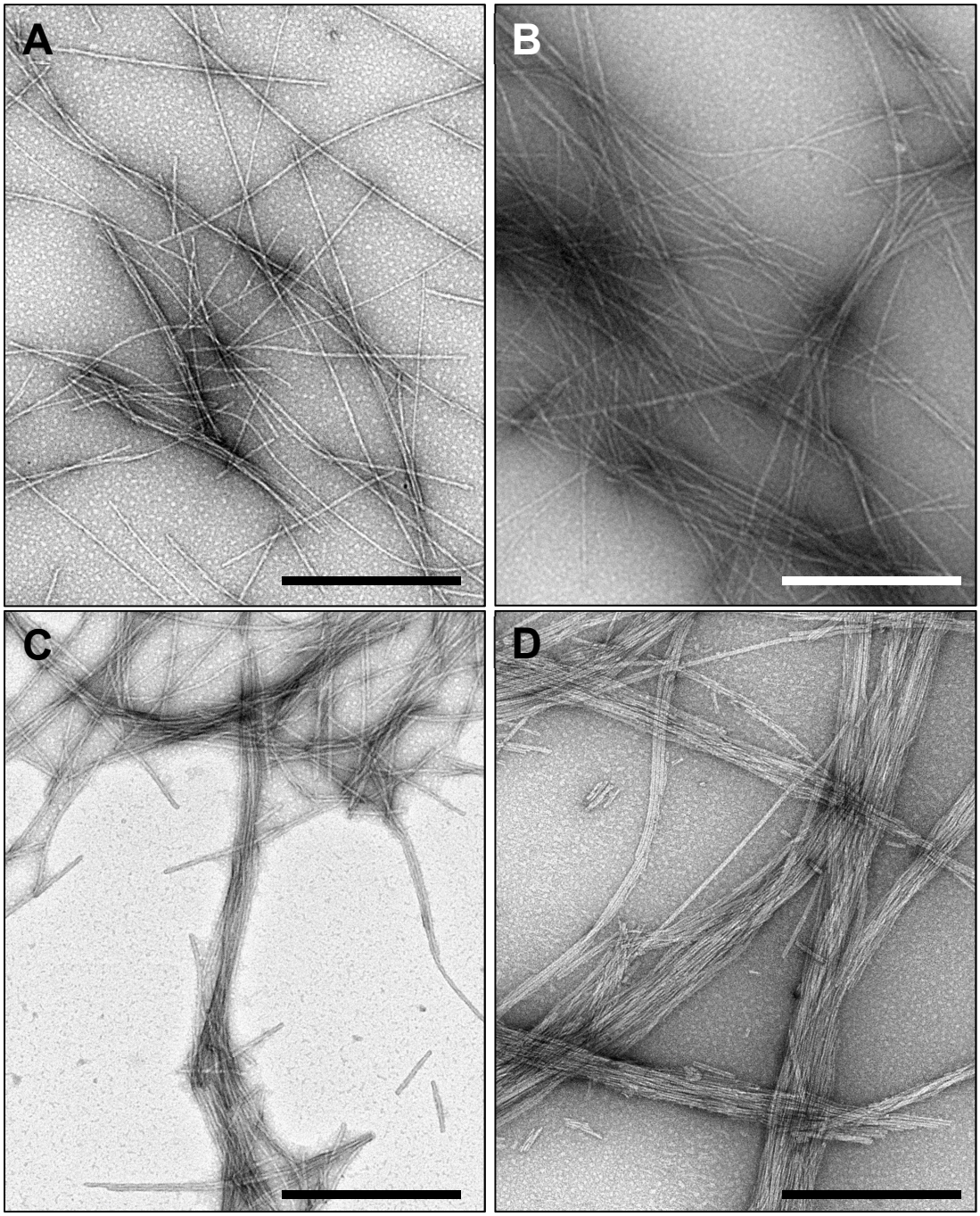

Figure 5.11. PHF6 fibrils bundle in the presence of phosphates. (A) PHF6 assembled at 1 mM in 20% MeCN then diluted with water to 300 μM. (B) PHF6 assembled at 1 mM in 20% MeCN then diluted with PBS to 300 μM. (C) 300 μM PHF6 + 5 μM CR in PBS. (D) PHF6 assembled in 10 mM phosphate buffer. Scale bars: 500 nm.

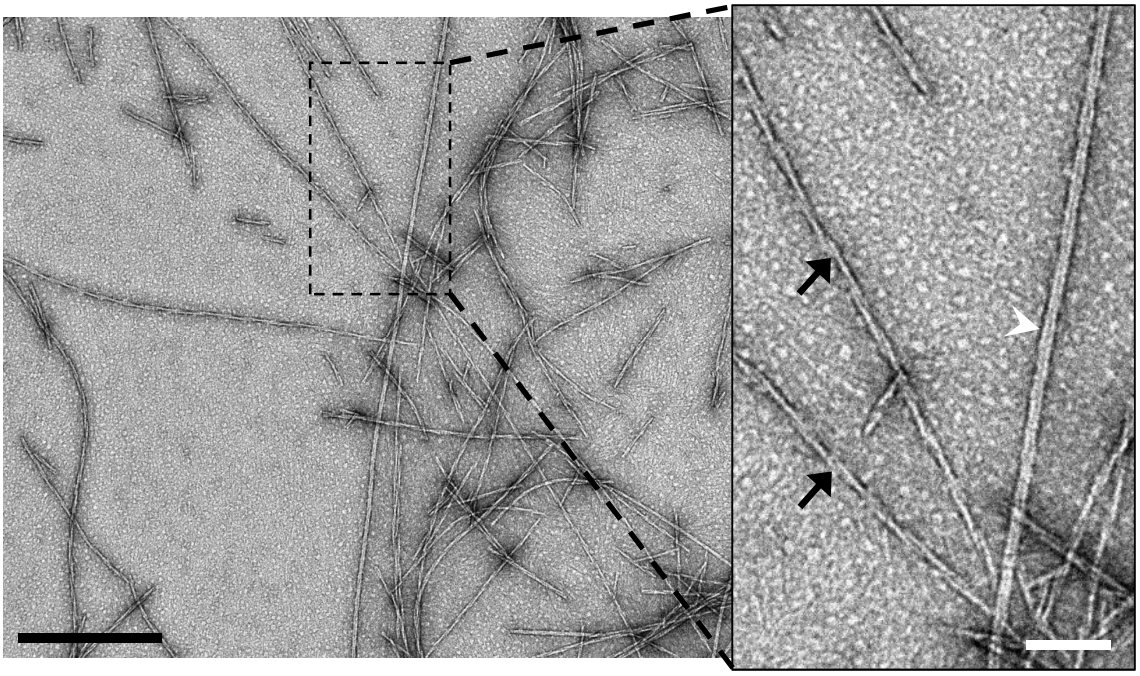

Figure 5.12. PHF6 fibrils do not bundle when assembled in tris buffer. 500 μM PHF6 was incubated in 50 mM tris-HCl pH 7.4 at r.t. and imaged. Black arrows indicate twisted fibrils and the white arrowhead points to a straight fibril. Black scale bar: 500 nm; white scale bar: 100 nm.

The CR binding to PHF6 fibrils were then repeated in tris buffer (**Figure 5.13**), but since the 300 μM PHF6 spectrum had a different profile and baseline, the 200 μM PHF6 spectrum was assumed to have 100% CR binding.

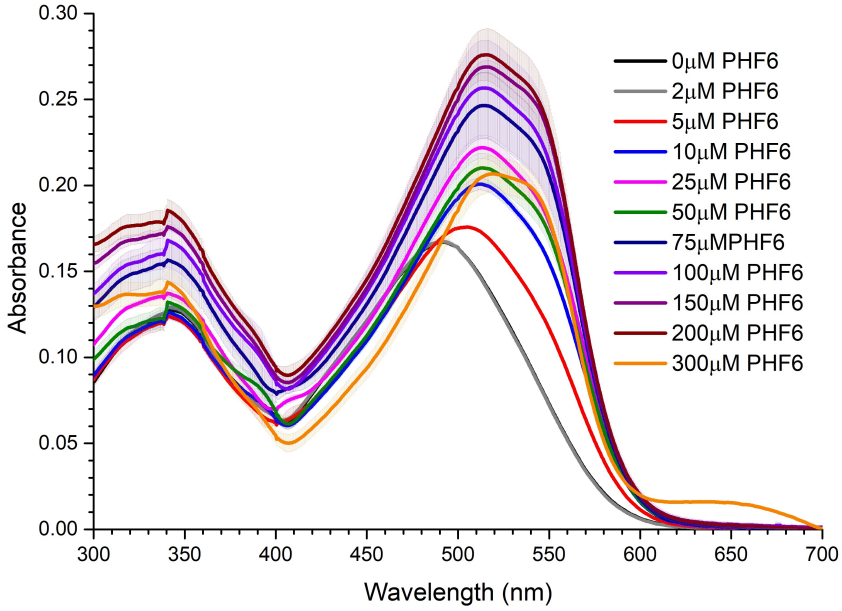

Figure 5.13. Corrected spectra of 5 μM CR bound to 0-300 μM PHF6 in tris buffer.

As described above, the extinction coefficients for bound and unbound CR at the point of maximal difference and isosbestic point can be calculated from the absorbance at those wavelengths:

Wavelength (nm)	$\varepsilon_{\text{bound CR}}$	$\varepsilon_{\text{unbound CR}}$
545	48 396	16 679
403	16 123	12 390

Which yields the following equation:

$$[\text{CR} - \text{A}\beta] = \frac{\frac{^{545}\text{A}}{16679} - \frac{^{403}\text{A}}{14256}}{\frac{48396}{16679} - 1}$$

$$= \frac{^{\mathbf{545}}\mathbf{A}}{\mathbf{31716}} - \frac{^{\mathbf{403}}\mathbf{A}}{\mathbf{27109}}$$

Plugging in the absorbance values into the above equation produces a binding isotherm that plateaus at high concentrations (**Figure 5.14**).

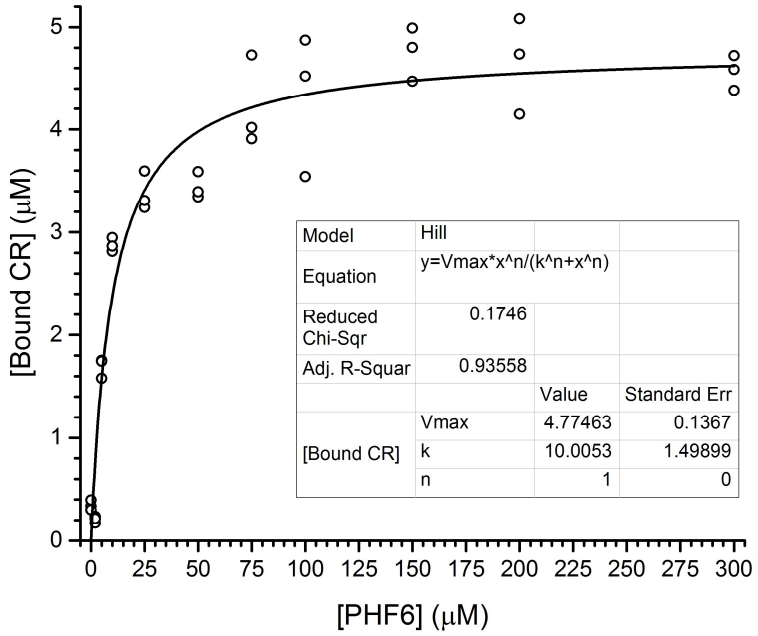

Figure 5.14. Binding isotherm of 5 μM CR to 0-300 μM PHF6 in tris buffer.

We then applied the above equation to 5 μM CR bound to the seeded ^{13}C-PHF6 assemblies to estimate the degree of assembly. **Figure 5.15A** shows that the self-seeded samples had higher CR binding over the unseeded controls throughout 4 weeks, indicating that seeding increases the extent of assembly. The E22L-seeded ^{13}C-PHF6 showed higher CR binding than the E22Q-seeded peptide from 1 day to 2 weeks, but this trend switches for the 4-week assembles. A closer analysis of the data points for the E22Q- and E22L-seeded samples showed that this difference is not significant (*t*-test, p=0.18), and in fact, the difference is only significant for the 1- and 4-day assemblies (**Figure 5.15B**). Since the seeds also contribute to CR binding, we quantified the binding of CR to the parent assemblies at a peptide concentration that is equivalent to the seed concentrations (5 μM). The E22Q fibers were found to bind more CR than the E22L nanotubes (**Figure 5.15C**), and this trend is

similar for the E22Q-seeded ^{13}C-PHF6 binding more CR than the E22L-seeded ^{13}C-PHF6 at 4 weeks, but is reversed for the 1-day to 2-week assemblies.

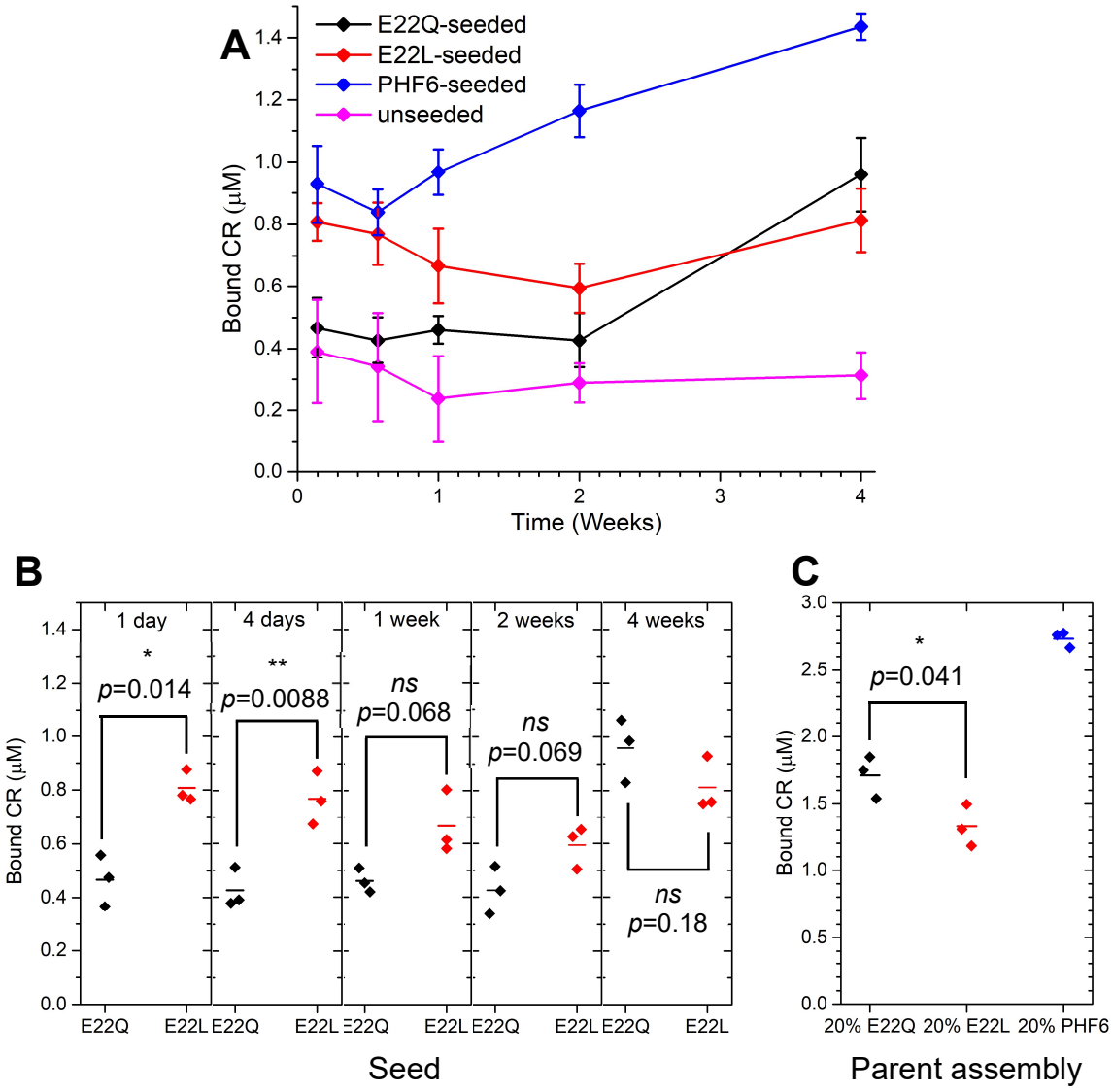

Figure 5.15. Quantification of bound CR concentrations in binding to ^{13}C-PHF6 seeded assemblies. (A) Absorbance spectra of 5 μM CR bound to 25 μM peptide were acquired and the absorbance values at 400 nm (isosbestic point) and 544 nm (point of maximal difference) were used to determine the concentration of CR bound to peptide. (B) Bound CR values of E22Q- and E22L-seeded ^{13}C-PHF6 showing the averages and Student's t-test of the replicates. (C) Bound CR concentrations of 5 μM CR in the presence of 100 μM mature E22Q, E22L and PHF6 assemblies.

5.2 Co-assembly of Aβ40 and 42 with PHF6

Despite the inclusive results from cross-seeding with Aβ(16-22) E22Q and E22L peptides, we moved on to using Aβ40 and Aβ42 which are more physiologically-relevant templates. Sequence alignments of Aβ40/42 with PHF6 show high similarity between ^{16}KLV^{19}F of Aβ and QIVY of PHF6, and therefore we hypothesized that Aβ and PHF6 may interact by either co-assembling into mixed fibrils and/or nucleating separately via cross-seeding.

We co-assembled 100 μM Aβ40 or 42 monomers with 500 μM PHF6 monomers since the molar mass of Aβ is approximately 5 times that of PHF6. After 6 hours of co-assembly, robust fibril formation was observed for the PHF6-only sample, and the fast kinetics might be because it was far above its critical assembly concentration in buffer (**Figure 5.16E**). TEMs of Aβ40 and Aβ42 alone showed mostly oligomers and protofibrils, indicative of peptides still in lag phase (**Figure 5.16C and D**). The Aβ40-PHF6 co-assembly, however, had a mix of large protofibrils and small particles, suggesting a different nucleation mechanism and peptide assembly taking place (**Figure 5.16A**). Networks of short fibrils were observed for the Aβ42-PHF6 sample (**Figure 5.16B**), which could be interpreted in either of two ways: (i) PHF6 accelerated Aβ42 fibrillization and/or (ii) Aβ42 inhibited PHF6 fibrillization.

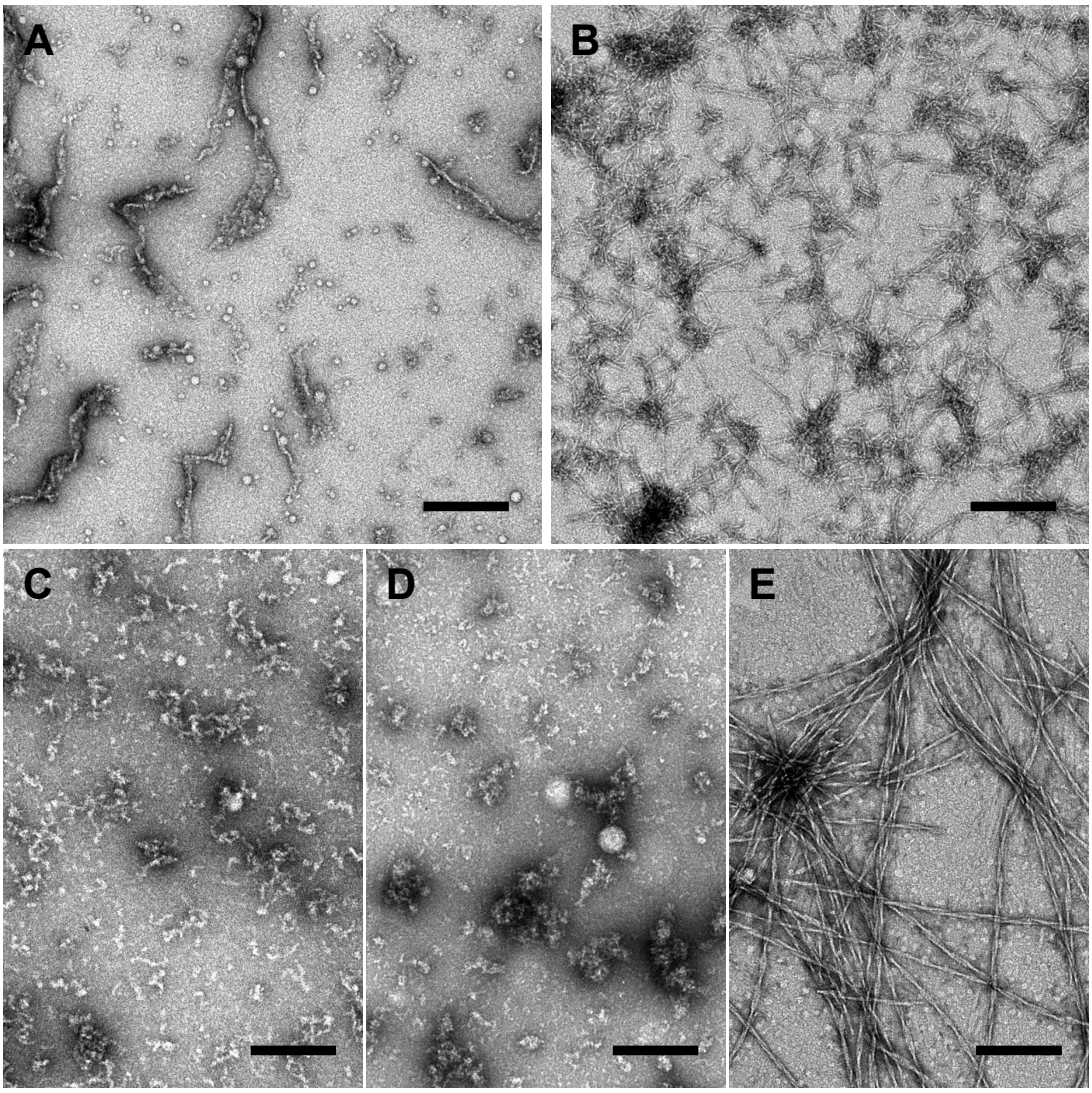

Figure 5.16. 1:5 mol ratio Aβ co-assembly with PHF6 after 6 hours. (A) 100 μM Aβ40 + 500 μM PHF6, (B) 100 μM Aβ42 + 500 μM PHF6, (C) 100 μM Aβ40, (D) 100 μM Aβ42 (E) 500 μM PHF6 in 50 mM Tris buffer, pH 7.4. Scale bars: 200 nm.

At two weeks, mature fibrils were observed in both of the mixed samples and for the PHF6 control while protofibrils were still present in the Aβ-only controls (**Figure 5.17**). Since the fibrils in the mixed samples appear morphologically distinct from PHF6 fibrils, we can conclude that the presence of PHF6 accelerated Aβ assembly.

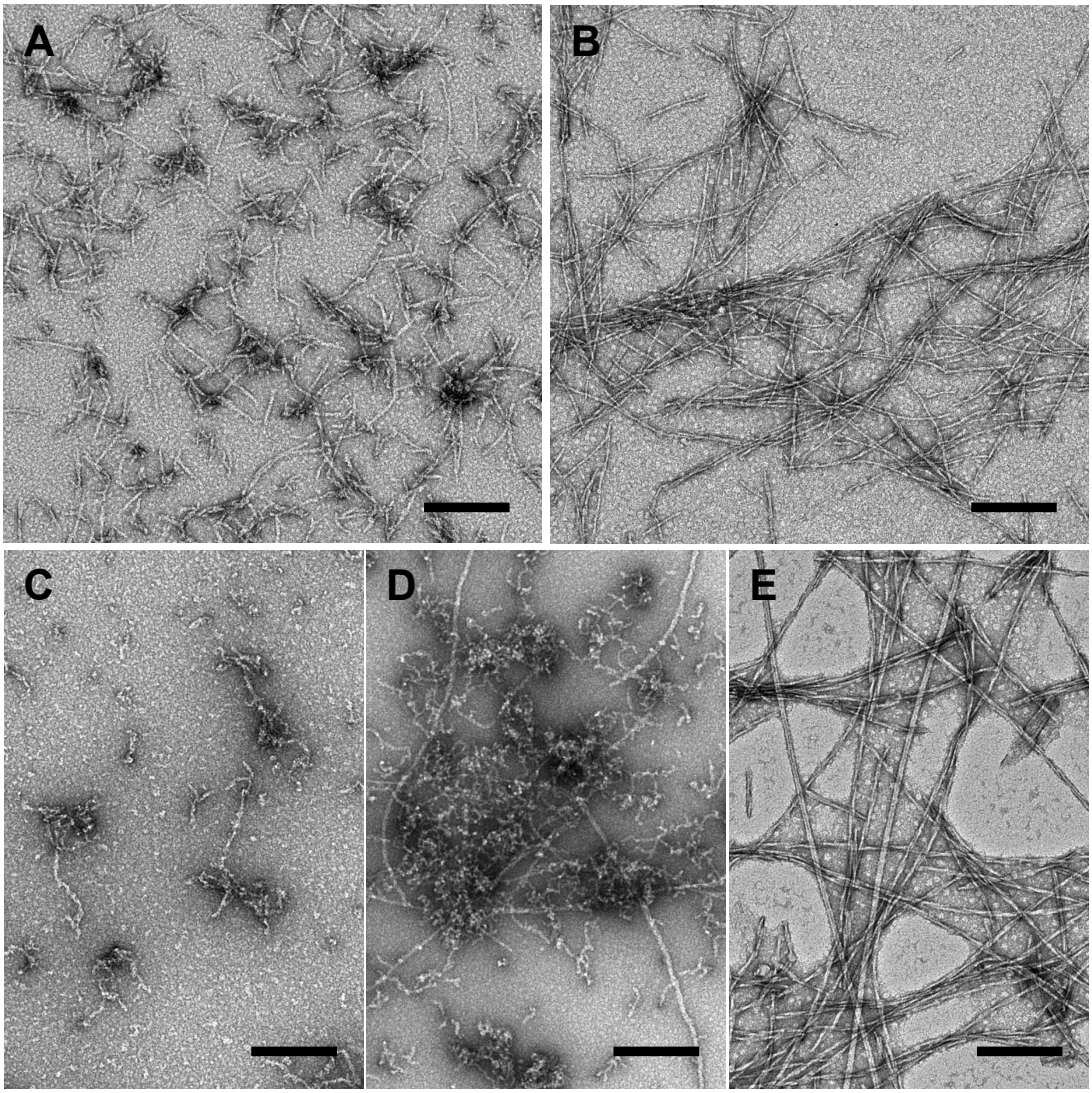

Figure 5.17. 1:5 mol ratio Aβ co-assembly with PHF6 after 2 weeks. (A) 100 μM Aβ40 + 500 μM PHF6, (B) 100 μM Aβ42 + 500 μM PHF6, (C) 100 μM Aβ40 (D) 100 μM Aβ42 (E) 500 μM PHF6 in 50 mM Tris buffer, pH 7.4. Scale bars: 200 nm.

To gain further insight into the Aβ-PHF6 interactions, we modified two variables in the next set of experiments. First, we used pre-assembled Aβ to cross-seed PHF6 monomers to emulate the scenario in AD progression. Second, we lowered the PHF6 concentration to 200 μM which we predicted should be close to its critical assembly concentration under these conditions. This should slow down the assembly kinetics and decrease self-nucleation, favoring Aβ-PHF6 interactions.

5.3 Cross-seeding of Aβ40 and 42 with PHF6

Using fragmented seeds made by sonicating Aβ fibrils, we added them to freshly dissolved PHF6 where we predict that Aβ seeds can template the growth of PHF6 monomers due to the sequence similarity between ^{16}KLV^{19}F of Aβ and QIVY of PHF6. Additionally, because tau aggregation follows amyloidosis in AD where the long Aβ fibrils are more likely to cross-seed tau by secondary nucleation at the sides rather than elongation at the ends, we also tested the seeding efficacy of unfragmented Aβ fibrils.

Figure 5.18 shows that at a concentration of 200 μM, PHF6 does not show an appreciable increase in ThT fluorescence over 48 hours and are in the protofibrillar morphology. In the presence of 1% molar equivalent Aβ40 or 42, the lag phase was bypassed and PHF6 entered the elongation phase promptly, indicative of a seeding mechanism. Since similar kinetic profiles were observed for both Aβ seeds and fibrils, the data suggest that the cross-seeding mechanism occurs via a combination of elongation and secondary nucleation. As the Aβ-only controls maintained ThT fluorescence at or below the level of PHF6-only samples, we can be confident that the cross-seeding was largely a result of PHF6 assembly and not Aβ re-assembly. No increase in ThT fluorescence was seen for the self-seeded PHF6 peptides and no mature fibrils were observed by TEM, indicating that a critical seed concentration must be attained for efficient PHF6 seeding as was the case for Aβ seeding in chapter 4.

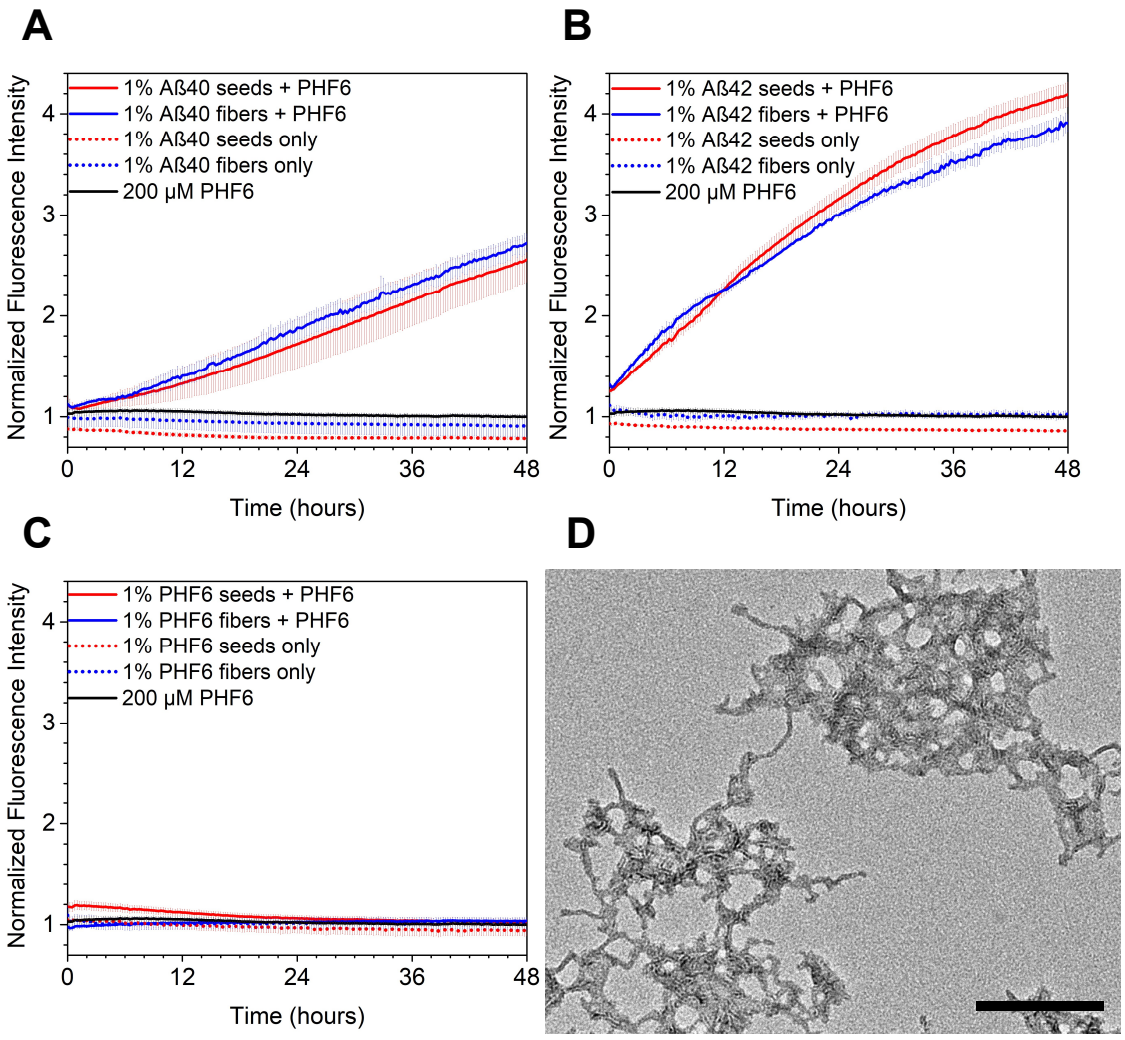

Figure 5.18. Aβ40 and Aβ42 are more efficient seeds for PHF6 assembly than PHF6 itself. ThT fluorescence was used to follow the fibrillization of 200 µM PHF6 monomers at 37 ºC seeded by (A) 1% molar equivalent Aβ40, (B) 1% Aβ42 or (C) 1% PHF6 seeds or fibrils. (D) TEM of the unseeded 200 µM PHF6 sample after 48 hours show aggregated protofibrils. Scale bar: 200 nm.

TEMs of PHF6 seeded by Aβ40 and 42 seeds show short but mature fibrils which stain differently from the control samples containing Aβ seeds alone (**Figure 5.19**). The self-seeded PHF6 however, remained as aggregated protofibrils similar to the unseeded PHF6 sample and at 2 µM, the disassembly kinetics of the PHF6 seeds-only was fast enough to dissolve the aggregates, where only artefacts were found on the TEM grid.

For the fibril-seeded PHF6, the presence of 1% Aβ40 fibrils appeared to have seeded the growth of curvilinear fibrils bound to the sides of longer and straighter fibrils, which appear morphologically similar to the Aβ40 fibrils alone (**Figure 5.20**). Aβ42 fibrils catalyzed the growth of longer PHF6 fibrils that are also distinct from the Aβ42 fibrils. In the absence of PHF6 monomers, the PHF6 fibrils disassemble over 2 days as was the case for PHF6 seeds mentioned above. With PHF6 fibrils and monomers, we saw aggregated protofibrils on the sides of the mature PHF6 fibrils, suggesting that secondary nucleation was dominant over fibril elongation. This interaction is sufficiently stable to prevent the added PHF6 fibrils from disassembling but does not catalyze fibril formation during the experimental timeframe.

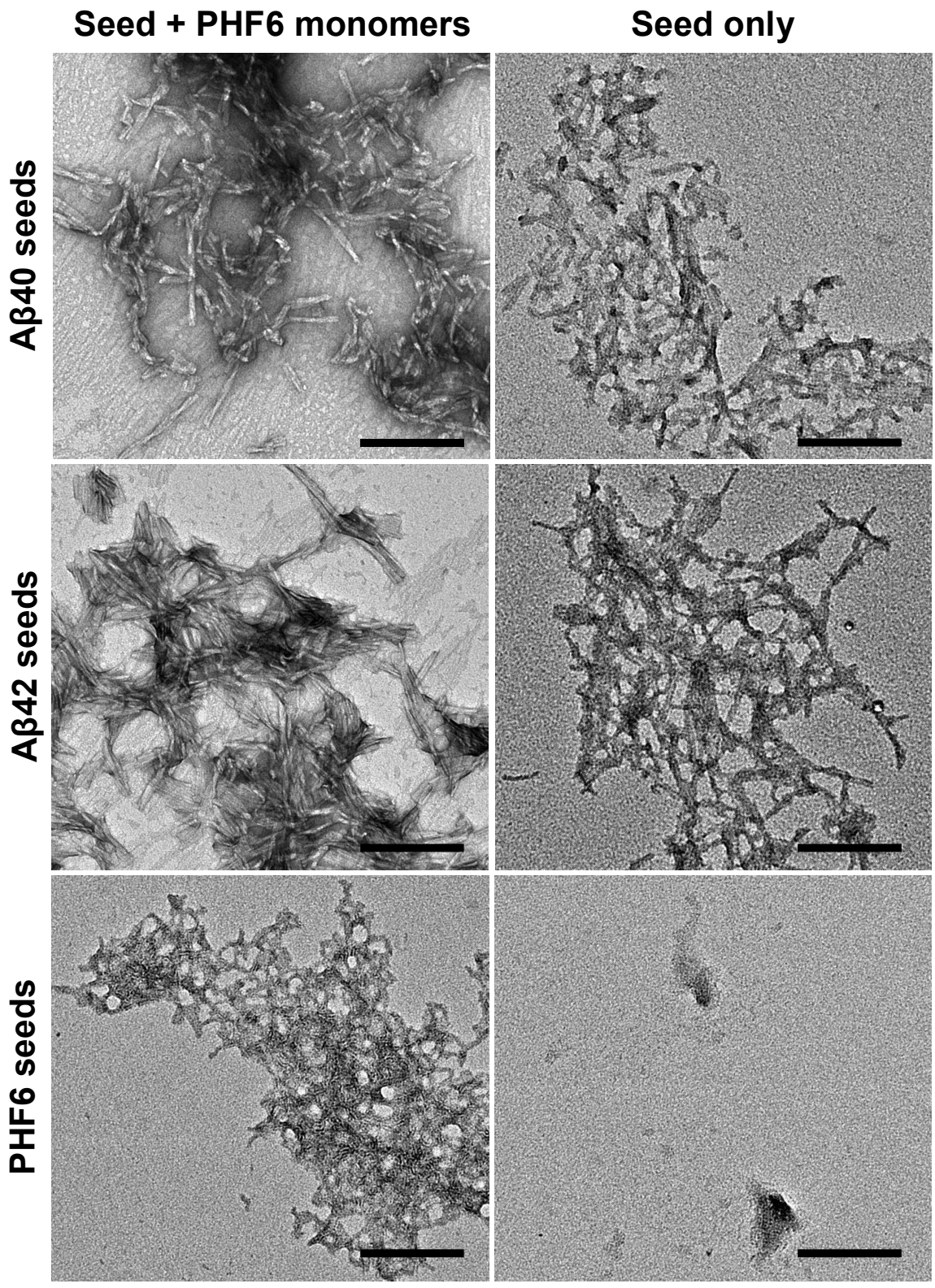

Figure 5.19. Aβ seeds accelerated PHF6 fibril formation. TEMs of 1% Aβ40, Aβ42 and PHF6 seeded-PHF6 samples (left) and seed-only controls (right) after 48 hours at 37 °C. Scale bars: 200 nm.

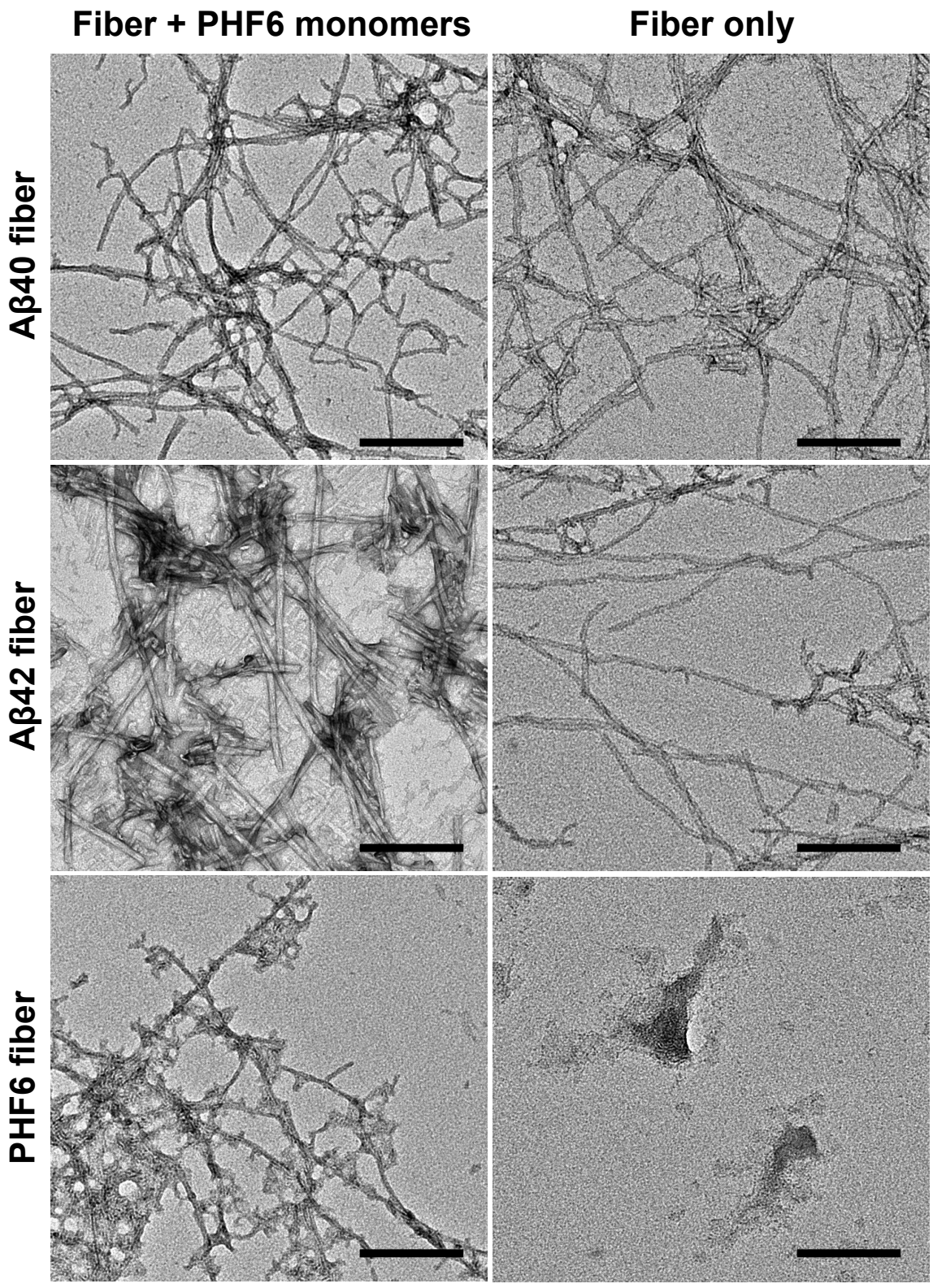

Figure 5.20. Aβ fibrils accelerated PHF6 fibril formation. TEMs of 1% Aβ40, Aβ42 and PHF6 seeded-PHF6 samples (left) and fibril-only controls (right) after 48 hours at 37 °C. Scale bars: 200 nm.

Having shown that various forms of synthetic Aβ are potent seeds for PHF6 fibrillization, we wondered if AD-seeded Aβ cross-seeds PHF6 more aggressively than ND-seeded Aβ, since the extent of tauopathy is more closely related to developing AD. Cross-seeding PHF6 with the brain-seeded Aβ42 granddaughter seeds showed that the AD2(O) and ND2(O) Aβ42-seeded PHF6 had similar kinetic profiles, while AD2(F) and ND2(F) Aβ42-seeded PHF6 had higher and lower profiles respectively. The growth of ND2(F) Aβ42-PHF6 plateaued at around 12 hours and reached a 4.5-fold fluorescence over ThT-only after 64 hours, while AD2(F) Aβ42-PHF6 maintained a steady growth after 12 hours to reach a 6.5-fold intensity at 64 hours (**Figure 5.21A**). The difference in cross-seeding efficiency does not appear to be a function of the amount of seeds, because the ND2(F) Aβ42 seed controls in buffer had higher ThT fluorescence (**Figure 5.21B**) but was the least potent seed for PHF6. Interestingly, this pattern was observed in pFTAA binding to the brain-seeded Aβ42 granddaughters, with the occipital-seeded Aβ42 having superimposable fluorescence excitation spectra, while the frontal-seeded Aβ42 had different relative intensities at 425 nm (**Figure 4.30**).

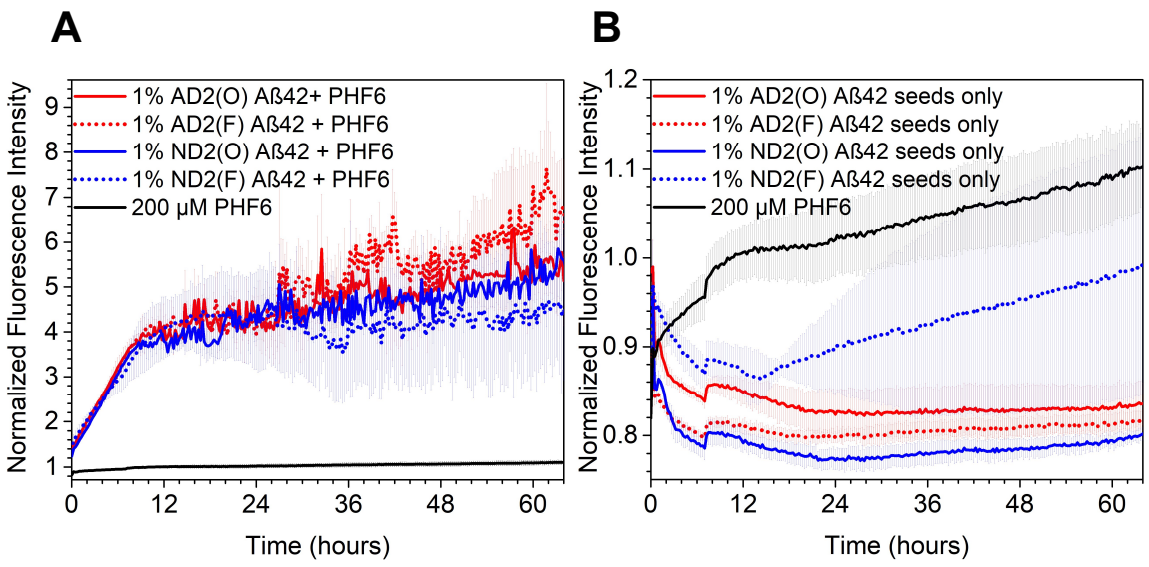

Figure 5.21. Brain-seeded granddaughter Aβ42 cross-seed PHF6 assembly differently. (A) Granddaughter Aβ42 seeded from enriched AD2(O), AD2(F), ND2(O) and ND2(F) fractions were added to PHF6 monomers and the growth was monitored by ThT fluorescence at 37°C over 64 hours. (B) ThT fluorescence of the corresponding Aβ42 seeds in 50 mM tris-HCl buffer pH 7.4.

TEMs of these cross-seeded PHF6 fibrils revealed short but mature fibrils associated with mixed (amorphous, oligomeric and protofibrillar) aggregates in the AD2(F) Aβ42-PHF6 sample, while networks of long, bundled fibers were observed in the ND2(F) Aβ42-PHF6 sample. Both occipital Aβ42-PHF6 assemblies had morphologies similar to each other that were intermediate between the two extremes of the frontal lobe-seeded assemblies (**Figure 5.22**). Therefore, the TEMs agree with the ThT kinetics observed in **Figure 5.21A**.

Taken together, the data suggest that in the initial 10 hours of the biphasic growth, Aβ42 cross-seeds PHF6 fibril formation where the differences between the samples are indistinguishable by ThT. When a critical mass of PHF6 fibers have formed after 10 hours, the PHF6 self-seeding dominates the cross-seeding between Aβ42 and PHF6. In the second growth phase, the rate of PHF6 growth depends on its ability to make its own seeds, with

the ND2(F) Aβ42-PHF6 forming mechanically stronger fibrils that are resistant to fragmentation and less efficient seeds, while the AD2(F) Aβ42-PHF6 forming weaker fibrils that are prone to fragmentation and are more efficient seeds. This is analogous to the strain phenotypes observed in yeast prion models, where Sup35 aggregates in stronger strains are more easily fragmented while in weaker strains, the Sup35 fibers resist breakage and are less efficient seeds [13]. The formation of different PHF6 polymorphs is due to the cross-seeding by different Aβ42 polymorphs, which is in turn due to different Aβ polymorphs in the brain tissues. A subset of Aβ42 structures enriched in ND2(F), to which pFTAA binds and fluoresces highly when excited at 425 nm, cross-seeded the formation of the stable PHF6 strain. Conversely, the subset of Aβ42 structures enriched in AD2(F) to which pFTAA does not bind, cross-seeded the formation of weaker PHF6 fibrils that aggressively seeded itself.

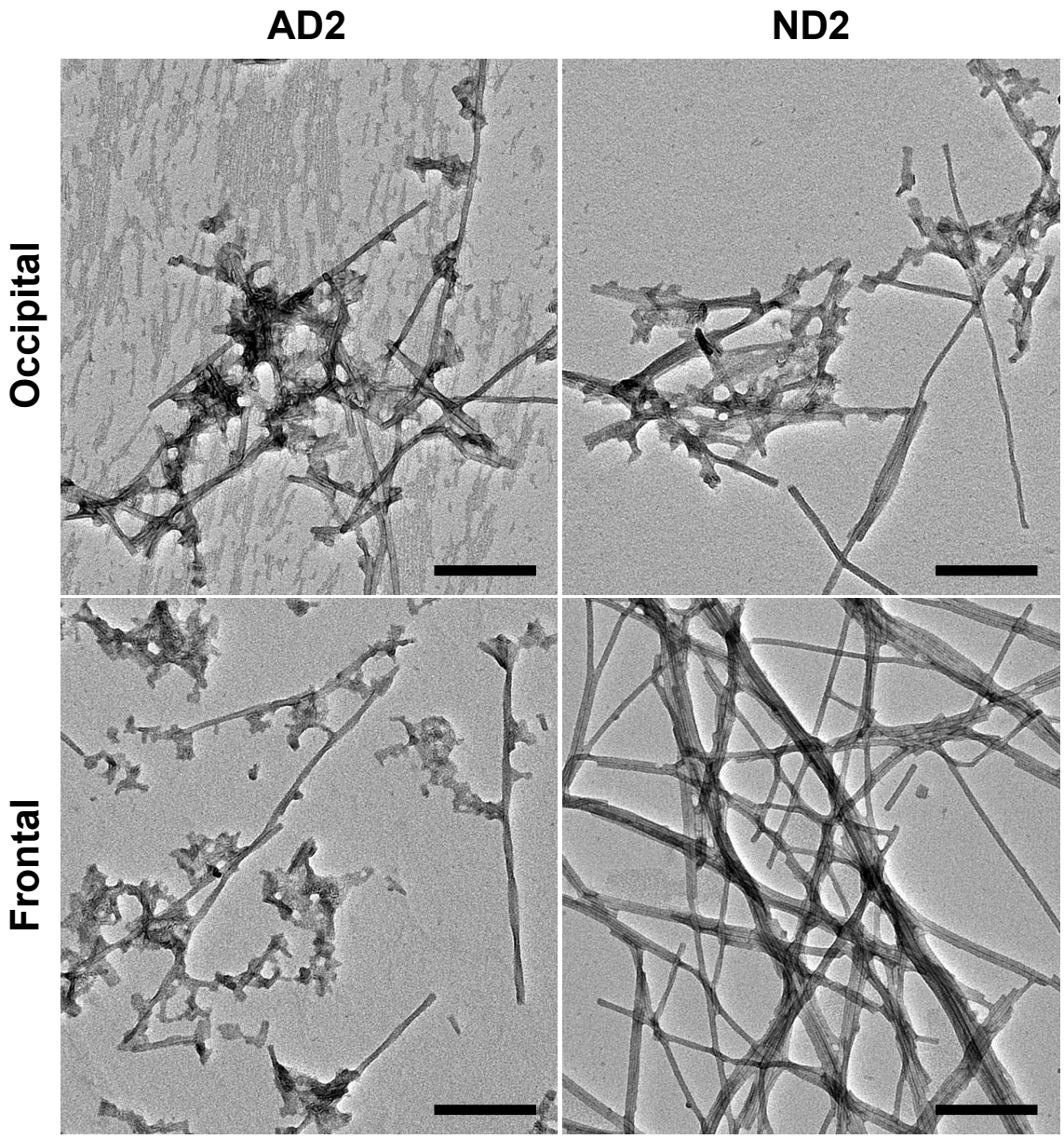

Figure 5.22. PHF6 cross-seeded by AD2 and ND2 Aβ42 granddaughter have different morphologies. TEMs of PHF6 monomers cross-seeded by seeds derived from AD2- and ND2-seeded Aβ42 granddaughters after 64 hours. Labels indicate the origin of the brain tissue used to seed into Aβ42. Scale bars: 200 nm.

Conclusion

Our experiments involving Aβ and PHF6 show conclusively that these two heterologous peptides can directly interact *in vitro*. The resulting assemblies however, tend to

be morphologically heterogeneous which makes structural characterization (by IE-IR, solid-state NMR, cryo EM, etc.) challenging. We have also observed that some peptides (E22Q, Aβ40, Aβ42) accelerate PHF6 assembly and can reduce its critical assembly concentration, while others (E22L) inhibit or kinetically trap PHF6 in intermediate forms, suggesting that Aβ has the potential to directly modulate the assembly pathway of tau into various structures other than PHF fibrils in NFTs. Future experiments will need to decipher the code that exists between Aβ and PHF6 and optimize conditions for obtaining more homogeneous structures to resolve differences between cross-seeded and unseeded PHF6 assemblies. Following that, the model system can be made more physiologically-relevant by scaling up to the cross-seed the R2 and R3 repeat domains (containing PHF6* and PHF6 sequences), the K18 protein (containing the four repeat domains) and full-length tau constructs. If the link between amyloidosis and tauopathy can be understood, then therapeutic targets can be designed to halt the triggering of tauopathy in early-MCI patients.

Materials and Methods

Fourier Transform Infra-Red (FT-IR) spectroscopy

Before peptide samples were analyzed with a Jasco FT-IR 4100 spectrometer, the background was taken after instrument startup. 8 μL of peptide solution was spotted onto the diamond surface of a GladiATR (Pike Technologies) ATR and allowed to dry to a thin film, which is when the broad peak at 3300 cm^{-1} has stabilized after declining. Spectra were recorded with the MCT-M (HgCdTe) detector cooled by liquid N_2, from 1000 to 4000 cm^{-1} at a resolution of 2 cm^{-1} for 512 accumulations. IR spectra were normalized by setting the absorbance at 1725 cm^{-1} to 0 and the ^{12}C amide I stretch (~1630 cm^{-1}) to 1.

Congo red preparation

Since commercially available preparations of Congo red (CR) are contaminated with NaCl and water, CR (Sigma-Aldrich) dye content was quantified and stock solutions were prepared following Klunk et. al.[14] CR (lot no.: 073K3520) was dissolved to 5, 10 and 20 μM in 60% 1 mM NaH_2PO_4, pH 7.0/40% EtOH and the absorbances at 505 nm were measured in a Jasco V-530 UV spectrophotometer (**Figure 5.23**). Using $\varepsilon_{505\ nm}$ = 59 300 L mol^{-1} cm^{-1}, the actual CR concentrations were calculated by the Beer-Lambert law and the dye content (actual concentration/concentration by mass of CR x 100%) was determined to be 84.6 ± 5.7%.

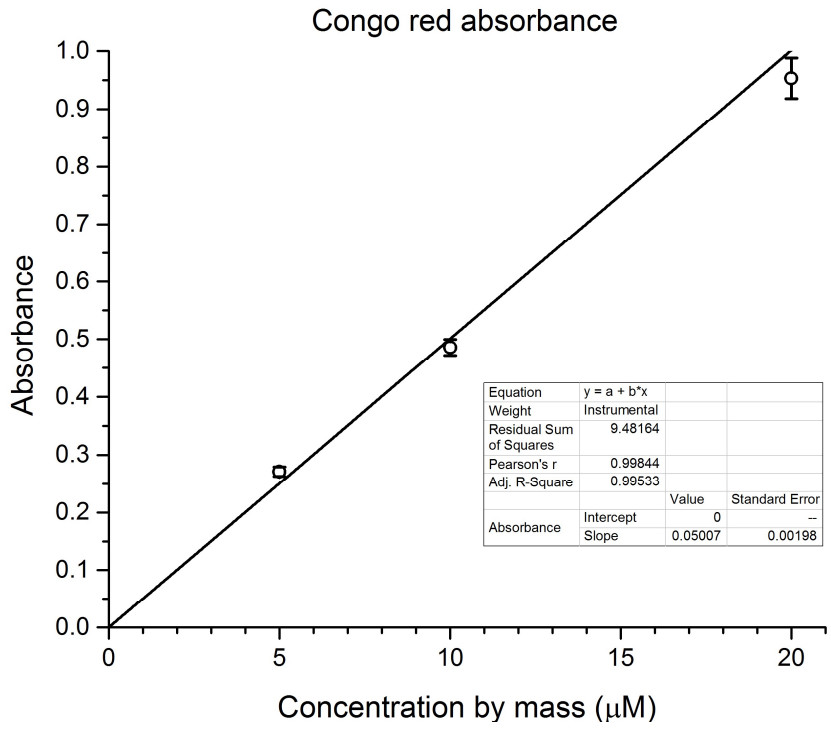

Figure 5.23. Absorbance of Congo red to determine dye content.

A 300 μM stock solution (taking into account the 85% dye content) of CR was prepared in 90% PBS, pH 7.4/10% EtOH and filtered three times through a 0.22 μm PES filter. Aliquots were then stored at -20 °C until ready for use.

Aβ40/42-PHF6 cross-seeding kinetic assays

HFIP-treated PHF6 was reconstituted to 220 μM in 50 mM tris-HCl pH 7.4 buffer and filtered through a pre-rinsed 0.2 μm filter. 200 μl of the PHF6 monomer was then added to each well in a 96-well plate (Corning, Cat. No. 3631) containing 20 μl of seeds or fibrils (20 μM for 1% seeding) and 10 μl of 100 μM ThT. Control wells had the seeds/fibrils or monomers replaced with tris buffer. The plate was sealed with a film and then incubated at 37°C for an hour before ThT fluorescence was measured as described in Chapter 4. Fluorescence intensities were then divided by the intensities of the ThT-only control wells at the respective time points.

References

1. Yamada K, Cirrito JR, Stewart FR, Jiang H, Finn MB, Holmes BB, Binder LI, Mandelkow EM, Diamond MI, Lee VM, et al.: **In vivo microdialysis reveals age-dependent decrease of brain interstitial fluid tau levels in P301S human tau transgenic mice**. *J Neurosci* 2011, **31**:13110-13117.
2. Frost B, Diamond MI: **Prion-like mechanisms in neurodegenerative diseases**. *Nature Reviews Neuroscience* 2009, **11**:155.
3. Walker LC, Diamond MI, Duff KE, Hyman BT: **Mechanisms of protein seeding in neurodegenerative diseases**. *JAMA Neurology* 2013, **70**:304-310.
4. Šimić G, Babić Leko M, Wray S, Harrington C, Delalle I, Jovanov-Milošević N, Bažadona D, Buée L, de Silva R, Di Giovanni G, et al.: **Tau Protein Hyperphosphorylation and Aggregation in Alzheimer's Disease and Other Tauopathies, and Possible Neuroprotective Strategies**. *Biomolecules* 2016, **6**:6.
5. Esbjörner Elin K, Chan F, Rees E, Erdelyi M, Luheshi Leila M, Bertoncini Carlos W, Kaminski Clemens F, Dobson Christopher M, Kaminski Schierle Gabriele S: **Direct Observations of Amyloid β Self-Assembly in Live Cells Provide Insights into Differences in the Kinetics of Aβ(1–40) and Aβ(1–42) Aggregation**. *Chemistry & Biology* 2014, **21**:732-742.

6. Götz J, Xia D, Leinenga G, Chew YL, Nicholas H: **What Renders TAU Toxic**. *Frontiers in Neurology* 2013, **4**:72.

7. Vitali A, Piccini A, Borghi R, Fornaro P, Siedlak SL, Smith MA, Gambetti P, Ghetti B, Tabaton M: **Soluble amyloid beta-protein is increased in frontotemporal dementia with tau gene mutations**. *J Alzheimers Dis* 2004, **6**:45-51.

8. Rapoport M, Dawson HN, Binder LI, Vitek MP, Ferreira A: **Tau is essential to beta -amyloid-induced neurotoxicity**. *Proc Natl Acad Sci U S A* 2002, **99**:6364-6369.

9. Li W, Lee VMY: **Characterization of Two VQIXXK Motifs for Tau Fibrillization in Vitro**. *Biochemistry* 2006, **45**:15692-15701.

10. Grabowski TJ, Cho HS, Vonsattel JP, Rebeck GW, Greenberg SM: **Novel amyloid precursor protein mutation in an Iowa family with dementia and severe cerebral amyloid angiopathy**. *Ann Neurol* 2001, **49**:697-705.

11. Tycko R, Sciarretta KL, Orgel JP, Meredith SC: **Evidence for novel beta-sheet structures in Iowa mutant beta-amyloid fibrils**. *Biochemistry* 2009, **48**:6072-6084.

12. Fitzpatrick AWP, Falcon B, He S, Murzin AG, Murshudov G, Garringer HJ, Crowther RA, Ghetti B, Goedert M, Scheres SHW: **Cryo-EM structures of tau filaments from Alzheimer's disease**. *Nature* 2017, **547**:185.

13. Tanaka M, Collins SR, Toyama BH, Weissman JS: **The physical basis of how prion conformations determine strain phenotypes**. *Nature* 2006, **442**:585.

14. Klunk WE, Jacob RF, Mason RP: **Quantifying amyloid beta-peptide (Abeta) aggregation using the Congo red-Abeta (CR-abeta) spectrophotometric assay**. *Anal Biochem* 1999, **266**:66-76.

Chapter 6. Conclusion

Summary

In chapter 2, we established methods for disaggregating the purified peptides for maximal seeding efficiency. We characterized Aβ and PHF6 when dissolved in HFIP, DMSO and NH_4OH, and found that the peptides tend to form particles in HFIP. Particle formation is unfavorable because it traps the monomers in a compartment where they nucleate instead of allowing them to diffuse to the seeds. DMSO was good at dissolving the bulk peptide powder into clear solutions, but widespread aggregates are still detectable by TEM. NH_4OH treatment produced the least amount of Aβ aggregates but caused PHF6 to form needle-like fibrils. Filtering the reconstituted monomeric peptide solutions also helped in removing the surviving aggregates. Given that all three solvents have been used to monomerize Aβ in the literature but only NH_4OH works best for us, we conclude that the peptide synthesis and purification processes influence the peptides' behavior in the solvents and disaggregation methods should be optimized in every lab.

In chapter 3, we explored the feasibility of quantifying PiB binding by fluorescence as an initial screen before performing radioligand binding assays. The fluorescence of PiB blue-shifted from 430 to ~400 nm upon binding to Aβ, but this blue-shift can also be induced by dissolving PiB in hydrophobic solvents. Total PiB (bound and unbound) fluorescence can therefore be measured, but we encountered unexpected challenges when trying to separate bound from unbound PiB. In the absence of Aβ, PiB binds non-specifically to filters and can be concentrated by centrifugation which makes it difficult to establish a negative control for the assay. As such, we decided that PiB fluorescence was only

good for probing for the presence of PiB binding by looking for a blueshift, but not for quantifying binding.

In chapter 4, we developed methods for seeding brain extracts into synthetic Aβ40 and 42. Low-speed supernatants of brain homogenates were ineffective seeds and required treatment with pronase, benzonase, sarkosyl and sodium phosphotungstate to enrich for Aβ. Also, the protocol for amplifying synthetic Aβ was not completely transferrable to brain-seeded Aβ40 which required extended sonication, suggesting that those fibrils are mechanically stronger than the pure synthetic fibrils and affirms that seeding proceeds by elongation at the fibril ends rather than by secondary nucleation at the sides. The HS-68 oligothiophene was able to differentiate between quiescent, agitated and brain-seeded Aβ40 granddaughters, but could not resolve differences between the AD2 and ND2 Aβ40 granddaughters. The LCOs showed more spectral differences upon binding to AD2 and ND2 Aβ42 granddaughters. Notably, the pFTAA excitation spectra showed different relative intensities at 425 nm, indicative of binding to unique populations of Aβ structures. This trend was also observed when they were cross-seeded into PHF6 (chapter 5), with AD2(F) Aβ42 having a low intensity at 425 nm but seeding PHF6 strains that are efficient seeds, and ND2(F) Aβ42 having a high intensity at 425 nm but seeding PHF6 strains that were inefficient seeds. Therefore, we have demonstrated that the structure of Aβ aggregates is directly linked to its ability to cross-seed PHF6 and perhaps tau in AD. Since PHF6 growth kinetics are similar when cross-seeded by long fibrils or short seeds, the mechanism is likely to be a combination of elongation and secondary nucleation. Within our experimental timeframe, a small molar equivalent (1%) of Aβ aggregates sufficiently lowered PHF6's critical assembly concentration and catalyzed its growth, highlighting a therapeutic opportunity for halting the progression of AD at this pivotal transition.

In conclusion, we have optimized the seed and monomer conditions for efficiently amplifying Aβ from brain tissues into synthetic Aβ. Although we have yet to define the structural differences between AD and ND Aβ assemblies that are disease-relevant, we have demonstrated the prion-like property of Aβ from human brains in transmitting structural information while crossing multiple seeding barriers and surviving at least two freeze-thaw cycles (**Figure 6.1**).

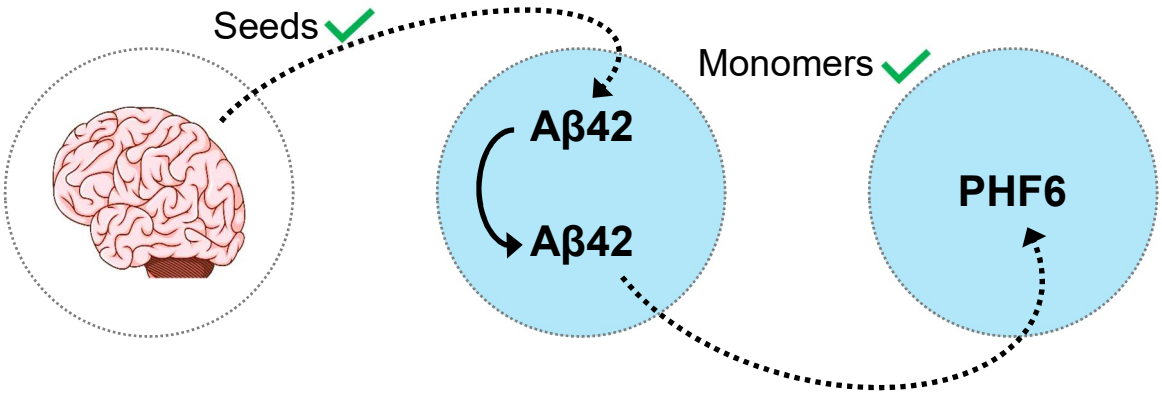

Figure 6.1. Prion-like propagation of amyloids in brain tissues to synthetic PHF6 via Aβ42. Efficient seeding requires the enrichment of amyloid in the seed fractions and disaggregation of synthetic peptides into monomers. Aβ strains crossed the first barrier (dotted arrow) when the enriched fractions from human brain homogenates were seeded into synthetic Aβ42. Homologous seeding (solid arrow) into another generation of Aβ42 further amplified the strains, which crossed another barrier during heterologous seeding into PHF6, spawning different fibril morphologies.

Outlook

Studies to explain why human-derived amyloids are more potent seeds compared to synthetic and recombinant amyloids will be useful to identifying the pathogenic entities. Are oligomers more toxic than fibrils and how are functional amyloids nontoxic to cells? Are there cofactors such as nucleic acids, metals or proteins in the extracts, or is the environment in the human brain more effective at templating neurotoxic amyloid? If so, can a cocktail of

cofactors and conditions be discovered to convert synthetic material into high-potency seeds for structural and functional studies?

Another mystery involves the similarities between protein aggregation diseases. Are there common pathological mechanisms between AD and other amyloid diseases such as Parkinson's, Huntington's, ALS, etc.? How do environmental forces such as TBI (traumatic brain injury) or CTE (chronic traumatic encephalopathy) increase the risk of AD?

Other unresolved questions include how cognitive reserve mitigates AD progression. Cognitive reserve is thought to be influenced by the individual's educational attainment, occupation, socio-economic status, diet and lifestyle. Postmortem analyses of cognitively normal individuals above 85 years old have shown that more than 25% have sufficient plaque and NFT loads to qualify for AD diagnosis, yet the patients' cognitive functions are resistant to dementia, at least until the time of death [1]. Understanding this connection could lead to treatments that rescue cognitive function in patients.

The development of reliable biomarkers for early detection, perhaps using a combination of CSF protein levels (Aβ, total tau, p-tau) and neuroimaging (PET and MRI) together with identification of risk factors (ApoE genotype, APP mutations, etc.) will continue to be a major goal. These biomarkers will be essential tools for the prognosis of presymptomatic and MCI patients, and evaluating AD drug candidates. However, virtually every drug candidate targeting Aβ (secretase inhibitors and humanized anti-Aβ antibodies) drops out of clinical trials due to the lack of cognitive improvement in the patients. One of the major reasons is that amyloid deposition has already plateaued when symptoms emerge, and the downstream events are more pathological than the amyloid plaques. The most ideal approach to treating AD will be to intervene at the prodromal phase because it precedes

neurodegeneration and the need to restore neurons can be avoided. With studies showing that amyloid plaques are dynamic, not static sinks for Aβ and the diverse polymorphs of Aβ aggregates that are likely to be disease-relevant, an Aβ-focused treatment would mean that multiple moving targets must be identified. Resolution of the mechanistic link between Aβ and tau aggregation, representing a bottleneck in the onslaught of the disease, may be a more attractive therapeutic opportunity. Pre- or early-MCI individuals identified through routine physical examinations may then be offered treatments that prevent the triggering of tauopathy to halt the progression of AD.

References

1. Maarouf CL, Daugs ID, Kokjohn TA, Walker DG, Hunter JM, Kruchowsky JC, Woltjer R, Kaye J, Castano EM, Sabbagh MN, et al.: **Alzheimer's disease and non-demented high pathology control nonagenarians: comparing and contrasting the biochemistry of cognitively successful aging**. *PLoS One* 2011, **6**:e27291.

Appendix 1: Structures of Amyloid ligands

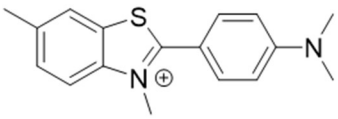

Thioflavin T (ThT)

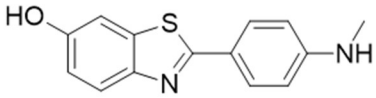

PiB (6-OH-BTA-1)

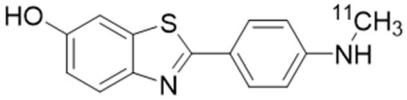

Pittsburgh Compound B ([^{11}C]PiB)

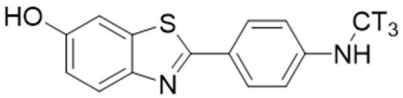

[^{3}H]PiB

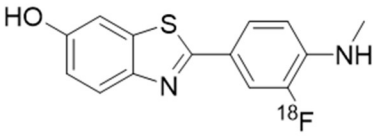

Flutemetamol, [^{18}F]3'-F-PiB, GE-067

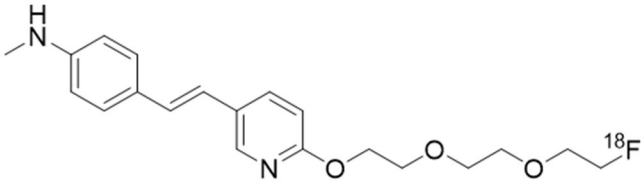

Florbetapir (Amyvid), [^{18}F]AV-45

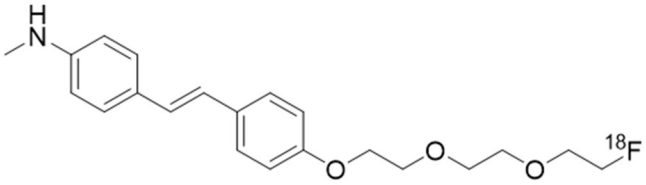

Florbetaben (Neuraceq), [^{18}F]AV-1

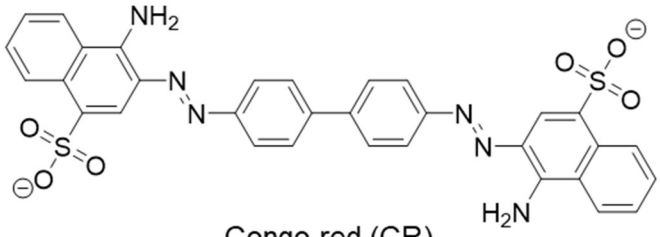

Congo red (CR)

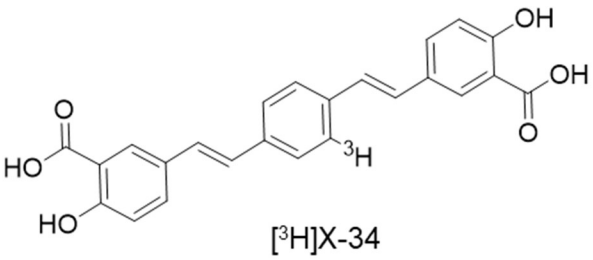

[^{3}H]X-34

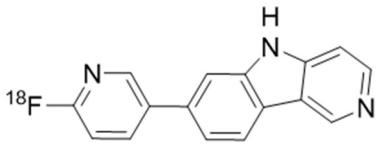

[^{18}F]T807 /AV-1451

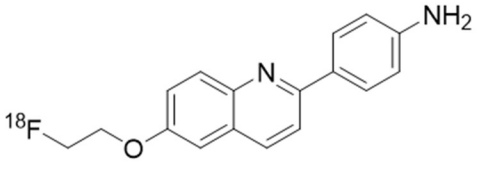

[^{18}F]THK-523

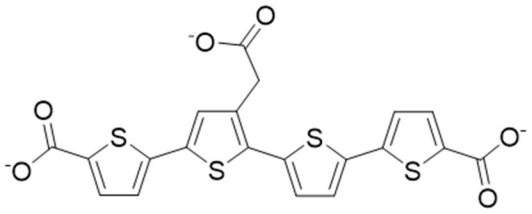

HS-68

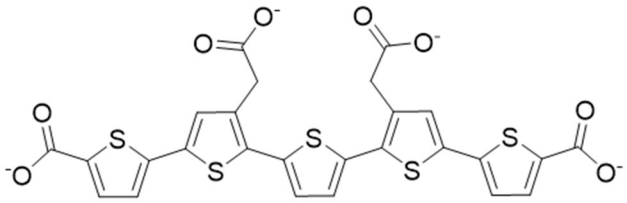

pFTAA

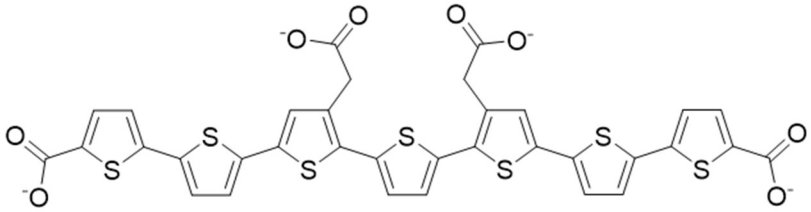

hFTAA